Universität Karlsruhe (TH)

IEKP-KA/2009-18

Entwicklung von hoch strahlenharten Siliziumstreifensensoren für den Einsatz am Super Large Hadron Collider

Martin Frey

Zur Erlangung des akademischen Grades eines
DOKTORS DER NATURWISSENSCHAFTEN
von der Fakultät für Physik der
Universität Karlsruhe (TH)

genehmigte

DISSERTATION

von

Dipl.-Phys. Martin Frey
aus Bad Bergzabern

Tag der mündlichen Prüfung: 19.6.2009

Referent: Prof. Dr. Thomas Müller, Institut für Experimentelle Kernphysik
Korreferent: Prof. Dr. Willem de Boer, Institut für Experimentelle Kernphysik

Inhaltsübersicht

Seit vielen Jahren werden in Experimenten im Bereich der Hochenergiephysik erfolgreich Halbleitersensoren eingesetzt, für einen schnellen und zuverlässigen Nachweis von ionisierenden Teilchen. Die Technologie hat bezüglich der Strahlenhärte derzeit im Compact Muon Solenoid (CMS) Spurdetektor am Large Hadron Collider (LHC) am CERN[1] ihren Höhepunkt erreicht, wo Siliziumpixel- und Siliziumstreifensensoren eine Oberfläche von ungefähr 207 m^2 bedecken. Die Streifensensoren müssen dabei die Schädigungswirkung von Strahlung mit Fluenzen bis hin zu $1,9 \cdot 10^{14}/cm^2$ überstehen. Pläne für ein LHC Upgrade, bekannt unter der Bezeichnung SLHC[2], sehen eine Luminositätssteigerung um einen Faktor zehn von bisher $10^{34}\ cm^{-2}s^{-1}$ auf $10^{35}\ cm^{-2}s^{-1}$ vor. Die Strahlenhärte von Sensoren, die einer wie am SLHC erwarteten Strahlenbelastung ausgesetzt sein werden, muss größer sein als die der derzeit verwendeten Sensoren. Dies erfordert eine Weiterentwicklung der Technologie, eine Entwicklung neuer Sensordesigns und die Identifizierung strahlenharter Materialien.
Strahlenschäden im Halbleitergitter führen zu drei makroskopischen Effekten die eine Verminderung der Sensorqualität und eine Veränderung der Sensoreigenschaften zur Folge haben. Leckströme nehmen zu, die Depletionsspannung verändert sich und die Ladungssammlungseffizienz nimmt ab. Es wurde nachgewiesen, dass durch den hohen Sauerstoffgehalt in Magnetic Czochralski (MCz) Silizium die Depletionsspannung mit höheren Fluenzen weniger stark zunimmt als im Falle von gewöhnlich verwendetem Silizium aus dem Zonenschmelzverfahren. Daher ist bei einer vorgegebenen Spannung ein größeres depletiertes und damit aktives Sensorvolumen vorhanden, wodurch Teilchendurchgänge höhere Signale zur Folge haben.
Die Eigenschaften von hoch bestrahlten MCz Sensoren sind noch nicht ausreichend erforscht. Insbesondere waren bislang die für einen Nachweis von minimal ionisierenden Teilchen so wichtigen Parameter, Ladungssammlungseffizienz und Signal zu Rausch Verhältnis, von mit SLHC Fluenzen bestrahlten segmentierten Sensoren noch nicht bekannt. Zwei im Rahmen der Dissertation durchgeführte Testprogramme waren ausgelegt für die Messung dieser Kenngrößen von p-in-n MCz Streifensensoren in Strahltests mit minimal ionisierenden Myonen einer Energie von 225 GeV. Ein Ziel der Untersuchungen war, festzustellen ob n-Typ MCz Silizium die notwendige Strahlenhärte für einen Einsatz in der gesamten Streifen- beziehungsweise Kurzstreifenregion eines CMS Spurdetektors am SLHC bietet. Es wurde zunächst die Qualität von speziell gefertigten Sensoren in einer Teststation überprüft. Es folgten Bestrahlungen der Sensoren mit Protonen und teilweise zusätzlich Neutronen von Gesamtfluenzen zwischen $1 \cdot 10^{14}\ neq./cm^2$ und $1,6 \cdot 10^{15}\ neq./cm^2$, bei denen der komplette erwartete Fluenzbereich eines zukünftigen CMS Streifen- beziehungsweise Kurzstreifen Spurdetektors am SLHC berücksichtigt wurde. Der Einfluss der Bestrahlungen auf wichtige Funktionskenngrößen wurde in der Teststation untersucht. Anschließend wurden aus einer Trägerstruktur, einem Sensor und einer adäquaten Ausleseelektronik Detektormodule gefertigt. Diese waren ausgelegt für

[1] Conseil Européen pour la Recherche Nucléaire
[2] Super Large Hadron Collider

Tests in einem neuen Strahlteleskop welches im Strahltest die notwendigen Informationen über die Teilchenspuren lieferte. Nach einer Modifikation einer am Institut für Experimentelle Kernphysik der Universität Karlsruhe geschriebenen Analyse-Software erfolgte die Datenauswertung. Um die Ergebnisse zu untermauern und weitere generelle Eigenschaften von hoch bestrahlten MCz Sensoren zu untersuchen, wurden weitergehende Laborexperimente und Simulationen des Ladungssammlungsprozesses durchgeführt. In einer Modulteststation wurden die Ladungssammlungseffizienzen und Signal zu Rausch Verhältnisse bei tieferen Temperaturen (bis zu -40°C) und höheren Spannungen (bis zu 1000 V) bestimmt. Der Vergleich der Simulationsdaten mit den Messergebnissen lieferte wichtige Erkenntnisse über Parameter die den sogenannten "Trapping Effekt" beschreiben, die Abnahme von gesammelter Ladung durch den Einfluss von Strahlenschäden. In einer "Transient Current Technique" Messanlage wurden außerdem Untersuchungen zum Auftauchen eines doppelten p-n-Übergangs ("Double Junction Effekt") durchgeführt.
Die Ergebnisse der Strahltests, der Labor-Untersuchungen und der Simulationen lieferten Informationen über die Eigenschaften von hoch bestrahlten n-Typ MCz Siliziumsensoren die nicht nur von allgemeinem Interesse sind, sondern zudem die Bewertung des Materials im Hinblick auf eine Verwendbarkeit in einem zukünftigen CMS Spurdetektor am SLHC ermöglichen.

Universität Karlsruhe (TH)

IEKP-KA/2009-18

DEVELOPMENT OF HIGHLY RADIATION HARD SILICON STRIP SENSORS FOR USE AT THE SUPER LARGE HADRON COLLIDER

Martin Frey

Zur Erlangung des akademischen Grades eines
DOKTORS DER NATURWISSENSCHAFTEN
von der Fakultät für Physik der
Universität Karlsruhe (TH)

genehmigte

DISSERTATION

von

Dipl.-Phys. Martin Frey
aus Bad Bergzabern

Tag der mündlichen Prüfung: 19.6.2009

Referent: Prof. Dr. Thomas Müller, Institut für Experimentelle Kernphysik
Korreferent: Prof. Dr. Willem de Boer, Institut für Experimentelle Kernphysik

Contents

Chapter 1

Introduction

For many years semiconductor sensors have been successfully used in many high energy physics experiments for a fast and reliable particle detection. The technology has its current peak in size and radiation hardness at the Compact Muon Solenoid (CMS) tracker at the Large Hadron Collider (LHC), where silicon pixel and mainly silicon strip sensors cover a surface of roughly 207 m^2. The strip layers have to withstand fluences of up to $1.9 \cdot 10^{14}/cm^2$. Plans for an LHC upgrade, known as the SLHC[1], foresee a peak luminosity increase by a factor of ten of so far $10^{34}\ cm^{-2}s^{-1}$ up to $10^{35}\ cm^{-2}s^{-1}$. The radiation hardness of semiconductor sensors that are exposed to total radiation fluences like the ones expected at the SLHC has to be higher than the one of the current sensors. Therefore the technology has to be improved, new sensor designs have to be developed and radiation hard basic materials have to be identified.
Radiation damages in the semiconductor lattice have three macroscopic effects that lead to a degeneration of the sensor quality. The leakage currents increase, the full depletion voltage changes and the charge collection efficiency decreases. It has been shown that the high oxygen content of Magnetic Czochralski (MCz) silicon has a positive influence on the development of the full depletion voltage with the radiation fluences. The full depletion voltage increases less with higher fluences than in the case of standard float zone (FZ) silicon, so that with a given bias voltage a larger depleted sensor volume results and thus the signal of traversing particles increases.
The properties of highly irradiated MCz sensors are still not sufficiently explored. Especially the important parameters for the detection of minimum ionizing particles, the charge collection efficiencies and the achievable signal to noise ratios, have not been known so far for segmented sensors, irradiated with SLHC fluences. The main test programs presented in this thesis were dedicated for the measurements of these parameters of p-in-n MCz strip sensors in two beamtests with minimum ionizing 225 GeV muons. One aim of the investigations was, to clarify whether n-type MCz silicon offers the necessary radiation hardness for an application in the complete strip or short-strip detector region of a CMS tracker at the SLHC. Special test sensors have been tested before and after the irradiations with protons and partly neutrons of fluences of up to $1.6 \cdot 10^{15}\ neq./cm^2$ (chapter 8). The total fluence range of a future CMS strip/short strip tracker at the SLHC has been considered by that. The highest fluences even correspond to outer pixel layers. Detector modules consisting of a carrier structure, a sensor and an appropriate readout electronics have been build, suitable for the use in a new beamtelescope which delivered the essential information of particle tracks. The results of the beamtests are presented in chapter 9. To substantiate the results and to investigate in general properties of highly irradiated MCz sensors, further experiments in the laboratory and simulations of the charge collection

[1] Super Large Hadron Collider

processes have been done. The important outcome of the comparison between the simulations and the experimental values can be found in chapter 11. In a module teststation, the charge collection efficiencies and the signal to noise ratio at deeper temperatures (-40°C) and higher voltages (1000 V) have been determined (chapter 10). In a transient current technique setup investigations for the appearance of the double junction effect have been done (chapter 12).
In a review of the results in chapter 13 the question whether p-in-n MCz sensors offer the necessary quality to deliver sufficiently high signal to noise ratios for a reliable application in the inner strip regions will be answered.

Chapter 2

The Large Hadron Collider and its Upgrade

2.1 The Large Hadron Collider and the CMS-Detector

2.1.1 The Accelerator Complex

The Large Hadron Collider (LHC) is a particle accelerator at CERN[1] near Geneva built in the tunnel of the former LEP[2] accelerator, with a circumference of around 27 km. It accelerates two proton beams in opposite directions, being brought to collision at four interaction points where dedicated detector facilities are arranged. The machine is designed for a center-of-mass energy of 14 TeV and a luminosity of $10^{34}\ cm^{-2}s^{-1}$. In addition to the protons, during dedicated periods also heavy ions will be accelerated for special experiments up to a luminosity of $10^{27}\ cm^{-2}s^{-1}$. [Pri02]
As for a circular accelerator the relation $p[GeV/c] \approx 0.3B[T]r[m]$ is valid, with the momentum p of the circulating particle, r the radius of curvature of its trajectory and B the bending magnetic field, a high magnetic field has to be applied at the given radius of the LHC. Therefore the field of the bending dipole magnets at 7 TeV reaches 8.4 T. To establish such a high field strength a current of 11.5 kA is necessary, which shows why superconducting materials are used to achieve this in a practical way without ohmic power loss [Pri02]. The chosen superconducting material for the 1232 14 m long bending magnets is NbTi, cooled by superfluid helium below 2 K.
The beam structure at the peak luminosity of $10^{34}\ cm^{-2}s^{-1}$ is, that 2808 bunches of about $1.15 \cdot 10^{11}$ particles will be in the ring with a bunch spacing of 25 ns [LHC]. Figure 2.1(a) gives an overview of the LHC and the arrangement of the associated detector complexes. In figure 2.1(b) the LHC injector chain can be seen, where the protons get an energy of up to 25 GeV. From there they are sent into the SPS[3], where they are further accelerated up to the energy of 450 GeV before being finally injected into the LHC main accelerator.
The detector facilities which can be seen in figure 2.1(a) belong to experiments with partly different purposes. With different design approaches the two big detector complexes ATLAS[4] and CMS[5] are foreseen for general purpose measurements. The ALICE[6] detector is specialized on heavy ion physics

[1] Conseil Européen pour la Recherche Nucléaire
[2] Large Electron-Positron Collider
[3] Super Proton Synchrotron
[4] A Toroidal LHC AparatuS
[5] Compact Muon Solenoid
[6] A Large Ion Collider Experiment

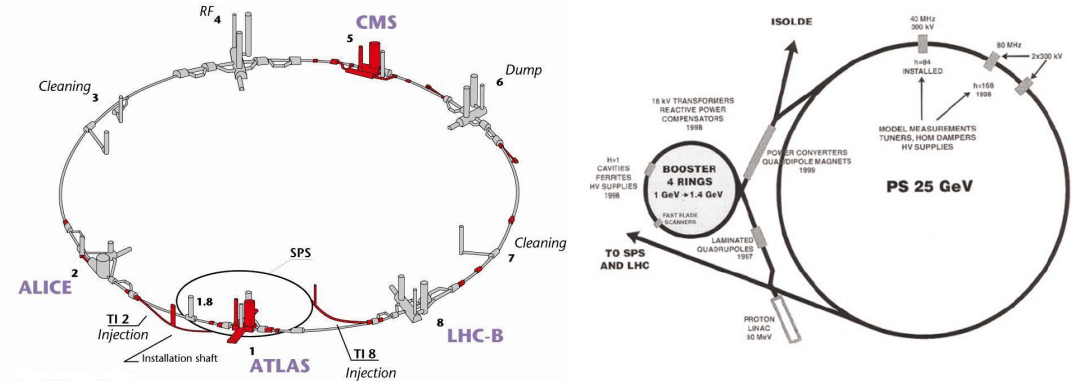

(a) (b)

Figure 2.1: ***Layout of the Large Hadron Collider.*** *a) Arrangement of the LHC accelerator complex and its detector facilities and service halls [Hei]. ATLAS and CMS are foreseen for general purpose measurements. The ALICE detector is specialized on heavy ion physics and the LHCb experiment has its focus on b-physics. b) LHC injector chain [CC2]. The protons get accelerated in linear accelerators and synchrotrons before being injected into the main LHC accelerator.*

and the LHCb[7] experiment has its focus on b-physics.

2.1.2 The Compact Muon Solenoid Detector

Figure 2.2 shows a 3D-view of the principle layout of the Compact Muon Solenoid (CMS) detector. The detector is divided into a barrel part of five slices and two end-cap parts of three slices each. The inner barrel slice holds a 13 m long superconducting solenoid magnet with a diameter of 5.9 m, which delivers the high magnetic field of up to 4 T to ensure measurements with a good momentum resolution. Its return field is strong enough to saturate the 1.5 m thick iron of the yoke at the outer part of the detector, where the muon chambers are embedded [Vir04]. Four layers of muon tracking chambers exist for the barrel as well as for the end-caps. The barrel part is equipped with Drift Chambers. Because of the high particle flux in the end-caps, Cathode Strip Chambers are used in the end-caps together with Resistive Plate Chambers for triggering.
Beside the two forward calorimeters at the end-caps and the muon chambers, all other sub-detectors are located inside the magnet coil. The tracking detector consists of layers of silicon pixel sensors near the interaction point, followed by layers of silicon strip sensors. In chapter 2.1.2 some more details will be presented. Around the tracker, an electromagnetic calorimeter is assembled based on lead tungstate ($PbWO_4$) crystal scintillators, where the scintillation light is detected by silicon avalanche photodiodes. It is surrounded by a brass/scintillator sampling hadronic calorimeter. Wavelength shifting fibres embedded in the material collect the scintillation light and channel it to the photodiode detectors.
The overall size of CMS is 21.6 m in length and 14.6 m in diameter. Despite its relative compactness compared with ATLAS, the facility is heavier and weighs 12500 tons.

[7] Large Hadron Collider beauty

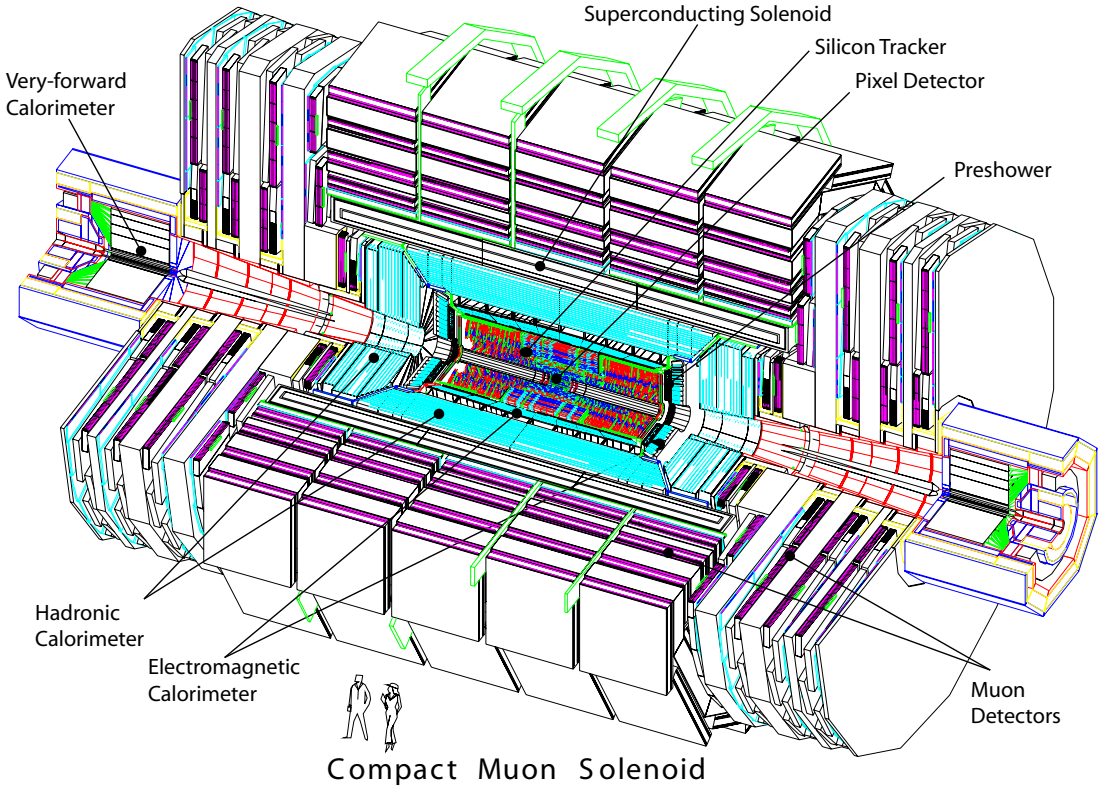

Figure 2.2: ***Layout of the CMS detector [CMSc].*** *Near the interaction point, a silicon pixel and a silicon strip tracker are arranged, followed by an electromagnetic calorimeter and a hadronic calorimeter. These subdetectors are placed inside the superconducting magnet. Outside of it, muon chambers are embedded in the iron yoke for the magnetic return field.*

The CMS-Tracker

The CMS tracker, illustrated in figure 2.3 is presented in more details here, as this thesis was accomplished in the framework of the research for an upgrade of this detector facility. Nevertheless the results are of relevance for a general understanding of radiation hard sensor materials.
Particles with very short lifetimes decay before reaching a tracking detector and can only be tagged by an identification of secondary vertices. The high track density near the interaction point demand a high granularity of the detector device, together with a good resolution. Therefore the inner tracker is equipped with three barrel layers and at both ends two end-cap layers of silicon pixel sensors. They are produced out of 250 μm thick oxygenated n-doped silicon of a resistivity of 2 $k\Omega cm$ and have n^+-doped pixels with a size of 100 x 150 μm^2. The inner layer is located at a distance of 4.3 cm from the beam pipe.
The pixel layers are surrounded by several layers of silicon strip detectors. There are ten layers in the barrel part, divided into the sub-parts Tracker Inner Barrel (TIB) and Tracker Outer Barrel (TOB), while at each of the two forward regions three Tracker Inner Disks (TID) can be found, completed by the Tracker End Caps (TEC) of which each consists of nine disks. The basic element of the layers are detector modules with one or two sensors connected to a so-called Front End Hybrid, which contains the readout electronic chips. Depending on the position in the tracker, different sensor and module

designs are applied, because of the different requirements resulting from the occupancy, the hit multiplicity and the radiation effects at that special position. Therefore sensors with strip pitches between 80 μm and 200 μm and thicknesses of 320 μm and 500 μm are in use with resistivities between 2 $k\Omega cm$ and 4 $k\Omega cm$ [CMSa]. The modules of the inner parts comprise one sensor, while outer ones are built of two daisy-chained ones. All sensors are produced out of n-type silicon with p-type strips. Overall there are 15148 modules out of 24244 strip sensors covering a surface of around 206 m^2 [CMS00]. The 5.4 m long tracker with a diameter of 2.4 m has to be cooled to -10°C to cope with the damaging effects of the radiation. The innermost layers of the strip tracker receive a fluence of fast hadrons of $1.91 \cdot 10^{14}\ cm^{-2}$. The sensors are designed to anyway not exceed a full depletion voltage of 450 V.

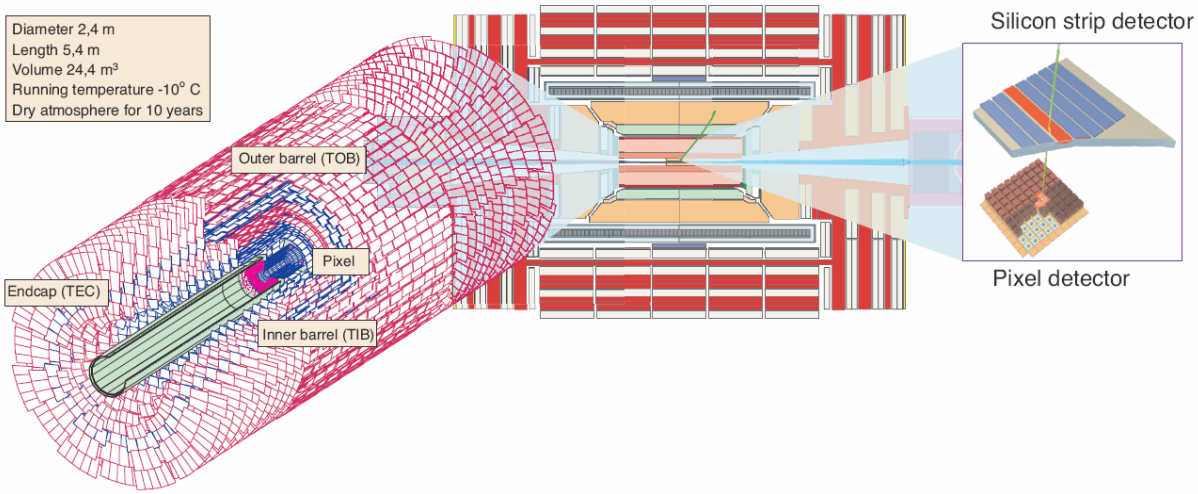

Figure 2.3: ***Layout of the CMS silicon tracker [Har02a].*** *15148 modules out of 24244 strip sensors cover a surface of around* 206 m^2 *[Har02b]. The modules differ in design according to the location in the tracker. Sensors with strip pitches between* 80 μm *and* 200 μm *and thicknesses of* 320 μm *and* 500 μm *are in use with resistivities between* 2 $k\Omega cm$ *and* 4 $k\Omega cm$.

2.2 The LHC Upgrade (SLHC)

After some years of operation of the LHC, the gain in the precision of the measurement results by reductions of the statistical errors, achieved in further operation, becomes marginal. The time to halve the statistical errors after eight years of operation is evaluated to be five years [Tri08]. In figure 2.4 the integrated luminosities for two possible LHC running scenarios are plotted (thick lines) against the runtime. The same plot also shows how much additional runtime is required at a specific time to halve the statistical errors of the measurements done so far. As in addition to that minor gain in precision, the lifetime of the LHC Interaction Region (IR) quadrupoles is expected to be around eight years and the radiation hardness of many detector components, especially of the tracker, will be nearly reached then, an upgrade of the accelerator and the detector systems to achieve an increased luminosity are reasonable. This upgraded accelerator complex is handled with the naming Super Large Hadron Collider (SLHC).

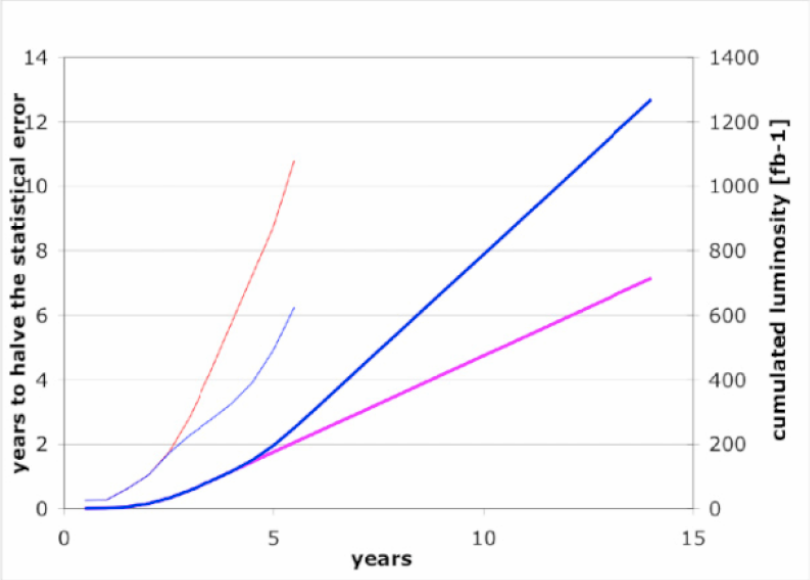

Figure 2.4: ***Additionally needed years of LHC operation to halve the statistical errors plotted against the years of operation (thick lines). [Nas07]*** *The integrated luminosities for two possible LHC running scenarios are plotted (thick lines) against the time in years after the LHC start, together with the required additional run-time to halve the statistical errors of the measurements done at that specific time. The gain in precision with further operation becomes marginal.*

2.2.1 Accelerator Upgrade Scenarios

Current plans foresee a luminosity increase by one order of magnitude towards a peak luminosity of $10^{35}\ cm^{-2}s^{-1}$ to deliver an integrated luminosity of around 3000 fb^{-1} during the machine's operation time. Due to this, the sensitivity for so far rate-limited measurements will enhance and the discovery reach for new particles will be extended, like for the ones predicted by Supersymmetry. The gain in the mass reach is calculated to be between $20-30$ % [Tri08]. Different upgrade scenarios are discussed. They can be found in reference [Zim07].
The number of simultaneously happening proton-proton collisions per bunch-crossing ("pile-up") must be in a range, with which the occupancies of the sub-detector channels remain low enough to guarantee a reliable particle separation. The occupancy of the current tracker channels would increase by a factor of roughly five in comparison to the LHC in the scenario with a doubled number of bunches, where the bunch crossing frequency changes to 80 MHz. As the estimated heat load from image currents, from the synchrotron radiation and from the contribution of electron clouds reach the maximum cooling capacity, another scenario is considered. The bunch crossing frequency would be shifted to 20 MHz and the bunches would be longer with a higher number of protons. The disadvantage of this concept is, that one has to cope with more than 300 pile-up events [Nas07].
In any scenario, the luminosity raise requires improvements in the injector chain. In figure 2.5 the LHC injector- and accelerator complex is illustrated together with proposals for changes and new machines. The current facility includes the Linac2, the Booster, the PS and the SPS. Plans propose to let the protons successively pass a chain with a new 160 MeV linear accelerator (Linac4), a several GeV-machine (the Low-Power Superconducting Proton Linac LPSPL), a new 50 GeV synchrotron (PS2) and the SPS [EL08].

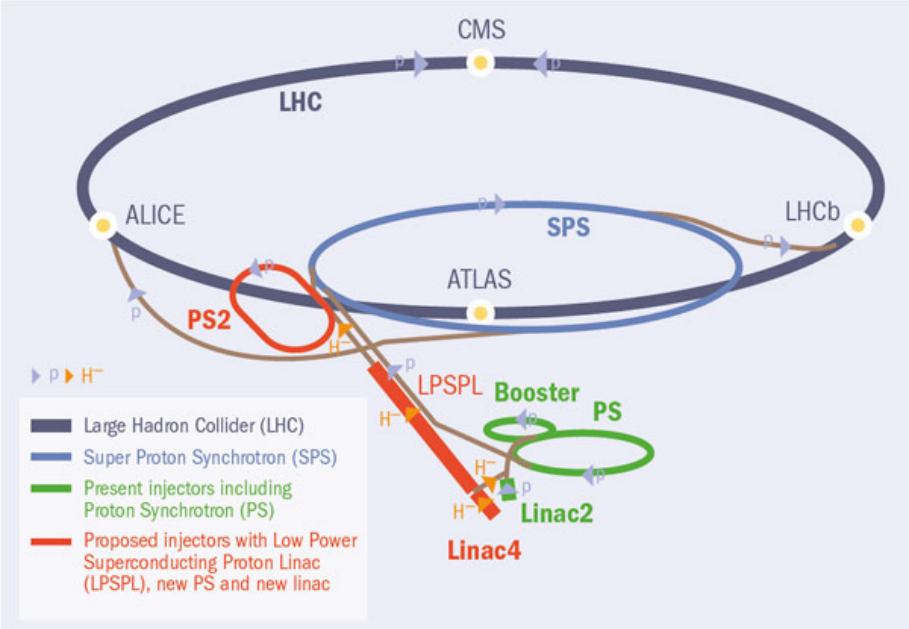

Figure 2.5: ***Sketch of the LHC injector chain upgrade. [EL08]*** *In any LHC upgrade scenario, an improvement of the injector performance is foreseen. Plans propose to let the protons successively pass a chain with a new* 160 *MeV linear accelerator (Linac4), a several GeV-machine (the Low-Power Superconducting Proton Linac LPSPL), a new* 50 *GeV synchrotron (PS2) and the SPS.*

2.2.2 CMS Upgrade Scenarios

The considerable increase of number of pile-up events leads to a drastically higher particle density in the detector sub-systems. The higher luminosity results in higher radiation exposures of the facilities. Therefore the radiation hardness of many sub-detector systems, mainly of the inner ones near the interaction points, has to be improved as mostly the limits of the current technology will be exceeded in a short time of the SLHC operation. Beside the sub-detectors, the trigger system is faced with serious challenges. The system has to find a fast and reliable trigger decision.
The consequences for CMS are, that the detectors of the muon system will still be adequate, as their radiation hardness is many times larger than the needed one for the LHC. Upgrades of the front-end electronics, the trigger and the readout electronics are foreseen [Nas07]. The hadronic calorimeter system HCAL can largely cope with the higher radiation level. Anyhow plans and R&D for upgrades and system improvements of detector-parts and electronics exist. A similar statement maintains for the electromagnetic calorimeter ECAL, where the current detectors offer a sufficient radiation hardness, but parts have to be improved [Nas07].
The subdetector which is mainly affected by the demands and problems of the higher accelerator luminosity is the tracker with its pixel- and strip-sensor systems. They have to be completely replaced. Because of the higher number of energetic jets with more particles and resulting higher track densities, the granularity of the tracker has to be increased, to cope with the higher occupancy and to provide the needed resolution. Pixels offer a fine granularity but they are cost-intensive, so that a replacement of maximally the inner strip layer by a pixel layer is considered. A possible solution is therefore to

reduce the strip length. For this short strip sensor concept (some name the sensors ”strixel”, for ”strip pixel”) a compromise must be found between occupancy reduction, resolution, complexity and cost effort. Plans and basic R&D for strixel sensors are in work [Die09].
Smaller strip or pixel sizes accessorily provide a higher signal to noise ratio, because the input capacitance for the readout electronics is reduced, as well as the leakage current per channel. This also means that on the one hand the power consumption per channel is lower, but that on the other hand their increasing number may nonetheless result in an overall higher power consumption and thereby to a higher heat production. The currents of the higher data traffic must also be considered as a heat source. Therefore also new cooling techniques have to be developed to cope with the higher heat load and to prevent thermal runaways (see chapter 4.5). For instance first tests have been done in the research for a cooling concept based on liquid carbon dioxide which uses the cooling pipes also for powering [dBE08]. This combination reduces the material budget, which is another important point to consider, as the radiation length should be minimized to avoid particle scattering at the detector and support material. The radiation stress on the sensors will be immense, exceeding the radiation tolerance of the current technology. In figure 2.6, the expected total fluences for a CMS tracker of a similar design like the current one, after the the operation time in the SLHC, is plotted against the distance from the interaction point [Huh04]. This shows that one of the main tasks is to find a radiation hard sensor technology that can withstand the harsh conditions of the SLHC. Several R&D programs on sensor basic materials and sensor designs for the different detector parts are proceeding [Die09], [L$^+$09], [H$^+$09a], [H$^+$09b].

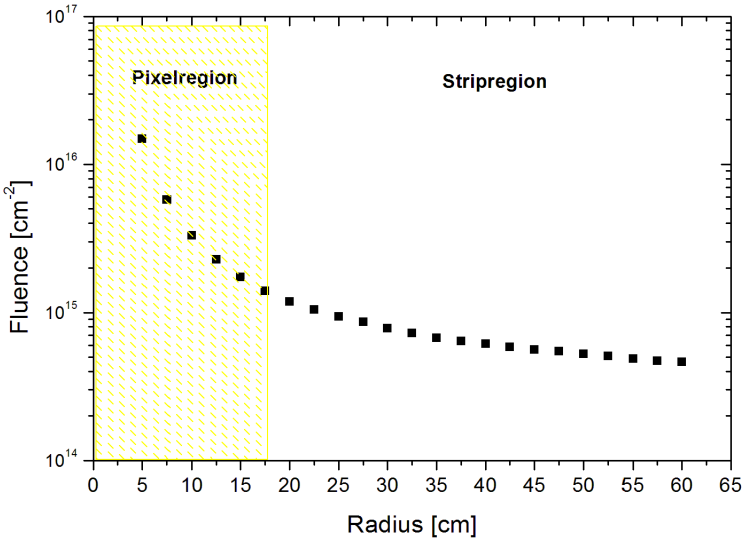

Figure 2.6: ***Total expected fluences for a CMS tracker at the SLHC plotted against the radius [Huh04].***

Chapter 3

Properties of Silicon

This chapter presents basic properties of semiconductors by means of silicon, which is the most important element for the semiconductor industry. In the earth's crust it is the the second most common element after oxygen with a mass fraction of 25.8 %. There it can be found mostly in compounds like SiO_2 or silicates, only rarely appearing in elemental form. With the atomic number 14 its place is in the fourth main group of the periodic table of elements. Table 3.1 lists a survey of some quantitative properties [Har08].

Parameter	Symbol	Unit	Value
Atomic number			14
Relative atomic weight			28.0855
Structure			diamond
Lattice constant	a_0	Å	5.4307
Lattice orientation			$\langle 111 \rangle$
Electron configuration			1s22s22p63s23p2
Density	ρ	gcm^{-3}	2.328
Melting point	T_m	°C	1414
Boiling point	T_b	°C	2355
Gap energy (300 K)/(0 K)	E_g	eV	(1.124)/(1.170)
Dielectric constant	ε_r		11.7
Intrinsic carrier density	n_i	cm^{-3}	$1.45\ x\ 10^{-10}$
Mobility			
- of the electrons	μ_e	$cm^2[Vs]^{-1}$	1350
- of the holes	μ_h	$cm^2[Vs]^{-1}$	450
Effective density of states			
- of the conduction band	N_c	cm^{-3}	$3.22\ x\ 10^{19}$
- of the valence band	N_v	cm^{-3}	$1.83\ x\ 10^{19}$
max. electrical field	E_{max}	$V\mu m^{-1}$	30
Thermal expansion coefficient		1/ °C	$2.5\ x\ 10^{-6}$
Intrinsic resistivity		$k\Omega cm$	235

Table 3.1: ***Properties of Silicon. [Har08].***

3.1 Properties of Intrinsic Silicon

As a member of the fourth main group, elemental silicon forms with four covalent bonds a crystal lattice of diamond structure. The allowed energy states of its electrons are structured in energy bands. This can be seen by solving the Schrödinger equation

$$\left(-\frac{\hbar^2}{2m}\triangle + V(\overrightarrow{r})\right)\psi(\overrightarrow{r}) = i\hbar\frac{\partial}{\partial t}\psi(\overrightarrow{r}) \tag{3.1}$$

using the Bloch theorem that suggests the solutions of the form [Kop93]

$$\psi_k(\overrightarrow{r} + \overrightarrow{R}) = e^{i\overrightarrow{k}\cdot\overrightarrow{R}} \cdot \psi_k(\overrightarrow{r}) \tag{3.2}$$

for a periodic potential energy

$$V(\overrightarrow{r}) = V(\overrightarrow{r} + \overrightarrow{R}) \tag{3.3}$$

as given by the lattice periodicity.

The band energetically above the last completely occupied one at $T = 0\ K$ is called conduction band, while the previous one is named valence band. The energetic distance E_G between these two is called bandgap.

$$E_G = E_C - E_V \tag{3.4}$$

(E_C energy of the lower edge of the conduction band, E_V energy of the upper edge of the valence band). The size of the bandgap is responsible for the physical properties that lead to the classification of solids into insulators, semiconductors and metals. Figure 3.1 illustrates this classification. If at absolute zero

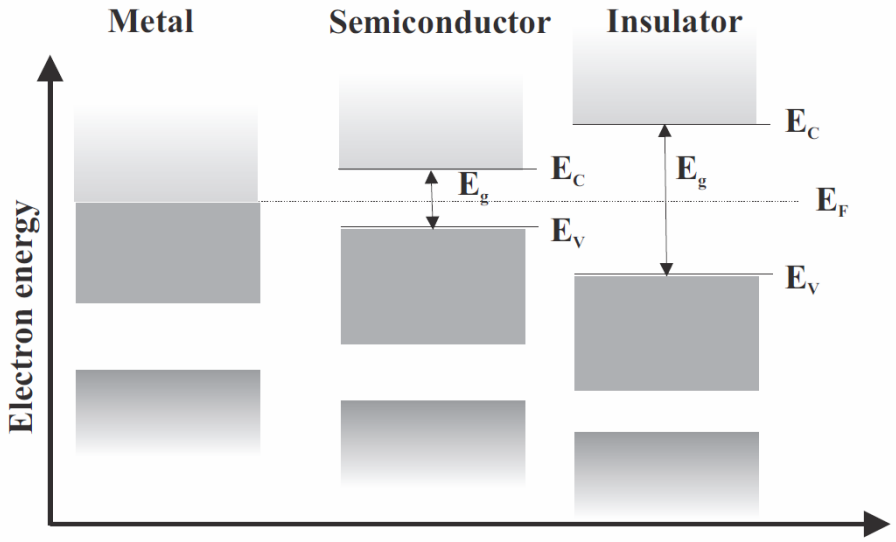

Figure 3.1: ***Simplified band structure to illustrate the classification of solids into metals, semiconductors and insulators [Fur06].*** *If the Fermi level lies in the conduction band, the material is a metal, while otherwise the material can either be an insulator or a semiconductor. The separation is done according to the size of the band gap. A relatively small one gives the solid the properties of a semiconductor.*

point one or more bands are only partly filled with electrons, the crystal is electrically conductive and

therefore one speaks of a metal, while in cases of completely filled bands, the material can either be an insulator or a semiconductor. The location of the Fermi level gives the answer which one is the case. Free charge carriers in a band can follow an external electrical field and thereby contribute to a current, which explains the conductivity. Materials like silicon with bandgaps of up to approximately 5 eV are considered as semiconductors, because the gap is low enough to allow electrons to transit it at higher temperatures, so that they become free charge carriers in the conduction band [Kop93]. This happens due to excitations of the electrons by phonons, which are the quasi-particles of the temperature dependant lattice vibrations. Crystals with higher band gaps behave as insulators.
When electrons get lifted into the conduction band, the charge balance in the valence band is disturbed so that positive holes are created in it, which can be treated as quasi-particles serving as charge carriers and thus contributing to a current as a result of an external field. To calculate the density of free charge carriers in a semiconductor at a certain temperature, one starts with the occupation probability of an energy state of an electron which is given by the Fermi-Dirac function [Har08]

$$f(E,T) = \frac{1}{e^{(E-E_F)/k_BT}+1} \tag{3.5}$$

where k_B is the Boltzman constant and the Fermi energy E_F is defined by

$$f(E = E_F) = \frac{1}{2} \tag{3.6}$$

so that for this energy level the occupation probability is exactly one half. In the conduction band, the electrons can be regarded as free charge carriers, so that with the state density $N(E)$ for electrons at the bottom of the conduction band one can calculate their density by

$$n = \int_{E_C}^{\infty} N(E) \cdot f(E,T) \cdot dE \tag{3.7}$$

The state density for free electrons is given by [Kop93]

$$N(E) = \frac{(2m_n)^{3/2}}{2\pi^2\hbar^3}\sqrt{E-E_C} \tag{3.8}$$

with Planck's constant $\hbar$ and the effective electron mass m_n. The latter depends on the orientation relative to the crystal lattice, but approximately a constant can be used. The total number of free electrons is then

$$n = N_C \cdot exp\left(-\frac{E_C - E_F}{k_BT}\right) \tag{3.9}$$

$$N_C = 2\left(\frac{m_n k_B T}{2\pi\hbar^2}\right)^{3/2} \tag{3.10}$$

In the same way one can find the formula for the density of holes

$$p = N_V \cdot exp\left(-\frac{E_F - E_V}{k_BT}\right) \tag{3.11}$$

$$N_V = 2\left(\frac{m_p k_B T}{2\pi\hbar^2}\right)^{3/2} \tag{3.12}$$

with the effective mass of a hole m_p. In an intrinsic semiconductor the concentrations of electrons and holes are equal in thermal equilibrium

$$n_i = n = p \tag{3.13}$$

From this one derives the density of charge carriers to be

$$n_i = \sqrt{n \cdot p} = \sqrt{N_C \cdot N_V} \cdot exp\left(-\frac{E_G}{2k_B T} \right) \tag{3.14}$$

Using this in equation 3.10 or 3.11, one can also calculate the Fermi level in an intrinsic semiconductor

$$E_{F_i} = \frac{E_C + E_V}{2} + \frac{3}{4} k_B T \cdot ln\left(\frac{m_p}{m_n} \right) \tag{3.15}$$

3.2 Properties of Extrinsic Silicon

The charge carrier concentration in metals accounts for 10^{22} to 10^{23} per cm^3 [Kop93]. In comparison to that the accordant values for the most important semiconductors silicon and germanium at a temperature of 300 K are rather small, being around $1.5 \cdot 10^{10}\ cm^{-3}$ and $2.4 \cdot 10^{13}\ cm^{-3}$ respectively [Kop93]. The means of doping, which is the replacement of semiconductor atoms in the lattice by atoms of elements of the third or fifth main group by diffusion or injection, allows the increase of the concentration of free charge carriers by many orders of magnitude. Silicon builds four covalent bonds in the lattice. If an atom is substituted by an element of the fifth main group like phosphorus, antimony or arsenic, the fifth valence electron of the foreign atom is not used for the covalent bonds to the silicon. It can be separated easily from its atom by a small amount of energy, so that it is lifted into the conduction band where it can take part in a charge transport. Impurities that show such an attribute are called donors. One is talking of an acceptor when an impurity can easily adopt an electron of the valence band of the semiconductor. This is the case for atoms of the third main group like boron, aluminium, indium or gallium which have only three valence electrons. Therefore an electron is missing to establish the four covalent bonds to the neighbors in the lattice. This gap is filled by a valence electron of the silicon, creating a hole in the valence band thereby, which then serves as a free charge carrier. The influence of dopants is illustrated in figure 3.2. In both cases the ionization energies of the impurities can be estimated by using an adjusted model of the hydrogen atom. In case of a donor, the excited electron leaves a positive hole which acts like the hydrogen nucleus. The influence of the lattice is respected by the dielectric constant of silicon ε and the effective mass of the electron m_n. Using the well-known formula for the energy levels of the hydrogen one gets

$$E_n = \frac{m_n e^4}{2(4\pi\varepsilon_0\varepsilon)^2\hbar^2} \frac{1}{n^2} \tag{3.16}$$

Phosphorus introduces a donor energy of $E_D = 45\ meV$ and arsenic one of $E_D = 54\ meV$, while boron shows an acceptor energy of $E_A = 45\ meV$ [Lut99]. These energies, that have to be brought up to create free charge carriers, are graphically illustrated in figure 3.3. If a semiconductor includes acceptors and donors, free electrons can recombine with holes decreasing the concentration of free charge carriers. When there are more donors than acceptors the material is called n-type while in the opposite way it is called p-type. To calculate the charge carrier concentration in the conduction band of n-type silicon (the approach for the hole concentration of p-type silicon works similarly) it has to

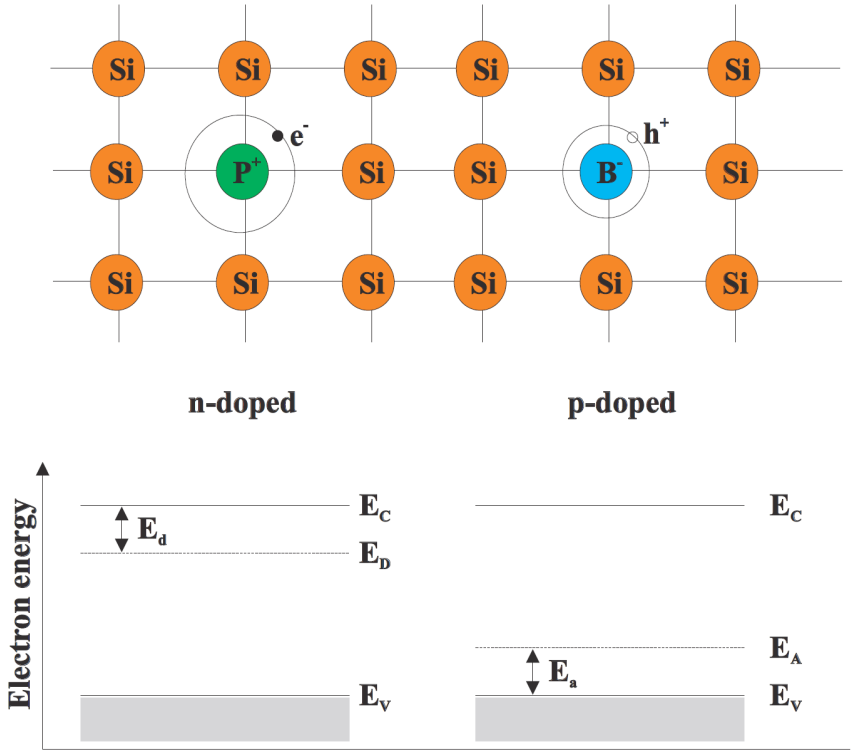

Figure 3.2: ***Doping method.Impact of the substitution of Si lattice atoms by atoms of the third or fifth main group [Fur06].*** *If a silicon atom is replaced by an element of the fifth main group, an energy level just under the lower conduction band edge arises from where an electron can be easily stimulated into the conduction band to increase the number of free charge carriers there. If the replacement is done with an atom of the third main group, like boron, an energy level near the valence band results in which electrons of the valence band can get lifted to leave a free hole in the valence band.*

be considered that the donors n_D can be divided into the ones being ionized n_D^+ and the neutral ones n_D^0.

$$n_D = n_D^0 + n_D^+ \tag{3.17}$$

The equation for the acceptors is

$$n_A = n_A^0 + n_A^- \tag{3.18}$$

where n_A^0 are the neutral ones and n_A^- the ionized ones. The total charge must be neutral so that there exists an equation for the charge balance in the semiconductor

$$n + n_A^- = p + n_D^+ \tag{3.19}$$

When E_G is the energy gap between the valence band and the conduction band and E_D the energy to ionize the donor atom like defined above, then the energy of the donor level is $E_G - E_D$ relative to the zero level. The concentration of electrons in that energy level, which is n_D^0, can be figured out with the help of the Fermi-Dirac statistic (3.5)

$$n_D^0 = n_D \frac{1}{e^{(E_G - E_D - E_F)/k_B T} + 1} \tag{3.20}$$

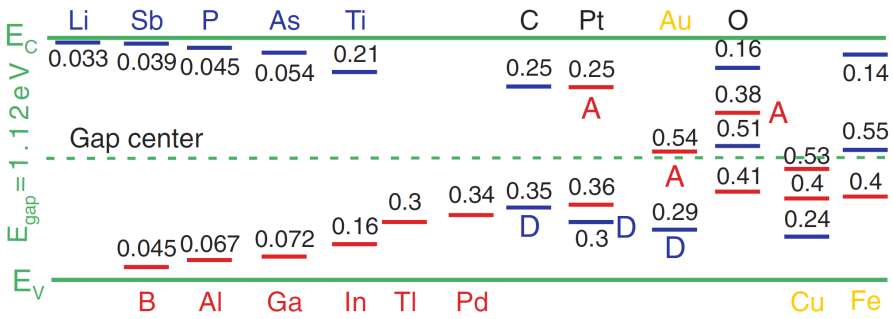

Figure 3.3: ***Energy levels of several foreign atoms in a silicon crystal [Har08].***

One gets for the concentration of electrons that were lifted from donor levels into the conduction band

$$n_D^+ = n_D - n_D^0 = n_D \frac{1}{e^{-(E_G - E_D - E_F)/k_B T} + 1} \tag{3.21}$$

The expression for the ionized acceptors can be found alike

$$n_A^- = n_A - n_A^0 = n_A \frac{1}{e^{-(E_F - E_A)/k_B T} + 1} \tag{3.22}$$

If the donor concentration is much higher than the acceptor concentration and when the temperature is low enough that there is almost no excitation of valence electrons, n_A^- can be neglected as well as p. Equation (3.19) then results in

$$n = n_D^+ \tag{3.23}$$

With the equations (3.9) and (3.21) one gets

$$n = N_C(T) e^{-(E_G - E_F)/k_B T} = n_D \frac{1}{e^{-(E_G - E_D - E_F)/k_B T} + 1} \tag{3.24}$$

This equation can be solved for the Fermi energy

$$E_F = E_G - E_D + k_B T \ln \left\{ \frac{1}{2} \left(\sqrt{1 + 4 \frac{n_D}{n_0(T)} e^{E_D/k_B T}} - 1 \right) \right\} \tag{3.25}$$

By inserting this in equation (3.21) the concentration of charge carriers in the conduction band of an extrinsic semiconductor can be obtained

$$n = \frac{2 n_D}{1 + \sqrt{1 + 4 \frac{n_D}{N_C(T)} e^{E_D/k_B T}}} \tag{3.26}$$

When the donor levels are almost completely ionized, the situation can be described by a movement of the Fermi level E_F towards the conduction band, so that there is a deviation of the Fermi level from the definition of the intrinsic one E_i in equation (3.15). Using this, the concentration for electrons and holes can be written in the following way

$$n = n_i e^{\frac{E_F - E_i}{k_B T}} \tag{3.27}$$

$$p = n_i e^{\frac{E_i - E_F}{k_B T}} \tag{3.28}$$

3.3 pn-Junctions

At room temperature the number of free charge carriers in an intrinsic silicon substrate is many orders higher than the number of electron-hole pairs that a traversing particle can produce. Therefore the concentration of free charge carriers has to be reduced, so that the signal becomes detectable. Like equation (3.26) shows, this number is exponentially dependent on the temperature, so that one possibility is to cool down the material remarkably. A more practical way, as it works without cooling, is to make use of the features of a pn-junction. It is the basics of a semiconductor detector. A pn-junction is built when a p-doped material and an n-doped one come to contact. The resulting structure is called a diode.

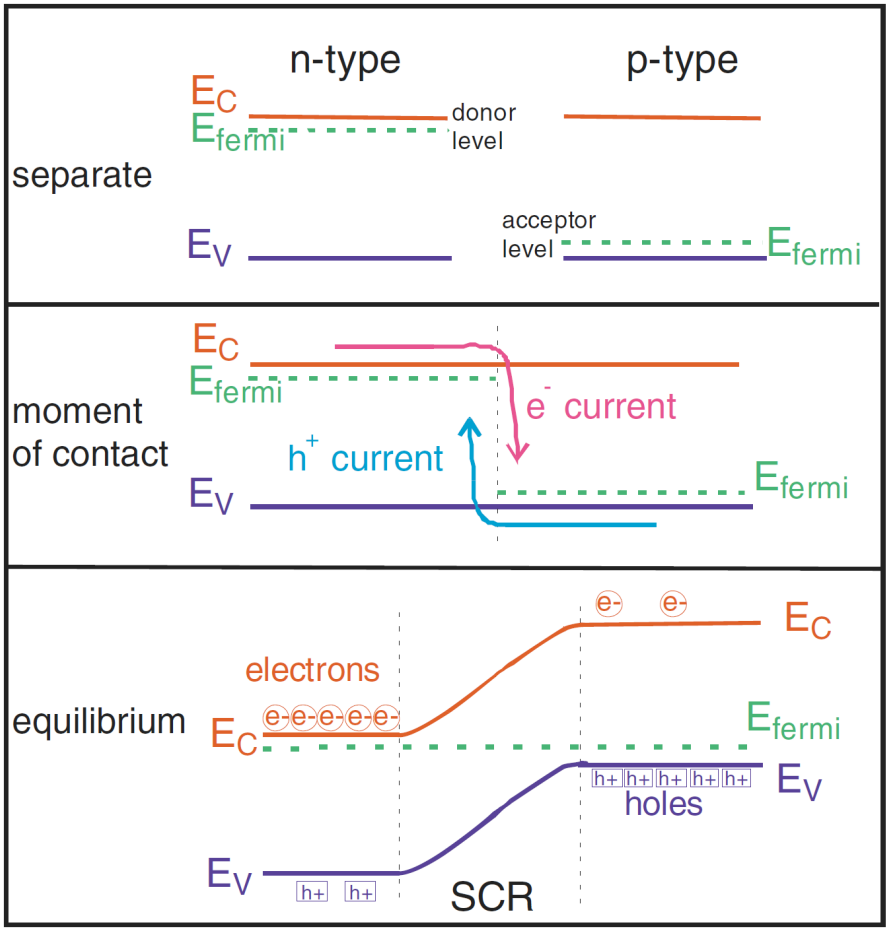

Figure 3.4: ***Formation of a pn-junction [Har08].*** *The Fermi levels of the n-type part and the p-type part differ. Free electrons in the conduction band of the n-material diffuse into the p-type region where they recombine with holes, which are the majority charge carriers there. Vice versa holes of the p-type material drift into the n-type part.*

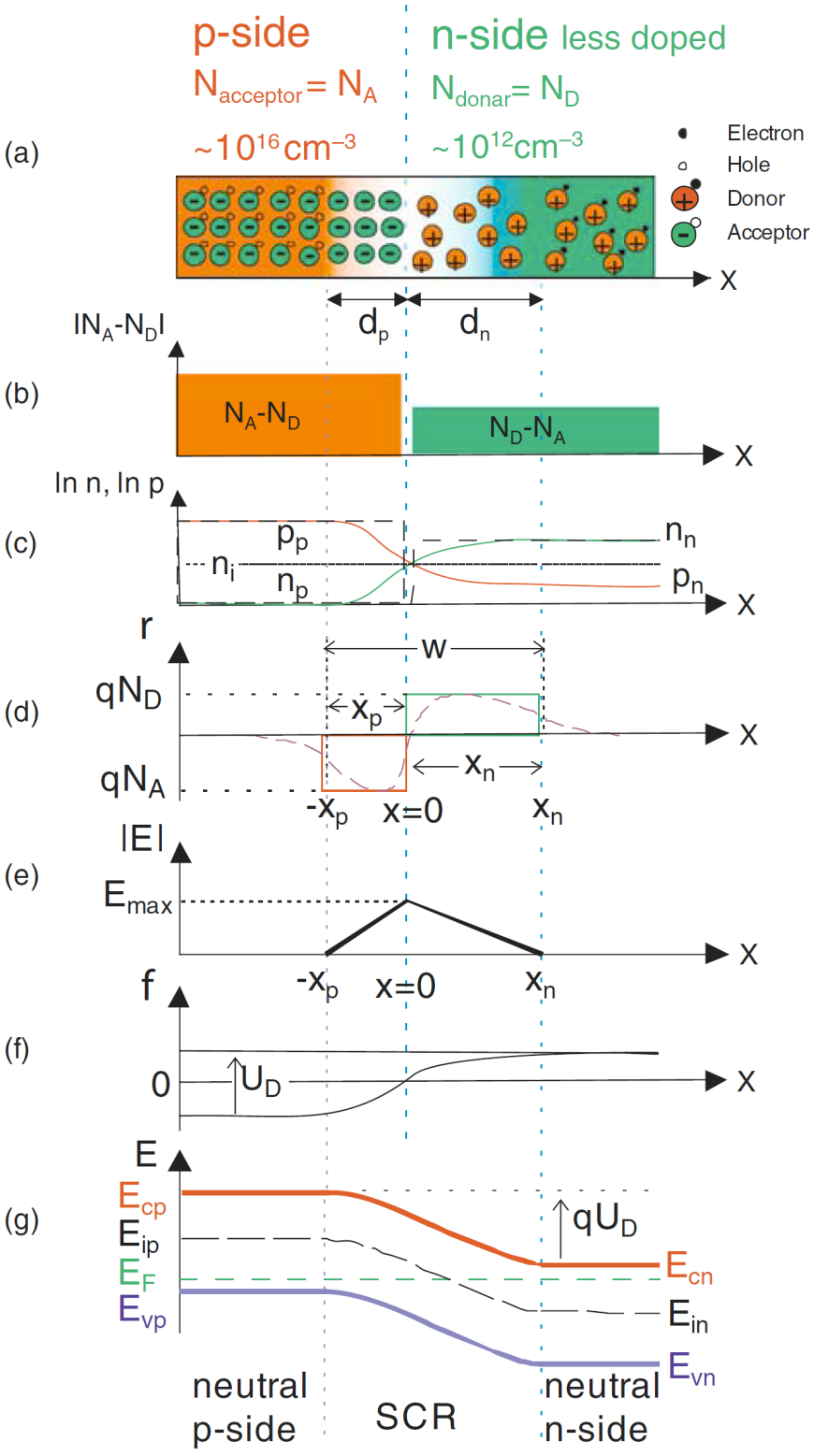

Figure 3.5: ***The pn-junction. [Fur06]*** *a) Illustration of the donor, acceptor and charge carrier distribution in a pn-junction. b) Drafted profile of the doping concentration. c) Drafted profile of the resulting charge distribution. d) Resulting electrical field. e) Potential distribution. f) Band structure of a pn-junction.*

3.3.1 Built-in Voltage and Depletion Depth

Free electrons in the conduction band of the n-material diffuse into the p-type region where they recombine with holes, which are the majority charge carriers there. Vice versa holes of the p-type material drift into the n-type part. This process is illustrated in figure 3.4. As the differently doped materials were electrically neutral before this process, the drifting charge carriers charge up the material where they catch on. The arising voltage is called built-in voltage V_{bi}. As it results of the different intrinsic Fermi levels in the differently doped materials [Lut99], it can be calculated using the equations 3.28. The free electrons in the n-type side almost completely derive from the donors, so that their concentration can be approximated by the one of the donors. An analogous situation exists for the holes on the p-type side where the concentration is equal to the acceptor concentration. The built-in voltage can be calculated in the following way

$$n_{n-type} = N_D = n_i e^{\frac{E_F - E_i^n}{k_B T}} \tag{3.29}$$

$$p_{p-type} = N_A = n_i e^{\frac{E_i^p - E_F}{k_B T}} \tag{3.30}$$

$$N_A \cdot N_D = n_i^2 e^{\frac{E_i^p - E_i^n}{k_B T}} \tag{3.31}$$

$$V_{bi} = \frac{1}{q}(E_i^p - E_i^n) = \frac{k_B T}{q} ln \frac{N_A N_D}{n_i^2} \tag{3.32}$$

The voltage is in the order of 0.5 V [Lut99]. The region where this voltage is built up is called space-charge region. It extends into the n and p parts. At the boundaries the electric field is zero and the potential difference equals the built-in voltage. The higher the concentration of the donors is, the more the space-charge region will extend into the p-type part and its width d_p there will grow. This is a result of the fact that the charges in both regions have to be equal. This can be expressed by [Sze81]

$$N_D d_n = N_A d_p \tag{3.33}$$

where d_n is the width in the n-type part. With the charge density

$$\rho(x) = -q[n(x) - p(x) + N_A - N_D] \tag{3.34}$$

the Poisson-equation describes the arising electrostatic potential $\phi(x)$. With the notations in figure 3.5, one can approximate for the n-region [Sze81]

$$-\frac{\partial^2 \phi}{\partial x^2} = \frac{\rho(x)}{\varepsilon_0 \varepsilon} \approx \frac{q}{\varepsilon_0 \varepsilon} N_D \quad \text{for} \quad 0 < x < x_n \tag{3.35}$$

Just as well, one can approximate for the p-region

$$-\frac{\partial^2 \phi}{\partial x^2} \approx \frac{-q}{\varepsilon_0 \varepsilon} N_A \quad \text{for} \quad -x_p \leq x < 0 \tag{3.36}$$

By integrating these equations, the electrical field is obtained, plotted in figure 3.5 d)

$$E(x) = -\frac{qN_A(x + x_p)}{\varepsilon_0 \varepsilon} \quad \text{for} \quad -x_p \leq x < 0 \tag{3.37}$$

and

$$E(x) = -E_{max} + \frac{qN_D x}{\varepsilon_0 \varepsilon} \quad \text{for} \quad -x_p \leq x < 0 \tag{3.38}$$

$$= \frac{qN_D x}{\varepsilon_0 \varepsilon}(x - x_n) \quad \text{for} \quad 0 < x < x_n \tag{3.39}$$

with the maximum electrical field strength at $x = 0$

$$E_{max} = \frac{1}{\varepsilon\varepsilon_0} qN_D x_n = \frac{1}{\varepsilon\varepsilon_0} qN_A x_p \tag{3.40}$$

(q the elementary charge)
A second integration of the Poisson-equations delivers the potential distribution $\phi(x)$ and the built-in voltage

$$\phi(x) = E_{max}\left(x - \frac{x^2}{2d}\right) \tag{3.41}$$

$$V_{bi} = \frac{1}{2} E_{max} d = \frac{1}{2} E_{max}(x_n + x_p) \tag{3.42}$$

Eliminating E_{max} from the equations (3.40) and (3.42) leads to the formula for the thickness of a two-sided abrupt junction

$$d = \sqrt{\frac{2\varepsilon\varepsilon_0}{q}\left(\frac{N_A + N_D}{N_A N_D}\right) V_{bi}} \tag{3.43}$$

In the case when $N_A \gg N_D$ or when $N_D \gg N_A$ the formula reduces to

$$d = \sqrt{\frac{2\varepsilon\varepsilon_0 V_{bi}}{qN_B}} \tag{3.44}$$

where N_B stands for the dominant doping.
If the mobility μ and the resistivity ρ of the material are known, the built-in voltage can also be calculated in the following way [Har08]

$$V_{bi} = \frac{1}{2} E_{max} d = \frac{1}{2\mu\rho\varepsilon} d^2 \tag{3.45}$$

$$\rho = \frac{1}{q(\mu N_B)} \tag{3.46}$$

3.3.2 Full Depletion Voltage

An external voltage V influences the depletion depth. If it is a forward bias, the case when the voltage is oriented in the opposite direction than the built-in voltage, the depletion depth will decrease [Lut99]

$$d = \sqrt{\frac{2\varepsilon\varepsilon_0}{q}\left(\frac{N_A + N_D}{N_A N_D}\right)(V_{bi} - V)} \tag{3.47}$$

In case of a reverse bias, when the external voltage has the same orientation like the built-in one, the depletion depth will increase. The voltage at which the depletion depth has exactly the size of the substrate thickness d_s and the sensor is fully depleted of free charge carriers is called the full depletion voltage. Normally the external voltage is much higher than the built-in voltage, so that the latter can be neglected and with (3.45) the depletion voltage becomes

$$V_{dep} = \frac{d^2}{2\varepsilon\varepsilon_0\mu\rho} = \frac{q}{2\varepsilon\varepsilon_0} |N_{eff}| d_s^2 \tag{3.48}$$

with an effective doping concentration $N_{eff} = N_D - N_A$ of the main substrate when the majority doping might be slightly compensated by impurities that lead to the opposite type of doping.

3.3.3 Current Behavior

Even after the formation of the built-in voltage, the concentration of free electrons in the n-doped part of the diode is higher, than in the p-type part. Electrons can drift from the higher concentrated side to the lower one, if they have got enough energy to overcome the potential barrier eV_{bi}. The resulting current is called recombination current, while a current in the opposite direction is called generation current, as it results of minority charge carriers that had to be thermally generated in the p-type region. In thermal equilibrium these currents have got the same magnitude. Similar currents exist for the holes. To get the expressions describing the currents one can first look at the carrier concentrations in an arbitrary position within the junction with the intrinsic energy level E_i. These are given by the formulas 3.32, so that the ratio between the free electrons (holes) in the neutral p-region at the edge of the junction n_p (p_p) and the free electrons (holes) in the neutral n-region at the edge of the junction n_n (p_n) can be expressed by

$$\frac{n_p}{n_n} = \frac{p_n}{p_p} = e^{-\frac{E_i^p - E_i^n}{k_B T}} = e^{-q\frac{V_{bi}}{k_B T}} \tag{3.49}$$

An external voltage changes these concentrations in the following way

$$n_p = n_n e^{-q\frac{V_{bi}-V}{k_B T}} \tag{3.50}$$

$$p_n = p_p e^{-q\frac{V_{bi}-V}{k_B T}} \tag{3.51}$$

The minority carrier diffusion currents are proportional to the deviation of the minority carrier concentrations from their equilibrium values so that the currents follow a similar behavior like the equations (3.51) describe. The total current is the sum of both, so that it can be expressed as [Lut99]

$$I = (I_{Sn} + I_{Sp})\left(e^{\frac{qV}{k_B T}} - 1\right) = I_S\left(e^{\frac{qV}{k_B T}} - 1\right) \tag{3.52}$$

I_S is the reverse bias saturation current [Lut99]

$$I_S = q\left(\frac{n_{p_0} D_n}{\sqrt{D_n \tau_{r_n}}} + \frac{p_{n_0} D_p}{\sqrt{D_p \tau_{r_p}}}\right) \tag{3.53}$$

with the diffusion constants $D_{n,p} = \frac{k_B T}{q}\mu_{n,p}$ for the electrons and holes, τ_{r_p,r_n} the charge carrier lifetimes, and n_{p_0} and p_{n_0} as the electron or respectively the hole density at the edge of the neutral p or n regions in thermal equilibrium. The presented current behavior is valid for a perfect pn-junction without impurities. The currents increase additionally when defect levels near the middle of the band gap exist, resulting of lattice damages and impurities.

3.3.4 Capacitance Voltage Characteristics

The analysis of the capacitance-voltage characteristic is a good tool for discovering the doping profile and the full depletion voltage of a diode. To derive this characteristic it is possible, without being too specific, to consider a highly doped p-region on a n-type bulk and a potential being zero in the neutral n-region. When the depth of the space-charge region is increased from x to x+dx, the surface charge of the p-side is increased by $qN_D dx$, while the electric field is changed by $qN_D dx/(\varepsilon\varepsilon_0)$ and

the surface voltage by $xqN_D dx/(\varepsilon\varepsilon_0)$. The total charge Q_p and the total potential ϕ_p are then obtained by integrations to the width W of the space-charge region

$$Q_p = -\int_0^W qN_D(x)dx \tag{3.54}$$

$$\phi_p = \int_0^W \frac{qN_D(x)}{\varepsilon\varepsilon_0} x dx \tag{3.55}$$

ϕ_p must be equal to $V_{bi} - V$. The capacitance per area of the diode is given by [Lut99]

$$c = \frac{\partial Q_p}{\partial V} \approx \frac{\varepsilon\varepsilon_0}{W} \tag{3.56}$$

so that the doping concentration N_D can be calculated from the equation

$$\frac{\partial(1/c^2)}{\partial V} = \frac{\partial(1/c^2)/\partial W}{\partial V/\partial W} = \frac{2W/(\varepsilon\varepsilon_0)^2}{qN_D W/(\varepsilon\varepsilon_0)} = \frac{2}{qN_D\varepsilon\varepsilon_0} \tag{3.57}$$

$$N_D = \frac{2}{q\varepsilon\varepsilon_0 \frac{\partial(1/c^2)}{\partial V}} \tag{3.58}$$

Equation (3.56) can be used in (3.48) to determine the full depletion voltage. Because of equation (3.57), the capacitance of a diode is finally given by

$$C = \begin{cases} A\sqrt{\frac{q\varepsilon\varepsilon_0 N_D}{2V_{Bias}}} & V_{Bias} \leq V_{FullDepletion} \\ A\frac{\varepsilon\varepsilon_0}{d_s} & V_{Bias} \geq V_{FullDepletion} \end{cases} \tag{3.59}$$

with the area A, the sensor thickness d_s and the external bias voltage V_{Bias}.

3.4 Thermal Generation of Charge Carriers

Free electrons in the conduction band and holes in the valence band can be generated by thermal energy. In silicon the probability for this process is low at room temperature but it can be increased by intermediate states in the band gap due to impurities or imperfections within the crystal. If this is the case, a thermal excitation of charge carriers into the conduction band can also happen in two steps via these intermediate states. Charge carriers get then first lifted into the energy levels inside the band gap by thermal energy and then from there into the conduction band. If the minimum of the energy of the conduction band and the maximum of the energy of the valence band cannot be found at the same momentum of the charge carrier, one speaks of an indirect semiconductor, while it is called a direct semiconductor if the minimum band gap appears at the same momentum. Therefore the minimum energy for a band transition is higher than the band gap in the case of an indirect semiconductor and for a transition of the lowest energy additional momentum has to be transferred [Lut99].

3.5 Charge Carrier Generation by Electromagnetic Radiation

Photons can interact with the electron clouds of the semiconductor by photo effect, Compton scattering or at high energies by electron positron pair production. When the transmitted energy is higher than the band gap, electrons of the valence band get lifted into the conduction band while leaving a

positive hole in the valence band. If this energy is much higher, the free electron will return from higher levels of the conduction band by either creating phonons or emitting low-energy photons. These can again generate electron-hole pairs. An absorption of energies smaller than the band gap in the material is possible if impurities or imperfections exist that offer local energy states located between the two bands [Lut99].

3.6 Charge Carrier Generation by Charged Particles

During the transition of charged particles through matter, they lose energy by the interaction with the Coulomb field of the lattice atoms. This happens because of inelastic scattering by emission of bremsstrahlung, excitation of atoms and ionization. The mean energy loss per unit length of the traversing particle in terms of $[MeV/cm]$ is described by the Bethe-Bloch formula [Lut99]

$$\frac{dE}{dx} = 2\pi N_A r_e^2 m_e c^2 \rho \frac{Z}{A}\frac{z^2}{\beta^2}\left[\ln\left(\frac{2m_e\gamma^2 v^2 W_{max}}{I^2}\right) - 2\beta^2 - \delta - 2\frac{C}{Z}\right] \tag{3.60}$$

with the following meanings of the different symbols

x : path length in g/cm^2
$r_e = \frac{e^2}{4\pi m_e c^2}$: classical electron radius
m_e : electron mass
N_A : Avogadro's number
I : effective ionization potential averaged over all electrons
Z : atomic number of the medium
A : atomic weight of the medium
ρ : density of the medium
z : charge of the traversing particle
$\beta = \frac{v}{c}$: velocity of the traversing particle in units of the speed of light $\gamma = \frac{1}{\sqrt{1-\beta^2}}$
δ : a density correction
C : a shell correction
W_{max} : maximum energy transfer in a single collision

Figure 3.6 shows the energy loss rate per length as a function of the energy of the traversing particle. A minimum can be seen. Particles with an energy corresponding to that minimum are called minimum ionizing particles (MIP). As the slope of the curve is quite flat for higher energies, in practice also particles of these energies are regarded as MIPs. The energy loss creates mainly electron-hole pairs, which sum up to the signal of a semiconductor sensor. Therefore it is important that a sensor can also detect MIPs, which is possible if the resulting signal to noise ratio (SNR) is high enough. Because of the properties of a MIP, the most probable signal height is known and the sensor and the electronics design as well as the environmental conditions have to keep the noise low.
In silicon the energy for an indirect band transition is 1.12 eV, while the mean energy for the creation of a electron-hole pair is higher and accounts for 3.6 eV, as only a part of the energy loss of a traversing particle is used for this pair production process [Bic88].

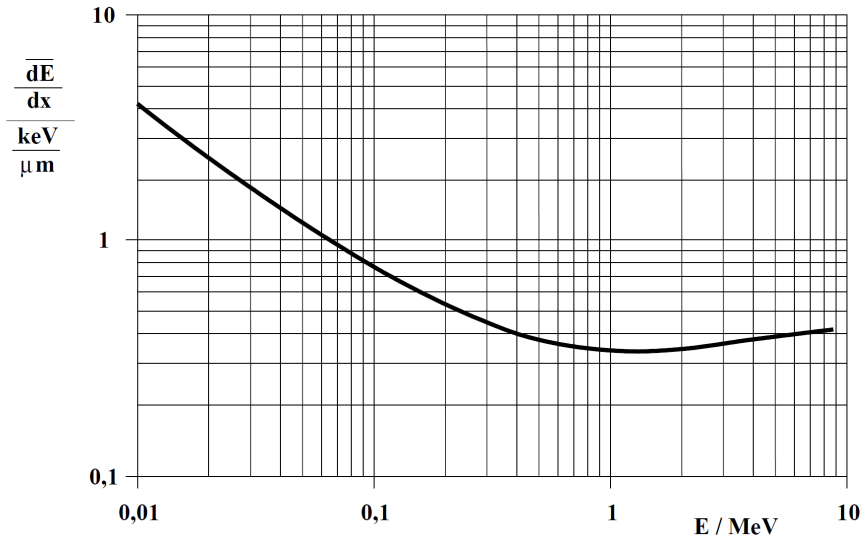

Figure 3.6: ***Energy loss of electrons in silicon according to the Bethe-Bloch formula. [Fur06]*** *Particles with an energy of the minimum in the energy loss rate are called minimum ionizing particles (MIP).*

3.7 Shape of a Radiation-Generated Charge Cloud

The Bethe-Bloch formula only describes the average charge loss per length, but the ionization process is a statistical one, so that for thin absorbers the mean value differs from the most probable one. In thick absorbers many collisions with atoms contribute to the total energy loss, so that the energy loss distribution approaches a gaussian one, while for thin absorbers it is a highly-skewed Landau distribution. The most probable value in $MeV \cdot g/cm^2$ in a material of the thickness x can then be calculated by [B$^+$04]

$$\Delta_p = \left(\frac{4\pi N_A r_e^2 m_e c^2}{2}\right)\left\langle\frac{Z}{A}\right\rangle\left(\frac{x}{\beta^2}\right)\left[ln\frac{2m_e c^2\beta^2\gamma^2}{I} + ln\frac{(4\pi N_A r_e^2 m_e c^2/2)\langle Z/A\rangle(x/\beta^2)}{I} + j - \beta^2 - \delta(\beta\gamma)\right] \tag{3.61}$$

with $j = 0.2$ according to [Bic92]. Exemplarily the energy loss distributions of 500 MeV pions in silicon slices of different thicknesses can be seen in figure 3.7. The long tails in the distributions are the results of rare single-collision energy transfers [Bic92] and they are the reason, that the mean energy loss is higher than the most probable one. Therefore the mean energy loss should not be considered for sensor devices. All charge collection values and signal to noise ratios are based on the most probable values of the distributions. For high energies, the most probable energy loss according to formula (3.61) reaches a plateau slightly above the minimum, so that basically all high energetic particles can be treated as MIPs. Figure 3.8 underlines this in the comparison of the Bethe-Bloch and the Landau-Vavilov-Bichsel energy loss of muons in silicon.

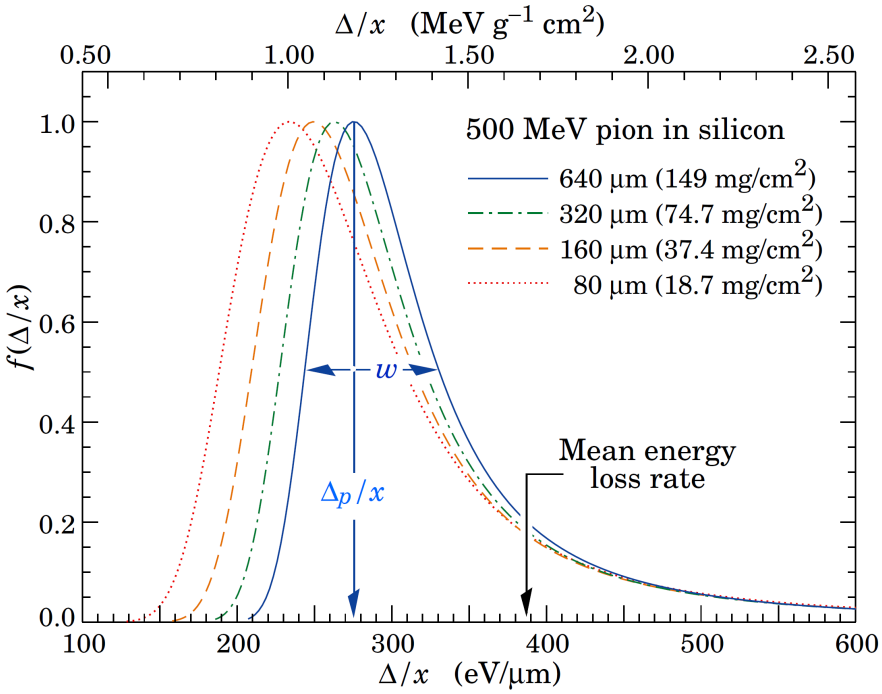

Figure 3.7: ***Energy loss distributions of*** 500 *MeV* ***pions in silicon slices of different thicknesses [B+04].*** *The long tails in the distributions are the results of rare single-collision energy transfers. They are the reason, that the mean energy loss is higher than the most probable one.*

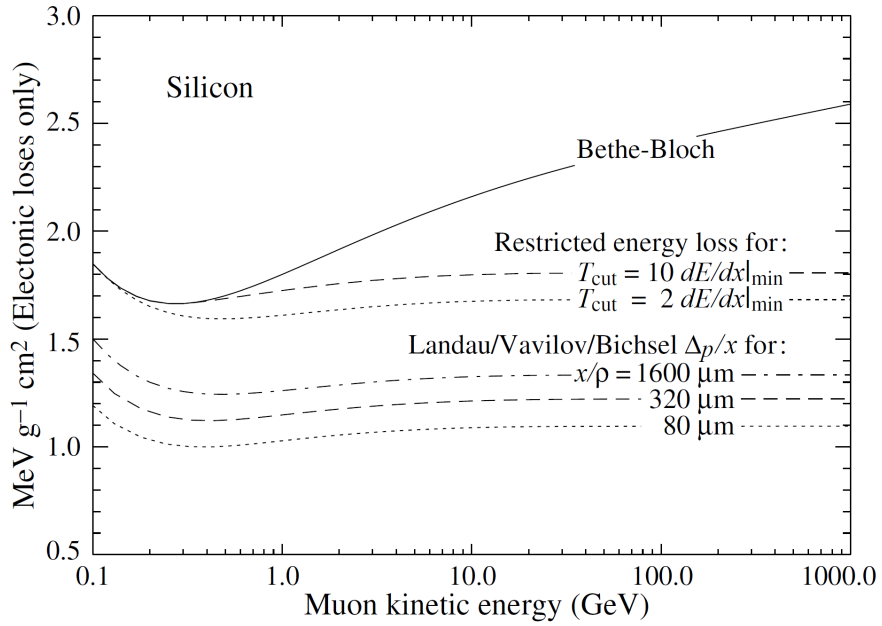

Figure 3.8: ***Comparison between the energy loss calculated by the Bethe-Bloch formula and the one according to Landau-Vavilov-Bichsel [B+04].*** *The most probable energy loss reaches a plateau slightly above the minimum, so that basically all high energetic particles can be treated as MIPs.*

3.8 Charge Carrier Transport

In non equilibrium states, when an electrical field is applied at the semiconductor or when macroscopical differences in the charge carrier concentrations exist, movements of the charge carriers are the consequence. One speaks of a drift when the charge carriers follow an external electrical field and of a diffusion when their movement is caused by inhomogeneous charge carrier distributions.

3.8.1 Drift

In the case of a missing external field and a homogeneous charge distribution, the existing thermal motion of the charge carriers does not displace free charge carriers. This changes when an electrical field is applied, as the resulting force on the carriers accelerates them in the direction of the field. As long as the drift velocity is smaller than the thermal velocity (around $10^7\ cm/s$) the drift velocity for electron and holes is given by

$$\upsilon_n = -\frac{q\tau}{m_n^*}E = -\mu_n E \tag{3.62}$$

$$\upsilon_p = -\frac{q\tau}{m_p^*}E = -\mu_p E \tag{3.63}$$

with the mean free time between two collisions τ (in the order of $10^{-12}\ s$), q the electric charge, μ_n the electron mobility, μ_p the hole mobility and m_n^* and m_p^* the effective masses of an electron respectively a hole. The critical field strength when the drift velocity becomes as large as the thermal velocity can be calculated by

$$\mid E_{crit} \mid = \frac{1}{\mu}\sqrt{\frac{3k_BT}{m_n^*}} \tag{3.64}$$

The estimation for room temperature delivers a value of $10^4\ Vcm^{-1}$.

3.8.2 Diffusion

Inhomogeneities in the charge carrier concentrations are the driving source for diffusion processes. Electrons or holes move to the regions of their lower concentration as a result of statistics, because the probability for charge carriers to move from the region of the higher concentration to the lower one is much higher than vice versa. With the help of diffusion constants for electrons (D_n) and holes (D_p), their flux can be described by the following diffusion equations

$$F_n = -D_n \bigtriangledown n \tag{3.65}$$

$$F_p = -D_p \bigtriangledown p \tag{3.66}$$

It is obvious that the flux F_n or F_p are higher, the higher the gradients of the densities n and p are.
With the mobilities μ_n and μ_p the Einstein equations allow to calculate the diffusion constants at a given temperature T

$$D_n = \frac{k_BT}{q}\mu_n \tag{3.67}$$

$$D_p = \frac{k_BT}{q}\mu_p \tag{3.68}$$

Chapter 4

Radiation Damages in Silicon

Radiation can cause surface and bulk damages in a sensor. At the surface regions of sensors, damages can happen due to transient or long term ionization in insulator layers or by the formation of interface defects. The degradation of the electrical sensor functions most importantly arise by the interaction of high energetic radiation particles with the lattice of the bulk. The interaction of charged particles with the electron cloud of the lattice atoms leads to the generation of electron-hole pairs by ionization. This effect does not create permanent damages, but it is the basis of the signal generation. It is whereas the displacement of lattice atoms that can lead to permanent damages.

4.1 Surface Damage

AC-coupled sensors (see chapter 5) or sensors covered with a passivation can suffer from radiation induced defects in the layers consisting of SiO_2 or Si_3N_4 and of resulting damages in the interfaces to the silicon. In contrast to the bulk damage of the semiconductor, the insulator damages which lead to observable effects on macroscopical sensor characteristics mainly result of ionization processes and not of atomic displacements. This means that the creation of electron-hole pairs is not fully reversible. One reason is, that charge carriers can get trapped, as energy levels of defects exist in the large band gap of the involved insulators ($E_G = 8.8\ eV$ for SiO_2 or $E_G = 5\ eV$ for Si_3N_4) [Har08]. The more relevant fact is, that the mobility of electrons and holes differ by several orders of magnitude in an insulator, which is not the case in a semiconductor. In SiO_2 the value for electrons is $\mu_e \approx 20\ cm^2/(Vs)$, which is much higher than $\mu_h \approx 2 \cdot 10^{-5}\ cm^2/(Vs)$ for holes [Har08]. Therefore electrons drift much faster to the metal electrodes (e.g. of the readout) in an electrical field than the holes drift towards the $Si - SiO_2$ interface. The trap density is higher at an interface, so that trapping becomes more probable for the holes. Therefore positive charge is accumulated, which attracts electrons from the silicon to the bulk side of the interface. The electrons reduce the interstrip resistance thereby, which increases cross talk between the strips. Further the polarisability of the layer increases, so that also the interstrip capacitance rises. This effect leads to an increase of the noise.

4.2 Bulk Radiation Damage Mechanisms

The first atom that is displaced by the hit of a radiation particle is called the primary knock on atom (PKA). Its movement from its original position results in a silicon interstitial and a vacancy. If the energy transfer to the PKA was low, the interstitial and the vacancy form a Frenkel pair, while at higher energies it becomes probable that the PKA and the traversing radiation particle interact with

additional atoms, building a cascade thereby. Therefore at lower energies mainly point defects are created, while at higher energies defect clusters appear. In figure 4.1 some defects are graphically displayed.

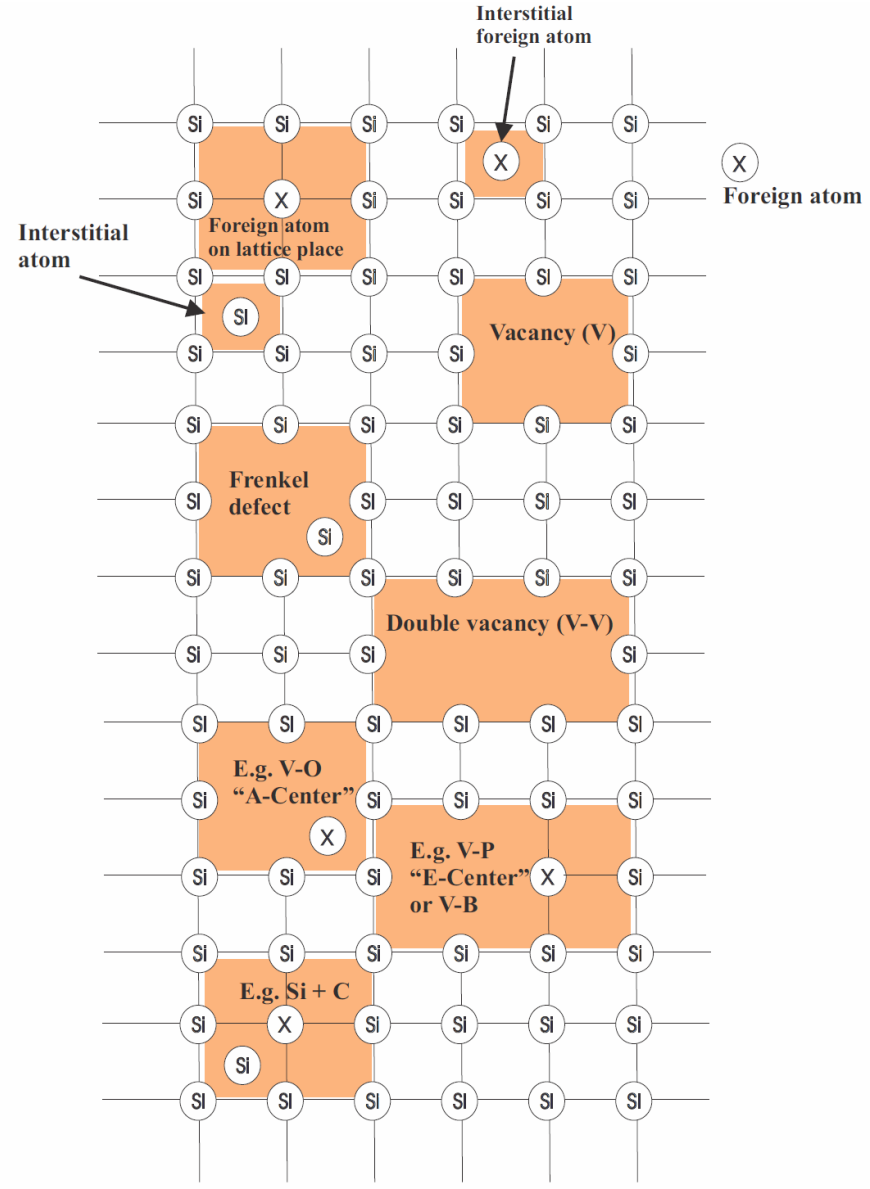

Figure 4.1: ***Illustration of some important defects in silicon [Fur06].*** *Interstitials, vacancies and a pair of these defects, a Frenkel-pair, can be seen. Further, double vacancies and some complexes of lattice defects with foreign atoms are displayed.*

The threshold energy E_d for the displacement of an atom lies in the range of 50 eV [Lin87]. At temperatures higher than 150 K the vacancies and the interstitials are mobile enough to migrate through the lattice. It is possible that they interact thereby with impurity atoms to form point defects. Vacancies V and interstitials I can form di-vacancies V_2, tri-vacancies V_3, di-interstitials I_2 or even

Defect	Charge state	Energy level [eV]
Interstitial	I^-	$E_C - 0.39$
	I^0	
	I^+	$E_V + 0.4$
Vacancy	V^{2-}	$E_C - 0.09$
	V^-	$E_C - 0.4$
	V^0	
	V^+	$E_V + 0.05$
	V^{2+}	$E_V + 0.13$
Divacancy	V_2^{2-}	$E_C - 0.23$
	V_2^-	$E_C - 0.39$
	V_2^0	
	V_2^+	$E_V + 0.21$
A-Center	VO^-	$E_C - 0.18$
	VO^0	
E-Center	VP^-	$E_C - 0.18$
	VP^0	
Phosphorus	P^0	
	P^+	$E_C - 0.44$
Boron	B^-	$E_V + 0.45$
	B^0	

Table 4.1: ***List of some important defects in silicon [Lut99].*** *The energetic distances from the valence band or conduction band show, that some defects act like dopants.*

more complex structures. Interactions of these defects with impurities can form new complexes which have different influences on the electrical material properties. One important defect is a vacancy plus a phosphorus atom VP, which removes the property of the phosphorus to act as a donor, leading to a decrease of the space charge. The complex of two vacancies and an oxygen atom (V_2O) acts in the same direction, concerning the impact on the space charge. Table 4.1 gives a survey of known or assumed defects. They are still topic of many studies. Defects can get removed by recombination processes between vacancies and interstitials, which is a consequence of their mobility allowing them the movement through the lattice.
Along the path of a PKA, its energy loss consists of competing losses due to ionization and further displacements. At the end of the range of heavy recoils, the non-ionizing effects prevail, so that agglomerations of defects are formed at the end of the path. For recoil energies between $1\,keV - 2\,keV$ only isolated point defects are created, while the clusters at the end of the path appear at energies higher than $10\,keV$. [Lut99]. In a non-relativistic approach, the maximum energy transfer in an elastic scattering between a particle with the energy E_p and the mass m_p and a silicon lattice atom with mass m_{Si} is given by [vL$^+$80]

$$E_{R_{max}} = \frac{m_p m_{Si}}{(m_p + m_{Si})^2} 4E_p \tag{4.1}$$

The range of a PKA can be calculated by [vL$^+$80]

$$R \approx 32 \frac{nm}{keV} \sqrt{E_R} \quad \text{for} \quad E_R < 10\,keV \tag{4.2}$$

E_R is the recoil energy of the PKA.

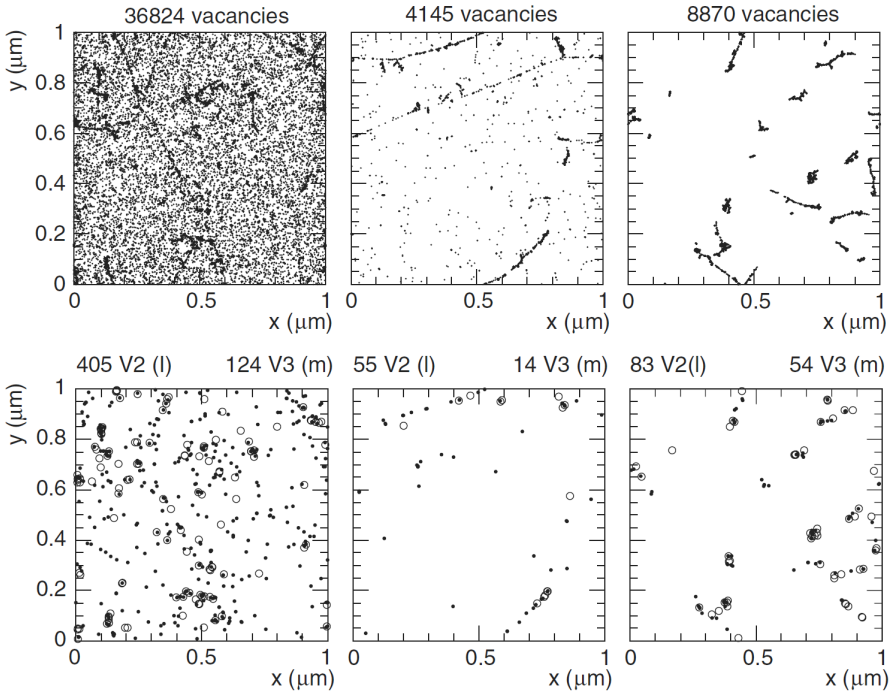

Figure 4.2: ***Simulation of radiation induced vacancy production and their annealing [Huh02].*** *The upper three figures illustrate the initial distribution of vacancies produced by radiation of a fluence of* $1 \cdot 10^{14}/cm^2$ *of the the following types. On the left hand side* 10 *MeV protons, in the middle* 24*GeV protons and on the right hand side* 1 *MeV neutrons. Protons create more point defects while neutrons create more clusters. After some annealing time the defects illustrated in the lower three figures build the final constellation. Dots reflect* V_2 *and circles* V_3.

Neutrons cannot interact with silicon via the coulomb interaction like charged hadrons do, which lose a part of their energy due to the reversible process of ionization. For neutrons the main interactions are elastic scattering and nuclear reactions at energies higher than $1.8MeV$ [vL$^+$80]. Therefore the interaction mechanisms vary between different radiation types, so that in general similar energies of different particles will not necessarily lead to similar damages. This can be directly seen in simulation results in figure 4.2.

Neutrons create mainly clusters, due to the dominance of strong nuclear interactions and the missing ionization energy loss along the path, while charged particles produce more homogeneous defect distributions. Nevertheless the NIEL (Non Ionizing Energy Loss) hypothesis tries to give a means to compare the radiation damages of different particle types with different energies. The approach bases on the assumption that the damage induced change of the material properties is a result of the total energy transferred in displacement collisions. The so called Lindhard partition function $P(E_R)$ [LN62] provides the fraction of the recoil energy of a dedicated interaction process that is spent for a displacement damage. Some values for $P(E_R)$ are, $P(E_R) \approx 50$ % for 10 MeV protons, $P(E_R) \approx 42$ % for 24 GeV protons and $P(E_R) \approx 43$ % for 1 MeV neutrons. A parameter which allows to describe the displacement damage is given by the displacement damage cross section, or damage function [Mol99]

$$D(E) = \sum_i \sigma_i(E) \int_0^{E_{R_{max}}} f_i(E, E_R) P(E_R) dE_R \tag{4.3}$$

It has to be summed up over all possible interactions between the incoming radiation particle with the energy E and the silicon atoms that lead to displacements. The belonging cross section to the interaction with index i is $\sigma_i(E)$, while $f_i(E,E_R)$ is the probability for the generation of a PKA with the recoil energy E_R. The integration has to be done over all possible recoil energies. The damage function allows the designated comparison of different radiation types in the definition of the hardness factor. This factor calculates the ratio between the damage produced by a given fluence of a specific radiation type and energy and the one produced by a standard type of the same fluence defined by neutrons of an energy of 1 MeV. For these neutrons the value of the damage function is $D(1\,MeV) = 95\,MeV \cdot mb$ [Lin03]. The hardness factor is therefore given by [Mol99]

$$\kappa = \frac{\int D(E)\phi(E)dE}{D(E = 1\,MeV) \cdot \int \phi(E)dE} \tag{4.4}$$

Thus it is possible to determine the equivalent 1 MeV neutron fluence $\phi_{eq.}$ that creates the same damage like the fluence ϕ of the specific type by

$$\phi_{eq.} = \kappa \int \phi(E)dE \tag{4.5}$$

In figure 4.3 plots of the displacement damage function D(E) of neutrons, protons, pions and electrons can be found, normalized to 95 $MeVmb$.

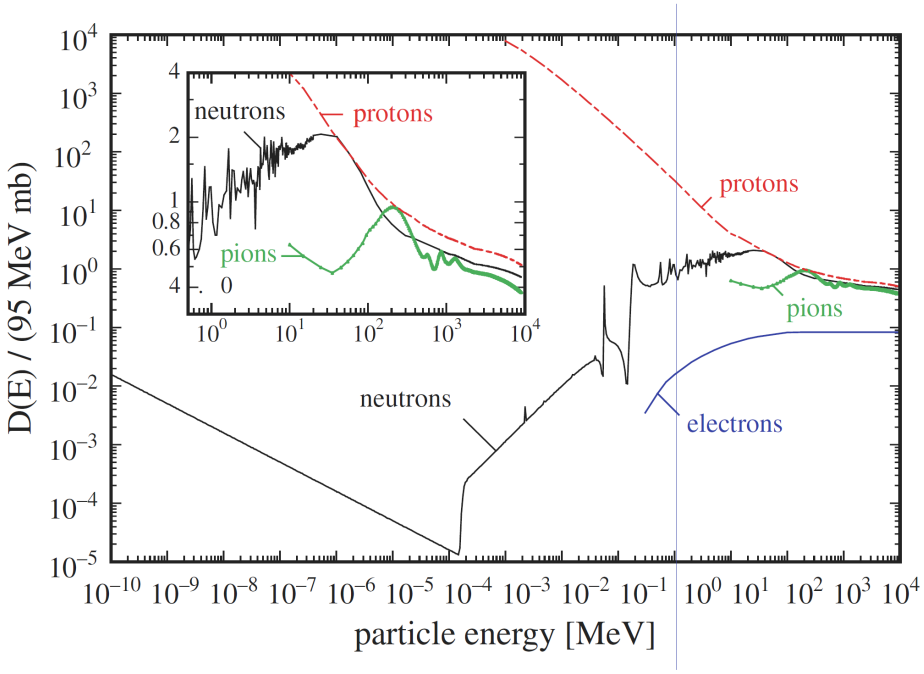

Figure 4.3: ***Displacement damage function [Lin03].*** *The plotted damage functions of neutrons, protons, pions and electrons are normalized to* 95 *MeVmb. The damage function allows the designated comparison of different radiation types in the definition of the hardness factor.*

4.3 Macroscopic Effects of Radiation Damages on Sensor Properties

The reason for the degradation of the sensor efficiency after irradiations lies in the additional energy levels in the band gap of the silicon that several point defects or cluster complexes offer. Levels that lie energetically close above the valence band behave like acceptors while the ones close underneath the conduction band show donor attributes. One is talking about deep acceptors or deep donors, if the levels lie near the Fermi level, while one calls them shallow when they lie near the edges of the accordant bands. The mentioned energy levels responsible for the effects presented in the following are illustrated in figure 4.4.

Similar to equations (3.21) and (3.22) the occupation of electrons in a trap of the energy E_t and the

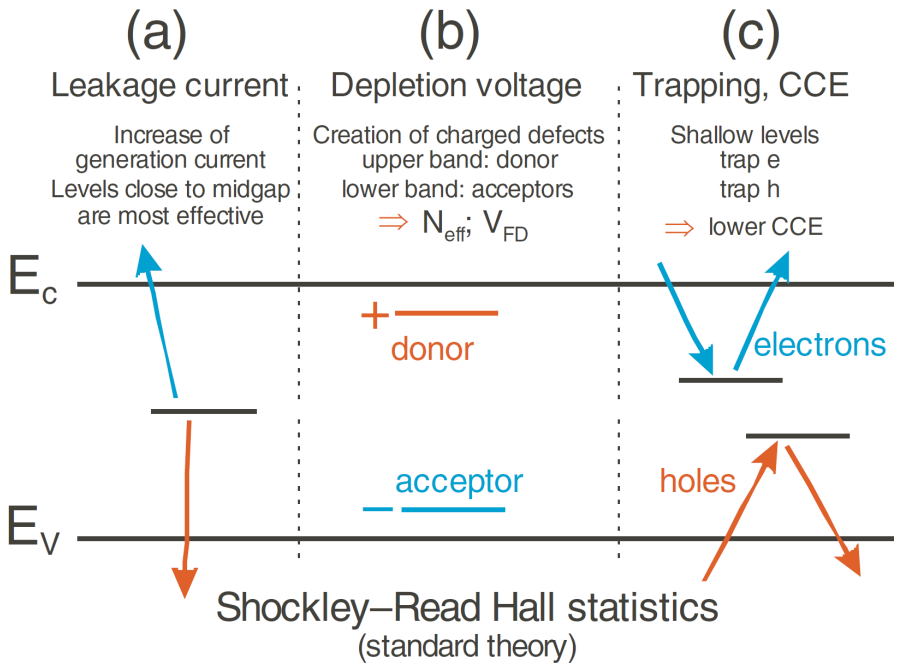

Figure 4.4: ***Illustration of the defect energy levels being responsible for several macroscopical effects on the silicon properties. [Har08].*** *a) Energy levels in the middle of the band gap are mainly responsible for the increase of the leakage current. b) Donor levels near the conduction band and acceptor levels near the valence band influence the full depletion voltage. c) The reduction of the charge collection efficiency by the effect of trapping is caused by levels near the middle of the band gap.*

concentration N_t is

$$n_t = N_t \frac{1}{e^{(E_t - E_F)/k_B T} + 1} \tag{4.6}$$

respectively the occupation concentration of holes in these traps is

$$p_t = N_t \frac{1}{e^{-(E_t - E_F)/k_B T} + 1} \tag{4.7}$$

The change of the occupation of traps depends on the electron capture rate R_{ec}, the electron emission rate R_{ee}, the hole capture rate R_{hc} and the hole emission rate R_{he} [Hön07]

$$\frac{dn_t}{dt} = -R_{ec} + R_{ee} + R_{hc} - R_{he} \tag{4.8}$$

The electron capture rate should be proportional to the electron concentration in the conduction band n and the concentration of traps that can capture electrons given by equation (4.7) so that R_{ec} becomes

$$R_{ec} = c_n n N_t \frac{1}{e^{-(E_t - E_F)/k_B T} + 1} \tag{4.9}$$

with the capture coefficient c_n for electrons. In similar considerations, which include that for an emission process only the occupation rate counts, the other rates can be found to be

$$R_{hc} = c_p p N_t \frac{1}{e^{(E_t - E_F)/k_B T} + 1} \tag{4.10}$$

$$R_{ee} = e_n N_t \frac{1}{e^{(E_t - E_F)/k_B T} + 1} \tag{4.11}$$

$$R_{he} = e_p N_t \frac{1}{e^{-(E_t - E_F)/k_B T} + 1} \tag{4.12}$$

e_n and e_p are called emission rates for electrons and holes. In thermal equilibrium when the capture and emission rates are equal, they can be found to be

$$e_{n,p} = c_{n,p} N_{C,V} e^{\left(\pm \frac{E_t - E_{C,V}}{k_B T}\right)} \tag{4.13}$$

with the intrinsic charge carrier densities $N_{C,V}$.
In the space charge region of a sensor under reverse bias, the concentrations of free charge carriers are low ($n \approx 0$, $p \approx 0$) so that the rates R_{hc} and R_{ee} can be neglected and equation (4.8) becomes

$$\frac{dn_t}{dt} = -e_n n_t + e_p p_t \tag{4.14}$$

Then the occupation concentrations in the space charge region are

$$n_t = N_t \frac{e_p}{e_n + e_p} \tag{4.15}$$

and

$$p_t = N_t \frac{e_n}{e_n + e_p} \tag{4.16}$$

4.4 Change of the Full Depletion Voltage

The precedent considerations deal with one energy level. Several ones exist and the sum of the donor-like levels occupied by holes and the acceptor-like levels occupied by electrons give the effective charge stored in the traps. The effective space charge density is given by $q_0 N_{eff}$, so that

$$N_{eff} = \sum_{donors} p_t + \sum_{acceptors} n_t \tag{4.17}$$

Ionized donor levels near the conduction band contribute a positive space charge and ionized acceptor levels near the valence band contribute a negative one thereby changing the effective doping concentration according to equation 4.17 and the full depletion voltage according to equation 3.48. Therefore energy levels near the band edges affect the full depletion voltage.
Oxygen rich silicon material has some slightly different macroscopic properties after irradiation. Especially the development of the full depletion voltage with fluence differs in a positive way regarding the applications of sensors. This will be presented in chapter 6.

4.5 Leakage Current Increase

Energy levels in the middle of the band gap influence the leakage current of a sensor. This will be shown in the following. The generation rate of free charge carriers G_t of a defect in the space charge region is given by

$$G_t = e_n n_t = e_p p_t \tag{4.18}$$

$$G_t = N_t n_i \frac{c_n c_p}{c_n exp\left(\frac{E_t - E_i}{k_B T}\right) + c_p exp\left(-\frac{E_t - E_i}{k_B T}\right)} \tag{4.19}$$

Under the assumption of equal cross sections for hole and electron capturing, the expression simplifies to [Lut99]

$$G_t = \frac{N_t n_i c_n}{2cosh\left(\frac{E_t - E_i}{k_B T}\right)} \tag{4.20}$$

The bulk generation current depends on the generation rates of the different defects in the space charge region

$$I = \sum_{traps} q_0 G_t V_{SCR} \tag{4.21}$$

so that equation 4.20 expresses why mainly defects with energy levels in the middle of the band gap are responsible for the increase of the bulk generation leakage current in the volume V_{SCR} after irradiation. As the creation of defects is proportional to the equivalent fluence of the radiation, it is expected that the total current increases proportionally as well

$$\Delta I = \alpha V_{SCR} \phi_{equ.} \tag{4.22}$$

with the so called current related damage rate α. Figure 4.5 proves this with measurements of the leakage current increase after irradiations of float zone and epi-materials of different resistivities. The linear increase with the fluence is evident.

The radiation induced current increase at a constant voltage goes along with a higher heat dissipation $P = U \cdot I$ in the sensor. If the heat transport around the sensor is insufficient, the sensor will heat up, which has the consequence that the bulk generation current increases further according to the exponential temperature dependence in formula 3.52. This produces even more heat, so that the temperature rises further and so on. This effect is called thermal runaway and has to be obviated in the sensor operation by appropriate cooling.

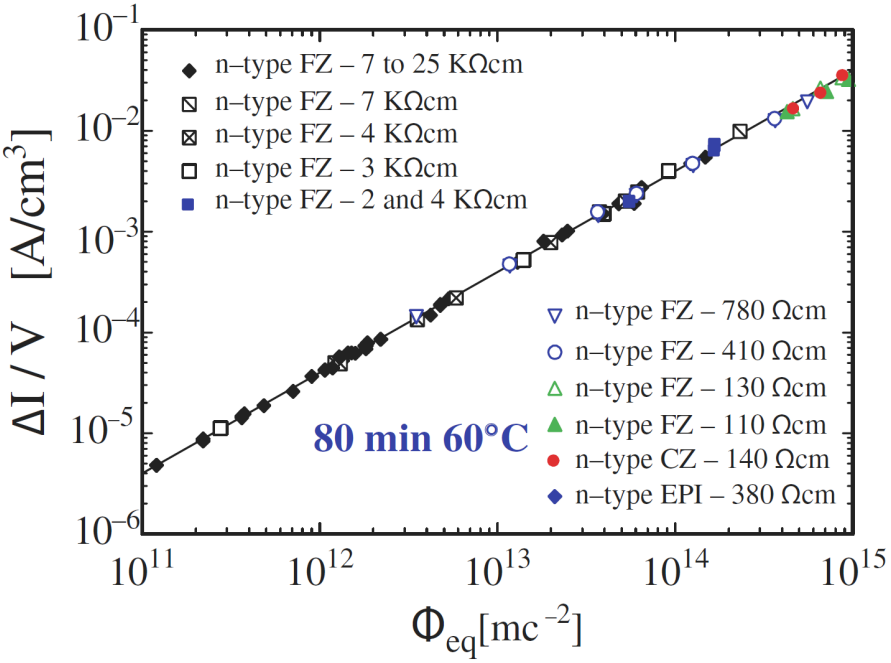

Figure 4.5: ***Linear fluence dependence of the leakage current increase of different silicon materials. [Mol99]*** *The slope of the straight is independent of the material (also for MCz) at a given temperature and defines the current related damage rate* α*. The value after a heat treatment of the silicon for 80 minutes at 60 °C is given to be* $(3.99 \pm 0.03)\ x\ 10^{-17}\ A/cm$ *[Mol99].*

4.5.1 Trapping, Reduction of the Charge Collection Efficiency

Another important consequence of radiation damages is the effect of trapping. When electron-hole pairs are created in the sensor by traversing particles, they drift to the electrodes forming the signal thereby. If on their way the charge carriers get into contact with damages with energy levels near the borders of the bands, they can be trapped at the defects in these levels. To handle the signal, the involved electronics have shaping times, during which the charge is collected. If this time is shorter than the time after which trapped charge carriers are emitted again, their part of the signal is lost so that the signal height is reduced. Therefore trapping leads to a decrease of the charge collection efficiency. The thermal drift velocity υ_{th} and the saturation drift velocities υ_{dr} of the charge carriers are in the same order of $10^7\ cm/s$ at room temperature and the temperatures considered here [C$^+$75], so that for a length l the charge q with the velocity υ needs the time

$$t = \upsilon / l \tag{4.23}$$

The more trapping centers N_i can be found on the drift path, the higher is the trapping probability, so that the effective free drift time of the charge carriers decreases, expressed in [K$^+$02]

$$\frac{1}{\tau_{eff}^{e,h}} = \sum_i N_i^{e,h} (1 - P_i^{e,h}) \sigma_i^{e,h} \upsilon^{e,h} \tag{4.24}$$

where P_i is the occupation probability of the trap i and σ_i the associated cross section. In a first order approach, the number of traps is proportional to the fluence ϕ_{eq} of the damaging radiation with an

introduction rate g_i and a function $f_i(t)$ which describes annealing effects (see chapter 4.7)

$$N_i = g_i \phi_{eq} f_i(t) \tag{4.25}$$

so that also the following can be written

$$\frac{1}{\tau_{eff}^{e,h}} = \beta_{e,h}(t,T)\phi_{eq} \tag{4.26}$$

With these definitions one can parameterize the charge which remains of an originally generated one $q_{0_{e,h}}$ after a given length for which the time t is needed to drift through

$$q(t) = q_{0_{e,h}} \cdot exp\big(-\frac{t}{\tau_{eff}^{e,h}}\big) \tag{4.27}$$

The probability for a charge carrier to get trapped at a certain kind of defect is proportional to the capture coefficient, its concentration and the concentration of not occupied defects. The overall trapping time constants $\tau_{T,n,p}$ of electrons and holes are given by

$$\frac{1}{\tau_{T,n}} = \Sigma_{traps} c_{n,t} N_t \frac{e_{n,t}}{e_{p,t} + e_{n,t}} \tag{4.28}$$

$$\frac{1}{\tau_{T,p}} = \Sigma_{traps} c_{p,t} N_t \frac{e_{p,t}}{e_{p,t} + e_{n,t}} \tag{4.29}$$

4.6 Type Inversion and Double Junction Effect

4.6.1 Type Inversion

The change of the effective doping concentration in the detector bulk under the influence of radiation can lead to the effect of type inversion [Pit92]. It has been shown by several groups, that in float zone n-type substrates (see chapter 6.1.1) the full depletion voltage first decreases with the fluence, even reaching the value zero. Therefore the effective doping concentration N_{eff} must also decrease with the fluence. With further irradiations the full depletion voltage rises again, which means that N_{eff} increases. Figure 4.6 shows an example. The effect has been explained by the combined impacts of a deactivation of dopants and a creation of acceptor levels. The latter should be the reason for the increase of N_{eff} after the minimum is reached, turning the substrate in an effectively p-doped material, so that an inversion of the bulk doping type occurs. Mobile defects, like interstitials, can migrate through the lattice and react with dopants by building complexes or they can move them from their position in the lattice. The emerging defects are mostly not ionized and in the space charge region the effective doping concentration changes, meaning that shallow donor levels get removed. In case of a phosphorus doped n-type silicon, donors get deactivated and additionally acceptors are created by the radiation. Therefore the initial space charge decreases with fluence up to the point of space charge sign inversion, when firstly the space charge vanishes and after further irradiation a linear increase of negative space charge is observed as the acceptor like levels get predominant.
Additional evidence for the type inversion model is given by measurements which show, that the pn-junction moves from the front side, where the strips are embedded, to the backside of the sensor, where a highly doped thin n^+-layer exists [Pit92]. The sensor was illuminated one time from the front and one time from the backside with LEDs producing light which gets absorbed after roughly 30 μm.

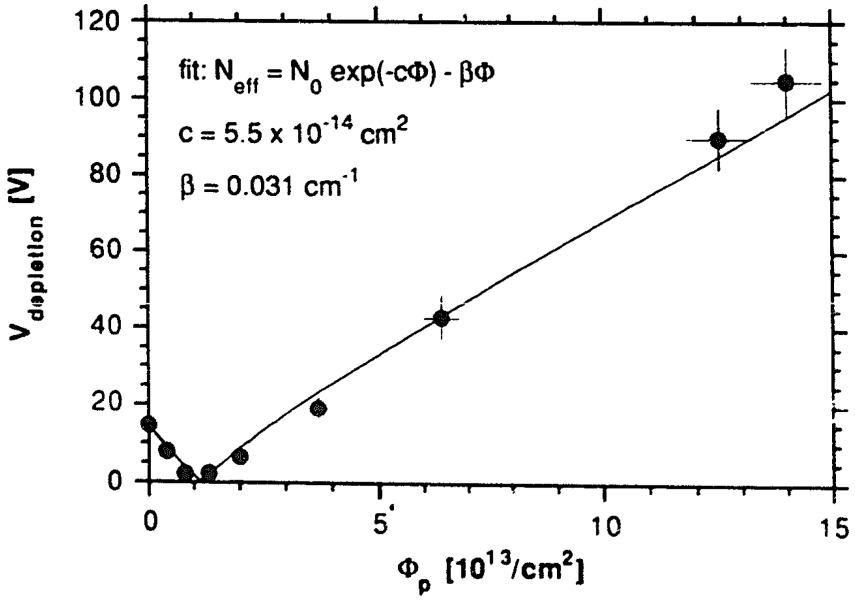

Figure 4.6: ***Evidence for the effect of Type-Inversion on the basis of the full depletion voltage characteristics. [Pit92]*** *In FZ n-type substrates the full depletion voltage first decreases with the fluence and even reaches the value zero. With further irradiation, the voltage increases again. The radiation induced change by the generation of acceptor-like defects is responsible for the change of the effective doping concentration and thereby the change in the full depletion voltage.*

The light induced signal was measured in dependence of the bias voltage. Measurements before and after irradiation were compared. Before irradiation the depletion zone grows from the front side, starting around the p-implants, so that the LED light is detected even before full depletion. In contrast to this, light illuminated at the backside could not be detected until the full depletion voltage was applied, which means that an active depleted zone was generated also at the backside. This picture flips when the effect of type inversion occurs, so that then the light at the backside creates signals even before full depletion. Figure 4.7(a) and 4.7(b) present the plots accordant to this observation. The sensitive volume at the backside before full depletion originates from the junction between the type inverted bulk, being now p-type, and the highly doped n^+-layer. The effect has been confirmed by measurements of the hole current pulse shapes of signals created at the front and at the backside by alpha-particles [KL93]. A microscopical explanation for type inversion given in [M$^+$96] includes that the donor removal is less important for the effect than the acceptor creation, like approved by DLTS[1] results.

[1]Deep Level Transient Spectroscopy

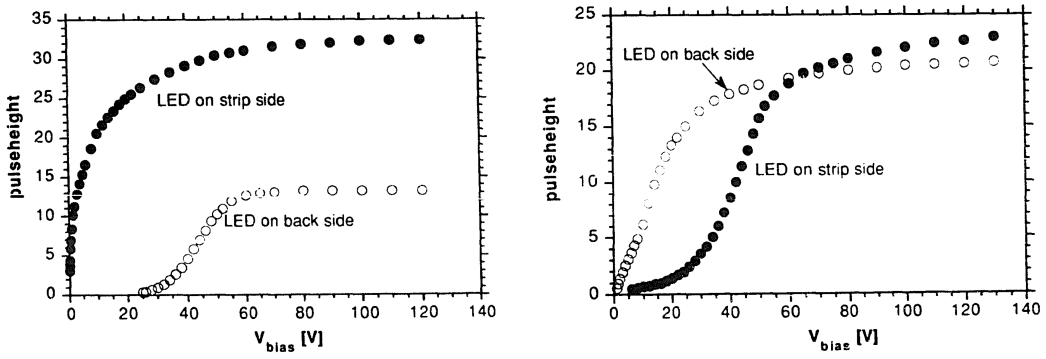

Figure 4.7: ***Measurements that give evidence for a bulk type inversion after a high irradiation, as the dominant junction growth with a reverse bias voltage moves to the backside of the sensor [Pit92].*** *The sensor was illuminated one time from the front and one time from the backside with LEDs producing light which gets absorbed after roughly* 30 *µm. a) Before irradiation the depletion zone grows from the front side, starting around the p-implants, so that the LED light is detected even before full depletion, while at the backside this is not possible. b) When the effect of type inversion occurs, the light at the backside can create signals even before full depletion, while at the front side it is suppressed as long as the sensor is not fully depleted.*

4.6.2 Double Junction Effect

The depletion zone in a type inverted sensor predominantly grows from the backside, which has consequences for the resolution of not fully depleted sensors, as the depletion around the position sensitive segments is suppressed. The picture becomes more complex at higher fluences by the observed effect of an appearing second junction at the front [KL93]. In addition to this observation, the electric field of fully depleted highly irradiated sensors has a non-regular distribution, compared with non- or minor irradiated sensors, with peaks at both sides of the sensor contacts (see figure 4.8)[Men99]. This has been explored by the transient current technique (TCT) [L$^+$96]. In reference [V$^+$02], the origin of this double peak is explained by a model where deep acceptor and donor levels, resulting from the radiation damage, can accumulate charge by trapping in steady state conditions. Positive charge mainly gets trapped near the p^+-region of the reverse biased sensor, while negative charge carriers mainly get trapped at the n-type part. The first Maxwell equation

$$div\,\overrightarrow{E}(x) = \frac{-eN_{eff}}{\varepsilon\varepsilon_0} \tag{4.30}$$

reveals that then two peaks in E(x) appear. Two deep levels, DA4 ($E_C - 0.53\ eV$) and DD2 ($E_V + 0.48\ eV$) which were observed in irradiations, were used in the model as the responsible trapping centers. Further it has been shown, that in this model the double junction effect appears for bias voltages lower than the full depletion voltage, so that it can be concluded that both effects have their origin in the presented trapping mechanism. The double junction effect is of importance as it leads to an improved behavior of the sensor in the way, that even for only partially depleted sensors an active volume around the implants exists.

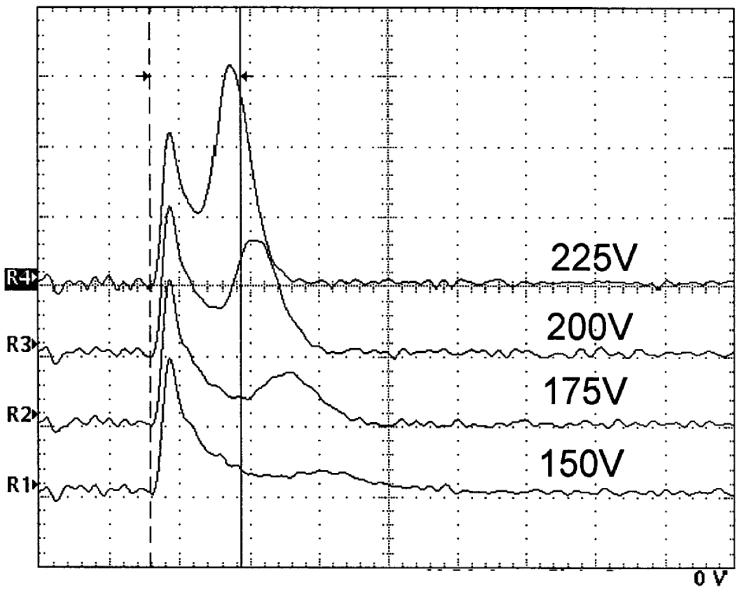

Figure 4.8: ***Double peaks in the laser induced transient currents of highly irradiated sensors. [Men99]*** *By using the transient current technique, peaks in the electrical field strength at both sides of the sensor contacts have been proved.*

4.7 Defect Annealing

The presented alterations of sensor properties due to irradiation can develop depending on temperature and time. This effect is called annealing and it can have beneficial and reverse impacts on the sensor behavior.
The main annealing mechanisms are the migration of defects so that the building of complexes is possible and the dissociation of defects, like in the case of a Frenkel pair when the interstitial moves back into a bound lattice position. Vacancies and interstitials are mobile already at room temperature while others, like divacancies (V_2) or vacancy oxygen complexes (VO_i), become mobile at temperatures higher than 250°C . The arising more complex defect structures can be more thermally stable and can offer different energy levels, which explains the change in the macroscopic properties of the sensor after annealing. In figure 4.9 it can be seen, how the current related damage rate α decreases with time at different temperatures. The higher the annealing temperature, the faster the changes proceed. After a heat treatment of an irradiated sensor, this has the positive effect of a reduced leakage current.
In contrast to the leakage current, the full depletion voltage does not decrease permanently with the annealing time and temperature, but shows a more complex behavior also dependent on the material and the fluence. The Hamburg model describes the change in the effective doping concentration by the following parametrization [Mol99]

$$\Delta N_{eff}(\phi_{equ.},t) = N_C(\phi_{equ.}) + N_A(\phi_{equ.},t) + N_Y(\phi_{equ.},t) \tag{4.31}$$

The stable damage $N_C(\phi_{equ.})$ can be described by

$$N_C(\phi_{equ.}) = r_C N_{eff,0}(1 - exp(-c\phi_{equ.})) + g_C\phi_{equ.} \tag{4.32}$$

The first term accounts for an incomplete donor removal of the initial effective doping concentration $N_{eff,0}$ and the second one for a linear increase of stable acceptors by fluence. For standard FZ silicon,

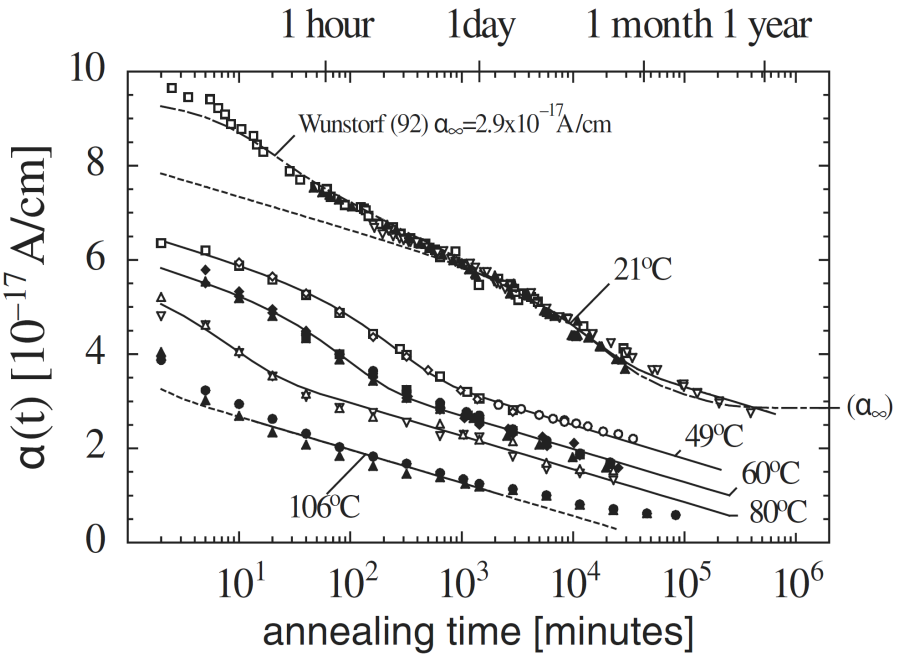

Figure 4.9: ***Annealing behavior of the current related damage rate. [Mol99]*** *The current related damage rate decreases temperature dependent with time, so that a positive effect concerning the leakage current appears.*

the constants are measured to be $r_C = 0.65$, $g_C = 1.49 \cdot 10^{-2} cm^{-1}$, $c = (10.9 \pm 0.8) \cdot 10^{-2} cm^{-1} / N_{eff,0}$ [Mol99].
In the first period of time directly after annealing, a significant change in the full depletion voltage can be observed, which the second term in formula (4.32) considers. The full depletion voltage increases before type inversion while it decreases after it in case of an n-type bulk material. This can be interpreted in the way, that the annealing increases N_{eff}. Before type inversion, N_{eff} is positive and becoming even more positive, so that the full depletion voltage according to equation 3.48 increases. After type inversion N_{eff} is negative so that an increase leads to a decrease of the absolute value and thus to a decrease of the full depletion voltage, as there only the absolute value of N_{eff} is important. The expression for this so-called short-term-annealing or beneficial annealing can also be found in reference [Mol99] as a sum of exponential terms

$$N_A(\phi_{equ.}, t) = \phi_{equ.} \sum_i g_{a,i} exp\left(\frac{t}{-\tau_{a,i}}\right) \tag{4.33}$$

($g_a = (1.81 \pm 0.14) \cdot 10^{-2} cm^{-1}$ as an effective mean value for standard FZ). The third term in (4.32) considers the fact, that after a longer period of annealing, the full depletion voltage develops in the opposite direction as the one seen directly after the irradiation. The reason for this is, according to the model, that stable acceptor-like defect complexes are created so that N_{eff} becomes more negative and after type inversion the full depletion voltages increases. The term for this reverse annealing is given by [Mol99]

$$N_Y(\phi_{equ.}, t) = N_{Y,inf}\left(1 - \frac{1}{1 + k_Y N_{Y,inf} \cdot t}\right) \tag{4.34}$$

annealing temperature [°C]	-10	0	10	20	40	60	80
short term annealing τ_a	306 d	53 d	10 d	55 h	4 h	19 min.	2 min.
long term annealing τ_γ	516 y	61 y	8 y	475 d	17 d	21 h	92 min.

Table 4.2: ***Hamburg Model time constants. [Mol99]***

with the reverse annealing amplitude $N_{Y,inf} = g_Y \cdot \phi_{equ.}$ where g_Y is measured to be $(5.16 \pm 0.09) \cdot 10^{-2} cm^{-1}$. The time constants are given in table 4.2 [Mol99]. The influence of the different terms on the effective doping concentration of a sample irradiated with a fluence of $1.4 \cdot 10^{13} neq./cm^2$ can be seen in figure 4.10.

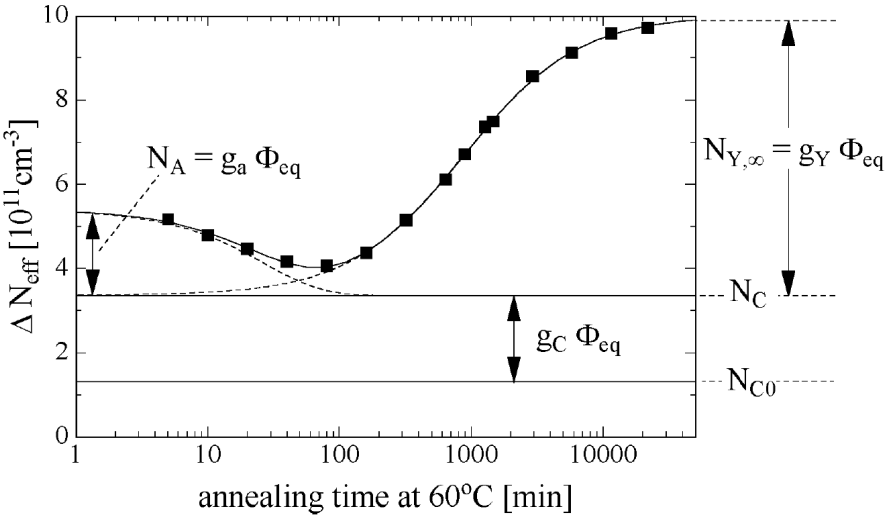

Figure 4.10: ***Annealing behavior of the effective doping concentration [Mol99].*** *The Hamburg model describes the change in the effective doping concentration by three different terms. They are the stable damage $N_C(\phi_{equ.})$, the short-term annealing $N_A(\phi_{equ.}, t)$ and the reverse annealing $N_{Y,inf}$.*

Chapter 5

Working Principles of Silicon Detectors

5.1 Principle Sensor Design

The task of a radiation tracking detector is, as the name says, to get a track information of a traversing radiation particle. In chapter 3 mechanisms of signal generation of charged particles in reverse biased pn-junctions have been presented. They are the means to reach the desired goal, if one structures the semiconductor material in a way that the signal also delivers a position information. For this purpose one takes either a p- or a n-doped bulk material and structures one or both sides with a high concentration of dopants of the opposite doping type or of the same type but with a significantly different doping concentration. A device with segmented pn-junctions results, which finally provide the position information. Common structures are strips or pixels.

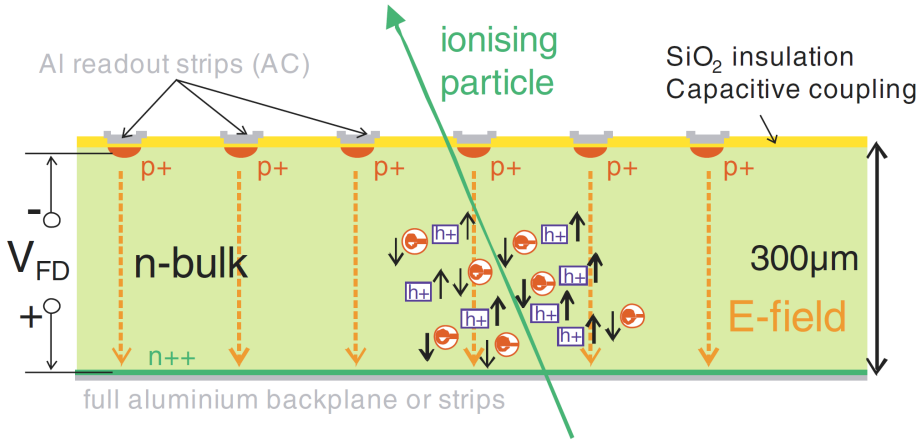

Figure 5.1: ***Sectional drawing of a popular silicon sensor layout. [Har08]*** *A thin n-type silicon bulk is structured at one side by p-type strips. Traversing ionizing particles generate electron-hole pairs in the bulk which drift towards the electrodes in the electrical field of an applied reverse bias voltage. Through a dielectric of commonly SiO_2 on the surface of the strip side the signal of the charge carriers (here holes) is coupled to aluminium strips that conduct it to the readout electronics where an amplification, shaping and data handling takes place. Due to the segmentation of the sensor by pn-junctions, position information of the traversing point can be achieved.*

The scheme of a very popular design, also used for the test sensors explored in this thesis, is presented in figure 5.1. In a bulk of n-type silicon, p-type strips are embedded. Charge carriers, generated by traversing particles, drift in the electrical field of a reverse bias to the appropriate electrodes and can be detected by a readout electronics. This can either be done directly with a DC-coupling or by a AC-coupled readout via coupling capacitors. Aluminium strips conduct the signal to the readout electronics where an amplification and a signal processing take place. The coupling capacitors are established by a dielectric between the p-implants and the adjacent aluminium strips. For the dielectric commonly silicon dioxide or silicon nitride is used.
If the electronics is connected to ground potential, which is a suitable way, then the p-implants have to be set at a certain, differing but low potential. Otherwise, in the case of a joint fixed potential between the strips and the electronics, the signal would be swallowed. The 3D Sketch in figure 5.2 shows how this potential difference is implemented by the usage of resistors and a decoupling of the individual strips is achieved. The ground potential is connected to an aluminium ring, the so-called bias-ring, which surrounds the strips and which is connected to the p-implants via these bias-resistors. Their resistance is in the order of 10^6 Ω and the resistance between the p-strips and the backplane is in the order of 10^9 Ω. Resistor materials can be for example poly-crystalline silicon or tungsten-nitride.

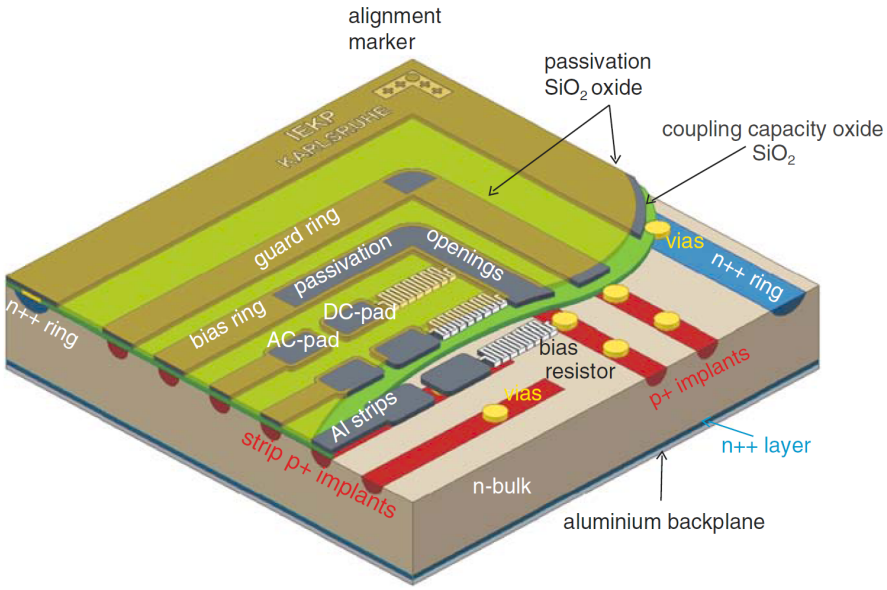

Figure 5.2: ***3D sketch of a sensor design. [Har08]*** *It can be seen how the p-type strips in the n-type silicon are set on a certain low potential differing slightly from ground potential by the usage of bias resistors. They are connected to the so-called bias-ring. The power supply is connected to this ring and to the backplane. The surrounding guardring serves for the shaping of the electrical field to ensure a homogeneous electrical field configuration in the active area. The readout electronics is connected to the AC-pads, while the DC-pads are implemented for testing purposes.*

One ore more further aluminium rings with defined or floating potentials are placed around the bias-ring at the edges of the sensor. They are called guardrings and their task is to shape the electrical field in the way that a homogeneous electrical field configuration in the active sensor area is ensured. The high potential of the bias-voltage is connected to the backplane of the sensor where a highly doped thin n++ layer enables a good contact to the covering aluminium. The readout electronics is

connected to the AC-pads via small wire bonds. The DC-pads, that can also be seen in the figure 5.2 are implemented for testing purposes.
To protect the functional components of the sensor of mechanical damage, the surface of the top of the sensor is normally covered with a passivation layer out of silicon-dioxide or silicon-nitride.

5.2 Readout Electronics

The task of the readout electronics based on ASICs[1] is, to collect the signal charge, which lies in the order of a few fC, and to process it in preparation of a following data handling. A signal gets amplified, shaped and temporarily stored until it is send to a higher data acquisition level on consequence of a trigger signal. The normally high number of readout channels necessitates multiplexing and in many cases also a pulsed power mode readout, where the chip is only active at presence of a signal to reduce power dissipation. To avoid filling of the bandwidth with zero information, often the sparsification technique is used that reads out the signals only if the charge exceeds a certain threshold.

The APV25 Chip

In more detail, the Analog Pipeline Voltage chip APV25 [T$^+$01] will be presented, as this readout chip was used for the research presented in the following chapters. The chip was developed to fulfill the demands arising at the LHC. Special design rules for the basic electronics functional elements allow to establish the intrinsical radiation hardness of the 0.25 μm CMOS[2] technology.
A schematic circuit diagram of the APV25 can be found in figure 5.3. The chip affords to read out 128 sensor channels, whereby at each input a low noise preamplifier with shaper, a 192-cell analog pipeline and an analog pulse shape processor (APSP) are applied. After the signal integration in the preamplifier, the signal polarity can be inverted in the inverter stage, depending on the application (n-type bulk, p-type bulk, forward bias, reverse bias). The charge output of the CR-RC shaper is stored in a 192 elements deep analog pipeline with the sampling time of the LHC system clock of 40.08 MHz.

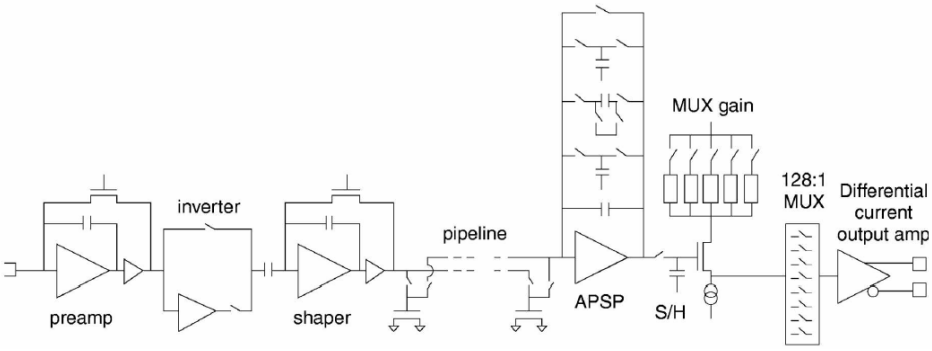

Figure 5.3: ***Schematic circuit diagram of the APV25 readout chip [T$^+$01].*** *The radiation hard chip is designed to read out 128 sensor channels. At each channel a low noise preamplifier with shaper, a 192-cell analog pipeline and an analog pulse shape processor (APSP) can be found. The signal is sent via a sample and hold stage into a multiplexer where all 128 channels are multiplexed to a single amplifier with a differential signal output.*

[1] Application Specific Integrated Circuits
[2] Complementary Metal Oxide Semiconductor

To avoid noise, the shaping times are relatively long, resulting in long output pulses of $\sim 100\ ns$ width at half maximum. On a trigger signal, the signal is sent from the shaper to the APSP. This unit can treat the signal in two different kind of modes. In the peak mode only one cell of the pipeline is read out. To ensure that it is the one of the maximum voltage of the shaped signal, the timing settings of the chip have to be adjusted accordingly. In the deconvolution mode, three consecutive pipeline cell signals of the shaper output are added with appropriate weights to a signal of around 25 *ns* width. The peak mode is foreseen for low data rates, while in the case of pile-up effects in a channel at higher rates, the deconvolution mode is the one to choose. The signal flow via a sample and hold stage proceeds into a multiplexer where all 128 channels are multiplexed to a single amplifier with a differential signal output.
Together with other functional elements like ASICs, meant for communication, triggering and environmental conditions control, the readout chips are mounted on ceramics. This structure is called hybrid.

5.3 Noise

Several functional elements of a sensor are sources for fluctuations of electrons and holes. They can get also detected and amplified by the readout electronics, creating noise thereby. Further, the electronics itself is a noise source dependant of its special design. A simplified equivalent circuit diagram for the noise sources is drawn in figure 5.4. Between the input of the electronics and the ground potential, parallel and serial resistances as well as serial and parallel capacitances exist which contribute different fractions to the total noise.

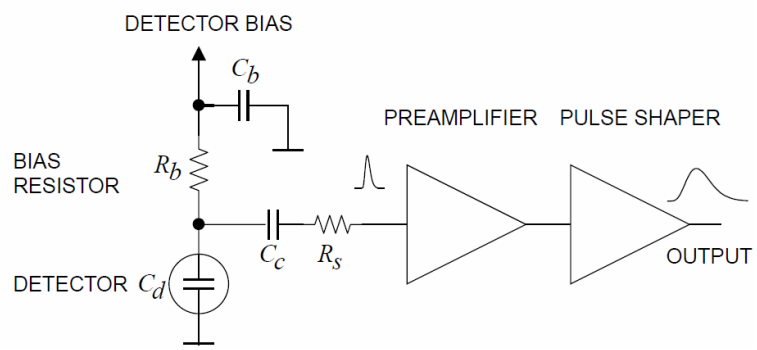

Figure 5.4: ***Simplified circuit diagram of a sensor and its readout electronics, illustrating possible noise sources. [H+02]*** *Principle noise sources are the load capacitance at the electronics input, the shot noise resulting from the leakage current, the parallel thermal noise from the bias resistance, the serial thermal noise from the metal strip resistance and the internal electronics noise.*

The dimension ENC [3] describes the noise in numbers of electron charges and the different contributions have to be summed up as [Har08]

$$ENC = \sqrt{ENC_C^2 + ENC_{I_{leak}}^2 + ENC_{R_p}^2 + ENC_{R_s}^2} \tag{5.1}$$

The contributions are
1. The load capacitance C_d at the electronics input and the internal electronics noise

$$ENC_C = a + b \cdot C_d \tag{5.2}$$

2. The shot noise, resulting from the leakage current I_{leak}

$$ENC_{I_{leak}} = \frac{e}{2} \cdot \sqrt{\frac{I_{leak} \cdot t_p}{q_e}} \approx 107 \cdot \sqrt{I_{leak}/nA \cdot t_p/\mu s} \tag{5.3}$$

3. The parallel thermal noise from the bias resistance

$$ENC_{R_p} = \frac{e}{q_e} \cdot \sqrt{\frac{k_B T \cdot t_p}{2 \cdot R_{Bias}}} \approx 44.5 \cdot \sqrt{\frac{T/K \cdot t_p/\mu s}{R_{Bias}/M\Omega}} \tag{5.4}$$

4. The serial thermal noise from the metal strip resistance

$$ENC_{R_s} = C_d \cdot \frac{e}{q_e} \cdot \sqrt{\frac{k_B T \cdot R_s}{6 \cdot t_p}} \approx 0.025 \cdot C/d/pF \cdot \sqrt{\frac{T/K \cdot R_s/\Omega}{t_p \mu s}} \tag{5.5}$$

The used characters have the following meaning, e the Euler number, t_p the peaking time, q_e the elementary charge, k_B the Boltzmann constant, T the Temperature and a and b constants which depend on the used electronics.

[3] Equivalent Noise Charge

Chapter 6

Properties of Magnetic Czochralski Silicon

The effects of radiation induced lattice damages on the performance of silicon sensors has been described in chapter 4. The three main macroscopic consequences are, the increase of the leakage current, the change of the effective doping concentration leading to a change of the full depletion voltage and the increased negative influence of trapping on the charge collection efficiency.
It has been shown by the ROSE / RD48 collaboration, that a higher oxygen concentration in the bulk material has a positive effect on the development of the full depletion voltage with irradiation as then the full depletion voltage increases less with the fluence. This feature is of interest for sensors that have to withstand high fluences, like it is the case for sensors used at the planned SLHC experiments. It allows to keep sensors fully depleted with lower voltages or at least to deplete a bigger volume at a given voltage. Possible influences of the oxygen on the trapping behavior and the general development of such oxygen enriched sensors at high SLHC fluences have to be explored.

6.1 Silicon Wafer Production Methods

6.1.1 Float Zone Silicon

Impurities in the silicon lattice can decrease the charge carrier lifetime to an unacceptable low level for the use in sensors. For many years float zone silicon (FZ) has been the standard material for the production of semiconductor particle sensors, as it includes only few impurities and as it is an industrial standard for high-resistivity silicon.
The principle of the production method can be seen in figure 6.1. In an inert gas, a rod of high-purity polysilicon is vertically placed on a small single crystal acting as a seed. By using a high-frequency induction heater, the polysilicon gets locally melted in a narrow horizontal zone, which is slowly moved upwards from the seed crystal on to the top of the rod. Thereby melted zones solidify in a pure single crystal, while foreign atoms drift upwards with the melt, because of their different diffusion constants. An additional advantage of the float zone method is, that there is no contact of the silicon to a crucible which could be the source of impurities.
The oxygen content of standard FZ silicon can be increased through an oxygen diffusion processing step. A $500 - 1000\ nm$ thick SiO_2 layer is grown on both sides of a FZ silicon wafer. Afterwards a high-temperature annealing in an inert gas atmosphere leads to a diffusion of the oxygen into the crystal [C$^+$05]. This kind of silicon is called Diffusion Oxygenated Float Zone (DOFZ) silicon.

6.1.2 Czochralski Silicon

Another important industrial standard for the production of single crystal ingots is the Czochralski (Cz) process, which is cheaper than the float zone method. It is only since nowadays that it can also deliver pure silicon with a high resistivity in the range of $1-3\ k\Omega cm$ [Mes07], so that it became interesting for the production of particle sensors.
From a silicon melt in a crucible, being kept just a few degrees above the melting point, a rotating seed single crystal initiates single crystal growth while it is drawn upwards in an inert gas atmosphere (see figure 6.1). The temperature, the pull velocity and the rotation velocity control the crystal growth. Due to the kind of growing, it is much more probable that in the silicon lattice impurity atoms get built in. This explains why the oxygen content of Cz silicon is naturally higher than the one of FZ silicon and why it can be easily increased when the process takes place in an oxygen atmosphere.

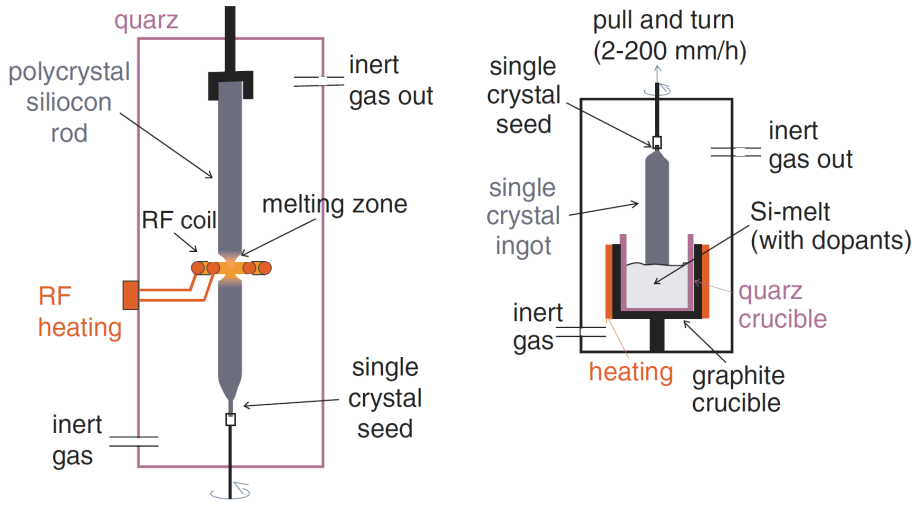

Figure 6.1: ***Silicon ingot production methods.*** *a) Float Zone process. A rod of polysilicon is placed on a small single seed crystal, from where the crystal growth starts as soon as the material around it is melted by a high-frequency induction heater. b) Czochralski process. From a silicon melt in a crucible a rotating seed single crystal initiates single crystal growth while it is drawn upwards in an inert gas atmosphere. The oxygen content in the Czochralski silicon is higher [Har08].*

6.1.3 Magnetic Czochralski Silicon

Beside the danger of getting contaminations in the silicon by the contact to the crucible, another disadvantage of the Cz process is, that thermal gradients in the melt cause partially turbulent flows which are largely responsible for crystal imperfections and microscopically inhomogeneous distributions of impurity atoms and dopants. Therefore also the oxygen concentration differs inside the ingot. A method to rectify the production process is the Magnetic Czochralski (MCz) technique, where the ingot is grown in strong magnetic fields. The melt flows and turbulences get controlled via the resulting Lorentz forces, as they dampen the amplitudes of melt oscillations and influence the flow directions. [S$^+$02]

Standard FZ silicon has an oxygen concentration of around 10^{16} atoms per cm^3 [BM05]. The DOFZ process increases the value up to the order of $10^{17}/cm^3$, while Cz and MCz silicon reach the highest content with $10^{17} - 10^{18}$ atoms per cm^3 [P$^+$05]
The ingots of the three described processes get cut into thin disks, called wafers, by usage of saws of diamond coated wires or blades. After several cleaning and polishing processes the wafers are ready for the processing in the production of sensors or, most common, in the production of microelectronics.

6.2 Beneficial Effect of high Oxygen Concentrations on the Radiation Hardness

The beneficial effect of increased oxygen contents in silicon sensors can be seen in figure 6.2. It shows the effective doping concentrations of different material types as well as the corresponding full depletion voltages against the received proton fluences. There are standard FZ silicon, oxygenated FZ silicon (DOFZ) and carbon enriched silicon. Starting from nearly the same effective doping concentration N_{eff}, the effective doping concentrations decrease to a minimum, which was interpreted as the point of type inversion (see chapter 4.6.1) and increase with different slopes afterwards. As it is important to keep the full depletion voltages of sensors in applications below the breakdown voltages or the limited voltages of the used power supplies, a low slope is of interest. Further, a bigger depleted and therefore a bigger sensitive sensor volume is possible at a given voltage in comparison to standard material, leading to a signal increase.

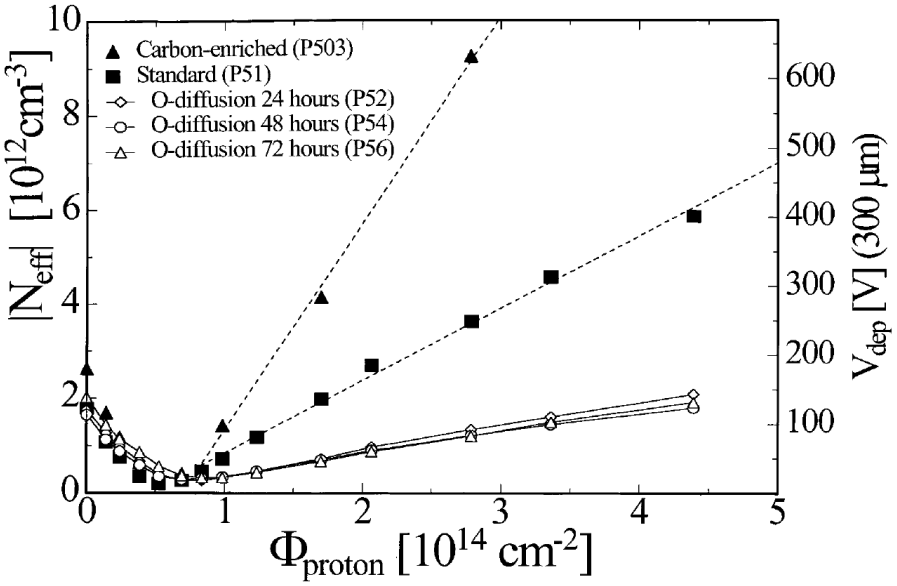

Figure 6.2: ***Full depletion voltages of different material types against the proton fluence.*** *This plot illustrates the differences in the evolution of the full depletion voltages of silicon materials with different oxygen contents. Oxygenated silicon shows positive attributes, as the effective doping concentration and the full depletion voltage increase less with the fluence of charged hadrons than in the case of standard float zone material [L$^+$01a].*

It can clearly be seen in figure 6.2, that the addition of carbon did not have a positive effect, but that oxygen gave a factor three in the gain of the radiation hardness concerning the full depletion voltage [L$^+$01a]. Therefore it can be assumed that the positive effect of oxygen is due to interactions of it with the defects. In these processes, complexes with donor-like levels are created or acceptor-like defects are disarmed as they get turned into inactive complexes of different energy levels or as their production gets suppressed. Several measurements have confirmed this result for irradiations with charged particles, while with neutrons nearly no difference to standard FZ silicon has been observed [L$^+$01b] beside with low resistivity material [Ruz00]. Such a result can be seen in figure 6.3.

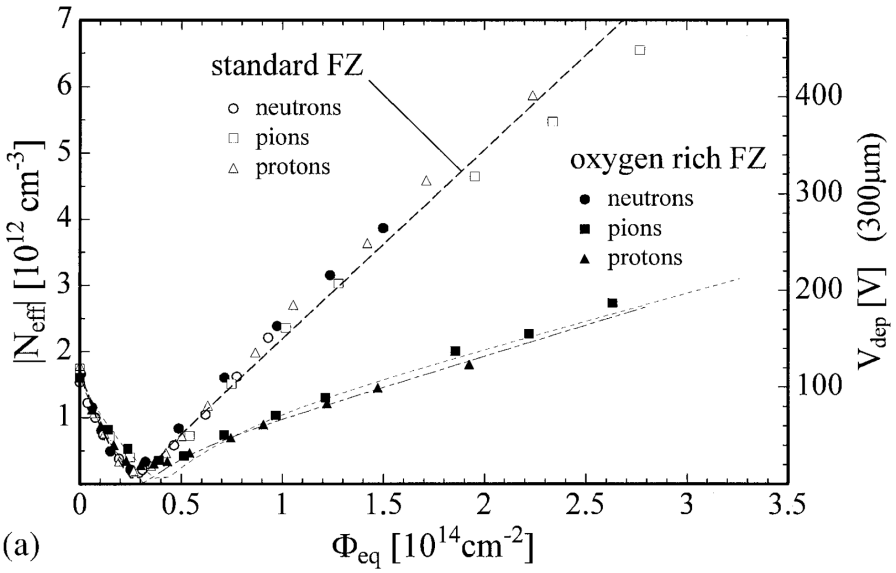

Figure 6.3: ***Difference in the development of the effective doping concentration and the full depletion voltage of standard FZ silicon and oxygen enriched FZ silicon after neutron and proton irradiation [L$^+$01b].*** *The plot shows that the beneficial effect of oxygen on the increase of the effective doping concentration and with this on the full depletion voltage is missing at neutron irradiations.*

6.3 Interaction Mechanisms between Oxygen and Defect Complexes

The divacancy defect complex (V_2), the complexes of a divacany and one oxygen atom (V_2O), the defect of three vacancies (V_3) and the more seldom complex of three vacancies and one oxygen atom (V_3O) show energy levels of deep acceptors. Therefore they are regarded as the main responsibles for the changes in the effective doping concentrations and in the introduction of negative space charge [Lut99], [P$^+$06]. The presence of more oxygen should increase the probability of the formation of the inactive VO-complex at the cost of V_2, V_2O and V_3O, so that less centers of negative space charge are produced.[H$^+$96]

Measurements by Deep Level Transient Spectroscopy (DLTS) and Thermally Stimulated Currents (TSC) have identified two more defect levels which also have a big influence on the detector performance. These are the so-called I_p center as a further deep acceptor and the bistable donor complex (BD) [P$^+$06], which can be found in two configurations differing slightly in energy. In certain conditions, the latter even seems to be able to overcompensate the negative space charge introduced by deep acceptors so that no type inversion appears. Although the assumption that the I_p level originates

from the V_2O or V_3 defects is still controversial, it is certain that its formation mechanism requires a low concentration of oxygen interstitials O_i. Experiments to detect the source of the BD level show a correlation of its irradiation induced production and the concentration of oxygen dimers (O_{2i}). Therefore it can be concluded that (O_{2i}) serves as a precursor for the BD complex [P^+06]. As the I_p centers contribute a negative space charge to the effective space charge and the BD centers contribute a positive one, the impact on N_{eff} strongly depends on their ratio and the balance of their occupation. This might explain, why the question of the appearance of a type inversion is still controversial. However, the described damages, energy levels and mechanisms in correlation with oxygen overall lead to a beneficial behavior concerning the evolution of the full depletion voltage with the irradiation fluence. Neutrons create more defect clusters than other radiation types do, so that the almost missing positive effect of oxygen on the effective doping concentration N_{eff} has to be somehow related to this. A natural explanation would be, that in defect clusters, the ratio between the described acceptor like defects and oxygen is locally much higher than in the case of the formation of point defects, so that less centers can be influenced by the oxygen.

Chapter 7

Testsensors, Testdevices and Analysis Methods

7.1 The MCz-Testsensors and the Testmodules

Like described in chapter 6 the full depletion voltage of Magnetic Czochralski silicon develops with the fluence in a different way like the one of Float Zone silicon with the same physical properties except for the lower oxygen content. The full depletion voltage increases less with high radiation fluences of mainly charged particles, which is of interest for the usage of the material as basis for particle sensors. Beside the full depletion voltage, the charge collection efficiency, the development of noise in interaction with dedicated readout chips and thereby the achieved signal to noise ratio are the most important characteristics that have to be determined for segmented sensors of this type for radiation fluences of different kinds. Furthermore one is interested in the sensor's efficiency to detect MIPs and in its resolution. Especially for the latter and for the annealing behavior of the material, it is of interest to know whether a type inversion takes place or not. All these characteristics might depend on the oxygen content in the substrate.
For the research of MCz sensors, one has to produce dedicated sensors for testing, whose design follows approved layout elements, so that also a comparison with other sensors is possible. In later steps towards applications, new designs can be developed. Modules are built out of the sensors by mounting them on support frames and connecting them to readout electronics. With modules of irradiated sensors and modules of non-irradiated sensors, one can clarify the questions mentioned above in a test with minimum ionizing particles, where the best sources are beams of accelerators.

7.1.1 Layout of the MCz Testsensors

The MCz sensors that have been analyzed during this work, were produced at the Centre for Micro- and Nanotechnology (Micronova) of the Helsinki University of Technology. They were processed out of n-type silicon of $< 100 >$ crystal orientation on wafers with a diameter of 100 *mm* and a thickness of $(300 \pm 2)\mu m$. The silicon has a resistivity of 900 Ωm and a measured oxygen content of $4.92 \cdot 10^{17}$ atoms per cm^3 [H$^+$07].

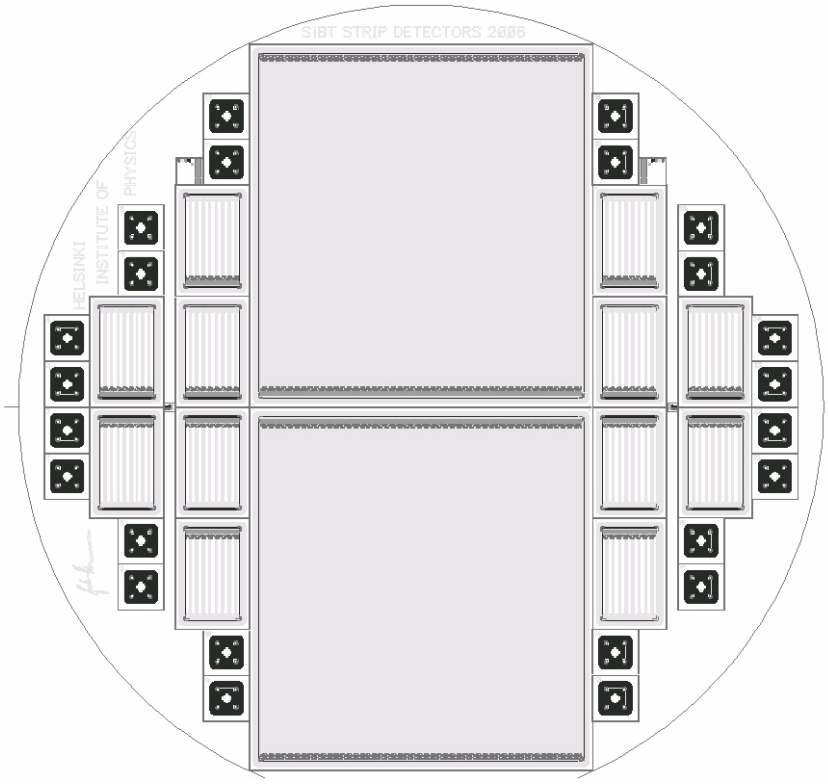

Figure 7.1: ***Waferdesign of the testsensors.*** *The wafers include two strip sensors of a size of* $4x4\ cm^2$ *each, twelve mini sensors of sizes of* $0.9x1.2\ cm^2$ *and* 24 *diodes. [Hae]*

Figure 7.1 shows a sketch of the wafer, which includes two strip sensors of a size of $4x4\ cm^2$ each, twelve mini sensors of sizes of $0.9x1.2\ cm^2$ and 24 diodes. The big test sensors comprise 768 AC-coupled strips with a pitch of 50 μm and a width of 10 μm. They are suited for the usage with CMS readout electronics with six APV chips. On one side of the sensor, p-type strips are embedded in the n-type bulk material. A layer of silicon oxide and silicon nitride (SiO_2/Si_2N_3) serves as a dielectric for the readout coupling capacitances between the p-strips and their belonging aluminium strips, which carry the signals to the readout electronics. On the other side, at the backplane, a higher doped thin n++ layer allows a good ohmic contact to an aluminium layer which covers the whole surface. The high potential of the bias voltage for the diode structures is connected there. The p-sides of the diodes are connected via bias resistors, made of tungsten nitride, and a common aluminium biasring to the ground potential. In the sketch in figure 7.2 the biasring and the resistors can be seen, as well as a second aluminium ring, called guardring. It is also connected to the ground potential and surrounds the biasring. Together with a closing multi-guardring structure with floating potential, it forms the electric field at the edges in such a way that for all strips a field configuration of similar type is ensured in the active sensor area. These structures can also be found in figure 7.2. The contact pads for the electronics on the strips and on the rings are also apparent.
The sensors for the beamtest in 2007 were passivated with a layer of Si_3N_4 to protect the sensor surface. Because of problems resulting from this layer, which will be described in chapter 8 the sensors in the beamtest in 2008 were not passivated.

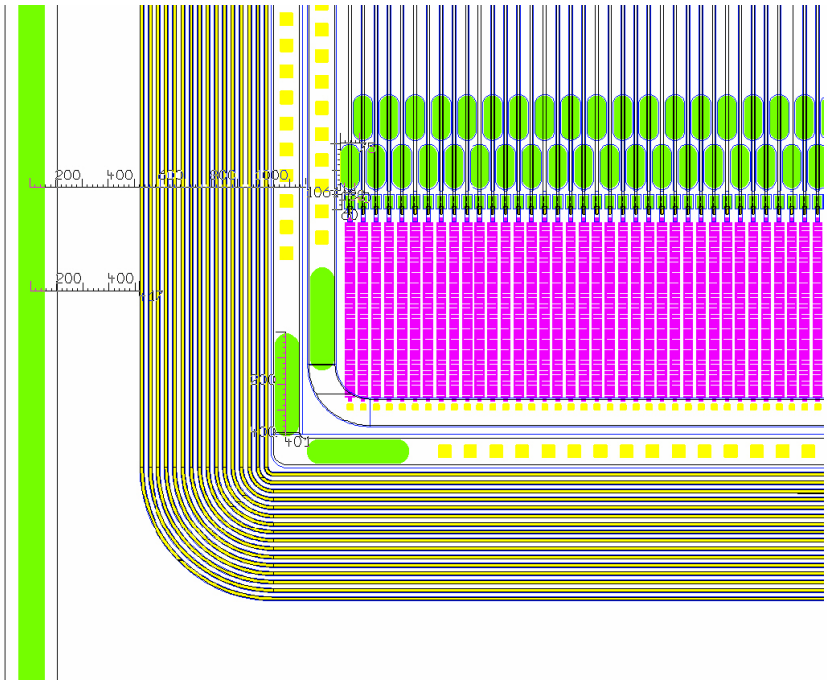

Figure 7.2: ***Detail of the testsensor sketch.*** *The sketch detail at a corner of the sensor shows the multi-guardring structure, the guardring, the biasring followed by the bias-resistors that connect the strips. The contact pads for the electronics on the strips and on the rings are also apparent. [Hae]*

7.1.2 Design of the Testmodules

The design of the modules for the tested sensors follows the demand to easily fit into the SiBT beamtelescope system (see chapter 7.2), which sets the special conditions of geometry, cooling, powering and the readout electronics. The support plate is the same PCB[1] based like the one for the reference sensors of the SiBT. The octagon structure offers the flexibility to install the sensors in $\pm 45^{\circ}$ orientations relative to the SiBT ground plate and allows an easy installation on the SiBT's support brass plates, coping with the geometrical limits thereby.
Figure 7.3 shows a complete module. The sensors are glued on the plate with conductive glue, which enables the electrical contact between the sensor backplane and a small contact pad in the middle of the octagon. The conductor line of this pad leads to the high voltage of the power supply and includes an RC-filter to suppress noise on the high voltage line. The powering cables are plugged at special contact pins. Further pins exist, to separately or additionally contact the guardring to ground. The readout electronics of the modules are CMS 6-APV-25 hybrids, with which the modules fit into the readout chain of the SiBT system. The electronics are fixed on ceramic plates that get glued on the octagon together with the pitch adaptor at which the readout chips and the sensor strips get bonded and which connects the both thereby. Special adaptor plugs on PCBs were produced to connect the module's electronics to the electronics on the SiBT plate in the two orthogonal sensor positions.
All irradiated sensors and the float zone reference sensor were mounted on octagon PCBs of the described type. Only for the MCz reference sensor a prototype plate of the same design but with copper surfaces was used. The modules were assembled at the facilities of the IEKP.

[1] Printed Circuit Board

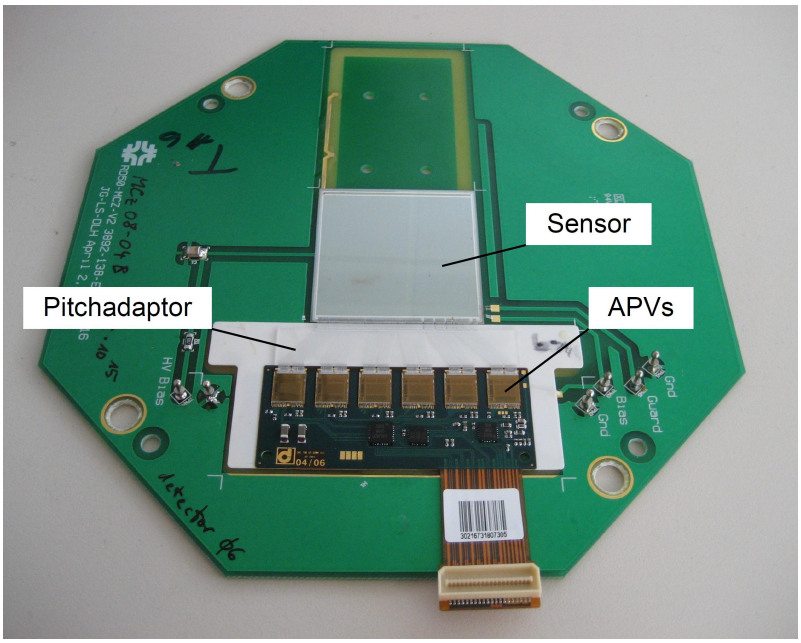

Figure 7.3: ***Picture of a testmodule.*** *The octagon structure design of the support plate was chosen to cope best with the geometrical conditions of the beamtelescope to achieve flexibility in the installation.*

7.2 The Beamtelescope SiBT

Future collider experiments, like the ones at the SLHC, require further improvements of particle sensors to satisfy the new arising special requirements on the functionality and especially to withstand the particular conditions during their application under a harsh radiation. Therefore new materials, designs, readout chips or operation setups have to be tested with the particles to detect. Like introduced in chapter 5 a sensor has to be sensitive to a minimum ionizing particle (MIP). The vast majority of radioactive sources does not provide radiations of this characteristic. Only some nuclides, like ^{90}Sr, offer decay products that are comparable, but in a broader energy range, so that low energetic particles have to be filtered out. Secondary particles of the cosmic radiation are mainly MIPs, but their rate for testing in a laboratory is quite low. Therefore one has to use the particle beams of accelerators (like the SPS [2] at the CERN) to get high energetic MIPs of high rates and beam profiles that satisfy the demands. For the measurements of mainly the charge collection efficiency (CCE), the cluster resolution, the signal-to-noise, the efficiency or the resolution, the use of a beam telescope is essential to get the track information of the particles which should produce the signal in the device under test (DUT). The Institut für Experimentelle Kernphysik of the Universität Karlsruhe was involved in the production of parts for the ”SiBT” (picture 7.4), a new beam telescope for the mentioned purposes, developed, planned and constructed under the management of the Helsinki Institute of Physics (HIP).[M$^+$08]

[2] Super Proton Synchrotron

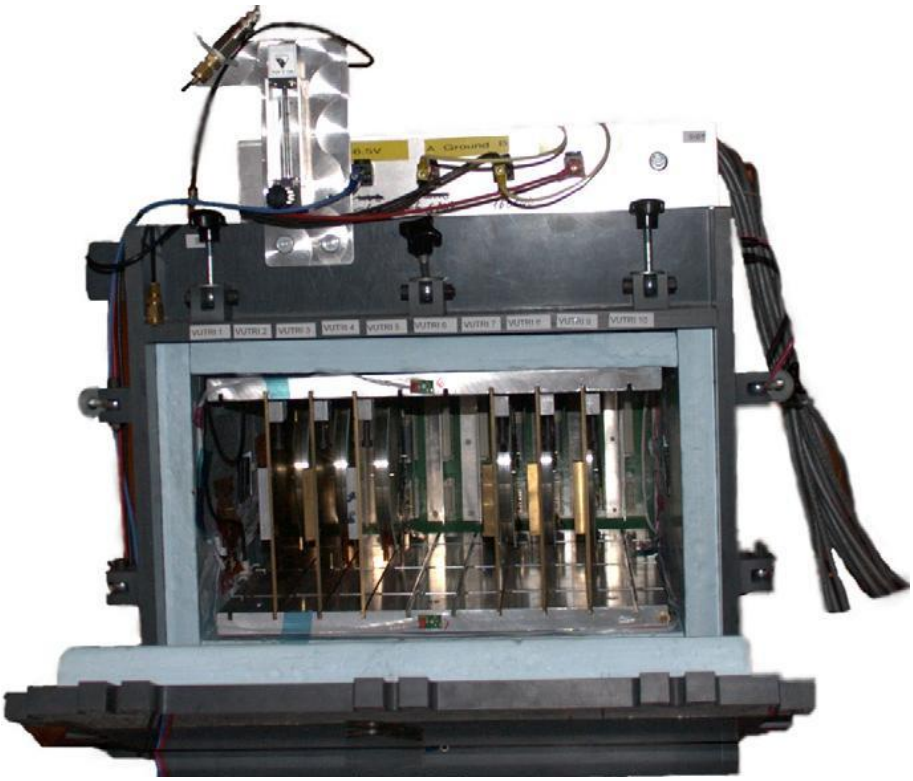

Figure 7.4: ***The Beamtelescope SiBT.*** *Eight telescope reference sensors and up to two DUTs are placed inside a protective box with Peltier cooling and APV readout electronics.*

7.2.1 Layout

The setup follows the demands of the dedicated main application of testing sensors in development for the SLHC-experiments. There the aimed resolution of the momentum measurements is in the same order like the one at the LHC-experiments, where the resolution of the tracking sensors is around $10-20\ \mu m$. Therefore the impact point resolution of the beam telescope with which the test sensors get studied, must be considerably better than that. Further in the telescope, a minimum of four space points is required to get a good efficiency of finding and reconstructing tracks of the charged particles of the beam. A strip sensor gives only a one-dimensional information of the passage position. If a second sensor is arranged perpendicular near to this one, a space point information of the track is achieved. With two sets of four sensors placed in the described way, the requirement of four space points can be fulfilled.
The sensors have to be operated in a well-defined protective environment without light and humidity. Furthermore it is important that the probed sensors, the devices under test, can be cooled if they had been irradiated before, as thereby the effects of the radiation damages can be reduced in a controlled way. As a solution of these demands, the usage of a cold chamber, known as the "'Vienna-Box"' in the CMS community, was chosen, which was originally in use for temperature cycling tests of modules for the CMS tracker. The box can house up to ten support brass plates on which the foreseen eight reference sensors and up to two DUT sensors get mounted with connections to CERN-made VUTRI-adaptors (see figure 7.5) [edm].

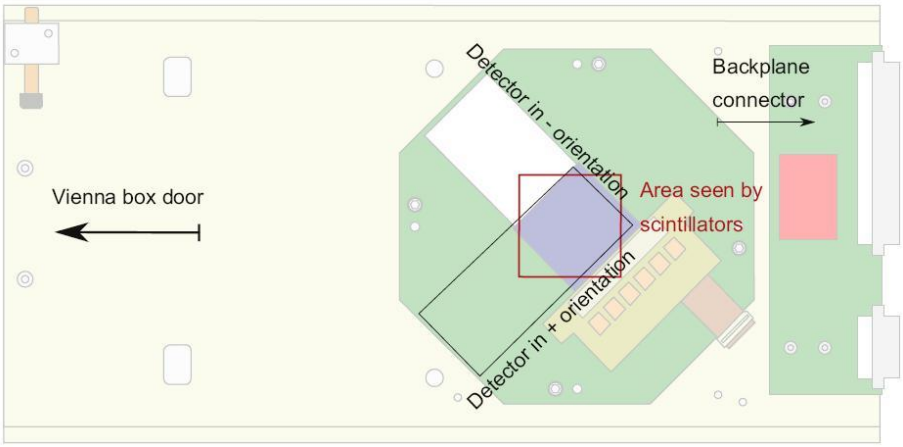

Figure 7.5: ***Sketch of a SiBT sensor carrier plate.*** *The SiBT reference sensor modules and the DUT modules get mounted on carrier brass plates equipped with readout electronics. They allow an easy insertion in dedicated slots with contact to Peltier cooling elements.*

A quick insertion of the modules in the belonging slots equipped with backplane connectors connecting to the readout electronics via VUTRI-cards outside is possible. The space between the slots is four centimeters.

7.2.2 Cooling and Temperature Control

The carrier brass plates enable a thermal contact to two temperature setting 350 W Peltier elements at the floor and the ceiling of the box. The elements are water-cooled by a chiller and can provide temperatures between -30°C and +70°C , while in the majority of the applications of the telescope, the chosen range is between -20°C and 0°C . The air temperature inside and outside of the box and the temperatures of the surface plates of the peltier elements are monitored and logged. The temperature information of the hybrids and the sensors is available by the Detector Control Unit (DCU) chips [M$^+$03] which are mounted on the hybrids and which can be read out and logged by the DAQ system [3]. Condensation in the box is prevented by a nitrogen flow.

7.2.3 Reference Sensor Modules

The sensors for the reference planes of the telescope are single sided AC-coupled strip sensors of high resistive float zone silicon with a thickness of $320 \pm 20\ \mu m$, fabricated by Hamamatsu Photonics (HPK). On an active area of approximately $98x38\ mm^2$, a sensor contains 639 active strips of a readout pitch of 60 μm. With electrically floating intermediate strips, the effective readout pitch becomes $30\mu m$ and the sensor reaches a binary resolution of $8.66\mu m$. The full depletion voltages are around 100 V, so that with a chosen bias voltage of 150 V the sensors are operated in an overdepleted mode. The sensors are bonded to pitchadaptors that connect each to five of the six readout chips of CMS APV hybrid boards. All elements are glued on a carrier structure, whose octagon form allows the insertion in $+45°$ and $-45°$ positions relative to the floor to get reference planes perpendicular to each other and to cope with the geometrical conditions of the housing box. The modules get mounted on the mentioned brass plates where the connection of the hybrids to the readout electronics of the Data

[3] Data Acquisition System

Acquisition System (DAQ) is done via the VUTRI adaptors and VUTRI-cards in the described way. Several parts of the the SiBT DAQ are based on prototypes of the CMS DAQ hardware. A connection scheme of the different subsystems can be seen in figure 7.6

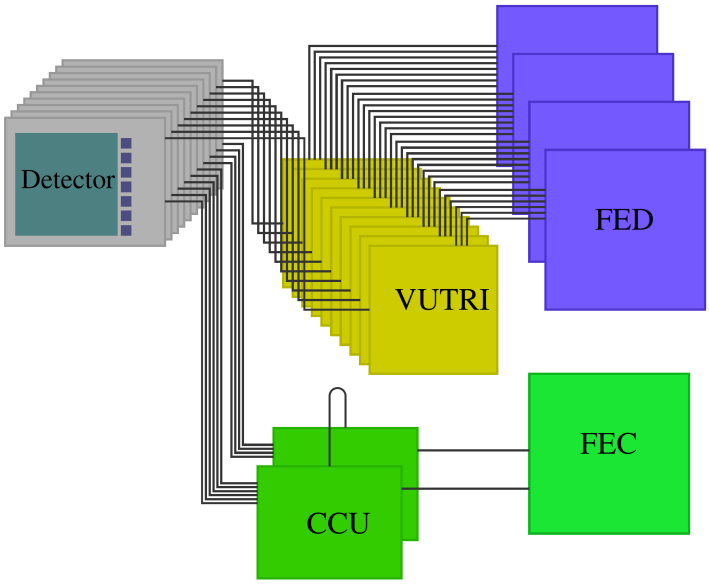

Figure 7.6: ***Communication scheme of the SiBT.*** *In order to communicate with the hybrids, a FEC and two CCUs are needed. Data flow via the VUTRI-cards to the FEDs.*

7.2.4 Communication Scheme

A Trigger Sequencer Card (TSC) [IPN] generates a local clock, to which the DAQ and the CMS APVs are synchronized. It is distributed to the front end chips via a Front End Controller (FEC), which is also needed to set the tunable parameters of the front end chips and to optionally read out operating parameters, like currents or temperatures, from the Detector Control Unit (DCU) being placed on the hybrids. In addition to the one FEC also two Communication and Control Units (CCU) [P$^+$02] are needed in order to communicate with the ten hybrids of the reference modules and the Devices under Test (DUT). With each trigger signal, the measurement data of all strip channels of all modules are transmitted through differential current signals from the front end chips to multiplexer ASICs[4] APVMUX[5] from where they are sent in multiplexed differential voltage signals to the VUTRI cards. The signals are amplified there and transmitted to the Front End Driver (FED) cards where a digitization of the data takes place. The FEDs also need the trigger information for this step.
Each FED can read out the data of up to eight APV pairs. Therefore three FEDs are needed to treat the data of the 8x3 APV pairs of the reference modules (five active and one unused APV) and a fourth FED is needed to read out the data of the up to 2x3 APV pairs of the test modules. To accomplish the need of reading out up to ten modules simultaneously with the old CMS hardware, the separate installation of the four FEDs on four computers with belonging PCI[6] Mezzanine Cards (PMC) was necessary. The digitized data are temporarily saved on these PCs until they are finally archived.

[4] Application Specific Integrated Circuit
[5] Analog Pipeline Voltage Multiplexer
[6] Peripheral Component Interconnect

7.2.5 Triggering

The coincident signal of two scintillators at the ends of the box on the height of the reference and the DUT sensors, builds the trigger signal of traversing particles. When the beam is asynchronous to the clock signal of the TSC, the problem of defining a time window in which particle signals are regarded as being coincident with the clock arises. If one renounces this necessity, the signal height is not always near its peak value when the APV hybrids sample it into the internal buffer ring. Operating the hybrids in the more time generous "peak mode", the signal loss in case of usage at the CERN SPS was estimated to be about 10 %, due to the asynchronous nature of the beam [M$^+$08]. The establishment of a narrow time window for coincidences decreases this value on cost of higher trigger rates, so that compromises have to be made.
The beamtelescope SiBT is used with an early version of the CMS XDAQ-based readout software, the rc1205, as newer versions make hardware related assumptions which are not compatible with the prototype boards. It is written in C and C^{++} on top of the XDAQ framework.

7.3 Analysis Methods

For the analysis of the measurement data of the experiments, several methods for the determination of the different detector parameters have to be exercised.
The analysis software, used to analyze the majority of the beamtest data presented in this thesis, was an adjusted version of SiBTStar, written by Bernhard Ledermann, based on his analysis software for GEM-TPCs[7] described in [Led06]. The analysis parameters and methods will be presented in the following.

Pedestals:

The pedestal of a given channel is the mean digitized read out charge of a channel i, given by counts of an analog to digital converter (ADC), averaged over the number of events N, by absence of a known physical signal. In the results in the following chapters, ADC is also used as the unit of the analog to digital counts.

$$Ped_i = \frac{\sum_{k=1}^{N} ADC_{value[k]}}{N} \tag{7.1}$$

The pedestal is mainly dependent of the electronics. Therefore the example in figure 7.7 features six substructures which reflect the six readout chips.

Noise:

The width of the distribution of all ADC-values of one channel, at the absence of a known physical signal, defines the noise of this channel (raw noise). This is mathematically expressed in root mean square, which is a measure of the magnitude of the fluctuations around the mean value given by the pedestal.

$$\sigma_i = \sqrt{\frac{\sum_{k=1}^{N} (ADC_{value[k]} - Ped_i)^2}{N}} \tag{7.2}$$

An example of channel noise plotted against the channel number can be found in figure 7.8.

[7] Gas Electron Multiplier - Time Projection Chamber

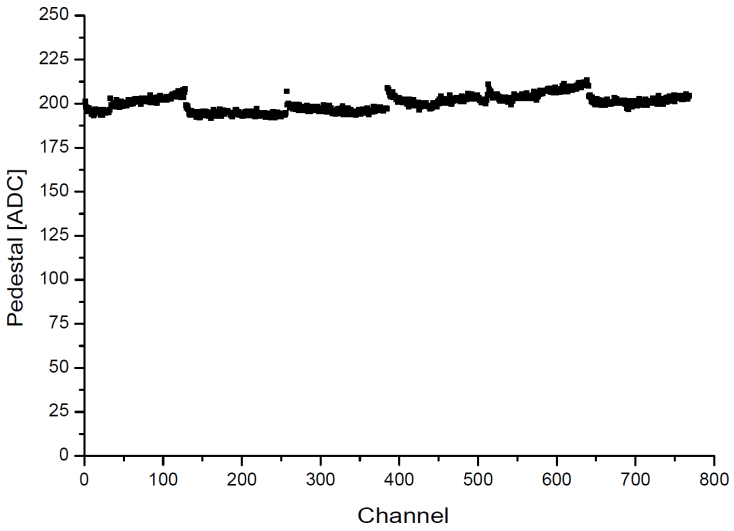

Figure 7.7: ***Example of a pedestal measurement result.*** *The pedestal values are plotted against the channel number. The six substructures reflect the six readout chips.*

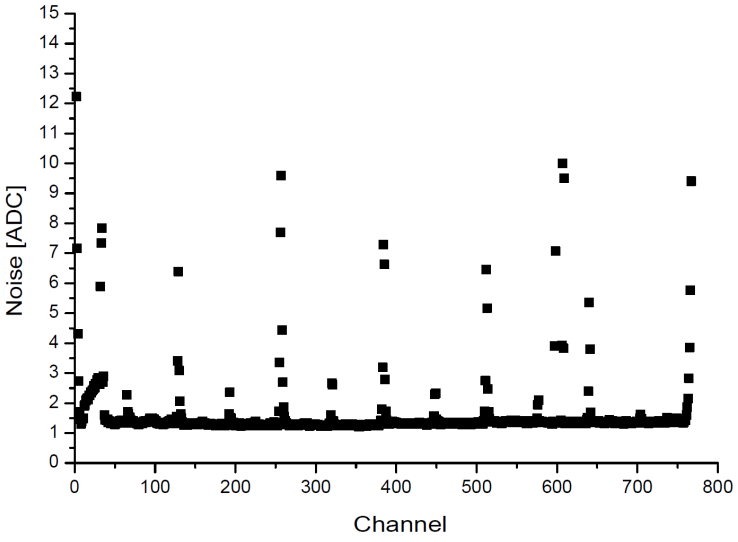

Figure 7.8: ***Example of a channel noise measurement result.*** *The channel noise is plotted against the channel number. The standard deviation of the distribution of many ADC-values of one channel, at the absence of a known physical signal, defines the noise of this channel.*

Common Mode:

The Common Mode (CM) reflects a common variation of a given signal which affects groups of channels in a coherent way. This can happen, for example, by electromagnetic pickup or noise on the powering system. As the CM usually differs from event to event, it is determined for every single event and channels belonging together to a group. It is done by first subtracting the pedestals and

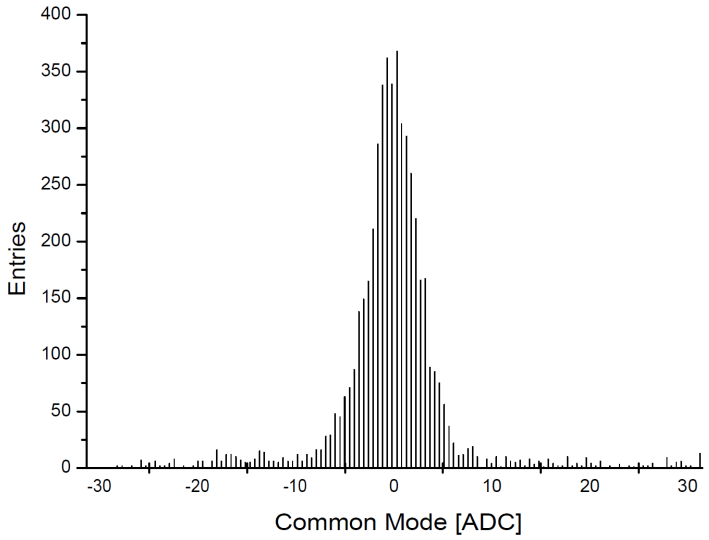

Figure 7.9: ***Example of a Common Mode distribution.*** *The Common Mode reflects a common variation of a given signal which affects groups of channels in a coherent way*

afterwards calculating the mean of the channel signals belonging to that event and group.

$$CM_{event} = \frac{\sum_{k=1}^{N_{channels}} (ADC_{value_{event}}[k] - Ped[k])}{N_{channels}} \tag{7.3}$$

Figure 7.9 shows an example of a CM distribution.

Common Mode Subtracted Noise:

The Common Mode Subtracted Noise is the standard deviation of the distribution of the charge, subtracted of the pedestal and the CM. It is thus defined as

$$ADC_{subtr[i]} = ADC_{value[i]} - ped[i] - CMN \tag{7.4}$$

Cluster, Cluster-Charge and Cluster-Noise:

A cluster is one channel or an accumulation of adjoining channels, where the read out pedestal and CM subtracted charge exceeds certain limits, so that it has to be assumed that it is a signal generated by a traversing particle. As it can still be the case that noise is the source of the cluster, one distinguishes between clusters and track clusters, where the charge conglomerate has been assigned to a particle track by the help of other detectors.
The read out channel with the highest ADC value in the accumulation is called seed channel. A cluster finding starts with identifying the seed, for which a lower limit has to be set, normally in multiples of the noise. This means that for the considered event the charge of all active channels is compared with the limit. If the search is successful, it is checked whether the adjacent channels exceed a second limit, lower than the one for the seed and if so, they and the seed together build the cluster. The cluster charge is the sum of the channels' charge.
The position of a cluster is defined as the center of gravity of its charge distribution. If the cluster

consists of k channels, the cluster noise is defined in the following way

$$\sigma_{Cl.} = \sqrt{\Sigma_{i=1}^{k}(\sigma_i)^2} \tag{7.5}$$

where σ_i is the noise of the channel i according to the definition above.
The collected charge is influenced by statistical fluctuations in the charge building process, so that the question arises which signal has to be expected by an ionizing particle of a given energy. The answer is given by the most probable value of the distribution of many signals, which follows a Gauss convoluted Landau-curve like described in chapter 3.7. An example can be seen in figure 7.10.
The signal to noise ratio of a cluster is the collected cluster charge divided by the cluster noise. For the definition of the signal to noise ratio to be expected by a sensor, the most probable value of a Landau-Gauss fit at the distribution of a large number of cluster signal to noise ratios is used.

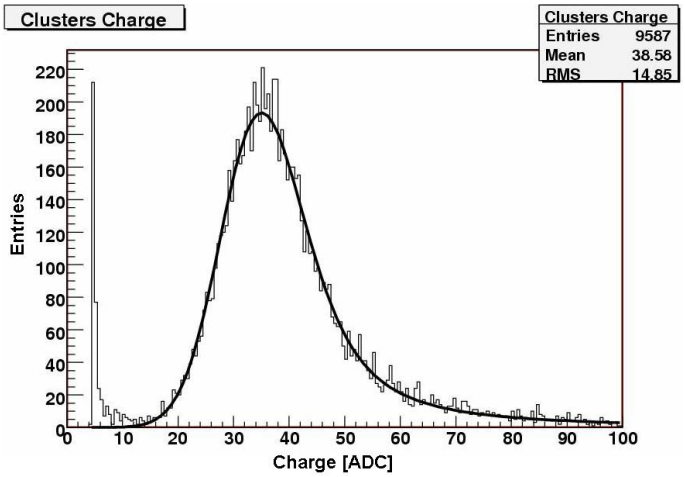

Figure 7.10: ***Example of a cluster charge distribution of a CMS module with a Landau-Gauss fit.*** *The most probable value of the fit defines the signal to be expected.*

Track Reconstruction:

For a reliable track reconstruction in an analyzed event, an adequate number of beamtelescope sensors has to show clusters. The lower limit of the total number of hit sensors needed to start a track finding is adjustable in the SiBTStar software. If enough cluster in different sensors are found, the track reconstruction can be accomplished by SiBTStar. Its method to find possible track clusters is to define, as a first approach, a track as the line between the clusters of the two outermost sensors in the telescope. Clusters of the modules in between are added to the track, if their position differs less than four times the cluster size from the fit line. Afterwards a linear fit including all the found clusters is done again, which improves the calculated track towards the actual particle track. If many clusters of one detector module fulfill the criterium to be in a distance less than four times the cluster size or if one cluster could belong to several tracks, the resulting track with the smallest χ^2 is chosen.

Resolution:

The distance between the cluster position and the actual traversing point of the particle is called the residual of the cluster. Under optimal conditions, the distribution of the residuals of a sensor is a

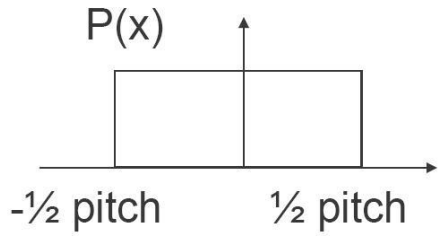

Figure 7.11: ***Sketch for the motivation of the definition of the binary resolution.*** *The probability for any position between two strips to be hit by an incoming particle is constant and the same for all hit points.*

gaussian one with a most probable value (MPV) of zero. Its standard deviation defines the resolution of the belonging sensor.
The real tracks are not exactly known and the considered cluster influences the determination of the track, so that an exclusive and an inclusive calculation of the track is done. In the inclusive method, the cluster position is considered in the track finding, while in the exclusive method this is not the case. Both normally lead to slightly different residuals. Therefore the resulting residual is defined as $\sqrt{\sigma_{incl}\sigma_{excl}}$ [Led06].
A most probable value different from zero hints to a shift of the whole sensor in comparison to its expected position. Then the cluster positions of this sensor get corrected by exactly this shift and the calculation of all residuals and the tracking are rerun. The whole procedure should be repeated as long as the MPVs of the residual of all sensors receive corrections towards the value zero. For the data analyzed in this thesis, the adjustment was done in ten steps.
The binary resolution sets the limit for the obtainable one. The probability for any position between two strips to be hit by an incoming particle is constant and the same for all hit points like illustrated in figure 7.11. Using the naming given there, the resolution is defined as

$$\sigma_x^2 = \int_{-\frac{1}{2}pitch}^{\frac{1}{2}pitch} (x - \langle x \rangle)^2 P(x) dx \tag{7.6}$$

As $\langle x \rangle = 0$, it follows that

$$\sigma_x^2 = \int_{-\frac{1}{2}pitch}^{\frac{1}{2}pitch} x^2 P(x) dx \tag{7.7}$$

so that the binary resolution becomes

$$\sigma_x = \frac{pitch}{\sqrt{12}} \tag{7.8}$$

Charge Collection Efficiency and Detection Efficiency:

The charge collection efficiency (CCE) is the ratio between the detected charge and the total charge of the electron-hole pairs generated by a traversing particle. Thus it corresponds to the fraction of the gained signal in comparison to the maximally possible one by the ionizing charge loss of a particle.
The detection efficiency of a sensor is the ratio between clusters allocated to tracks and the whole number of tracks.

Chapter 8

Investigations of Sensor Parameters before and after Irradiation

The test program to explore radiation dependent characteristics of segmented sensor devices based on MCz silicon starts with the testing of their functionality and quality. After irradiations with different fluences of different radiation types, the sensors are tested again to find out the influence of the radiation damages on the important parameters which describe the sensor functionality.
The irradiations were done mainly with 25 MeV protons of the Kompakt-Zyklotron (KAZ) in Karlsruhe and with neutrons of an average energy of 20.4 MeV of the Louvain-la-Neuve irradiation facility.

8.1 The Sensor-Teststation

For the quality testing and the research on semiconductor radiation sensors, the Institut für Experimentelle Kernphysik of the Universität Karlsruhe (TH) possesses two dedicated probe-stations. One of them can be seen in picture 8.1. The second station has been redesigned for an upgrade to be finished in spring/summer 2009 to be prepared for new challenging tasks in the R&D for sensors of future collider complexes or in the semiconductor sensor business in general.
The basic principle of the stations is, that operational elements of the sensors can get connected with different measurement devices and power supplies via relay stations to apply voltages and to fulfill measurements. The contact is done with small probe needles by the use of micro-manipulators. A LabView software on a PC controls the devices and relays according to flexible user-defined test-programs. Further it controls microstep-motors for x-, y- and z-direction, which allow to move an isolated metal-table, called jig, on which the sensor is fixed by the suction of vacuum channels. The several contact pads for the functional elements of the sensor can get automatically contacted with the probe needles. The jig can get cooled via Peltier-elements down to -30 °C or even heated up if necessary [Hof08]. It is housed in the Faraday box that can be seen opened in the picture 8.1. Also a microscope with a camera is placed inside the box. Initially it is needed for the first setting of the needles on the pads and further it is essential for the alignment of the sensor and the micro-steppers for which also the monitor on top is needed. On the left of the box, three important devices can be seen. The upper one is a Keithley K6517A electrometer with a power supply unit for voltages of up to 1000 V. The sensors get biased with this device and any of the appearing currents are measured with it. A second power supply Keithley K617 delivers voltages to be applied at dedicated operational elements. The third device is a Hewlett Packard LCR meter 4284A with which all involved capacitances can get measured in a test frequence range between 20 Hz and 1 MHz. Details of the measurement

methods for the several sensor parameters can be found in [Fre04].

Figure 8.1: ***One of the two sensor teststations of the IEKP Karlsruhe.*** *The station is used for the quality testing and the research on semiconductor radiation sensors. Operational elements of the sensors can get connected with different measurement devices and power supplies via relay stations to apply voltages and to fulfill measurements. A LabView software on a PC controls the devices and relays according to flexible user-defined test-programs.*

8.2 Testing Conditions

The performance and the quality of the sensors for the test-programs in 2007 and 2008 were checked before the irradiations. After each irradiation step the influence of the radiation damages on the sensor characteristics were investigated. Like described in chapter 3, the developments of the total leakage current with the voltage (IV) and the sensor capacitance with the voltage (CV) are two important parameters that indicate the overall behavior of a sensor. Before the irradiations, these were measured at room temperature (20°C) while afterwards the sensors were cooled down to -10°C which was the dedicated temperature for the testbeams and which is the operating temperature for the CMS tracker at the LHC. In both cases the relative humidities were less than 30%. The temperature during all measurements of the strip parameters was also -10°C . The tests of the strip parameters of the non-irradiated sensors were done over-depleted at 400 V. After irradiation the 2007 sensors were tested at 700 V and the 2008 sensors at 900 V, as they were irradiated with higher fluences. Standard annealing processes were not carried out, but some annealing at room temperature happened for a few days during transports and installation work.

8.3 Results of the 2007 Test Sensors

8.3.1 Total Leakage Currents and Full Depletion Voltages

Figure 8.2 shows that before the irradiation, the total leakage currents of the 2007 sensors were on relatively high levels and differed from sensor to sensor up to two orders of magnitude. Further, the shape of the IV-curves was not like expected for reverse biased sensors. In some cases the slopes did not saturate, but followed straight lines. In case of the sensor n224A, a current break through appeared immediately after reaching the calculated full depletion voltage. These anomalies of the total leakage current characteristics made deeper investigations necessary.

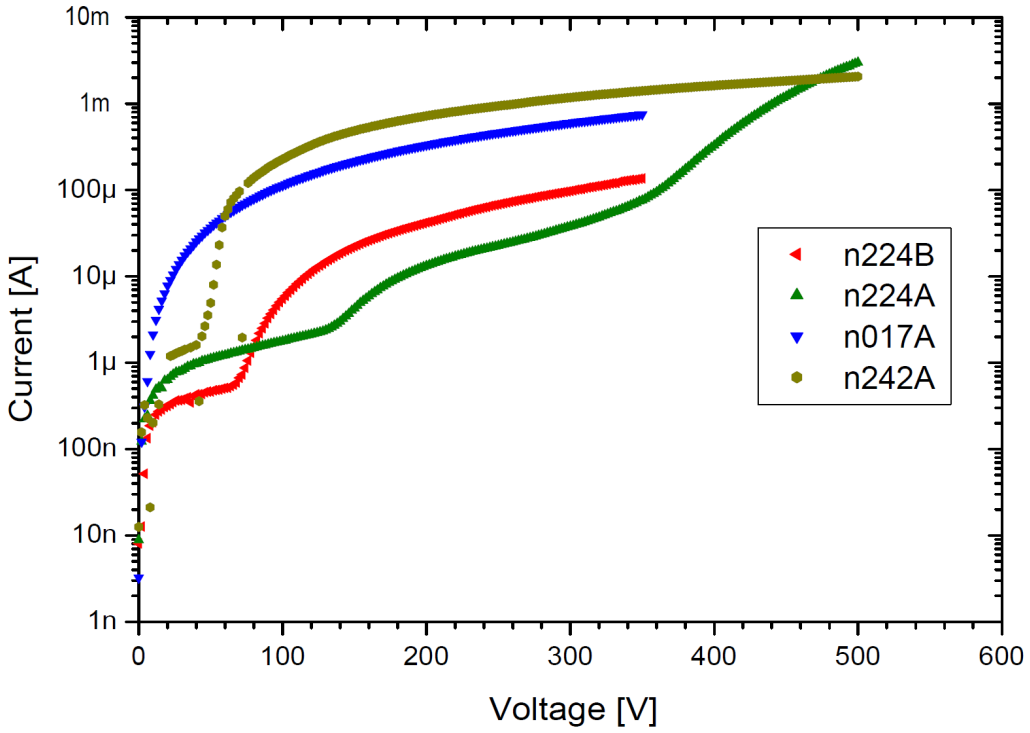

Figure 8.2: ***IV curves of the sensors tested in the 2007 beamtest before irradiation.*** *The leakage currents were on a relatively high level. Investigations lead to the conclusion that this was due to surface currents.*

The total measured current is a sum of the bulk leakage current and surface currents, as long as no guardring is connected to the biasring potential in a second line conducting a part of the current, which was not the case here. A test was done to clarify the source of the current. According to equation (3.52), the bulk current is strongly temperature dependent, in contrast to the surface current. Therefore a deviation of the total current from the behavior given by this formula points to a presence of surface currents. The current of a non-irradiated sensor (n312B) of the same production batch was mapped in dependence of the sensor's temperature between -7.5°C and 30°C in steps of circa 1°C [Lia07]. The expected current over temperature curve, based on the data point at the measured leakage current of 2.09 μA at the reference temperature of 20°C was calculated and compared with the measured one. For the latter the following fit function with a temperature-independent offset was

used, according to the recommendations of the RD50 collaboration [RD5]

$$I(T) = P_1 \cdot T^2 \cdot exp\left(\frac{P_2}{T}\right) + P_3 \tag{8.1}$$

$$P_1 = \frac{I(T_{Ref})}{T_{Ref}^2} \cdot exp\left(\frac{E_g}{2k_B T_{Ref}}\right)$$

$$P_2 = -\frac{E_g}{2k_B}$$

$$P_3 = const. \tag{8.2}$$

$I(T_{Ref})$ is the measured total leakage current at the reference temperature T_{Ref}. The value of the Boltzmann constant k_B is $8.614 \cdot 10^{-5}\ eV/K$ and the bandgap E_g in silicon accounts for $1.12\ eV$. The result of this investigation is shown in figure 8.3. Going to lower temperatures, the current does not decrease like expected, as it does not follow the curve of the theory (circular dots) for the case in which the main fraction consists of a bulk current. It clearly hints to an offset current P_3 so that a considerable surface current exists. For higher temperatures its fraction is reduced and the bulk current prevails due to the exponential temperature dependence. This observation and the behavior of the coupling capacitances that will be presented in chapter 8.3.4 both indicated problems with the dielectric or passivation layer.

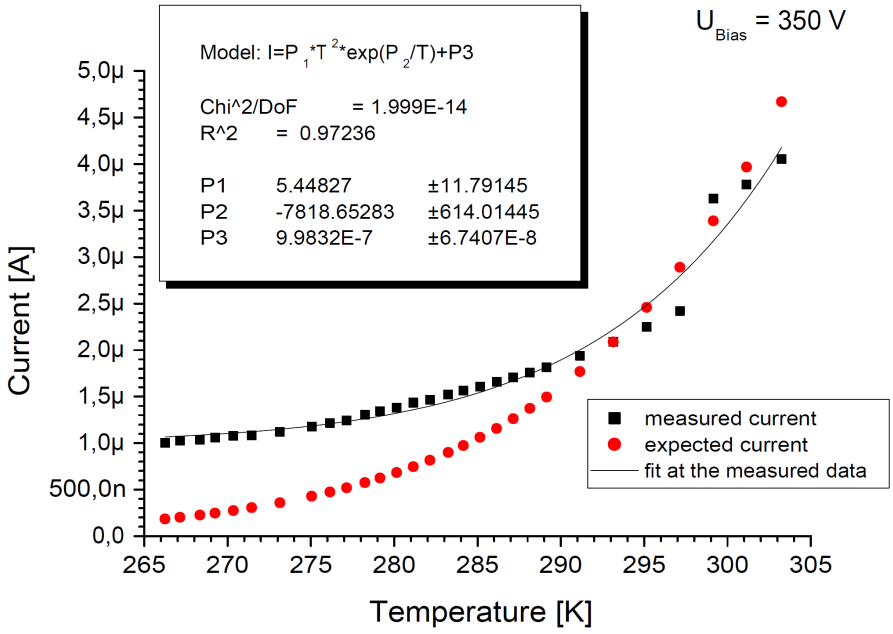

Figure 8.3: ***Comparison between the expected and the measured I(T) curves.*** *The plot reveals the surface current problem, in the way that the measured I(T) (black curve, squared dots) behavior differs from the calculated one (red curve, circular dots), so that the high currents can not be the result of bulk generation currents but have their origin in surface currents.*

For the full depletion voltage, a value of around 350 V is expected, because of the nominal resistivity of 1 $k\Omega cm$ and the thickness of 300 μm. Using the example of sensor n224A, figure 8.4 shows that this could be confirmed. In some cases, the high currents lead to problems in the determination of the full depletion voltages by CV measurements and plotting $1/C^2$ over the voltage.

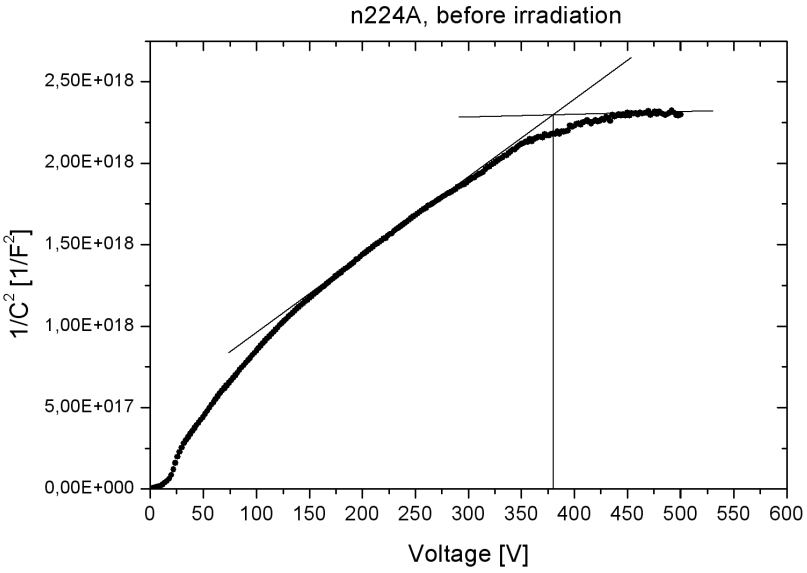

Figure 8.4: ***Full depletion voltage of the sensor n224A before irradiation*** *The $1/C^2$ over V plot helps to identify the full depletion voltage. The result is representative for the ones of the other tested MCz sensors.*

Under the influence of radiation damages, the leakage currents increase and the full depletion voltages change, like explained in chapter 3. The higher leakage currents make it necessary to cool the sensors. Therefore the aspired temperature for the measurements in the probestation after irradiation was -10°C . Because of problems with the chiller, mainly only temperatures down to -8 °C were reachable. This was not problematic, as the measurements were foreseen as a quality check after the irradiations and were not meant for quantitative analysis, so that the slight difference was tolerable. Figure 8.5 shows the IV-curves of the three irradiated sensors. As one can see, the leakage current of sensor n017A, which was irradiated with a proton fluence of $1 \cdot 10^{14} neq./cm^2$, increases strongly at voltages higher than around 200 V. The other two sensors, n224A irradiated with a proton fluence of $5 \cdot 10^{14} neq./cm^2$ and n242A, irradiated with a neutron fluence of $5 \cdot 10^{14} neq./cm^2$, do not show such an increase and remain on lower current levels, although they were irradiated with higher fluences. Normally a current breakthrough does not arise before full depletion, so one can assume that the full depletion voltage of n017A is lower than 200 V. The $1/C^2$ over voltage plot (figure 8.6) of that sensor gives no conclusive information, which might be due to problems with the measurement method at high currents, but it will be shown later that the saturation of the signal height in the beamtest hints to a full depletion voltage of 200 V. Therefore the current increase can be understood.

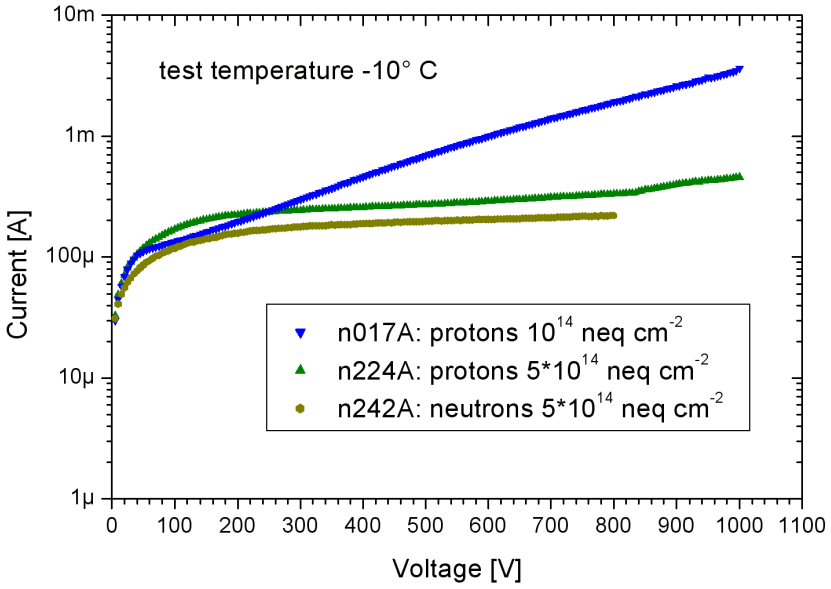

Figure 8.5: ***IV curves of the sensors tested in the 2007 beamtest after irradiation.*** *The strong current increase after* 200 V *of the sensor n017A happens after the full depletion voltage.*

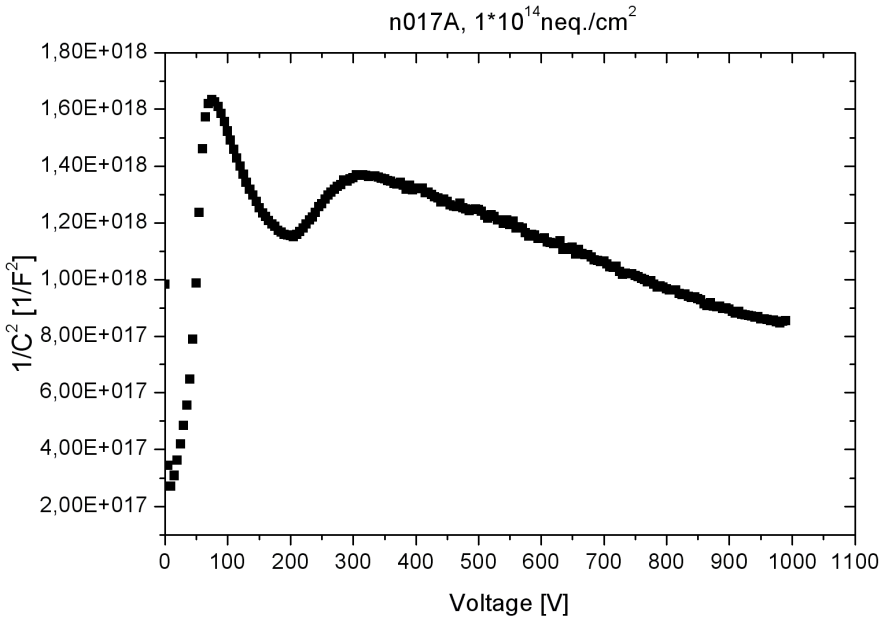

Figure 8.6: $1/C^2$ ***against voltage plot of the sensor n017A after irradiation with*** $1 \cdot 10^{14}$ $neq./cm^2$ *The curve does not follow the expected shape and gives therefore no conclusive information on the full depletion voltage, which might be due to problems with the measurement method at high currents.*

According to figure (8.7) the full depletion voltage of n224A is around 300 V and the one for n242A can be evaluated to be around 700 V. Despite having achieved the same neutron equivalent fluence, the neutron irradiated sensor depletes at a higher voltage which is in agreement with observations described in chapter 6. Therefore the current concept of the hardness factor is not valid for the full depletion voltage in the case of MCz silicon and has to be adjusted accordingly.

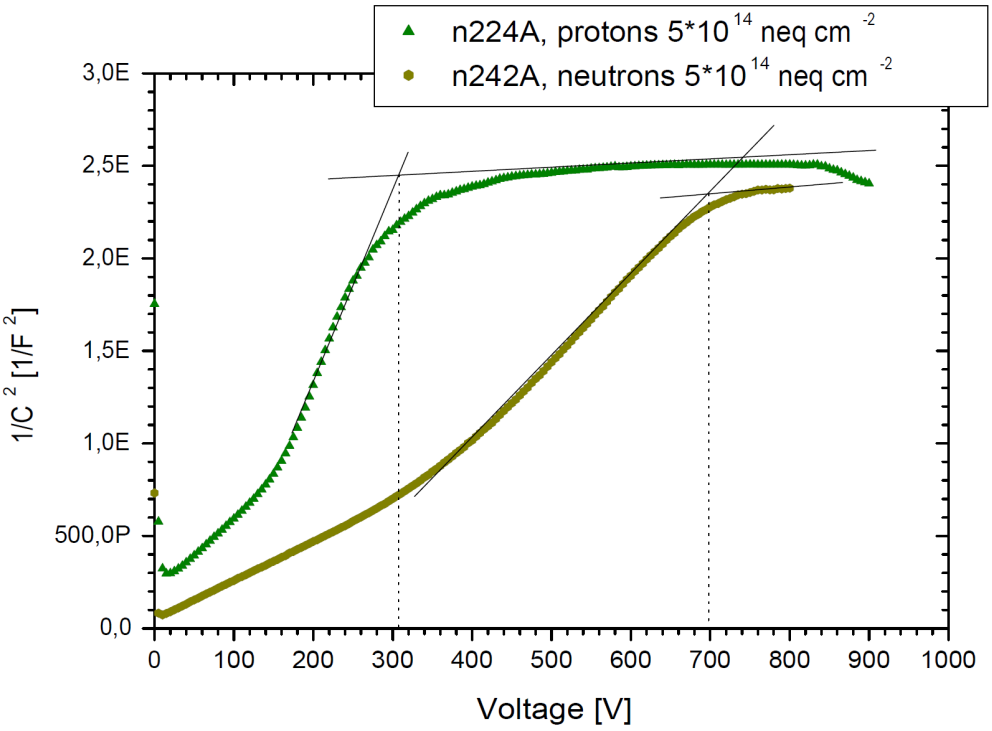

Figure 8.7: $1/C^2$ ***against voltage plot of the two higher irradiated sensors tested in the 2007 beamtest after irradiation.***

8.3.2 Strip Leakage Currents

Just like the total leakage current, the leakage currents of the single strips increase strongly after the irradiations. Figure 8.8(a) to 8.8(c) show the measurement results before irradiation. Sensor n017A, which has a relatively high total leakage current, shows a problematic region on the sensor where the currents are conspicuously higher than for the rest. The strip currents of the other two sensors are much more equally distributed and stay on a lower level. The results of the random inspections after irradiation in figure 8.9 show, that for n017A the region stays problematic as the strip currents are higher than the ones of the other two sensors, although n017A received a lower fluence. Because of the overall sufficiently low total leakage current around full depletion and a good strip region, like it can be seen in figure 8.5, the sensor was nevertheless regarded as being useable for the experiment. The strip leakage currents of the higher irradiated sensors were unproblematic.

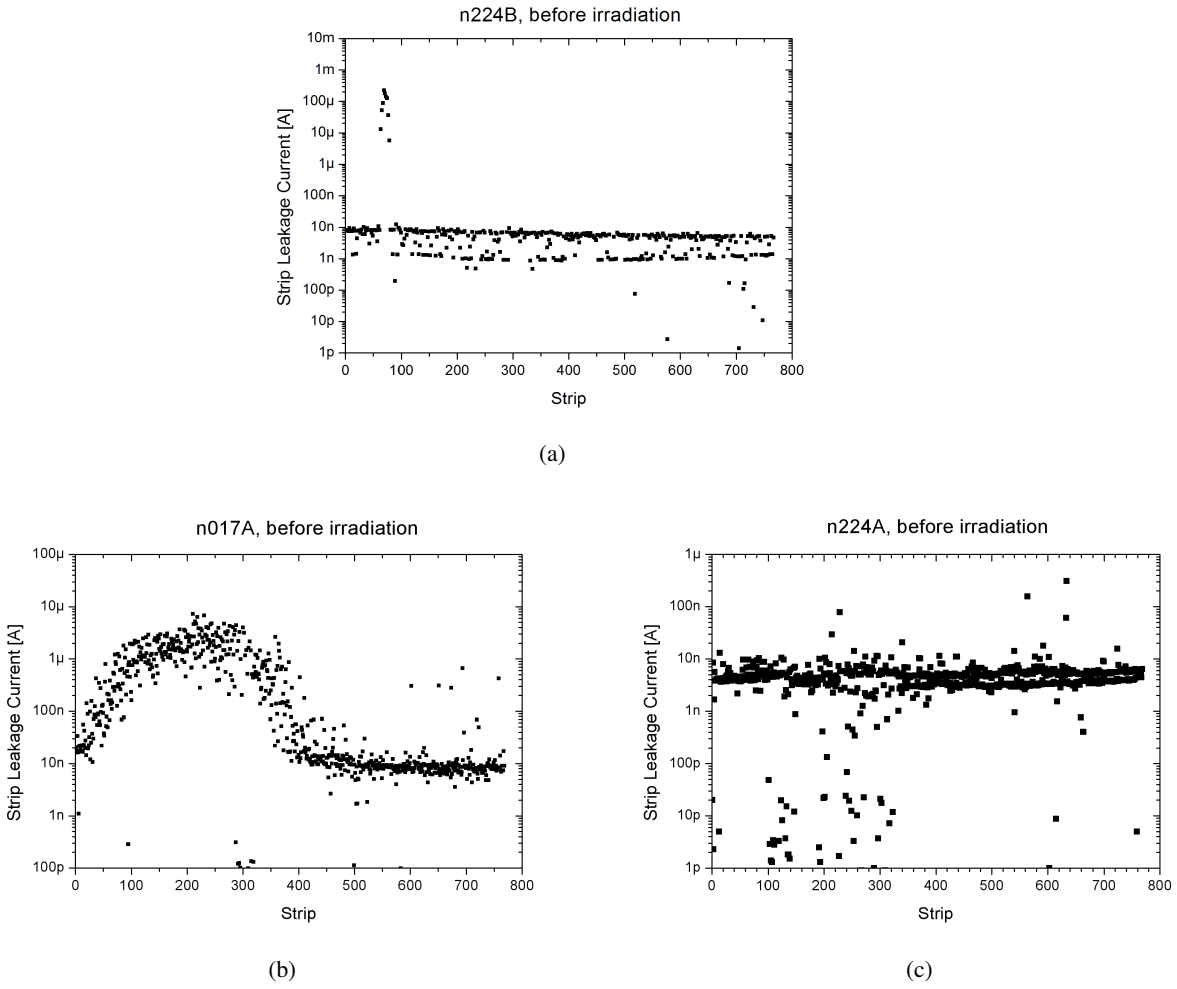

Figure 8.8: ***Strip leakage currents of the sensors tested in the 2007 beamtest before irradiation.*** *a) n224B. The good strip leakage behavior is visible. Only some leaky strips existed. b) n017A. One half of the sensor showed relatively high strip leakage currents. As the overall behavior of the sensor was satisfactory and at least one part was definitely good, the sensor was used for the test. c) n224A. All strip leakage currents were on a low level.*

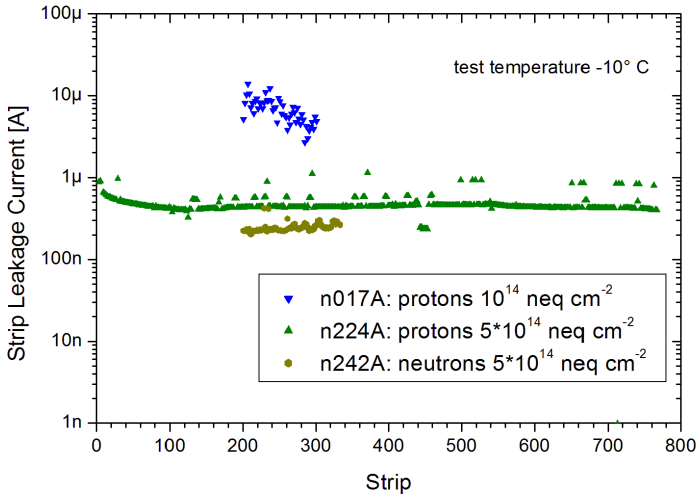

Figure 8.9: ***Strip leakage currents of the sensors tested in the 2007 beamtest after irradiation.*** *For two sensors only random inspections were done.*

8.3.3 Bias Resistors

The bias resistors were produced with a target resistance of 1 $M\Omega$. This was successfully realized, like the results in figure 8.10(a) demonstrate. According to the distribution in 8.10(b) the majority of the values of all sensors lies around 0.95 $M\Omega$ and 1.05 $M\Omega$. The resistances do not change under the influence of the neutron irradiation in contrast to the observations with the proton irradiations. It can be seen in 8.11(a) that the values drop with the proton fluence so that they get decreased by approximately 0.2 $M\Omega$ after a fluence of $5 \cdot 10^{14}$ $neq./cm^2$ (n224A). The corresponding histogram can be found in figure 8.11(b). The resistances were nevertheless still high enough for the application.

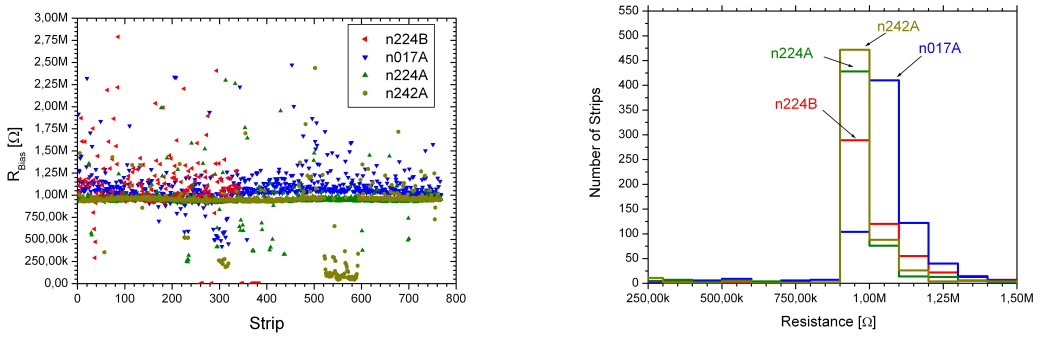

(a) (b)

Figure 8.10: ***Bias resistors of the sensors tested in the 2007 beamtest before irradiation.*** *a) Resistances against strips. b) Histogram. The majority of the resistors had the design value of around* 1 $M\Omega$.

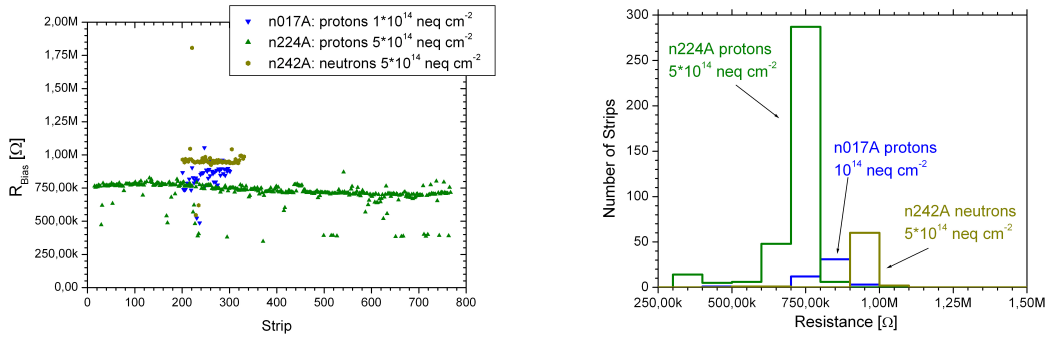

(a) (b)

Figure 8.11: ***Bias resistors of the sensors tested in the 2007 beamtest after irradiation.*** *a) Resistance over strip b) Histogram. A slight decrease of the resistances after the proton irradiations was measured.*

8.3.4 Coupling Capacitances

The coupling capacitance (CC), between the strip-implant and the metal-strip, which couples out the signal to the readout chip, has to be significantly higher then the interstrip capacitances, like explained in chapter 5. The first measurements in 2007 showed that this was not the case for any of the sensors. The CC values mainly averaged out at around 2 pF with some of them reaching a maximum at the expected value. To find the cause of this problem, further investigations were necessary. They finally lead to the hypothesis, that charge accumulations in the dielectric existed. In a further test, it could be shown, that applying a voltage over the coupling capacitances, between the AC- and DC-pads, could reduce the problem of the too low capacitances or even eliminate it. Good effects were achieved after 30 seconds with a voltage of 70 V (ground at the implant). The sensors were kept depleted during that procedure. Figure 8.12 illustrates the effect at the example of sensor n224B by comparing the measured coupling capacitance values before and after that "discharging" process. A solution of the problem with the much too deep coupling capacitances was found by the investigations and the procedure was introduced for all sensors. The results of the CC measurements can be seen in the figures 8.13(a) to 8.13(c). Still some strips showed too low values, but this was mainly due to bad probe contacts. The important outcome was, that the number of "repaired" strips, reaching the plausible coupling capacitance value of around 70 pF, was high enough that all sensors could be used in the experiment. Figure 8.13(d) shows the distributions of the values.
After the irradiations only the coupling capacitances of the sensor n224A, irradiated with $5 \cdot 10^{14}$ $neq./cm^2$ protons, were fully tested. The results in figure 8.14 show, that only a negligible fraction of the strips did not reach the level of 70 pF. With the other two sensors only random inspections were done.

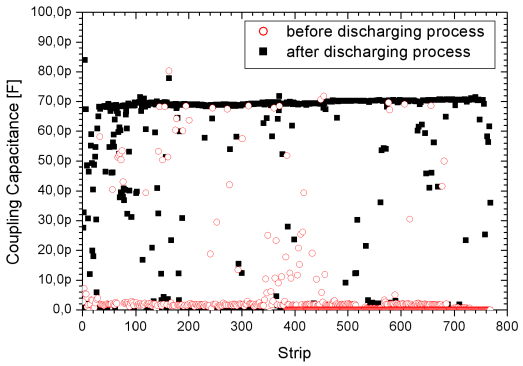

Figure 8.12: ***Beneficial effect of the "discharging" process on the bad coupling capacitances*** *The coupling capacitances showed much too low values. Applying a voltage of* 70 *V over the dielectric for 30 seconds brought the coupling capacitances to their nominal value, so that the sensors could be saved for applications.*

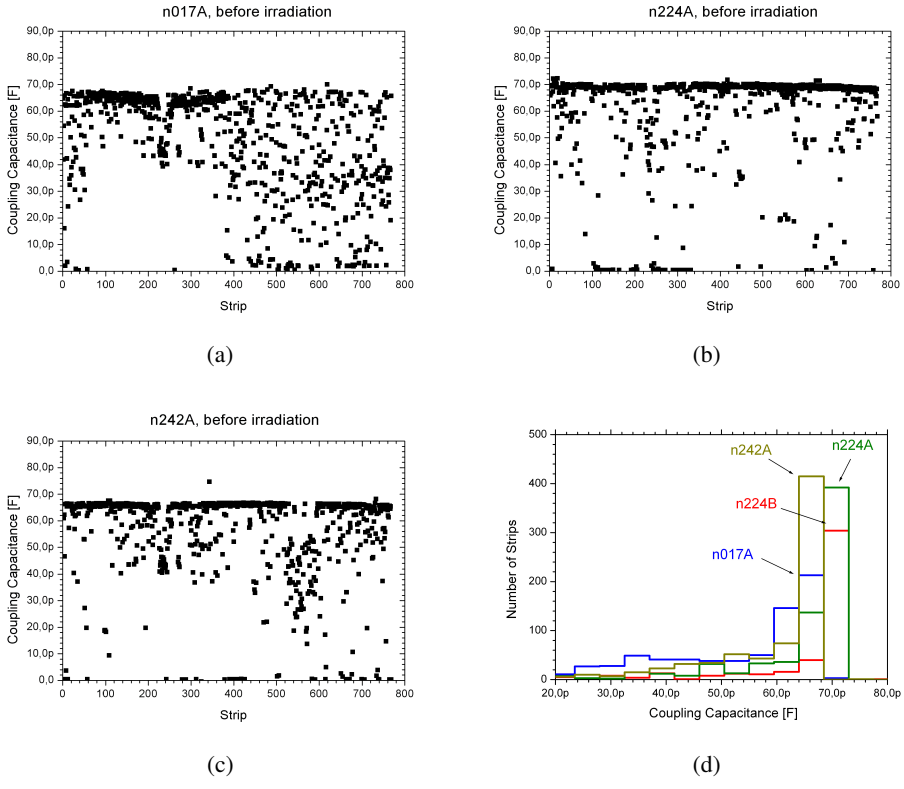

Figure 8.13: ***Coupling capacitances of the non-irradiated sensors tested in the 2007 beamtest after the "discharging" process.*** *Even after the "discharging" some strips still showed too low values. This was most probably due to bad contacts of the probing needles. The number of "repaired" strips was high enough that all sensors could be used in an application in the experiment. a) Sensor n017A. b) Sensor n224A. c) Sensor n242A. d) Histogram of the coupling capacitances.*

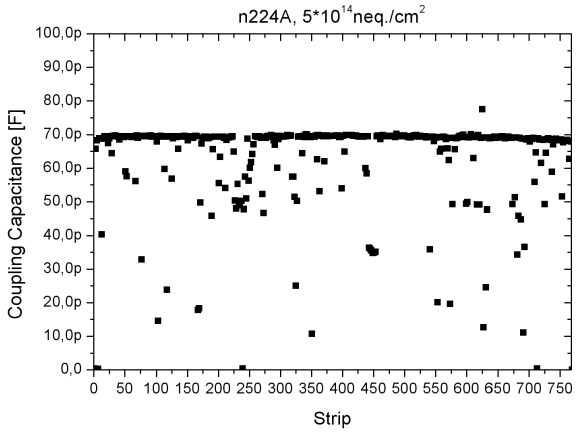

Figure 8.14: ***Coupling capacitances of the sensor n224A, after the irradiation with protons of a fluence of*** $5 \cdot 10^{14}$ *neq./cm*^{2}***.*** *Only a negligible fraction of the strips did not reach the level of* 70 *pF*.

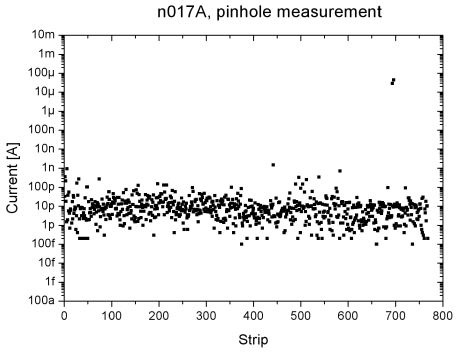

(a)

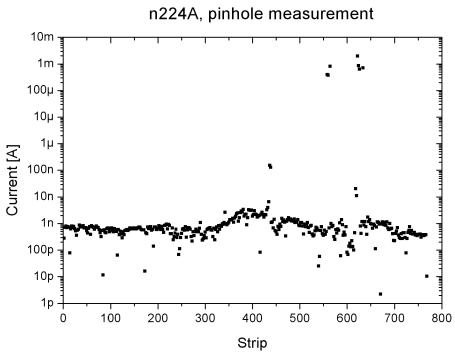

(b)

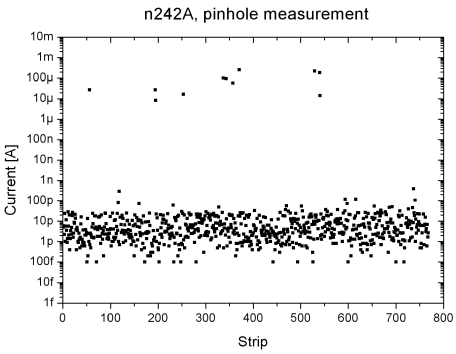

(c)

Figure 8.15: ***Pinhole measurements of the sensors tested in the 2007 beamtest before irradiation.*** *a) n017A b) n224A c) n242A. Strips with a too high current over the dielectric were not bonded to the readout electronics.*

8.3.5 Currents over the Dielectric (Pinholes)

Strips with ohmic contacts over the dielectric, between the strip implant and the aluminium layer, have to be detected, as they allow a high charge flow into the amplifier on the readout chips. The amplifier could reach its saturation and as a consequence the read out of even a larger sensor region could be blocked. To prevent this, these strips are not bonded to the chip. Only a few of these ohmic contacts, called pinholes, were found on the sensors. The results of the measurements can be seen in the figures 8.15(a) to 8.15(c).

8.4 Results of the 2008 Test Sensors

The Helsinki Institute of Physics decided to produce the sensors for the 2008 test without a passivation layer, due to the experience with the problems of the high leakage currents and the bad coupling capacitances in 2007. This lead to a significant improvement of the concerned parameters.

8.4.1 Total Leakage Currents and Full Depletion Voltage

Like it can be seen in figure 8.16, the total leakage currents before irradiation, measured at room temperature with a relative humidity of less than 30 %, were on a significantly lower level than the ones of the 2007 sensors.

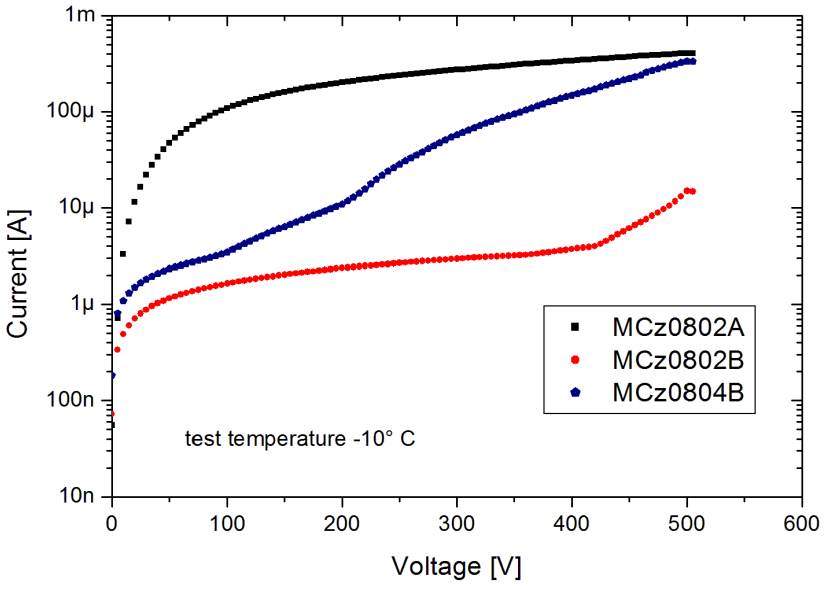

Figure 8.16: ***IV curves of the sensors tested in the 2008 beamtest before irradiation.*** *The total leakage currents before irradiation were on a significantly lower level than the ones of the 2007 sensors, where problems with the passivation existed. The 2008 sensors were produced without a passivation layer.*

Figure 8.17 shows the $1/C^2$ over voltage plots of the sensors that were irradiated afterwards. There it can be seen that the full depletion voltages were between around 330 V and 380 V. For the sensor MCz0802A, which was irradiated with a total fluence of $1.1 \cdot 10^{15}$ $neq./cm^2$, probestation measurements only exist after the irradiation with protons of a fluence of $5.2 \cdot 10^{14}$ $neq./cm^2$ and additional neutrons of a fluence of $6.6 \cdot 10^{13}$, but not after the second irradiation. The full depletion voltage changed to roughly 520 V according to figure 8.18.

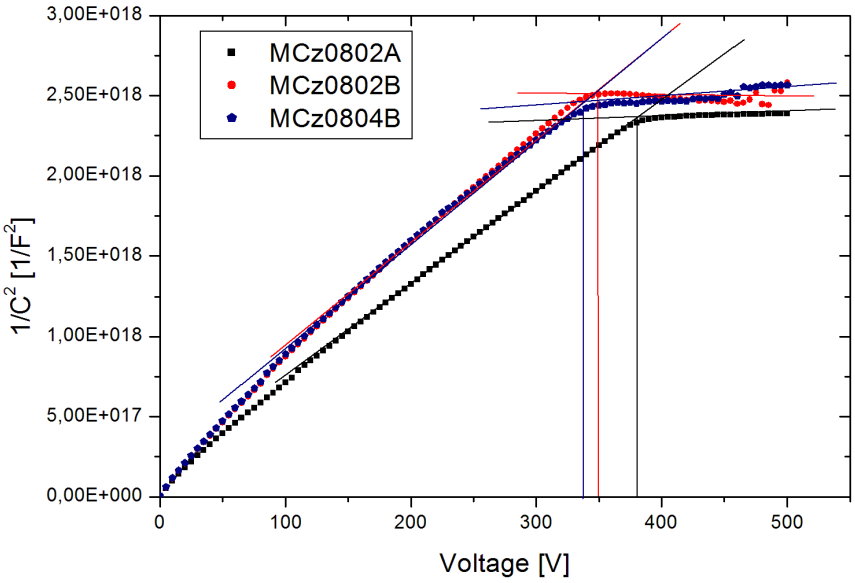

Figure 8.17: ***Full depletion voltages of the sensors tested in the 2008 beamtest before irradiation*** *The $1/C^2$ over V plots helps to identify the full depletion voltages. The conformity with the specification values was shown.*

The sensor MCz0802B was first irradiated with a fluence of $7 \cdot 10^{13}$ $neq./cm^2$ of neutrons and afterwards with a fluence of $5.1 \cdot 10^{14} neq./cm^2$ of protons, which should change the full depletion voltage to a value slightly higher than 300 V, by taking the result of the 2007 sensor n224A. In spite of this relatively low voltage, the CV-measurement did not give a clue to that value, which figure 8.18 reveals. A possible explanation for the result could be, that the sensor was checked directly after the irradiation without any annealing. The full depletion voltage of MCz0804B, with a total equivalent fluence of $1.6 \cdot 10^{15}$ $neq./cm^2$, could not be determined with this measurement method as it should be higher than the maximally applicable test voltage.
The result of the IV measurements can be seen in figure 8.19. As a consequence of the highest fluence of $1.6 \cdot 10^{15}$ $neq./cm^2$, the current level of the sensor MCz0804B is the highest of the explored sensors. The currents can be compared with the ones measured in the beamtest and with the theoretical prediction. The errors of the calculation are big due to the reasons discussed above. Nevertheless the observed values match quite well with the prediction (see table 9.2).

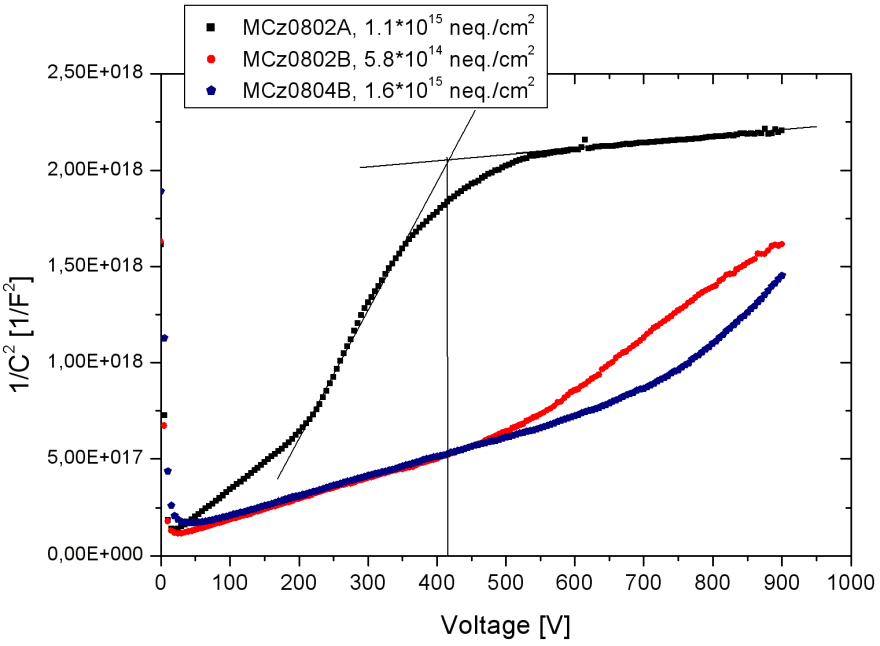

Figure 8.18: $1/C^2$ ***against bias voltage plots of the sensors tested in the 2008 beamtest after irradiation.*** *Only for the lowest irradiated sensor with a fluence of* $5.8 \cdot 10^{14}$ $neq./cm^2$ *the full depletion voltage could be determined (black curve).*

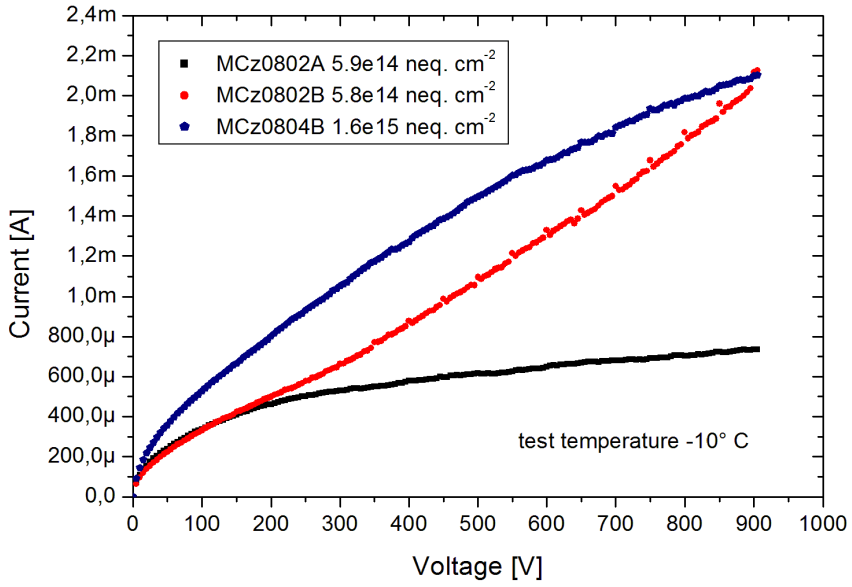

Figure 8.19: ***IV curves of the sensors tested in the 2008 beamtest after irradiation.***

8.4.2 Strip Leakage Currents

Figure 8.20(a) shows the comparison of the strip leakage currents before and after irradiation of the sensor MCz0802B. The corresponding plot of sensor MCz0802A is drawn in figure 8.20(b) and the one of MCz0804B in figure 8.20(c). There seems to be a substructure between odd and even strips before the irradiation, but this is only a consequence of a slightly different temperature during the separated measurements of the odd and even strips. All three plots show good uniformities of the strip leakage currents.

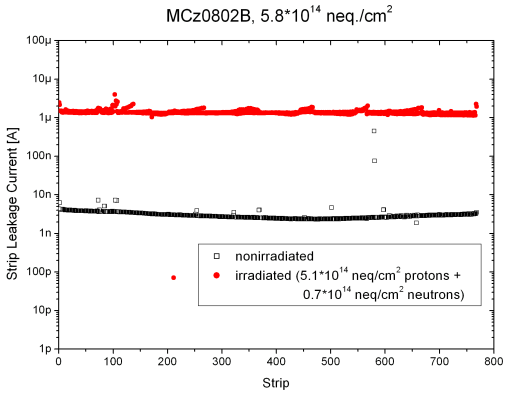

(a)

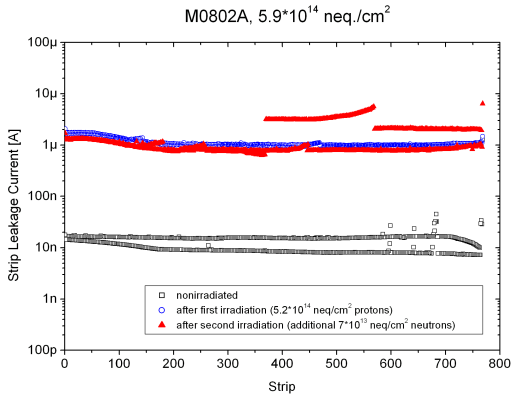

(b)

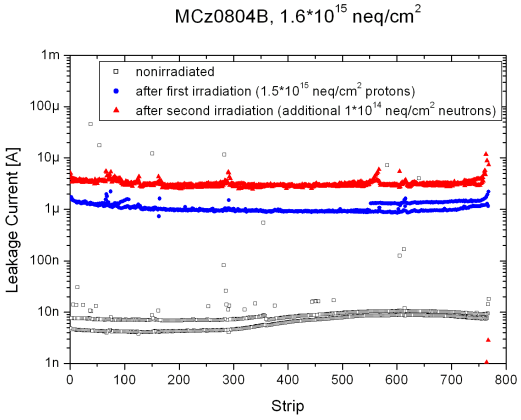

(c)

Figure 8.20: ***Comparison of the strip leakage currents before and after the irradiations.*** *a) MCz0802B, irradiated with* $5.8 \cdot 10^{14}$ *neq./cm*^{2} *b)MCz0802A, irradiated with* $5.8 \cdot 10^{14}$ *neq./cm*^{2} *c) MCz0804B, irradiated with* $1.6 \cdot 10^{15}$ *neq./cm*^{2}*. The black quadratic dots show the values before irradiation, the blue circular dots show the ones after the first irradiation and the red triangular dots the ones after the second irradiation. Measurements after the final irradiation to the* $1.1 \cdot 10^{15}$*neq./cm*^{2} *do not exist. A good uniformity of the strip leakage currents can be seen at all three sensors.*

8.4.3 Bias Resistors

The bias resistors (figures 8.21(a) to 8.21(c)) were also of a good quality. The plots show that the values nearly did not change for the sensors MCz0802B and MCz0802A after the irradiations and that for the highest irradiated sensor MCz0804B they only decreased by around 10 % – 15 %. The target value of the production of $\sim 1\ M\Omega$ was reached very well again.

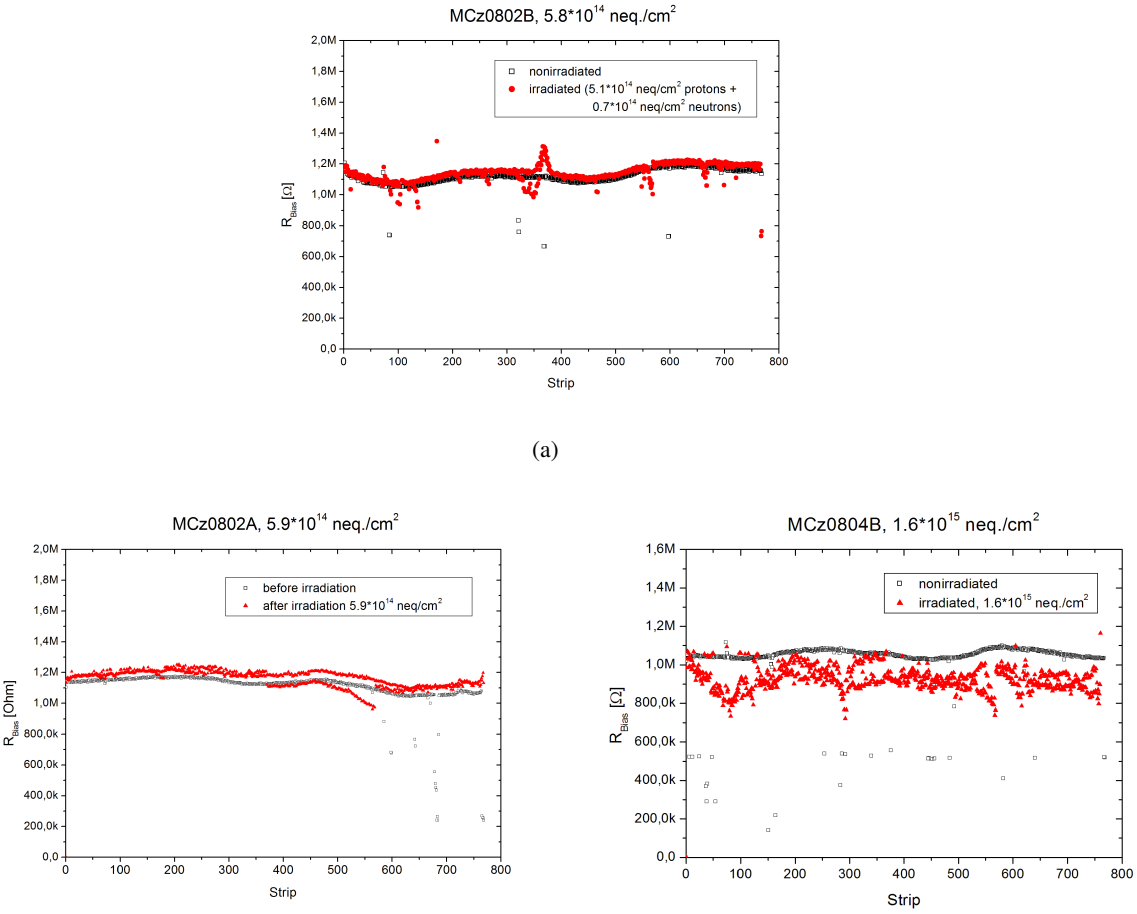

Figure 8.21: ***Comparison of the bias resistances of the sensors tested in the 2008 beamtest before and after irradiation.*** *a) MCz0802B, irradiated with* $5.8 \cdot 10^{14}$ *neq./cm*^{2} *b)MCz0802A, irradiated with* $5.8 \cdot 10^{14}$ *neq./cm*^{2} *c) MCz0804B, irradiated with* $1.6 \cdot 10^{15}$ *neq./cm*^{2}.

8.4.4 Coupling Capacitances

The choice to produce the sensors without a passivation layer to prevent the problems that appeared with the sensors of 2007 had the desired success. Figure 8.22(a) compares the coupling capacitances of the sensor MCz0802B. Before irradiation they lay perfectly on one level at 80 pF and nearly did not change after the irradiation. The same can be said for sensor MCz0802A (figure 8.22(b)) and MCz0804B (figure 8.22(c)).

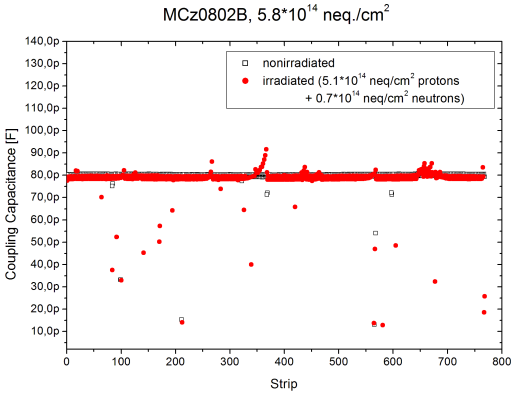

(a)

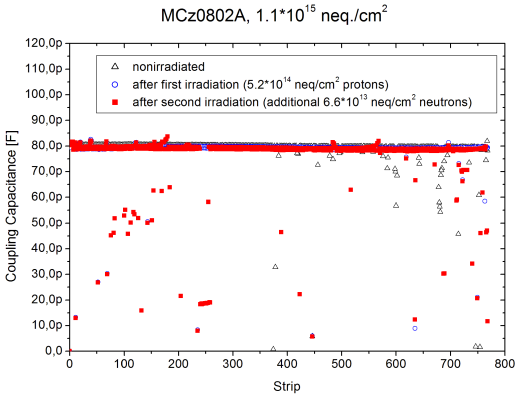

(b)

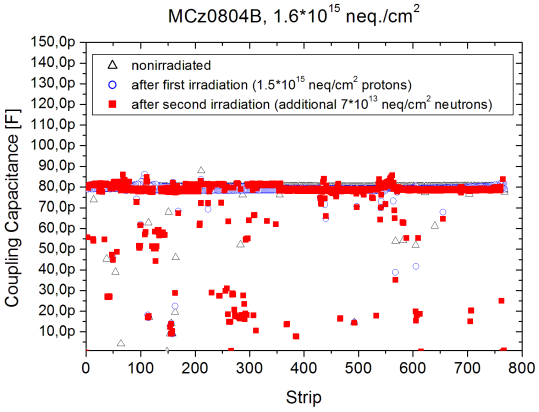

(c)

Figure 8.22: ***Comparison of the coupling capacitances before and after irradiation.*** *a) MCz0802B, irradiated with* $5.8 \cdot 10^{14}$ *neq./cm*^{2} *b)MCz0802A, irradiated with* $5.8 \cdot 10^{14}$ *neq./cm*^{2} *c) MCz0804B, irradiated with* $1.6 \cdot 10^{15}$ *neq./cm*^{2}

8.4.5 Currents over the Dielectric (Pinholes)

Again pinhole measurements (figure 8.23(a) to 8.23(c)) showed, that only a few strips were not useable. These ones were not bonded during the module production, as well as some few leaky strips.

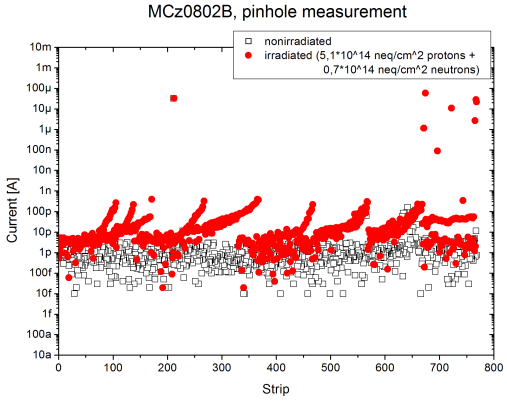

(a)

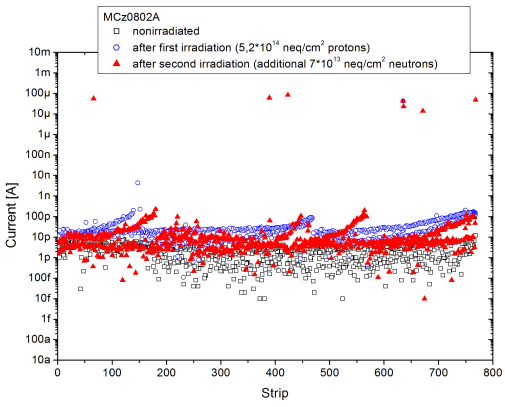

(b)

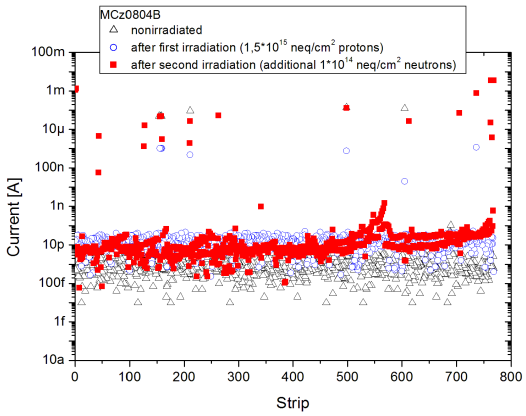

(c)

Figure 8.23: ***Comparison of the pinhole measurements before and after irradiation of the sensors tested in the 2008 beamtest.*** *a) MCz0802B, irradiated with* $5.8 \cdot 10^{14}$ *neq./cm*^{2} *b)MCz0802A, irradiated with* $5.8 \cdot 10^{14}$ *neq./cm*^{2} *c) MCz0804B, irradiated with* $1.6 \cdot 10^{15}$ *neq./cm*^{2}*. Only a few strips were not useable. These ones were not bonded to the readout electronics during the module production.*

8.4.6 Results of the Float Zone Sensors

Beside the MCz sensors, also FZ sensors were tested in the 2008 beamtest. The design of these p-in-n sensors and their modules was the same like the one for the MCz sensors. Their special characteristic was the high resistivity, that differed strongly from the MCz sensors and the sensors used for the CMS experiment.
The expected full depletion voltage was 8 V. This was perfectly confirmed by CV measurements and $1/C^2$ over voltage plots (see figure 8.24(a), using the example of sensor FZ0802B). The total leakage

current was low and no breakthrough appeared even at strong overdepletion, like the plot of the reference sensor FZ0802B shows (8.25(a)). After the irradiation with a fluence of $2.2 \cdot 10^{14}$ $neq./cm^2$ of protons, sensor parameters were measured without significant annealing. The measured total leakage current can be found in figure 8.25(b) and the full depletion voltage in figure (8.24(b)).

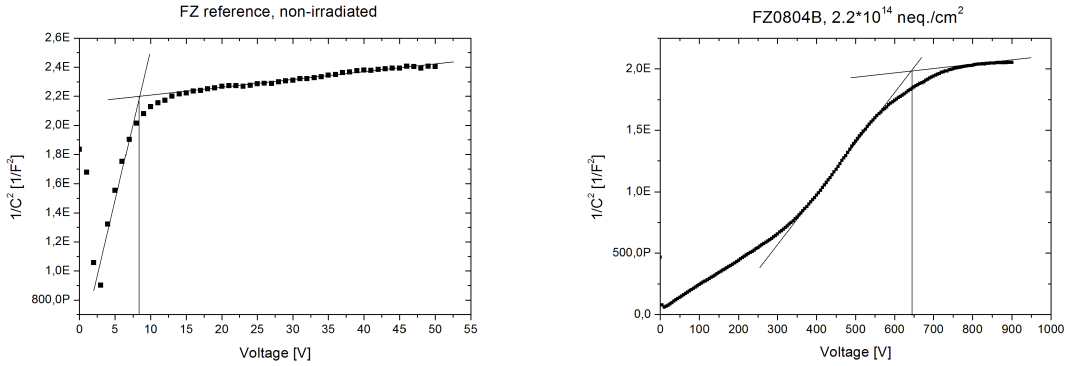

(a) (b)

Figure 8.24: $1/C^2$ ***against voltage plot of the FZ sensors before and after irradiation.*** *a) FZ0802B before irradiation. b) FZ0804B after irradiation. Due to the high resistivity, the sensor depleted at around* 8 V *before irradiation. After a fluence of* $2.2 \cdot 10^{14}$ $neq./cm^2$ *the full depletion voltage was around* 700 V.

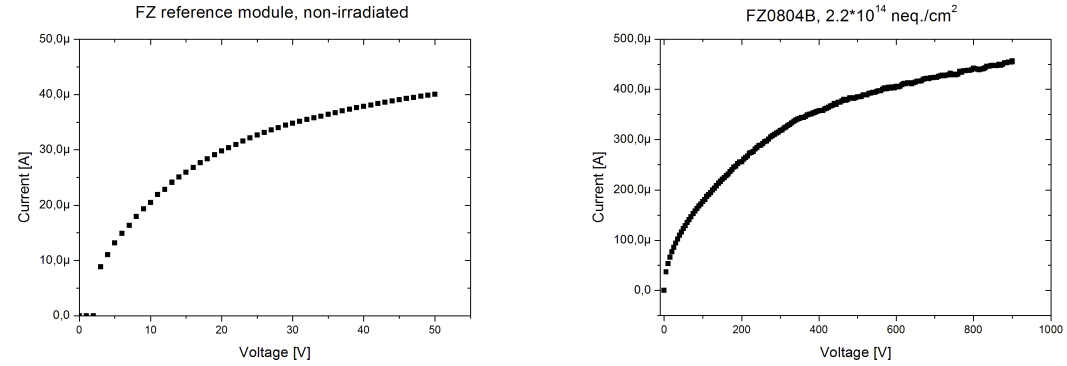

(a) (b)

Figure 8.25: ***IV curves of the FZ sensors before and after irradiation.*** *a) FZ0802B before irradiation. b) FZ0804B after irradiation.*

The quality of the FZ sensors concerning other important parameters was also very good. The figures 8.26(a) to 8.26(c) show the results of the non-irradiated reference sensor FZ0802B, while figures 8.27(a) to 8.27(c) show the ones of sensor FZ0804B after the irradiation (without annealing).

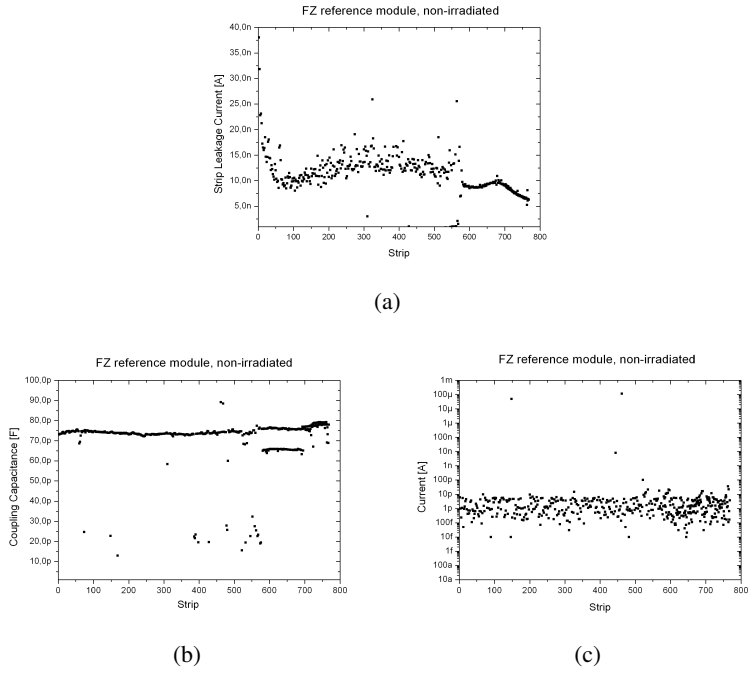

Figure 8.26: ***Strip parameter measurements of the FZ reference sensor.*** *a) Strip leakage currents. b) Coupling capacitances. c) Pinholes. The overall quality of the FZ sensors concerning important parameters was comparably good like the one of the MCz sensors of 2008.*

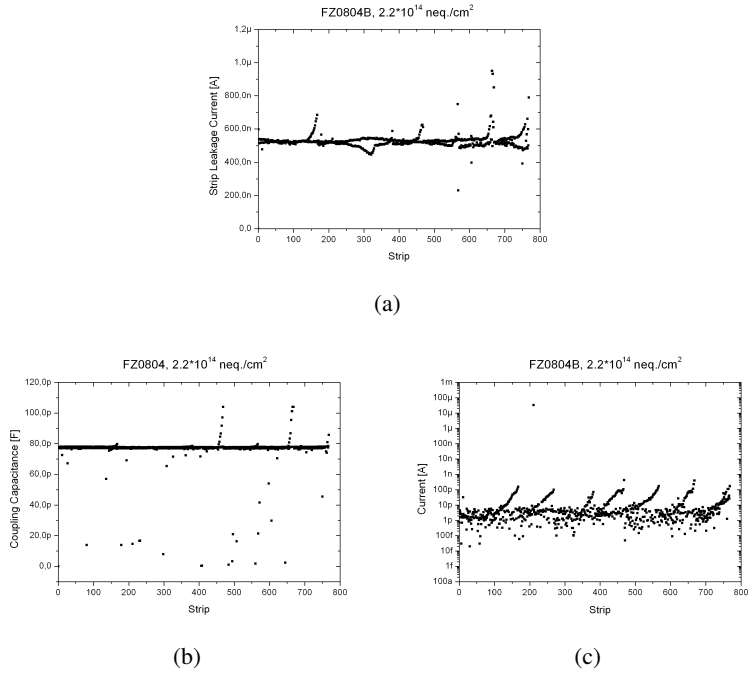

Figure 8.27: ***Strip parameter measurements of the FZ sensor irradiated with*** $2.2 \cdot 10^{14}$ *neq./cm*^{2}**.** *a) Strip leakage currents b) Coupling capacitances c) Pinholes. No problematic strips existed after the irradiation.*

8.5 Summary

The sensor quality testing as a preparation step towards the actual test is mainly intended to prevent the contacting of faulty strips and to sort out defective sensors, but after an irradiation it can additionally already deliver essential information for the research on radiation induced defects. After the successful irradiations, the comparison of the measured full depletion voltages confirmed in this way again, that neutrons and protons have different effects on that parameter for MCz sensors. It could also be checked that damage models predict quite well the leakage current increase.
The detection of the bad coupling capacitances and the relatively high leakage currents in 2007 acts as an example for the importance and the indispensability of an intensive quality investigation on the sensors and materials to be used in an experiment. After the reason for the too low coupling capacitances was identified, a recovery process was found and established, so that all sensors were useable. The overall quality of the 2007 sensors was good.
In consequence of the experiences with the coupling capacitances and the high surface currents in 2007, the sensors for the 2008 beamtest were produced without a passivation layer, which was regarded as the source of the problems. This step had the desired success, as all sensor parameters of the 2008 MCz sensors and the FZ sensors matched very well the specifications.

Chapter 9

Beam Test Results

To investigate important sensor parameters, like the charge collection efficicency or the signal to noise ratio resulting of traversing minimum ionizing particles, one has to use enough adequate particle events to get a statistically significant information. An accelerator beam is predestinated for this. The experiments with the sensor modules took place at the CERN SPS H2 experimental area with a 225 GeV muon beam of the SPS [1]. The testsensor modules were installed inside the beam telescope SiBT (see chapter 7.2) with which the particle track information could get reconstructed. They were included in the readout chain of the SiBT, so that the data acquisition was done via the SiBT software, the specially adapted early version of the CMS XDAQ. The signals were handled in the peak mode (see chapter 5.2).
The analysis of the data was done with an adjusted version of the software SiBTStar, using the tools and definitions given in chapter 7.3. The special settings in the cluster finding were, that a cluster seed channel had to show a signal being at least four times higher than the channel's noise and the acceptance criterium for adjacent strips was, that they had to show a signal being at least two times higher than the noise. The summed charge of the seed and its neighbors gave the cluster charge. In the further analysis of the explored sensor parameters, only clusters that belonged to a track were considered. The most probable value of a Landau-Gauss fit at the track cluster charge histogram defined the collected charge generated by a MIP in the conditions of the treated run. In the same way the accordant signal to noise ratio was obtained.

9.1 Beamtest for Sensors with Fluences of up to $5 \cdot 10^{14}$ $neq./cm^2$ (2007)

In 2007 three sensors were tested. These were the sensors n017A, irradiated with a fluence of $1 \cdot 10^{14}$ $neq./cm^2$ of protons, n224A with a fluence of $5 \cdot 10^{14}$ $neq./cm^2$ of protons and the non-irradiated one n224B serving as a reference detector. The study of the neutron irradiated sensor n242A had to be stopped at a bias voltage of 450 V, because of a thermal runaway after the failure of a Peltier element of the cooling system of the SiBT. Out of the same reason, n017A was tested at 0°C and after an annealing process also n224A was tested at only 0°C instead of the planned -10°C . While this was sufficient for n017A and tolerable for n224A, the data of the neutron irradiated sensor had to be dropped, as the full depletion voltage could not be reached by far. A nitrogen gas flow through the beamtelescope preserved the correct atmosphere for the sensors to inhibit condensation. Figure 9.1 illustrates the arrangement of the sensors in the beamtelescope during the test. Table 9.2 shows the used modules of the tests in 2007 (together with the 2008 modules) and the conditions under which

[1] Super Proton Synchrotron

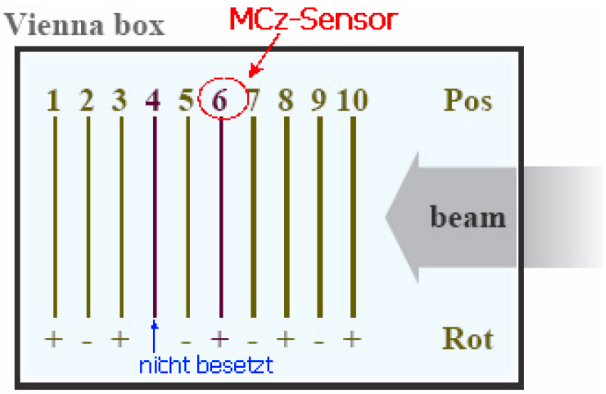

Figure 9.1: ***Module orientation in the beamtelescope during the test.*** *The modules were installed in the presented orientations of +45° and -45° positions relative to the beamtelescope ground plate, to cope with the geometrical conditions and to achieve a sufficient number of sensors being perpendicular to each other.*

they were tested.
For each change of the external parameters like temperature and especially the bias voltage, a pedestal run and a physics run were accomplished, to determine the pedestal level (see chapter 7.3) and the noise of the sensor under the given conditions. In a pedestal run, one reads out the detectors by absence of the signal or, if the particle rate is low, with a random trigger. Approximately 20000 events were recorded during the physics runs to get a high statistical significance.

9.1.1 Noise

Noise Distribution

As it can be seen from the noise plot of the reference sensor at different bias voltages in figure 9.2, the two APVs were obviously not working properly, showing high noise levels or abnormally low ones. The concerned APV channels were therefore not considered any further in the analysis. Further a noise cut method was introduced, in which channels with noise values lower or higher special limits were regarded as being broken and which were thus taken out of the further analysis by the analysis software. This method was especially necessary for the irradiated sensors, where many more channels showed very high noise levels, which is noticeable in figure 9.3(a) and figure 9.3(b). The distribution of the noise values does not follow a Gaussian profile as expected. In figure 9.4(a) histograms of all channels of sensor n017A at different voltages are plotted, while figure 9.4(b) shows the analogous histograms of only the APV with the lowest noise. The values are widely distributed. The corresponding histograms for sensor n224A can be found in figure 9.5(a) and figure 9.5(b). Here in addition, at many voltages a second peak in the noise distribution appears.

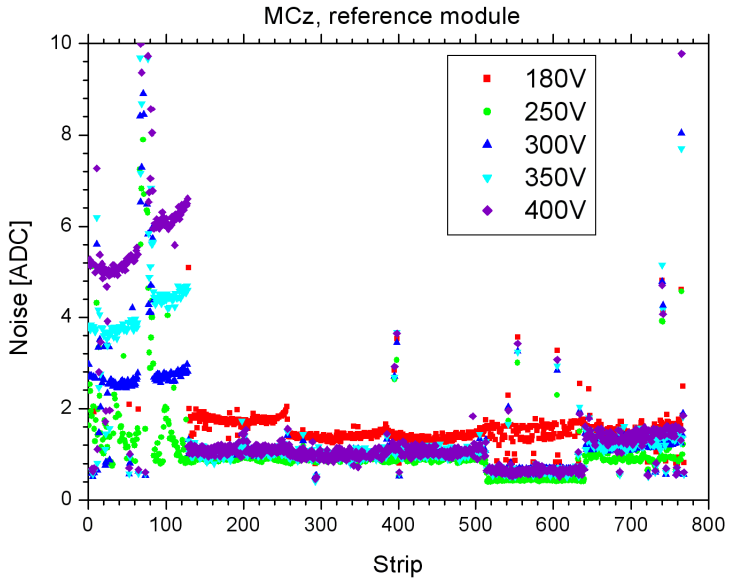

Figure 9.2: ***Channel noise of the reference module.*** *Two APVs were not working properly, so they were not considered in the analysis as well as the noisy channels.*

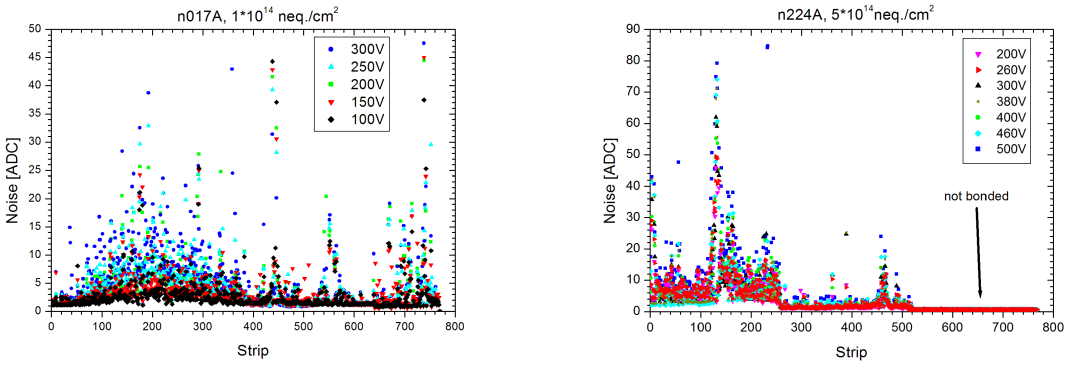

(a) (b)

Figure 9.3: ***Channel noise of two irradiated sensors.*** *a) n017A, irradiated with* $1 \cdot 10^{14}$ $neq./cm^2$ *b) n224A, irradiated with* $5 \cdot 10^{14}$ $neq./cm^2$*. The general noise behavior was not good as many strips were noisy. They were not considered in the analysis after a flagging by the definition of cuts.*

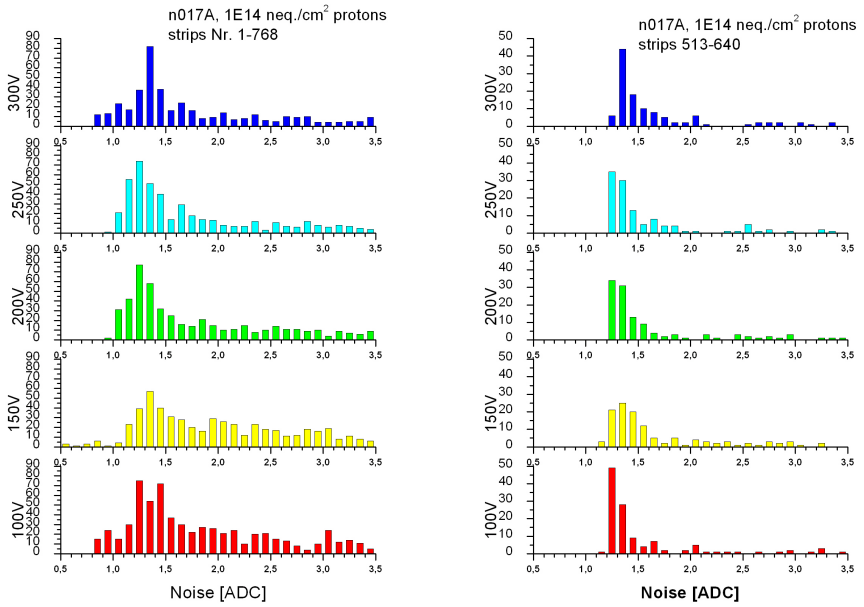

(a) (b)

Figure 9.4: ***Noise histograms of the module n017A, irradiated with*** $1 \cdot 10^{14}$ *neq./cm*^{2}**.** *a) All channels. The values are widely distributed. b) Channels of the APV with the lowest noise.*

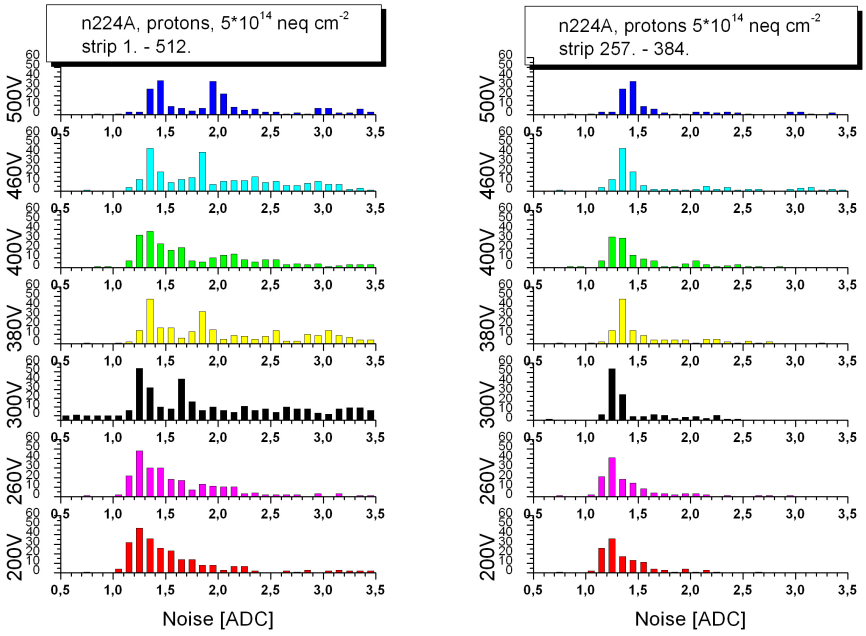

(a) (b)

Figure 9.5: ***Noise histograms of the module n224A, irradiated with*** $5 \cdot 10^{14}$ *neq./cm*^{2}**.** *a) All channels. The values are widely distributed and even a second peak appears at higher voltages. b) Channels of the APV with the lowest noise.*

Consequences of the Strip Flagging

The importance of the introduced strip flagging by the noise cut method is less striking in the analysis of the collected cluster charge, but it becomes evident for the determination of the signal to noise ratios. Using the example of the sensor n224A (irradiated with $5 \cdot 10^{14}$ $neq./cm^2$) at 500 V, figure 9.6(a) shows the histogram of the collected cluster charge by usage of all channels, 9.6(b) shows the same for the channels of the APV with the lowest mean noise and in figure 9.6(c) the histogram after the noise cut is plotted. The noise cut method leads to an improvement, as the second peak, which broadened the distribution, is reduced, so that the resulting histogram shows a better shape of the expected Landau-Gauss curve. The analogous plots for the SNR histograms can be found in figures 9.7(a) to 9.7(c), which make it obvious that there the effect of the noise cut is very important as the differences are even more significant.

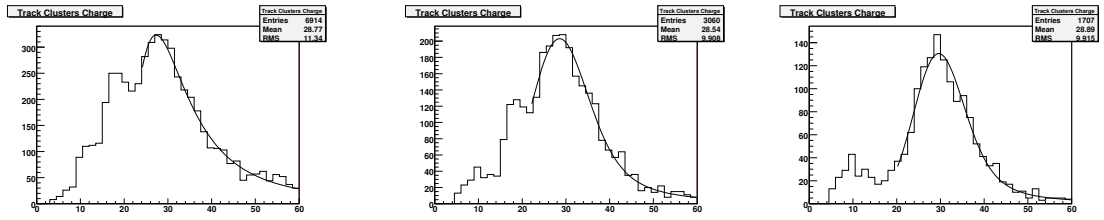

(a) (b) (c)

Figure 9.6: ***Impact of the noise cut method on the cluster charge. Module n224A, irradiated with*** $5 \cdot 10^{14}$ $neq./cm^2$***, 500 V.*** *a) Histogram of the collected cluster charge of all channels. b) Histogram of the collected cluster charge of the APV with the lowest noise. c) Histogram of the collected cluster charge after the noise cut. The noise cut method improves the shape of the distribution towards the expected one of a Landau-Gauss curve.*

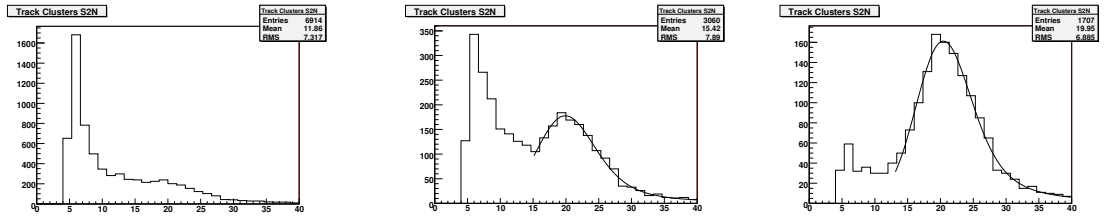

(a) (b) (c)

Figure 9.7: ***Impact of the noise cut method on the signal to noise ratio. Module n224A, irradiated with*** $5 \cdot 10^{14}$ $neq./cm^2$***, 500 V.*** *a) Histogram of the signal to noise ratio by usage of all channels b) Histogram of the signal to noise ratio by usage of the APV with the lowest noise c) Histogram of the signal to noise after the noise cut. The importance of the noise cut is significant in the case of these sensors with problematic channels, as without it a signal to noise analysis was not possible. It was the method that permitted the measurement of this important parameter.*

In figure 9.8 the mean noise after the cut method is plotted over the voltage to get an impression of the general noise behavior. Because of the difference of the curve shape of the belonging distributions compared to the one of a Gauss curve, the mean noise is used and not the most probable value of an accordant fit. The noise values of the strips used for the physics data analysis are between 0.9 and 1.8 ADCs. A slight increase of the noise with the voltage can be seen for the higher irradiated sensors. There are some possible explanations for the relatively poor noise behavior of the excluded strips. It is a known fact, that pinholes can be sources of noise. Contacts between different bonds or badly contacted ones, resulting of bonding problems, are also possible noise sources [Hon]. Finally it can also not be excluded, that the module design is problematic, if it possesses a bad grounding scheme. Nevertheless enough working channels existed during the beamtest, so that enough meaningful data could be taken and a bad influence of the broken strips was suppressed by the flagging.

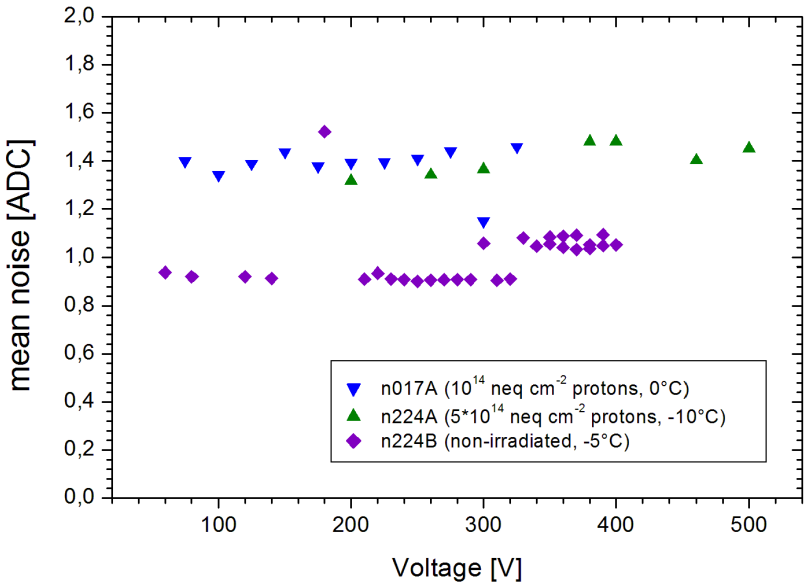

Figure 9.8: ***Evolution of the mean noise with the bias voltage.*** *The plot shows the evolution of the mean noise of the used channels with the bias voltage.*

9.1.2 Charge Collection

The collected charge should increase with the applied voltage until the full depletion voltage is reached. Some slight further increase should be possible, because of the increasing field strength which enables a faster charge collection. The voltage-dependent signal height of track clusters of the non-irradiated MCz reference module can be found in figure 9.9. A saturation at roughly 40 *ADCs* is emerging, beginning at a bias voltage of around the full depletion voltage of 370 V.

After irradiations the saturation value of the charge in track clusters drops. The sensor irradiated with a neutron equivalent fluence of $1 \cdot 10^{14}$ $neq./cm^2$ of protons shows a slightly decreased value of around 35 ADCs in figure 9.10. The saturation starts at about 200 V and not as before at around 350 V, reflecting the change of the full depletion voltage, as described in chapter 4. It has to be noticed, that

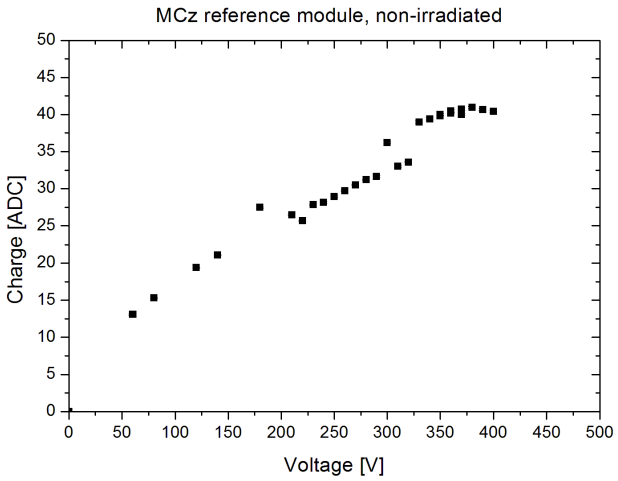

Figure 9.9: ***Track cluster charge of the reference module.*** *The plot shows the collected track cluster charge in ADCs of the reference module at different bias voltages. A saturation at roughly* 40 *ADCs seems to appear, beginning at a bias voltage of around the full depletion voltage of* 370 V.

the measuring temperature was at 0°C , being five degrees higher than during the measurement of the reference sensor, because of the broken Peltier cooling element. As a lower temperature should decrease the influence of trapping and increase the collected charge thereby, the observed value of 35 ADCs can be regarded as a lower limit. Figure 9.10 also shows the cluster charge over the bias voltage of the other irradiated sensor. The statistical errors are that small that the error bars nearly completely vanish in the size of the symbols.

A saturation of the values can be seen, which means that the full depletion voltages were reached during the test. In the test at -10°C , the collected cluster charge of the sensor n224A started to saturate at about 400 V to 450 V, reaching approximately 25 ADCs. Looking at the full depletion voltage of this sensor, determined by CV measurements and apparent in figure 8.4, confirms that again the saturation started at the full depletion voltage.

The important measurements of the collected charge produced by a MIP therefore show, that trapping leads to a charge loss in the order of 12.5 % for the fully depleted MCz sensor irradiated with a fluence of $1 \cdot 10^{14}$ $neq./cm^2$ of protons and about 37.5% for the fully depleted MCz sensor irradiated with a fluence of $5 \cdot 10^{14}$ $neq./cm^2$ of protons.

9.1.3 Signal to Noise Ratios

The irradiation induced relative reduction of the signal to noise ratios should be even higher than the relative loss in the collected charge, because of the additional increase of the noise with higher fluences. The measured SNRs of the tested sensors at different voltages can be seen in figure 9.11. The values start to saturate again near the same voltages as the ones where the collected charge saturates, which reflect the full depletion voltages. The SNR of the non-irradiated module reaches 40 ADCs at full depletion. After an irradiation with a neutron equivalent fluence of $1 \cdot 10^{14}$ $neq./cm^2$, the value of the tested sensor reduces to 24 ADCs and to roughly 18 ADCs after a neutron equivalent fluence of $5 \cdot 10^{14}$ $neq./cm^2$. Some measurements with the highest irradiated module after annealing

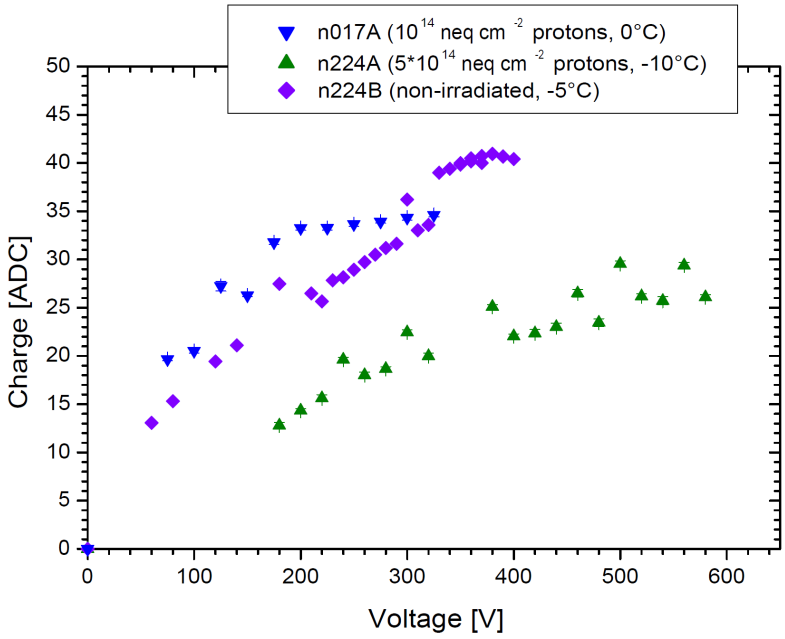

Figure 9.10: ***Track cluster charge of the tested sensors.*** *The plot shows the collected track cluster charge in ADCs at different bias voltages of all tested modules. The saturations start at the full depletion voltages. The charge loss is in the order of* 12.5 *% for the fully depleted MCz sensor irradiated with a fluence of* $1 \cdot 10^{14}$ *neq./cm*^{2} *of protons and about* 37.5% *for the fully depleted MCz sensor irradiated with a fluence of* $5 \cdot 10^{14}$ *neq./cm*^{2} *of protons.*

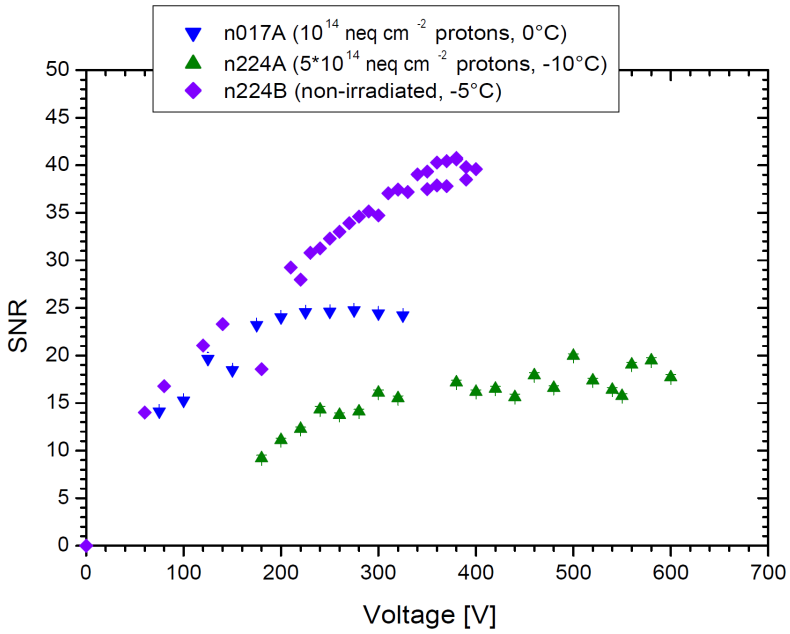

Figure 9.11: ***Signal to noise ratios of the tested sensors.*** *The plot shows the signal to noise ratios of all tested modules at different bias voltages.*

could be done at lower voltages that did not lead to thermal runaways, but the lower SNRs are not that meaningful as the temperature was higher, which increases noise and the sensor was not fully depleted.
Like expected, the relative loss in signal to noise is higher than the relative loss in the collected charge. Here it accounts for 40 % for the module with a neutron equivalent fluence of $1 \cdot 10^{14}$ $neq./cm^2$ and around 55 % for the one irradiated with a neutron equivalent fluence of $5 \cdot 10^{14}$ $neq./cm^2$.

9.1.4 Resolution

The spatial resolution, as defined in chapter 7.3, of the tested sensors and the D0-sensors of the beamtelescope SiBT, can be seen in the figures 9.12(a) to 9.12(c). Because of the effective pitch of 30 μm of the telescope sensors by considering the intermediate strips, one can calculate a binary spatial resolution for these sensors of approximately 8.7 μm. A slightly better resolution confirms this expected upper limit. The pitch of the MCz testsensors is 50 μm, so that the binary spatial resolution is 14.4 μm. The measured value for the non-irradiated sensor is 13 μm (9.12(a)) in agreement with the given upper limit. As an effect of the radiation damages, the measured spatial resolution changes to higher values. Under the influence of a fluence of $1 \cdot 10^{14}$ $neq./cm^2$, the parameter changes to 14 μm and to 16.5 μm after a fluence of $5 \cdot 10^{14}$ $neq./cm^2$. The results have to be handled with some care, as the software most probably can not find a perfect alignment if the sensors are marginally twisted. The only explored parameter that is concerned by a poor alignment is the resolution, so that the results serve as upper limits. An improvement of the SiBTStar software concerning this matter must be foreseen. Nevertheless, the observed upper limit on the spatial resolution of the highest irradiated sensor is still satisfactory.

9.2 Beamtest for Sensors with Fluences of up to $1.6 \cdot 10^{15}$ $neq./cm^2$ (2008)

The aim of the beamtest in 2008 was the test of MCz sensors, irradiated with fluences up to the ones expected at the inner layers of a CMS tracker for the SLHC at the radius of 20 *cm*. At the current CMS tracker, the pixel layers end at 17.5 *cm* and the strip sensor layers follow at the outer radii. The expected fluences of a SLHC CMS tracker of a similar design and the accordant ratios of charged particles to neutrons can be found in table A in the appendix.
Because of the experience with the different influences of neutrons and protons on the full depletion voltages of MCz sensors and to follow more realistically the calculated radiation exposure scenarios, the sensors were irradiated with both kinds of particles. For a comparative purpose, sensors based on very high resistive FZ material were explored too. The process technology could also be checked thereby with an established material.
The geometry of the test sensors was the same like of the sensors used in the 2007 beamtest, but a passivation layer was missing due to the reasons explained in chapter 8. In principle the design of the modules remained the same. Only minor changes in the contacting lines and pins were done for practical reasons. The SiBT beamtelescope and its readout system were used again for the test of the sensors. They were installed in orientations of $\pm 45^\circ$ relative to the beamtelescope and laboratory ground in the way like it can be seen in figure 9.13.
Table 9.2 gives a survey on the tested sensors, including the irradiated sensors of 2007. The table shows the fractions of the neutrons and protons of the total fluence, the according radius at the tracker for this fluence, the measured full depletion voltage according to the CV-curves or, if this measurement was problematic the estimated ones, the test temperature and the comparison of the measured currents

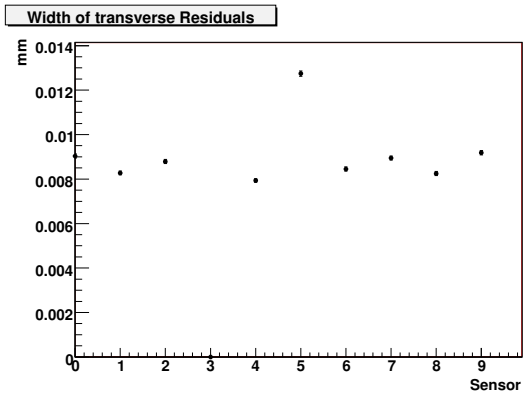

(a)

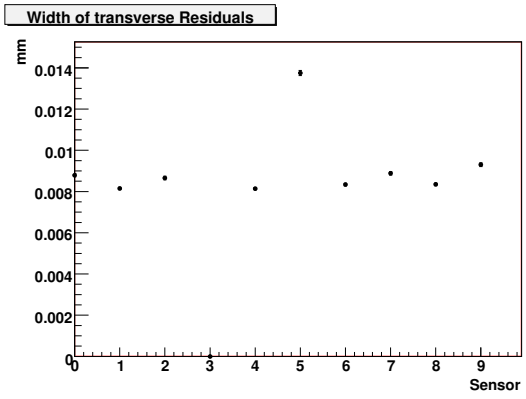

(b)

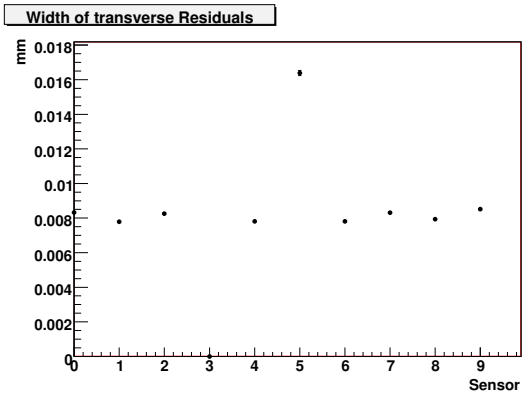

(c)

Figure 9.12: ***Measured spatial resolution of the tested sensors and the beamtelescope sensors.*** *a) Reference Sensor b) Sensor, irradiated with* $1 \cdot 10^{14}$ *neq./cm*^{2} *c) Sensor, irradiated with* $5 \cdot 10^{14}$ *neq./cm*^{2} *The results have to be handled with some care, as the software most probably can not find a perfect alignment if the sensors are marginally twisted. The resolutions have to be regarded as upper limits, which are still satisfactory.*

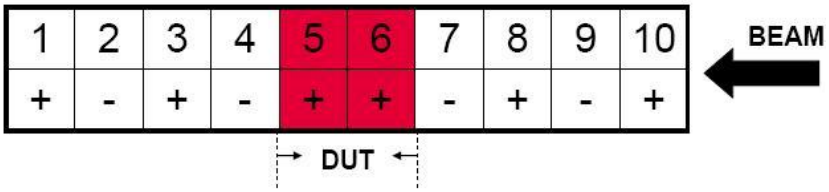

Figure 9.13: ***Module orientation in the beamtelescope***

	n017A	n224A	MCz0802B	MCz0802A	MCz0804B
beamtest	2007	2007	2008	2008	2008
fluence in $neq./cm^2$	$1 \cdot 10^{14}$	$5 \cdot 10^{14}$	$5.8 \cdot 10^{14}$	$1.1 \cdot 10^{15}$	$1.1 \cdot 10^{16}$
protons in % / neutrons in %	100 / 0	100 / 0	84 / 16	91 / 9	94 /6
radius	$> 60\ cm$	$\approx 55\ cm$	$\approx 45\ cm$	$\approx 17.5\ cm$	$\approx 15\ cm$
full depletion voltage in V	200	380	420	870 (e)	1300 (e)
test temperature	0°C	-10°C	-10°C	-10°C	-10°C
theo. current in μA	399	690	788	1210	1380
error theo. current in %	60	63	63.3	70.3	64.5
meas. current in μA	650	471	722	1200	1790
current diff. in %	62.9	-31.8	-8.4	-0.4	30.4
reference voltage in V	200	460	625	550	380

Table 9.1: ***Table of properties and test conditions of the tested irradiated sensors.****The table shows the fractions of the neutrons and protons of the total fluence, the according radius at the tracker for this fluence, the measured full depletion voltage according to the CV-curves or, if this measurement was problematic the estimated ones, the test temperature and the comparison of the measured currents and the theoretically expected ones together with the calculated errors.*

and the theoretically expected ones together with the calculated errors. According to formula (4.22) the current increase at a given temperature in a depleted volume V is proportional to the equivalent fluence. For silicon at 20°C , the value of the proportional factor α is $(3.99 \pm 0.03) \cdot 10^{-17}\ A/cm$ [Mol99] after a heat treatment at 60°C for 80 minutes, which corresponds to roughly two weeks annealing at room temperature (compare table 4.2). Although a controlled annealing was not foreseen for the tested sensors, the overall time that they were kept at room temperature is comparable to the standard time so that the introduced value of the current related damage rate α should be sufficient to give a rough estimate of the expected current at 20°C , especially as observations are reported that concerning α no difference between MCz and FZ silicon can be seen [RD507]. Using formula (4.22) one can calculate the expected currents at the measurement temperatures and compare them with the measurement results. The error of this calculation is big. This is mainly due to the uncertainties in the irradiation fluences and in the measurement temperatures. The active volume is also not perfectly known, especially in cases of not fully depleted sensors. When the IV curve has a steep slope after full depletion, an additional error appears due to the significantly different currents of the possible reference voltages. Further, some authors suggest a modification of E_g in formula (8.2) (or better to say the characteristic energy in that formula) from 1.12 eV to 1.21 eV [H^+00] or even 1.26 eV [A^+99] to account for trapping after irradiation. Table 9.2 in the appendix compares the expected currents with the measured currents in the beamtest. For the chosen reference voltage, the current of sensor n017A is higher than expected. The strong increase of the current after depletion, resulting in a bad IV behavior might explain the discrepancy, as the influence of the reference voltage is significant. The currents lay within the error ranges. Despite the big uncertainties, it can be concluded that formula 4.22 estimates the magnitudes of the currents after irradiation sufficiently well.

9.2.1 Thermal Runaway Problem

Low humidity in the SiBT was achieved via a nitrogen gas flow. The mean atmosphere temperature near the sensors was around -6.6°C, so that it can be estimated that the sensor temperature was around -8°C. The leakage currents of the irradiated sensors were still high at this temperature and lead finally

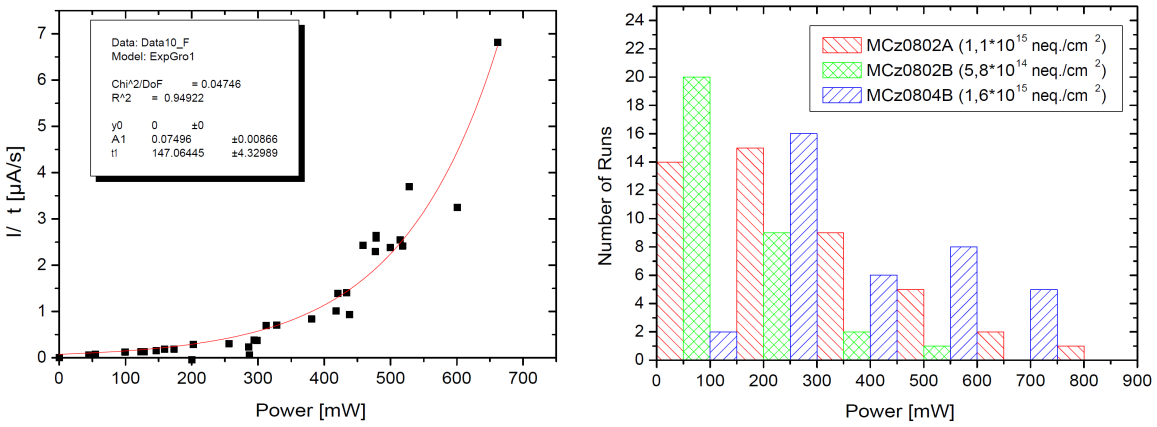

(a) (b)

Figure 9.14: ***Thermal runaway problem.*** *a) Total leakage current increase plotted against the start heating power b) Histogram of the start heating power. Runs with a start heating power higher than* 300 *mW are affected by thermal runaways.*

to thermal runaways for the highest irradiated sensors, due to an insufficient cooling performance in the setup. Out of that reason, data taking with a sensor irradiated with a total neutron equivalent fluence of $1.6 \cdot 10^{15}/cm^2$ was not possible at the high voltages necessary for its full depletion. Even if a thermal runaway appears, the conditions at the start of a measurement run reflect nevertheless the aspired ones, as the negative influence of the thermal runaway is still negligible. The analysis of the data of the begin of a run should therefore deliver reasonable approximations for the values of stable conditions. By a more efficient cooling of a setup with a better heat transport, thermal runaways can be inhibited and stable conditions can be achieved.

One may ask which criterium separates the runs into stable ones or into ones to incur thermal runaways. A hint is given, if one takes the data of all sensors and all runs that lasted roughly the same given time period and plots the mean current increase versus the heating power $U \cdot I$ at the start of the according run (figure 9.14(a)). The comparable time span between the start and the end of the runs ensures a similar heating period, so that the influence of the starting conditions becomes apparent. It can be seen that for runs with a heating power less than about 300 mW the current increase is negligible. A separation criterium is found thereby. An exponential growth can be fitted at the curve and expresses why for higher power values the current increase becomes considerably stronger. Therefore the picture of a thermal runaway problem gets substantiated. The histogram of the start heating power of all taken runs of all tested sensors (figure 9.14(b)), clearly shows, that for the lowest irradiated sensor MCz0802B only three runs exceed the 300 mW limit, exactly the ones that show the highest current increase. On the contrary this number is much higher for the higher irradiated sensors. Consequently data taking was problematic with these sensors, in the way, that either establishing a full depletion was impossible when the current limit of the power supply was reached, or in the way that the measurement data at the start of the run differ from the ones taken at the end because of the higher current and the higher noise. Therefore an error occurs.

In general, about 30000 to 50000 trigger events with complete readouts of all channels were taken per run and saved in several files of bundles of 10000 events. This offers an easy option to analyze the effect of the increasing current by separately analyzing the different files. The influence of the increased currents on the noise, on the charge collection, on the signal to noise and on the resolution

of the sensor can be explored with this. In any application of silicon sensors, a thermal runaway must be excluded.
Under guaranteed stable conditions in the application of sensors irradiated with the explored fluences at the presented temperatures, one should be faced with the currents measured at the begin of a run. This argument is underlined by the fact that these currents match the theoretically expected values (table 9.2). Therefore only the first data file has been considered in the further analysis, so that the following results are based on conditions closely to the aspired ones.
The module MCz0804B, irradiated with a fluence of $1.6 \cdot 10^{15}$ $neq./cm^2$ of protons (94%) and neutrons (6%), referring to a radius of 15 *cm* in the tracker, which is already in the pixel region, had also been tested. Because of the fact, that for almost all runs and even for low voltages the heating power was higher than 300 *mW* (figures 9.14(a) and 9.14(b)), thermal runaways occurred far below reaching a full depletion of the sensor. Therefore it was abstained from further and deeper analysis of the testbeam data of this module. Instead, the module was tested in the Karlsruhe module test station at deeper temperatures and higher voltages. The results will be presented in chapter 10.

9.2.2 Noise and the Consequences of Noise Cuts

Noise of the MCz Module irradiated with a Fluence of $5.8 \cdot 10^{14}$ $neq./cm^2$

The MCz sensor with the naming MCz0802B was mixed irradiated with protons (84%) and neutrons (16%) with a total equivalent fluence of $5.8 \cdot 10^{14}$ $neq./cm^2$, which is 16 % more than for the highest irradiated and tested sensor in 2007. This gives a chance for a comparison with a sensor irradiated only with protons. The fluence is expected at a radius of about 43 *cm*. The analysis of the beamtest data of this module shows, that some problematic regions of channels existed, together with some single noisy channels. Figure 9.15(a) and the belonging histogram 9.15(b) illustrate this, using the example of a run with 550 *V* bias voltage, with which full depletion of the sensor was already achieved and which was one of the highest applied voltages. Comparable pictures exist for runs with lower voltages. Beside some single noisy strips, a few regions with quite low noise values of around 0.5 *ADC* existed. As the majority of channels showed reasonable noise values of around 1.4 *ADC*, which is comparable to the observed values of working strips of the 2007 sensors, these lower regions were regarded as being defect, which turned out to be correct. Therefore some cut limits were defined, so that channels with noise values less than a lower limit and more than an upper limit were disregarded in the data analysis of cluster finding and tracking. Also cluster seeds with defect neighbor strips were not considered any further. For this sensor, the lower limit was set to 1 *ADC* and the upper limit to 1.6 *ADC* for all runs and all voltages. This step sorted out 237 strips, so that the number of 531 remaining channels was still high and the designated sensor parameters could be measured.
The definition of the general noise level of a run needs some care, as the cut method sets limits on it. Only the used strips are of interest for the SNR values. Thereby the question arises, whether the method selects mainly the same channels in all voltage steps, or whether the noises of the channels differ that much from voltage to voltage, that the used channels do not mainly remain the same ones over the whole range. To clarify this, the voltage dependent noise development of the strips used at the lowest voltage was compared with the according development of the noise determined by the channels chosen from run to run. The general noise was defined by the most probable value of a Gauss curve fitted at the noise distribution of all considered strips. The comparison of the results can be seen in the figure 9.16(a). It is obvious in figure 9.16(b) that there is no difference in the results, so that in the further analysis the noise of the selected and active channels of each run was considered. Further

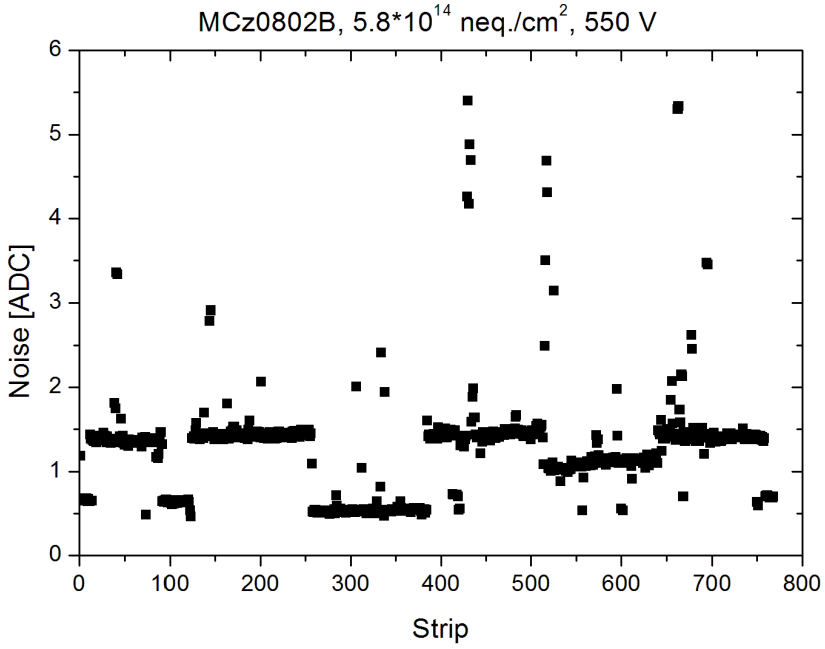

(a)

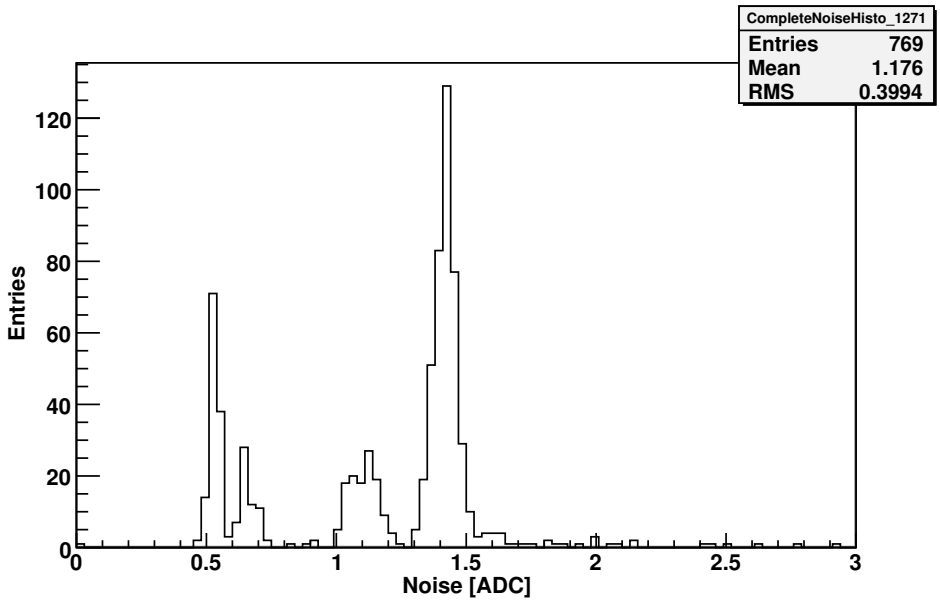

(b)

Figure 9.15: ***Noise of the module MCz0802B, irradiated with*** $5.8 \cdot 10^{14}$ *neq./cm*^{2}***, at 550 V.*** *a) Channel noise b) Noise histogram. Beside some single noisy strips, a few problematic regions with quite low noise values of around* 0.5 *ADC existed. Both were excluded of the analysis, as they did not deliver useful data.*

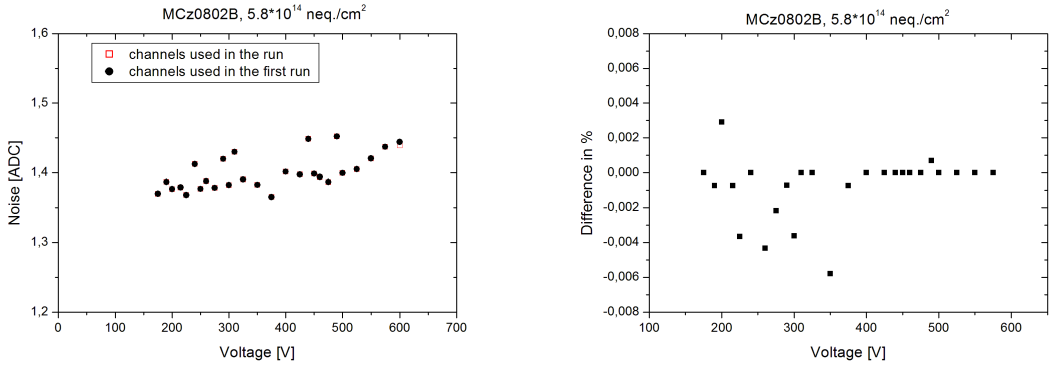

(a) (b)

Figure 9.16: ***Comparison of the noise evolution of the strips used at the lowest voltage with the noise determined by the channels chosen from run to run.*** *a) Direct comparison b) Difference in percent. No significant difference existed, so that the selected channels at the lowest voltage were used in all runs.*

results of the noise analysis and a comparison between the measured values and the theoretically expected ones can be found in [Neu09].

The test conditions for this sensor MCz0802B concerning the temperature and possible thermal runaways were regarded as having remained stable, as the mean current increase by a sensor temperature rise during data taking at a given voltage was only 8.7 %, so that only a minor noticeable effect on the noise existed.

Noise of the MCz Module irradiated with a Fluence of $1.1 \cdot 10^{15}$ $neq./cm^2$

At the radius of 20 cm in the tracker, one expects a fluence of $1.19 \cdot 10^{15}$ $neq./cm^2$. To test the sensor performance after such a high irradiation, the sensor MCz0802A was irradiated accordingly ($1.1 \cdot 10^{15}$ $neq./cm^2$), with a neutron fraction of 9% and a proton fraction of 91%. Also this module possessed some problematic strip or channel regions like it can be seen in the case of a run with a bias voltage of 475 V in figure 9.17(a) and 9.17(b). Although the sensor could not be fully depleted in the whole test, so that some noisy strips had to be expected, it could already be seen throughout all voltage steps, that regions of ”dead” channels existed, which showed much too low noise values. To work only with the channels of the reasonable noise value region of around 1.5 ADC, referring to the third peak in the histogram 9.17(b), the lower cut limit was set to one and the higher to two. 414 of the total 768 channels showed noise values inside the limits, so that still a high and sufficient number of channels were used for the further analysis.

One important fraction of the noise has its origin in the leakage current (see chapter 5.3). The current data of this sensor show, that not only the current level was high due to the radiation damages of the high fluence, but that also the current did not remain constant during a run and increased in one case up to 240 % percent, indicating a thermal runaway. The necessity of the approach to only use the first 10000 events of a run in the case of a thermal runaway problem can be seen in figure 9.18. It shows a comparison of the voltage dependant evolution of the mean noise calculated from the first file with the one calculated from the last file of the sensor MCz0802A. The mean noise is defined by the most probable value of a Gauss fit to the resulting strip noise histogram after the cut method. It

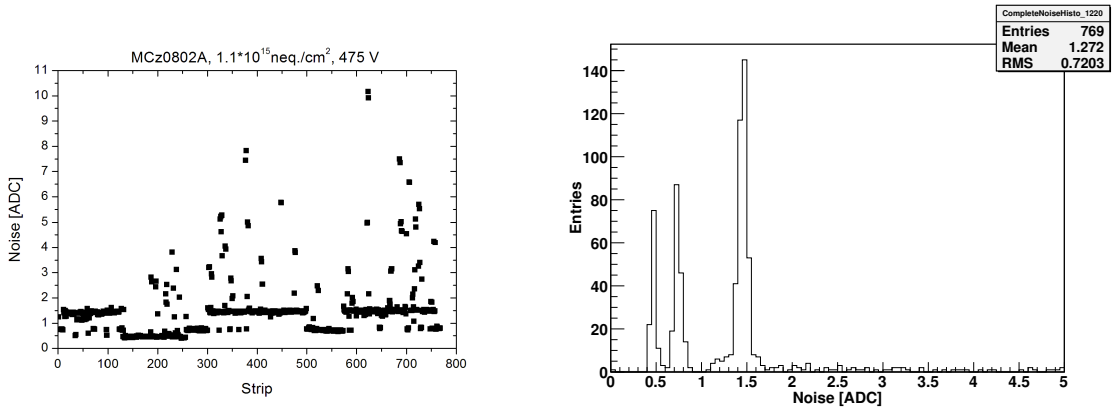

(a) (b)

Figure 9.17: ***Noise of the module MCz0802A, irradiated with*** $1.1 \cdot 10^{15}$ *neq./cm*^{2}***, at 475 V.*** *a) Channel noise b) Noise histogram. Also this sensor showed defect and noisy channels. They were excluded in the analysis.*

is obvious, that for higher bias voltages the discrepancy between the results from the first file and the ones from the last file becomes larger, reaching more than 26 % at the highest test voltage. This rise is again explainable by a discussion like the one above for figure 9.14(a). For lower voltages the heating power was too low to lead to an effect. The plot 9.18 also shows, that even for the first file there is an increase of the noise with the applied bias voltage of up to 17 % between the lowest test voltage of 275 *V* and the highest test voltage of 550 *V*.

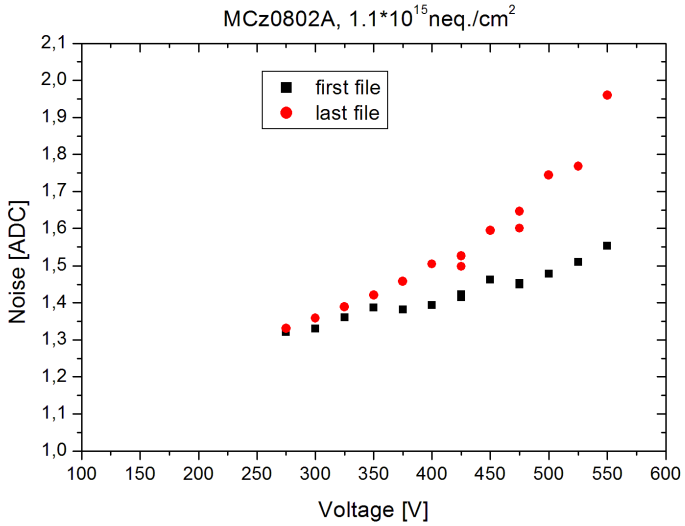

Figure 9.18: ***Impact of thermal runaways on the noise.*** *The black quadratic dots show the mean noise calculated out of the first 10000 events of the run, while the red circular ones show the noise of the last 10000 events of around 50000 per run in average. The noise increases by the increased leakage currents which result of thermal runaways.*

Noise of two FZ modules

Two modules build with very high resistive float zone silicon sensors were also tested in the beamtest. One of them was irradiated with a fluence of $2.2 \cdot 10^{14}$ $neq./cm^2$ of protons, while a non-irradiated one served as a reference module. Both modules were not affected by strip regions of problematic noise (figures 9.19(a) and 9.19(b)). Only some single strips were sorted out by the noise cut method with a lower limit of 1.0 *ADC* and an upper limit of 1.4 *ADC*. The evolution of the mean noise of the used strips can be found in figures 9.20(a) and 9.20(b). Higher bias voltages lead to a reduction of the noise and no thermal runaway appeared.

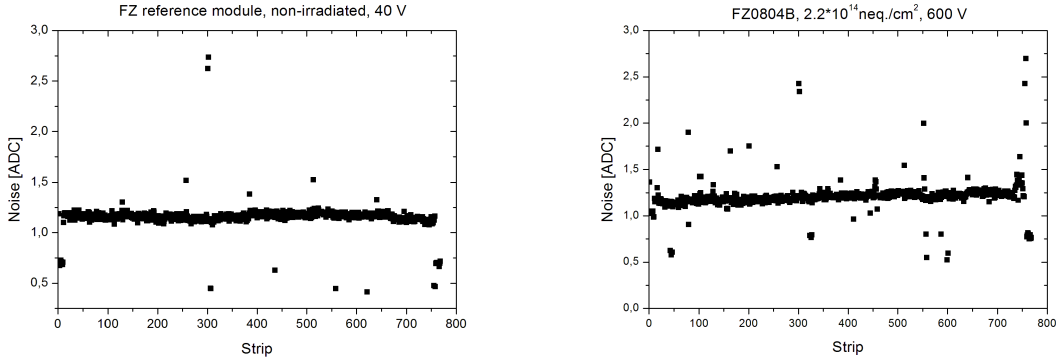

(a) (b)

Figure 9.19: ***Channel noise of the FZ modules.*** *a) Channel noise of the reference module at* 40 V. *b) Channel noise of the FZ module irradiated with* $2.2 \cdot 10^{14}$ $neq./cm^2$ *at* 600 V.

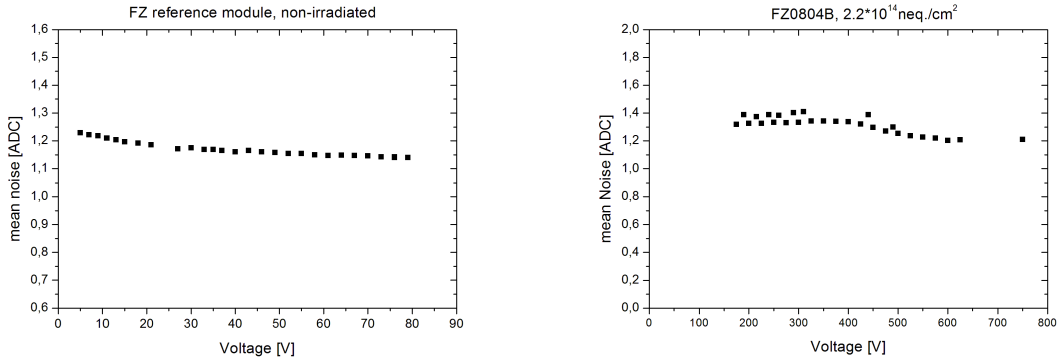

(a) (b)

Figure 9.20: ***Mean noise of the FZ modules.*** *a) Reference module. b) Module irradiated with* $2.2 \cdot 10^{14}$ $neq./cm^2$.

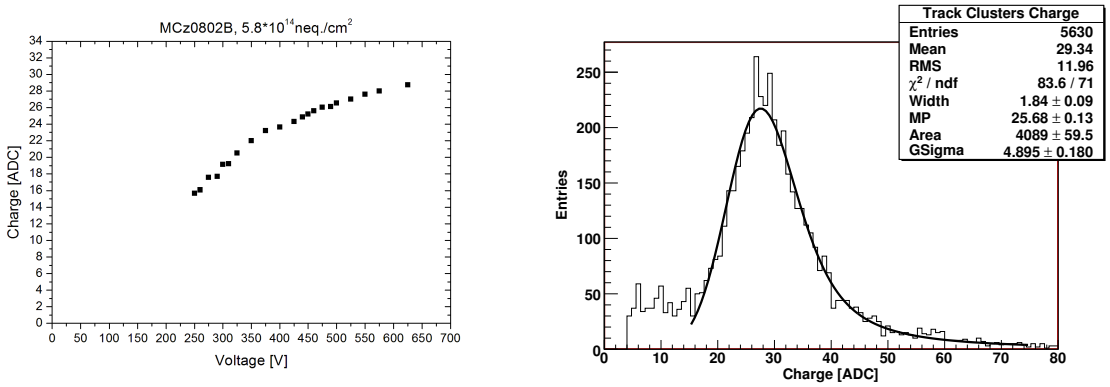

(a) (b)

Figure 9.21: ***Track cluster charge of the sensor MCz0802B irradiated with*** $5.8 \cdot 10^{14}$ $neq./cm^2$**.** *a) Evolution of the track cluster charge with the bias voltage. b) Histogram of a run with* 550 V *bias voltage. The most probable value of a Landau-Gauss fit at the distribution defines the collected charge for this run.*

9.2.3 Charge Collection

The sensor MCz0802B ($5.8 \cdot 10^{14}$ $neq./cm^2$) was tested with bias voltages between 150 V and 625 V. The collected charge of clusters that had been allocated to tracks of traversing particles is plotted against the bias voltage in figure 9.21(a). The slope of the curve is decreasing and seems to aim asymptotically at a line at 30 ADC. At the highest test voltage of 625 V the highest signal is seen with the value 28.7 ADC. This means, that the collected charge does not saturate after reaching the full depletion voltage (around 420 V), but that a minor increase is still visible. This is explained by a faster charge collection by the increased electrical field strength. Figure 9.21(b) presents the track cluster charge histogram of a run with a bias voltage of 550 V, exemplarily pointing out that a Landau-Gauss curve could be fitted at the distribution.

The histogram in figure 9.22(a) belongs to the module MCz0802A, irradiated with a fluence of $1.1 \cdot 10^{15}$ $neq./cm^2$ and a bias voltage of 475 V. This example shows again that Landau-Gauss curves could be fitted at the distributions of the different runs. Figure 9.22(b) shows the evolution of the charge collection with the applied bias voltage. No decreased slope of the curve appears, so that it confirms that the full depletion voltage, estimated to be around 870 V was not reached during the test and a signal increase has still to be expected for higher bias voltages.

Surprisingly, despite the expected low full depletion voltage of around 8 V, the collected charge of the track clusters of the FZ reference module (figure 9.23(a)) does not show an early and clear saturation in the bias voltage range of $0-73$ V. The curve shows a kink around 30 V to 40 V and a lower slope afterwards, which is nevertheless far above the full depletion voltage. Such a kink also exists in the analogous plot of the irradiated FZ sensor at a voltage between 400 V and 500 V. The sensor was tested with bias voltages of up to 750 V. Even after the kink, an increase of the collected charge can be seen in figure 9.23(b), but with a lower slope. If one takes the highest measured charge at 750 V of 33.9 ADC and compares it with the highest one of the FZ reference module, the FZ detector irradiated with a fluence of $2.2 \cdot 10^{14}$ $neq./cm^2$ still provides a signal of 88.3 % of the reference one. Examples of the track cluster charge distributions with appropriate Landau-Gauss fits can be found in figure 9.24(a) (FZ reference, 70 V) and in figure 9.24(b) (FZ0804B, $2.2 \cdot 10^{14}$ $neq./cm^2$, 750 V).

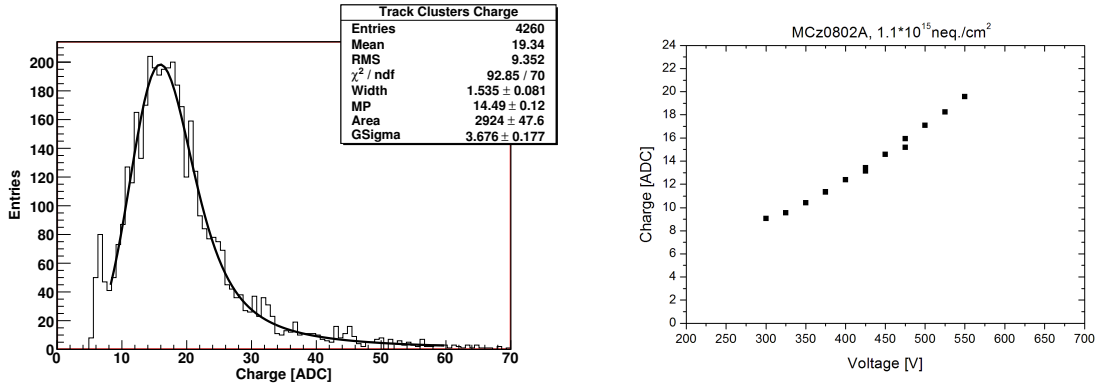

(a) (b)

Figure 9.22: ***Track cluster charge of the sensor MCz0802A irradiated with*** $1.1 \cdot 10^{15}$ *neq./cm*^{2}***.*** *a) Histogram of a run with* 475 *V bias voltage. The most probable value of a Landau-Gauss fit at the distribution defines the collected charge for this run. b) Evolution of the track cluster charge with the bias voltage.*

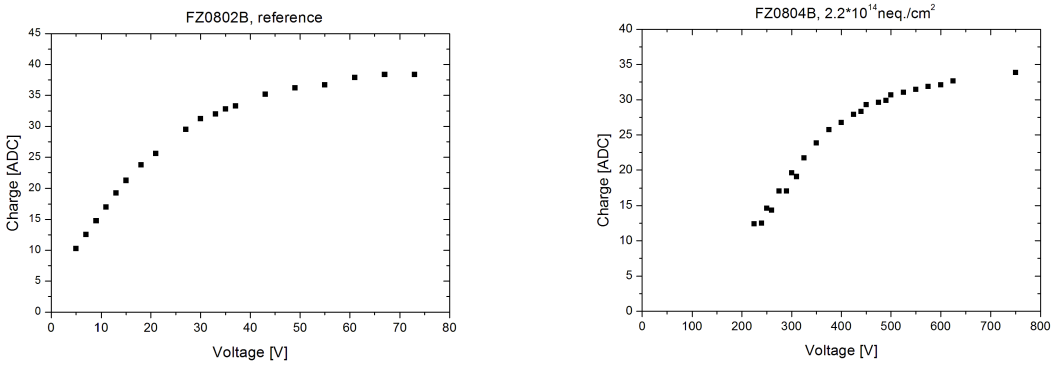

(a) (b)

Figure 9.23: ***Track cluster charge of the FZ sensors plotted against the bias voltage.*** *a) Non-irradiated FZ module. The saturation does not occur at the expected full depletion voltage of* 8 *V, but at higher values. b) FZ module, irradiated with* $2.2 \cdot 10^{14}$ *neq./cm*^{2}*. According to the bend in the curve, the full depletion voltage can be expected at around* 500 *V. The sensor still provides a signal of 88.3% of the reference one.*

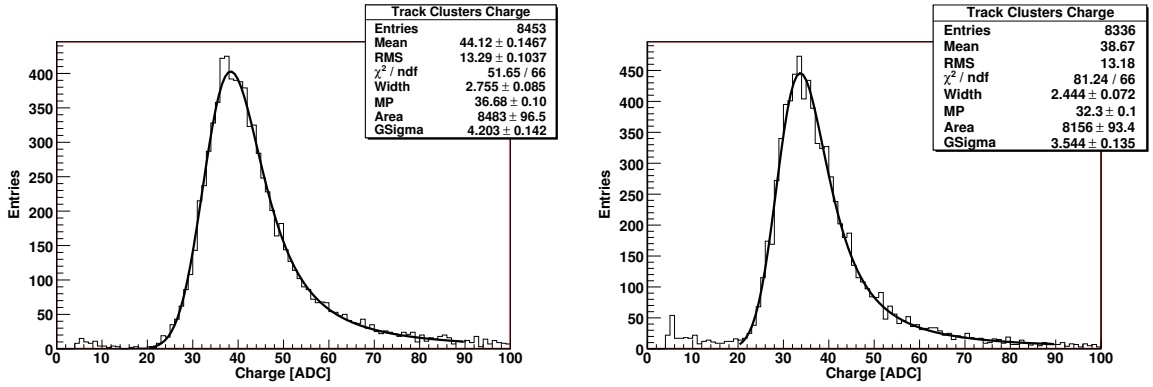

(a) (b)

Figure 9.24: ***Track cluster charge histograms of the FZ sensors.*** *a) Non-irradiated FZ module, bias voltage* 70 V. *b) FZ module, irradiated with* $2.2 \cdot 10^{14}$ $neq./cm^2$, *bias voltage* 750 V. *The Landau-Gauss curves fit very well the distributions.*

9.2.4 Signal to Noise Ratios

The signal to noise ratios of the sensor MCz0802B, irradiated with $5.8 \cdot 10^{14}$ $neq./cm^2$, do not clearly show a saturation with an increasing bias voltage, but a bend towards a lower slope aiming at a saturation in the region around the expected full depletion voltage of 425 V. The SNRs reach values slightly higher than 19 (figure 9.25(a)). The highest applied voltage of 625 V leads to a SNR of 19.4. A histogram of the measured SNRs of a run with a bias voltage of 550 V is displayed in figure 9.25(b).

It is hardly surprising that no saturation of the SNRs of the higher irradiated module MCz0802A ($1.1 \cdot 10^{15}$ $neq./cm^2$) exists, as the maximally applied bias voltage was lower than the full depletion voltage. For the highest applied voltage of 575 V a SNR of 12.6 was achieved, which is in spite of the non full depletion of the sensor a satisfactory and sufficiently high value. All of the presented results are defined by most probable values of Landau-Gauss fits at the corresponding data histograms, like exemplarily shown in figure 9.26(b) for a run with a bias voltage of 475 V. As well as the collected charge, the SNR of the non-irradiated FZ reference module does not show a clear saturation in the test voltage range, as it is apparent in figure 9.27(a). The maximal measured ratio is slightly lower than the one of the MCz reference module. As well as in the curve for the collected charge, a bend around 30 V to 40 V is visible. According to the plot in figure 9.27(b), the signal to noise ratio of the irradiated FZ module ($2.2 \cdot 10^{14}$ $neq./cm^2$) seems to reach a saturation within the test range around 700 V. This SNR lies roughly at 28. Figure 9.28(a) presents a SNR histogram of the FZ reference module at a run of 70 V and figure 9.28(b) shows one for the irradiated FZ module at a bias voltage of 750 V.

9.2.5 Resolution

The pitch of the explored test sensors is 50 μm. Therefore one calculates a binary resolution of 14.4 μm. The resolutions were determined by the width of the residual distributions, according to the definition given in chapter 7.3. For the module MCz0802B ($5.8 \cdot 10^{14}$ $neq./cm^2$) the distribution with a Gauss fit for a run at 525 V is exemplarily shown in figure 9.29. The measured values in figure 9.30(a) are persistently lower than the binary resolution, so that the resolution is even better. Coming

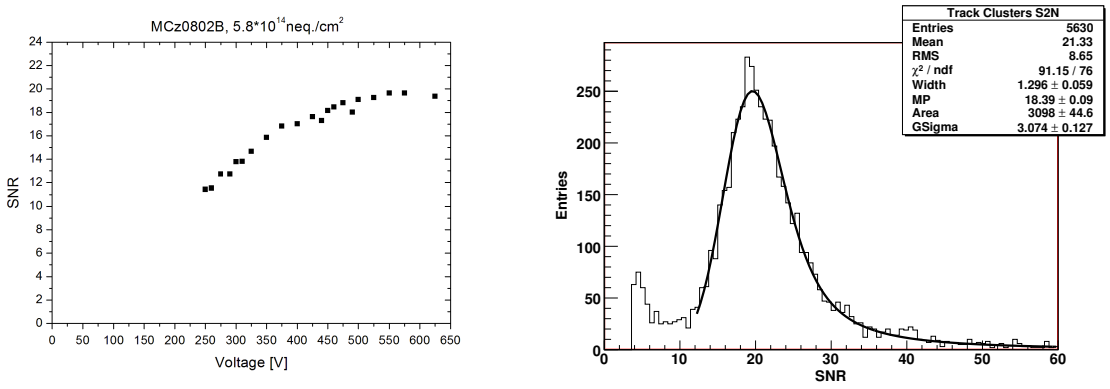

(a) (b)

Figure 9.25: ***Signal to noise ratios of the sensor MCz0802B irradiated with*** $5.8 \cdot 10^{14}$ *neq./cm*^{2}**.** *a) Evolution of the signal to noise ratios with the bias voltage. A bend towards a saturation value of 19 can be seen. b) Example of a histogram of the measured SNRs with a Landau-Gauss fit of a run with* 550 *V bias voltage*

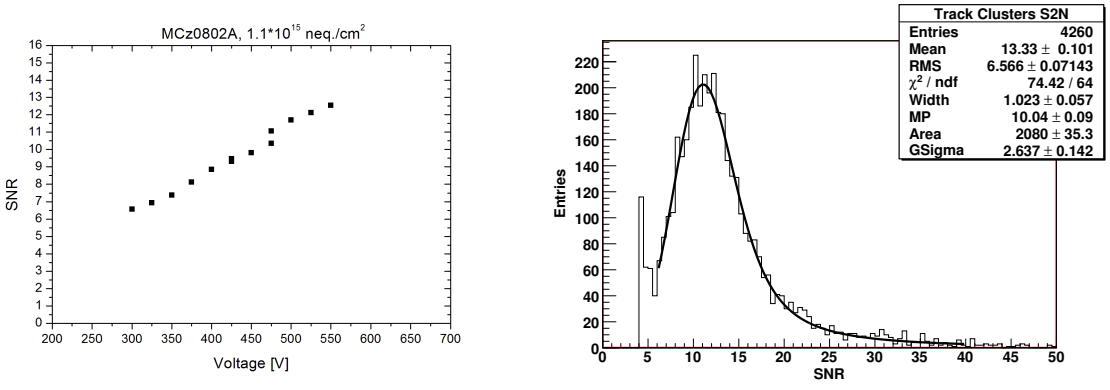

(a) (b)

Figure 9.26: ***Signal to noise ratios of the sensor MCz0802A irradiated with*** $1.1 \cdot 10^{15}$ *neq./cm*^{2}**.** *a) Signal to noise ratios against the bias voltage. No bend exists as the full depletion was outside the test range. Nevertheless the measured SNR at the highest applied voltage was roughly 12.6. b) SNR histogram of a run with a bias voltage of* 475 *V*.

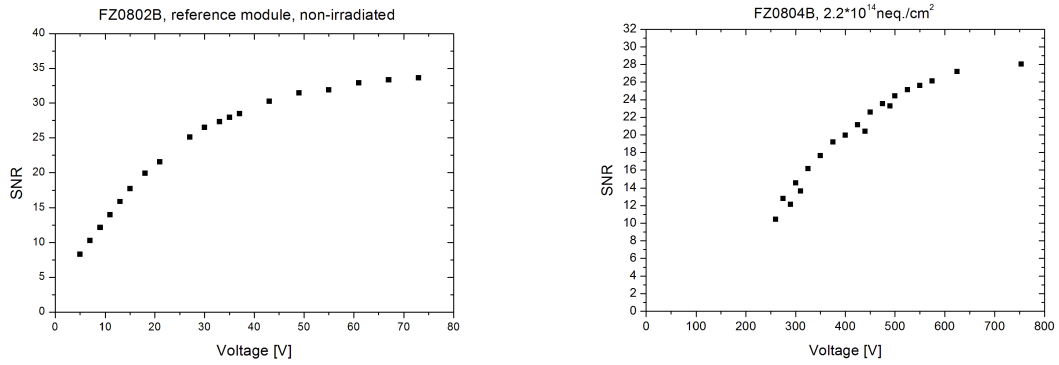

(a) (b)

Figure 9.27: ***Signal to noise ratios of the FZ modules against the bias voltage.*** *a) Non-irradiated FZ module. b) FZ module, irradiated with* $2.2 \cdot 10^{14}$ *neq./cm*^{2}.

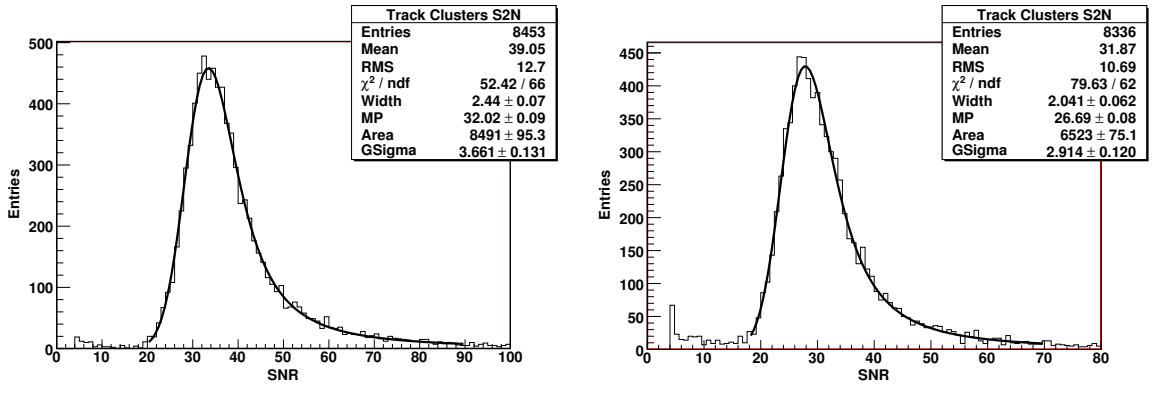

(a) (b)

Figure 9.28: ***Signal to noise ratio histograms of the FZ modules.*** *a) Non-irradiated FZ module,* $70\,V$*. b) FZ module, irradiated with* $2.2 \cdot 10^{14}$ *neq./cm*^{2}*,* $750\,V$.

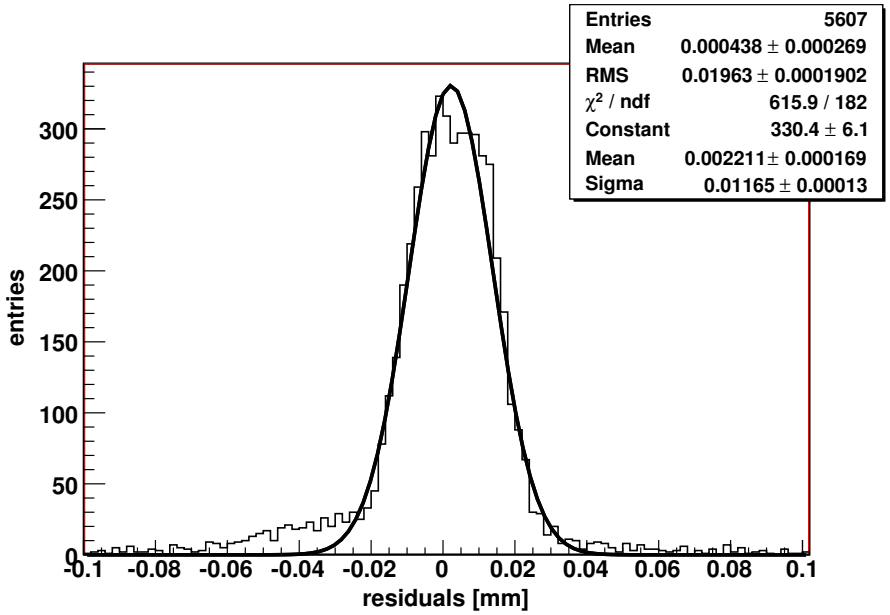

Figure 9.29: ***Residual distribution of the module MCz0802B, irradiated with*** $5.8 \cdot 10^{14}$ $neq./cm^2$***, at a run with*** 525 V ***bias voltage.***

from lower voltages, the resolution decreases slightly to a nearly constant value of roughly 11.5 μm with start at around 350 V. At this voltage the mean number of hit strips in a cluster (figure 9.30(b)) decreases from around 2.25 to 1.75 at the highest test voltage.

The measured resolution of the module MCz0802A ($1.1 \cdot 10^{15}$ $neq./cm^2$) is also sufficient, as it is better than the binary resolution of 14.4 μm throughout the applied voltages, with the best observed resolution of 12.8μm at the run with 525 V (see figure 9.31(a)). In this voltage range, the mean number of hit strips of the track clusters rose up to a saturation value of around 2 at the voltage of 450 V (figure 9.31(b)). The Gauss curves fit again quite well the residual distributions, which can be seen in figure 9.32 using the example of a run with a bias voltage of 525 V.

A residual distribution of the FZ reference module at a bias voltage of 37 V is given in figure 9.33. Looking at the resolution of this sensor, again the voltage range between 30 V and 40 V is important, as the resolution reaches its minimum and stays nearly constant at 9.5 μm (figure 9.34(a)), which is in accordance with the upper limit of 14.4 μm of the binary resolution. Shortly before this minimum is reached, the mean number of hit strips in a track cluster gets maximal with a value of 3 (figure 9.34(b)). Because of this total behavior one might guess, that the full depletion voltage lies around $30 - 40$ V, so that probably the resistivity of this sensor differs from the one of the specification. A similar behavior in the resolution and the mean number of hit strips in track clusters exists for the irradiated FZ sensor ($2.2 \cdot 10^{14}$ $neq./cm^2$) at higher voltages. Just before attaining at a minimum in the resolution (figure 9.36(a)), a maximum in the mean number of hit strips (figure 9.36(b)) is reached. The resolution increases slightly towards a saturation value of roughly 11 μm after the minimum of 8.7 μm at a voltage of 375 V, while the maximum mean number of hit strips is 3.2 at 300 V. The residual distribution of this sensor at the highest applied bias voltage of 750 V, shown in figure 9.35, points out exemplarily that also for this sensor good agreements with Gauss distributions could be found.

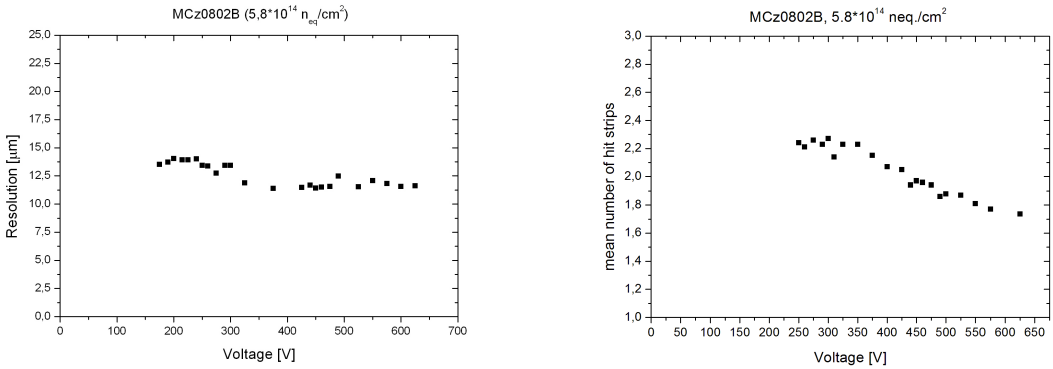

(a) (b)

Figure 9.30: ***Results of the sensor MCz0802B, irradiated with*** $5.8 \cdot 10^{14}$ *neq./cm*^{2}. *a) Resolution. The measured values are persistently lower than the binary resolution of* 14.4 *µm. b) Mean number of hit strips. The behavior is explainable by the changes in the electrical field configurations*

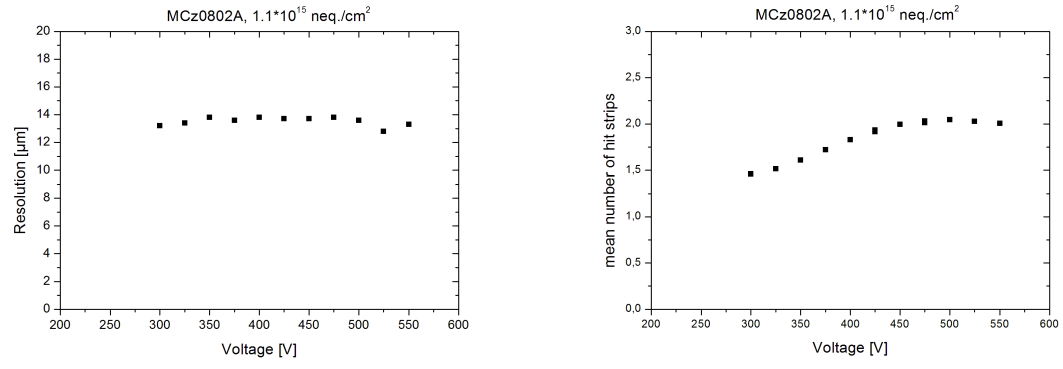

(a) (b)

Figure 9.31: ***Results of the sensor MCz0802A, irradiated with*** $1.1 \cdot 10^{15}$ *neq./cm*^{2}**.** *a) Resolution b) Mean number of hit strips. A similar behavior in the resolution and the mean number of hit strips like for the other sensors could not be completely seen, as the sensor could not be fully depleted.*

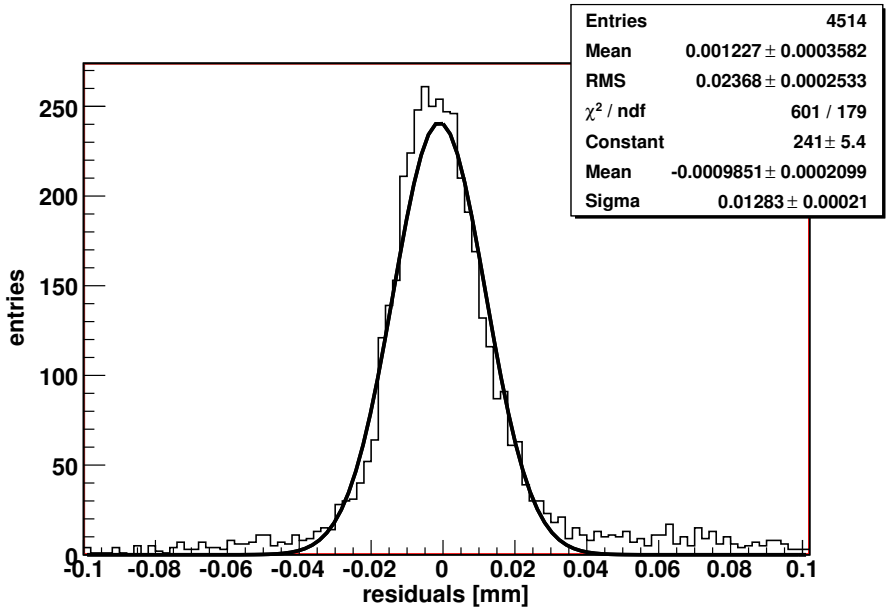

Figure 9.32: ***Residual distribution of the module MCz0802A, irradiated with*** $1.1 \cdot 10^{15}$ $neq./cm^2$***, at a run with*** 525 V ***bias voltage.***

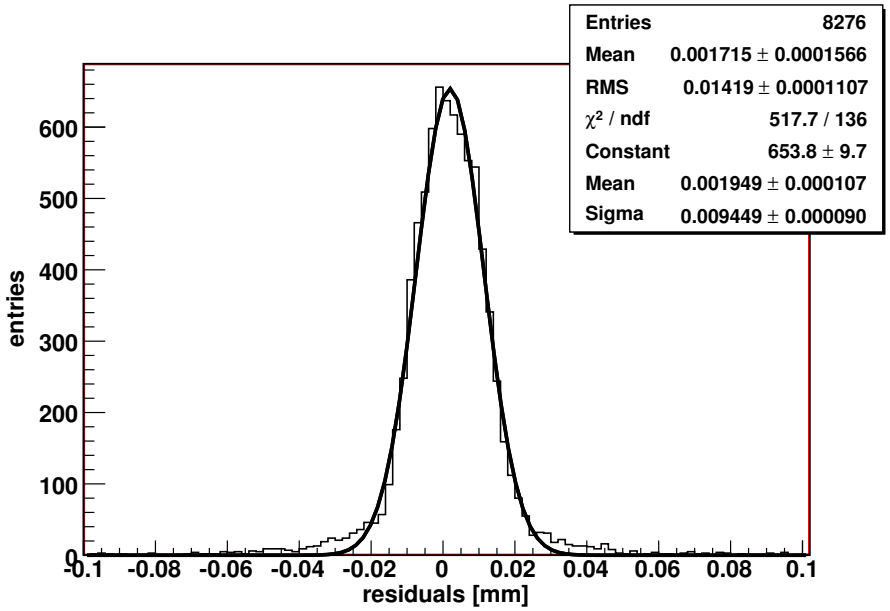

Figure 9.33: ***Residual distribution of the FZ reference module, at a run with*** 37 V ***bias voltage.***

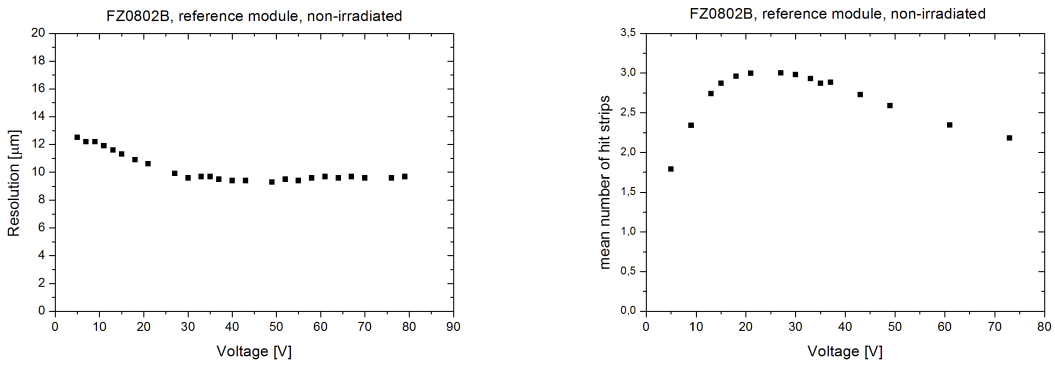

(a) (b)

Figure 9.34: ***Results of the FZ reference module.*** *a) Resolution. The resolution reaches its minimum between* 30 V *and* 40 V *and stays nearly constant at* 9.5 μm*. b) Mean number of hit strips. Shortly before the minimum in the resolution is reached, the mean number of hit strips in a track cluster gets maximal with a value of* 3*.*

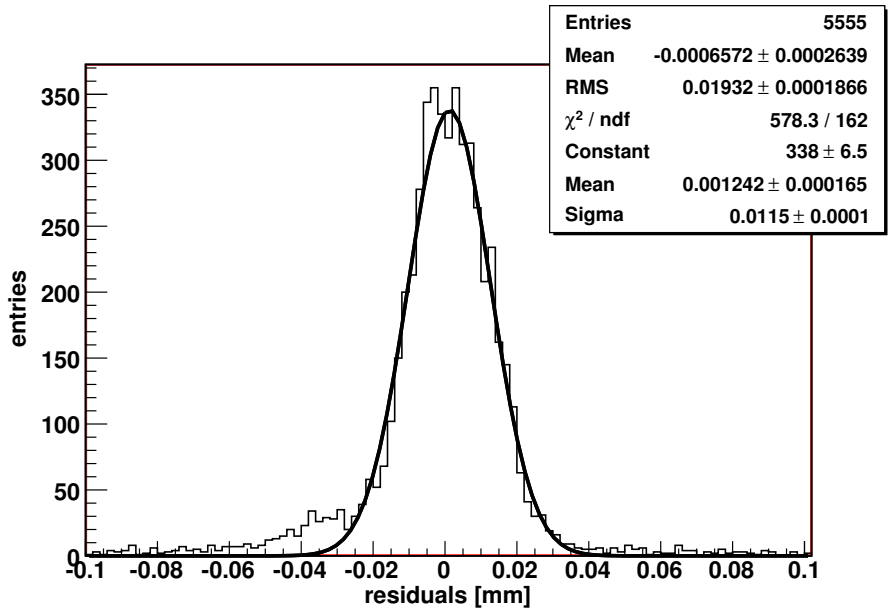

Figure 9.35: ***Residual distribution of the FZ sensor irradiated with*** $2.2 \cdot 10^{14}$ $neq./cm^2$***, at the highest applied bias voltage of*** 750 V**.**

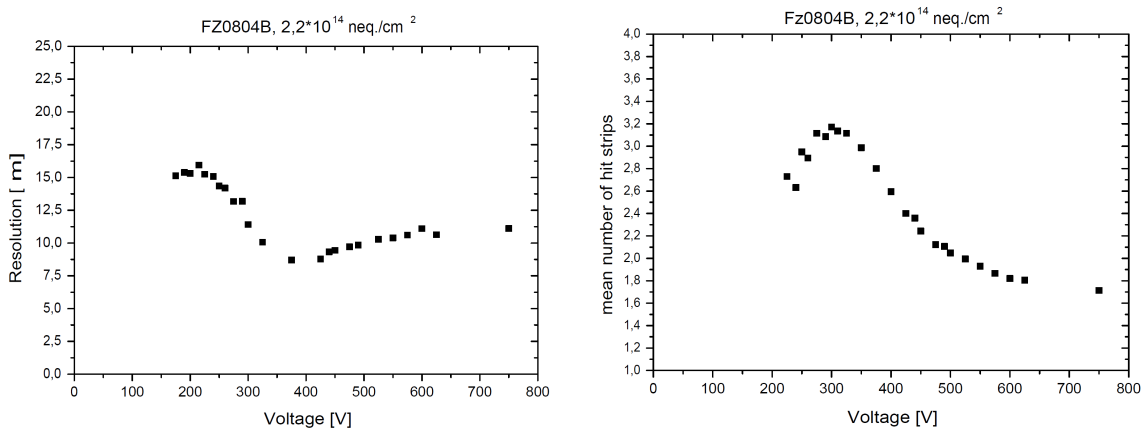

(a) (b)

Figure 9.36: ***Results of the FZ module, irradiated with*** $2.2 \cdot 10^{14}$ *neq./cm*^{2}**.** *a) Resolution. The resolution increases slightly towards a saturation value of roughly* 11 μm *after the minimum of* 8.7 μm *at a voltage of* 375 V*. b) Mean number of hit strips. The maximum mean number of hit strips is* 3.2 *at* 300 V*. The sensor shows a comparable behavior in these parameters like the lower irradiated MCz sensor. The shape of the curve should be explainable by the configuration of the electrical field.*

9.3 Comparison of the Results and Conclusion

Despite some problems with regions of noisy channels, the aspired physical sensor parameters could be measured for the majority of the tested detector modules. The cut method sorted out strips which are defect, not due to physical effects of changes in the sensor properties after irradiation, but due to technical problems in the production, not exceptional for test devices or prototypes. The remaining active channels deliver the information on the important sensor parameters of charge collection efficiency, signal to noise, noise and resolution, like presented above. The results for these attributes have to be compared with the accordant ones of non-irradiated reference sensors. For this, the 2007 results of the MCz reference module have been used, where a MIP produced a signal of 40.9 *ADC*. The most probable energy deposit of a MIP generates roughly 80 electron-hole pairs per μm in silicon [Mos09], so that for the used thickness of 300 μm, about 24000 pairs could be detected in fully depleted, non-irradiated silicon, where trapping is insignificant. This means, that one ADC approximately represents 587 electron-hole pairs. In figure 9.37 the measured signal, relative to the discussed reference signal of 40.9 *ADC*, is plotted against the bias voltage for all explored sensors. This allows to compare the charge collection efficiencies, if the one of the fully depleted reference sensor (around 350 V) is set to 100 %. It can be seen in figure 9.37, that for none of the irradiated sensors a saturation exists and that the collected charge increases with increasing bias voltage, albeit with a smaller slope after the expected full depletion voltage. Apparently the full depletion of the MCz sensor irradiated with the highest fluence of $1.1 \cdot 10^{15}$ *neq./cm*^{2} has not been reached, so that all results for this detector have to be regarded as lower limits for the ones to expect in an application under full depletion.
The maximal charge collection efficiency of the MCz module irradiated with $5.8 \cdot 10^{14}$ *neq./cm*^{2} under the given special conditions was 70 % and for the one irradiated with $1.1 \cdot 10^{15}$ *neq./cm*^{2} it was 48 %. The ongoing signal increase is a result of the increasing electrical field strength in the detector bulk, which stronger accelerates the generated charge carriers, so that they get collected faster and the

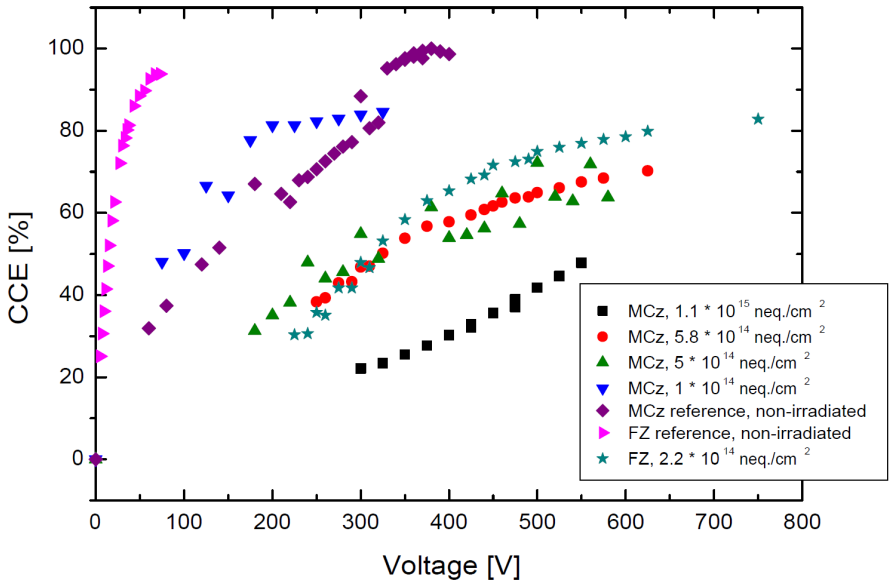

Figure 9.37: ***Charge collection efficiency of the tested sensors.*** *The collected charge of the fully depleted non-irradiated reference sensor defines 100%. The maximal collected charge of the MCz module irradiated with* $5.8 \cdot 10^{14}$ *neq./cm*^{2} *was 70 %. For the one irradiated with* $1.1 \cdot 10^{15}$ *neq./cm*^{2} *it was 48 %, despite a missing full depletion.*

chances for trapping get suppressed. Unfortunately this feature does not provide a higher signal to noise ratio, as it can be seen in figure 9.38. The values of nearly all sensors remain on their maximum level, as also the noise increases. Even the irradiated FZ sensor seems to have reached its maximum at the highest voltage. The only exception is the highest irradiated MCz sensor, which confirms again the evidence that it was not fully depleted during the test. Measurements with higher voltages and a further highly irradiated module were done in a teststation and will be presented in chapter 10.

The development of the electrical field configuration should explain the structure in the mean number of hit strips, where the values reach a maximum and decrease with higher voltages with a tendency to a saturation (figure 9.39). With an increasing voltage, more charge is collected, as the depleted volume gets bigger. Therefore the probability rises, that the charge is sufficient that not only the seed strips exceed the acceptance limit for a hit (4 σ), but that also neighbor strips get accepted (2 σ). In addition the not fully depleted volumes and the relatively low drift velocity in the depleted parts with low electrical field strength allow sideward diffusion of the charge carriers, so that the charge cloud gets broader. As this cloud contains more charge in the case of lower or non-irradiated sensors, because of the weaker trapping, more strips can exceed the cut limits so that the mean number of hit strips in the maximum is larger as in the ones for the higher irradiated sensors. A further increase of the voltage increases the accelerating electrical field, so that the time for the sideward diffusion becomes smaller and the mean number of hit strips decreases. This goes on asymptotically towards a saturation value, which should be dependent on the geometrical conditions of the sensor strips and the actual tracks of the traversing particles. When the electrical field configuration reaches its final ”shape” after the full depletion voltage, one should expect a saturation of the resolutions at lower values. At least for three of the 2008 sensors this can be supposed, like the survey plot 9.40 suggests. The sensor MCz0802A could not be fully depleted, so that this feature can not be seen there. Although the measured reso-

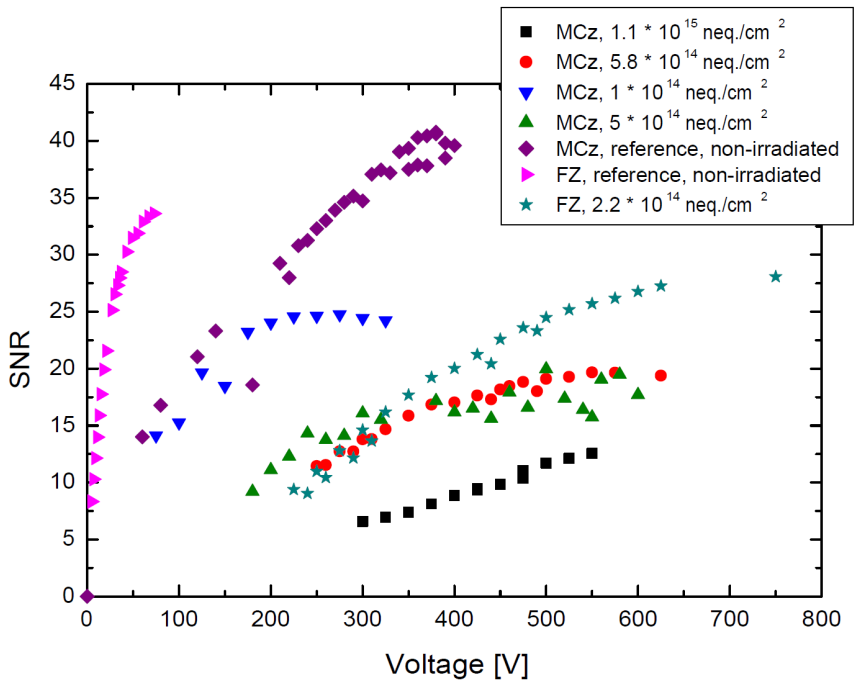

Figure 9.38: ***Comparison of the measured signal to noise ratios of all tested sensors.*** *The increase of the collected charge after the full depletion does not lead to higher SNRs as also the noise increases.*

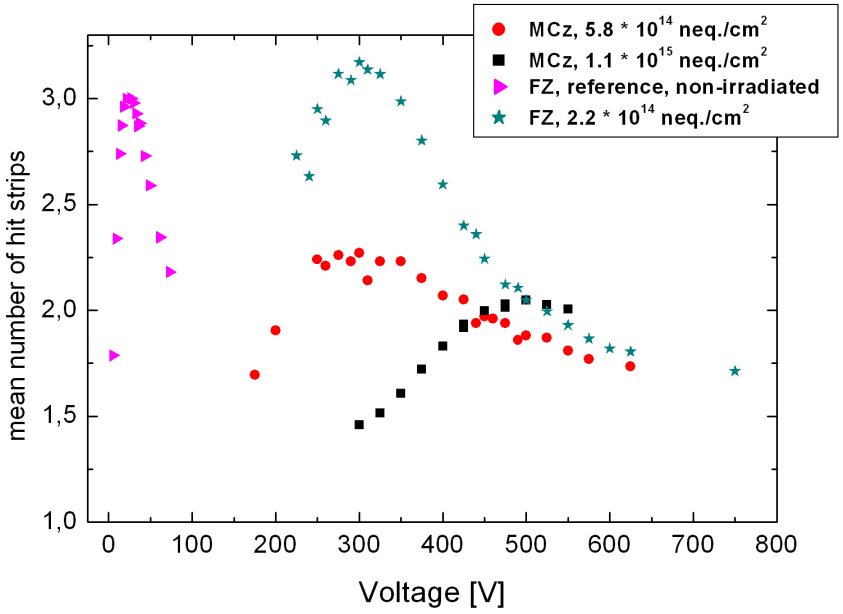

Figure 9.39: ***Mean number of hit strips of all tested sensors.*** *The development of the electrical field configuration should explain the structure in the mean number of hit strips.*

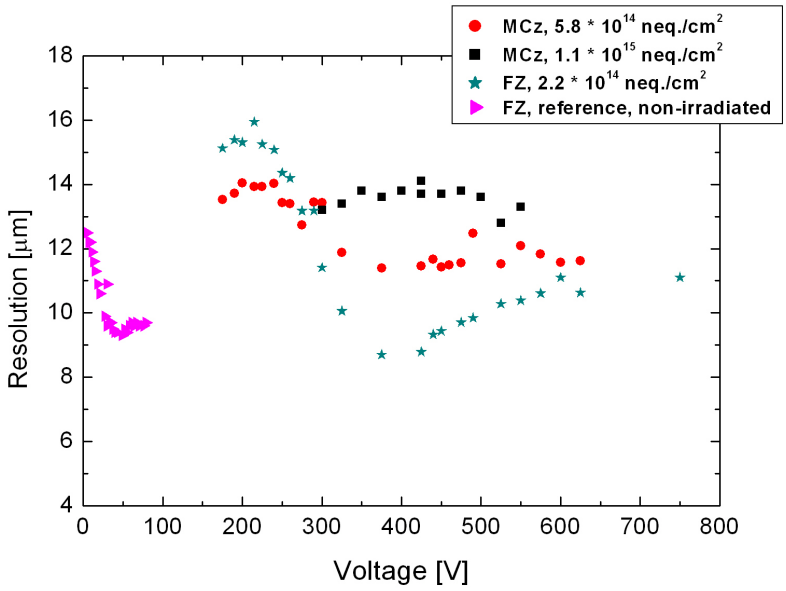

Figure 9.40: ***Resolution of all tested sensors*** *When the electrical field configuration reaches its final "shape" after the full depletion voltage, one should expect a saturation of the resolutions in the regions of their lowest values.*

lutions at these saturation conditions should be regarded as upper limits, the values are already that good to fulfill the requirements for the resolution of tracking detectors.
An appraisal of the beamtest and the following teststation results in the context with the needs and the possible consequences for an SLHC tracker will be presented in chapter 13.

Chapter 10

Module Investigations in the Karlsruhe Diagnostic Teststation

During the beamtest in 2008, described in chapter 9, not all sensors could be tested or could be tested under full depletion, because of thermal runaway problems. Therefore these modules were explored in the Karlsruhe Diagnostic Teststation [Dir03] with the usage of a ^{90}Sr source. In this station experiments at deep temperatures are possible in controlled laboratory conditions.
Two modules were explored. The module with the sensor irradiated up to $1.1 \cdot 10^{15}$ $neq./cm^2$ had already been used in the beamtest at around -8°C with voltages up to 550 V, but it could not be fully depleted. The highest irradiated module with a fluence of $1.6 \cdot 10^{15} neq./cm^2$ (MCz0804B) suffered of thermal runaways in the beamtest already at voltages far below the full depletion voltage, so that no significant data could be taken. Both modules were analyzed in the teststation with voltages up to 1000 V and temperatures between -30°C and -40°C . Tests at higher temperatures, especially around -10°C failed again because of thermal runaways. For comparison, also a non-irradiated CMS module was tested.

10.1 The Karlsruhe Diagnostic Teststation

The Karlsruhe Diagnostic Test Station was developed in the framework of the production and the quality testing of modules for the CMS tracker. Its flexible design and its comprehensive equipment does not only allow standard tests, but it also offers a wide range of non-standard testing possibilities for modules equipped with APV electronics.
A $100x70x70$ cm^3 big metal box with a light thermal isolation, houses connections for the modules to the readout electronics, a microscope for the possible work with probe needles and a controllable moving equipment with a carrier for specially designed LEDs, lasers or sources to be used as signal generators (photo 10.1). Further, two scintillators outside the box provide the possibility to trigger in coincidence on particles created by cosmic rays. The box can be flooded by dry air to avoid condensation, which is of importance when cold tests are accomplished. The standard cooling is done via Peltier elements inside a jig on which the modules can be fixed. Temperatures down to roughly -20°C are possible.
A further option for cooling with the possibility to reach even deeper temperatures, is realized by the usage of a small plexiglas box, in which the module can be installed and which can be flooded with very cold dry air. The dry air gets cooled down outside the box during its passage of a tube loop inside

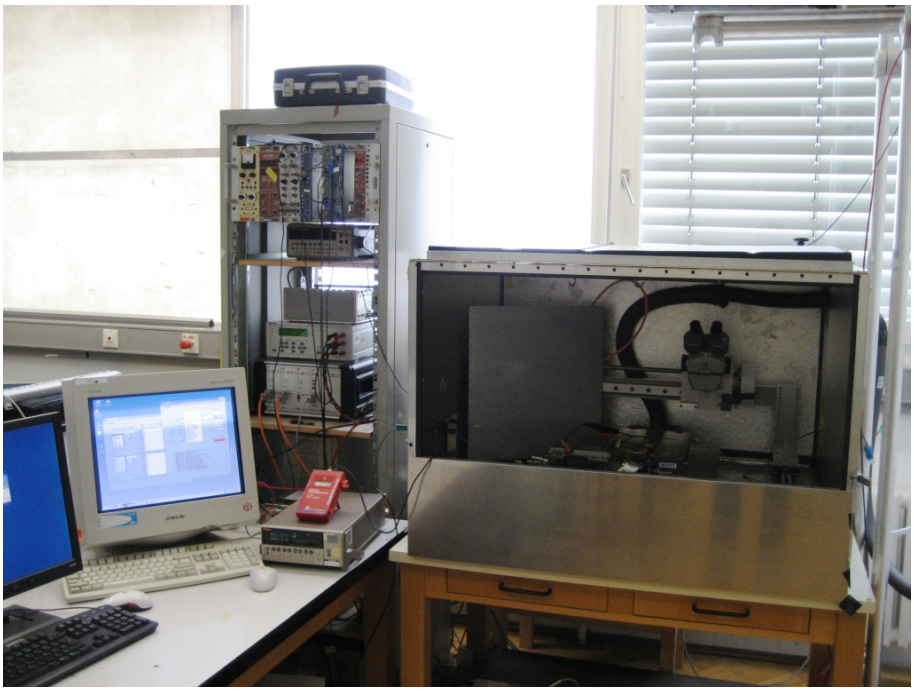

Figure 10.1: ***The Karlsruhe Diagnostic Teststation.*** *A* $100x70x70\ cm^3$ *big metal box, serving as a Faraday cage, houses connections for the modules to the readout electronics, a microscope and a controllable moving equipment with a carrier for specially designed LEDs, lasers or sources to be used as signal generators. Two scintillators outside the box provide the possibility to trigger in coincidence on particles created by cosmic rays. The standard cooling of modules is done via Peltier elements inside a jig. A special equipment allows to cool with dry air that was cooled during its passage through liquid nitrogen.*

a Dewar vessel filled with liquid nitrogen. The environmental conditions are measured with several sensors and are monitored with a PC. The adjustment of the temperature has to be done by hand in the latter case, by controlling the dry air flow with an adjustable valve, while in case of a Peltier cooling, a PC handles this task [Hof08]. Parts of the readout system in form of PCB cards, the power supplies for the low voltages and the high voltages, the controller for the motor stepper and the readout PC are placed outside the box. The module readout is done via the Karlsruhe Readout System, which is designed for the usage with APV electronics. Information about it can be found in [Dir03].

10.2 The special Setup for the Coldtest of the MCz-Modules

After an adjustment of the control and data acquisition software [Fah06] of the teststation and some hardware enhancements, a data taking with the testmodules used in this work was possible. The beta particles of a ^{90}Sr source served as MIPs, as the majority of them has the necessary energy. Low energy particles were filtered out by the two layers of plexiglas of the housing, so that basically only the high energetic electrons caused signals in the scintillator placed underneath the source with the module in between, ensuring data taking of MIPs only. Two Pt100 sensors, one on top and one at the backplane of the MCz sensor, were installed with direct contact to the sensor (photos 10.2(a) and

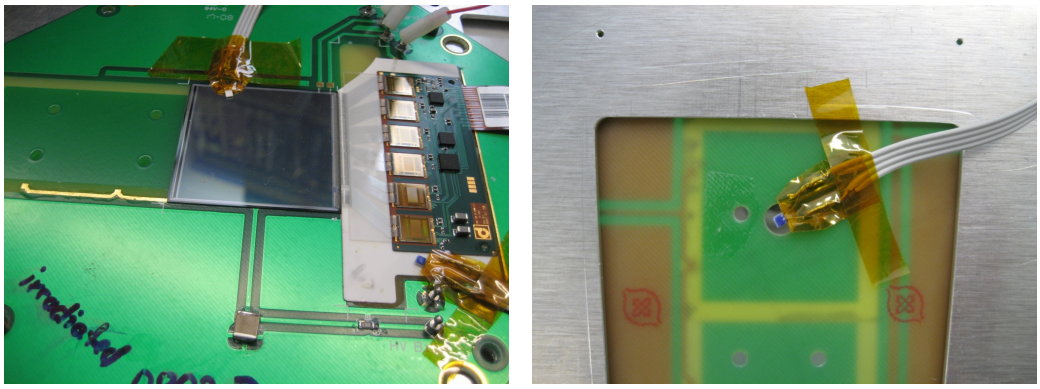

(a) (b)

Figure 10.2: ***Mounting of the Pt100 temperature sensors on the module during the test.*** *The electrically isolated temperature sensors were mounted on the MCz sensors with direct contact to ensure a reliable temperature control. a) Pt100 sensors on the surface and near the electronics. b) Pt100 sensor at the backplane.*

10.2(b)) and read out via a PC. Two further Pt100 surveyed the temperature near the hybrids and in the dry air of the box. An additional device controlled the temperature in the cold air flow. Before the start of the data taking, the humidity was checked to exclude condensation. Picture 10.3 shows the setup for the cold test of a MCz-testmodule. The Plexiglas housing and the cooling tubes can be seen, as well as the electronics connections and the ^{90}Sr source.

After each voltage or temperature step, 5000 random triggers were used to read out all channels to determine their pedestal and their noise like described in chapter 7.3. The computation was done by the readout software immediately after the data taking. During the experiment, only triggers which were in coincidence with the internal readout clock signal, in the way that they fell into a short time window around it, were accepted, so that the timing settings of the chip provided a signal readout quite well around the signal maximum. The data taking was only started when stable conditions were reached, meaning that the temperature and the module current had stayed constant for some minutes. Up to 10000 events were recorded in each run during physics data taking. For the cluster finding, the limit for the acceptance of a seed cluster was, that the signal had to be higher than four times the noise (4σ) and neighbors were accepted if their signal was higher than two times the noise (2σ).

While the measured signal to noise ratios are independent of different amplifier electronics settings of different setups, differences in the signal height might exist, impeding direct comparisons. Therefore measurements with a non-irradiated detector as a reference one were done, for the determination of the charge collection efficiency and to get an estimate for the effective number of collected charge carriers. For this purpose a fully depleted 500 μm thick CMS FZ module was used, where the generated signal should be 5/3 higher than for a thinner non-irradiated MCz testmodule. This was considered in the calculation of the charge collection efficiencies, when 3/5 of the charge collected by the reference module was set to 100%.

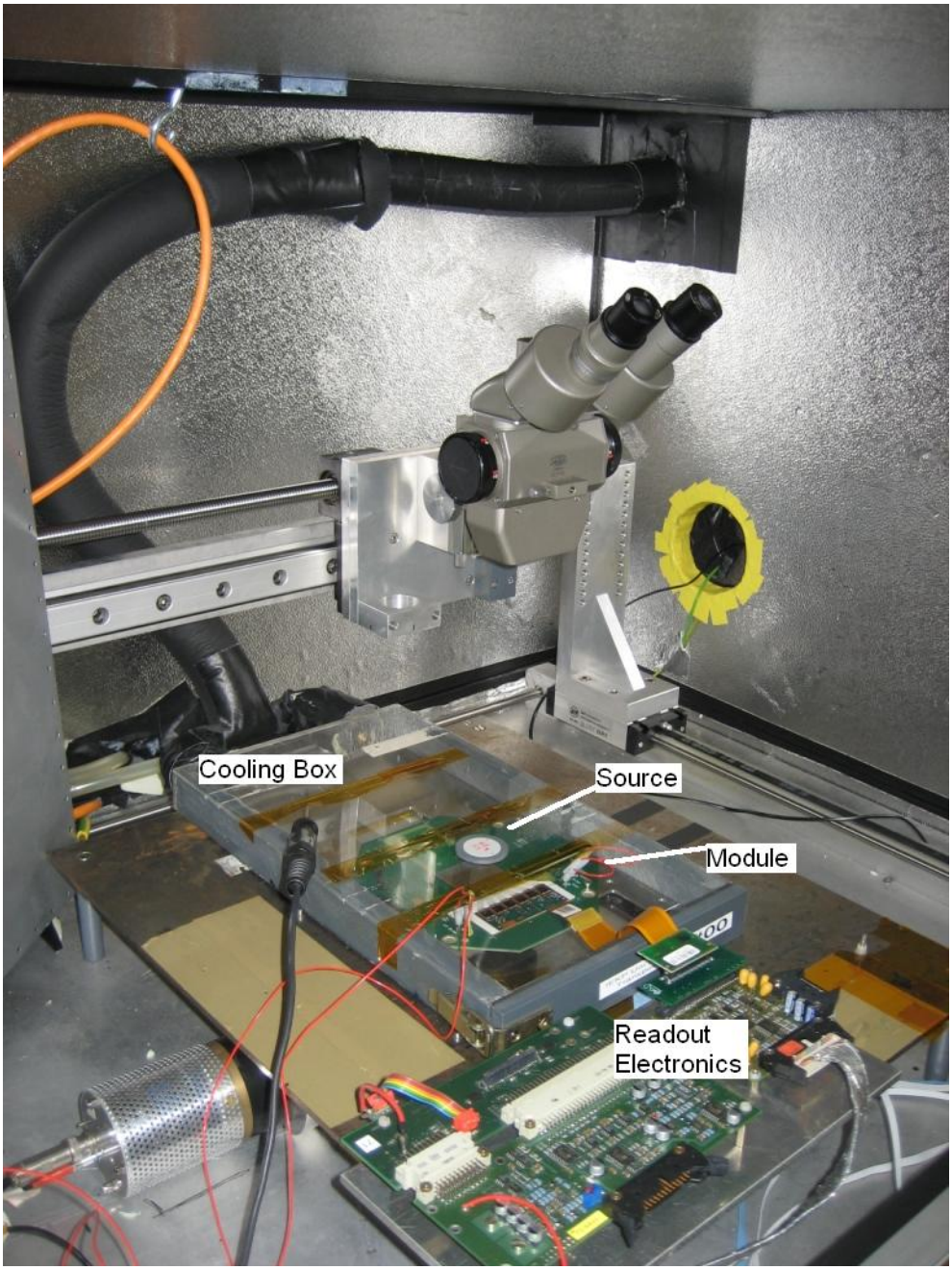

Figure 10.3: ***View inside the Karlsruhe Diagnostic Teststation on the special assembly for the cold test.*** *The Plexiglas housing and the cooling tubes can be seen, as well as the electronics, the* ^{90}Sr *source and the scintillator.*

10.3 Results of the Coldtests

10.3.1 Noise Levels and Noise Cuts

The strip noise of the MCz testmodules shows again what had already been seen in the beamtest. Noisy strips and problematic regions existed, possibly due to production problems. Therefore the cut method (chapter 9) was used again to sort out these channels to neglect them in the analysis. To give an example, figure 10.4(a) shows the strip noise of the module MCz0802A at a temperature of -40°C and at a voltage of 840 V. Figure 10.4(b) shows the associated histogram.

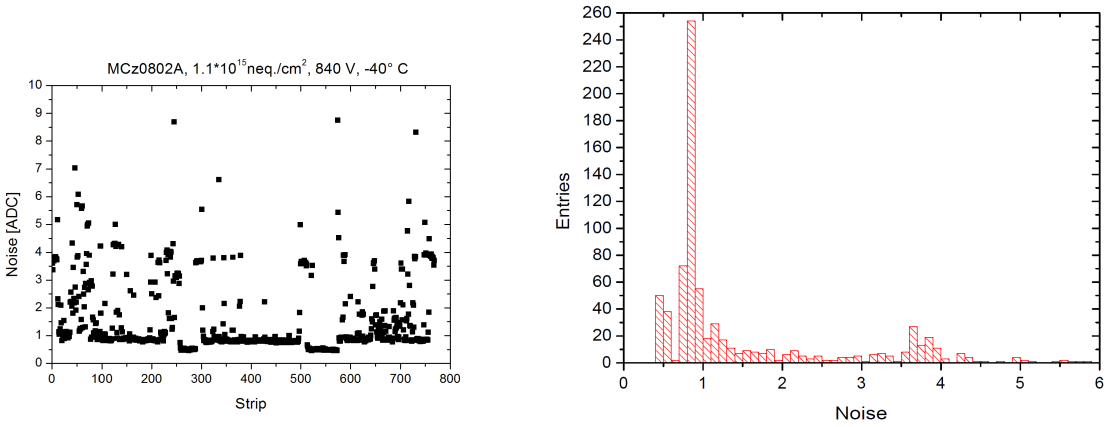

(a) (b)

Figure 10.4: ***Strip noise of the module MCz0802A, irradiated with*** $1.1 \cdot 10^{15}$ *neq./cm*^{2} ***at a temperature of -40°C and at a voltage of*** 840 V**.** *a) Channel noise b) Noise histogram. The criterium for channels to be included in the analysis was a noise between* 0.5 *ADC and* 2 *ADC, as here the majority of good channels could be found.*

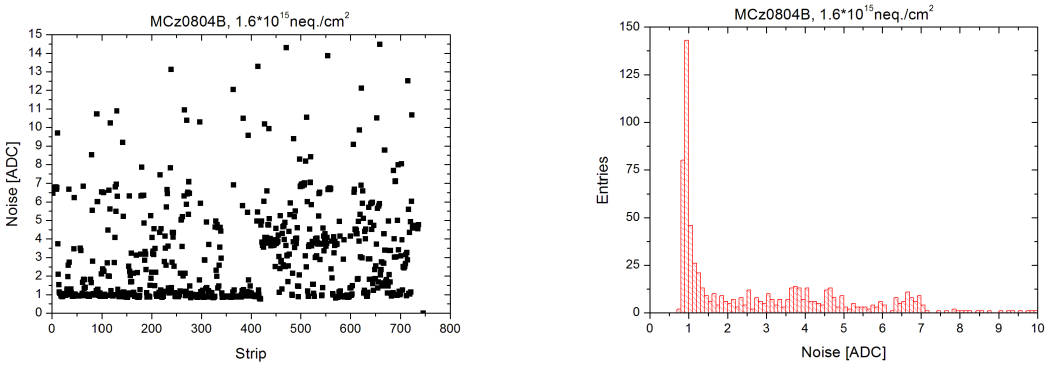

(a) (b)

Figure 10.5: ***Strip noise of the module MCz0804B, irradiated with*** $1.6 \cdot 10^{15}$ *neq./cm*^{2} ***at a temperature of -30°C and at a voltage of*** 800 V**.** *a) Channel noise b) Noise histogram. The lower cut limit was set to* 0.8 *ADC and the upper one to* 2.5 *ADC, for channels to be included in the analysis.*

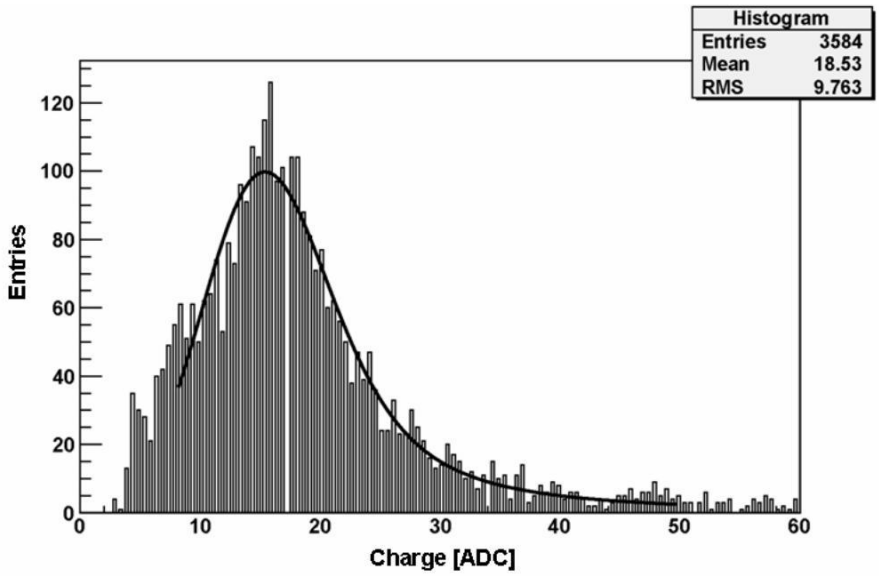

Figure 10.6: ***Cluster charge histogram of the module MCz0802A, irradiated with*** $1.1 \cdot 10^{15}$ $neq./cm^2$ ***at a temperature of -40°C and at a voltage of*** 880 V**.** *The most probable value of a Landau-Gauss fit gave the accordant cluster charge value of this run.*

For this module, the acceptance criterium for channels was a noise between 0.5 *ADC* and 2 *ADC*, as here the majority of good channels could be found. Similar plots for the highest irradiated module MCz0804B at the temperature of -30°C and the voltage of 800 V can be found in figure 10.5(a) and 10.5(b). It is apparent, that many noisy strips exist, but that there is also a band of good channels around the noise value of 1 *ADC*. Thus the lower cut limit was set to 0.8 *ADC* and the upper one to 2.5 *ADC*.

10.3.2 Results of the MCz Module, irradiated with $1.1 \cdot 10^{15}$ $neq./cm^2$

Although the sensor with the fluence of $1.1 \cdot 10^{15}$ $neq./cm^2$ could not be fully depleted in the beamtest, it still provided a charge collection of nearly 50% (chapter 9). This good result could even be outperformed in the teststation at higher voltages, as nearly 60% were achieved at 1000 V. The deep temperatures (-30°C to -40°C) ensured low leakage currents in the order of 50 μA to 140 μA and prohibited thermal runaways thereby. The most probable value of a Landau-Gauss convolution fit at the measured cluster charge histogram of a run defined the collected charge of it in the same way as in the analysis of the testbeam data. As an example figure 10.6 presents such a fit at the data of a run with a bias voltage of 880 V and a temperature of -40°C. The results of the charge collection measurements can be found in figure 10.7(a) and it can be seen that no saturation or a bend in the curve exist, so that it seems as if a further signal increase is possible with higher bias voltages, as long as no current breakthrough appears. No significant differences in the results of the measurements at the several temperatures can be seen. The signal to noise plot also shows no saturation at any of the applied voltages (see figure 10.7(b)). At the highest voltage of 1000 V, a signal to noise ration (SNR) of around 20 was seen, which is an excellent value for any application.
The comparison between the beamtest outcome and the teststation outcome reveals a discrepancy between the charge collection efficiency results of the two experiments at the highest beamtest voltages. If one follows the slope of the teststation curves in figure 10.8(a), an agreement between the two data

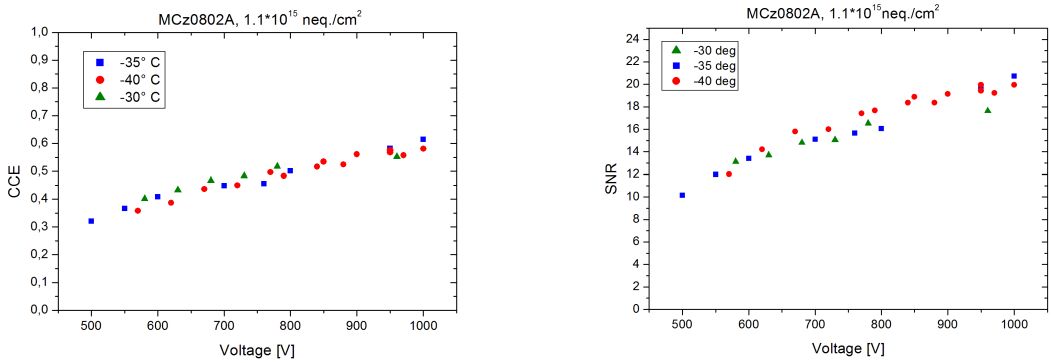

(a) (b)

Figure 10.7: ***Results of the module MCz0802A, irradiated with*** $1.1 \cdot 10^{15}$ *neq./cm*^{2} *a) Charge collection efficiency. No saturation or a bend in the curve exist, so that a further signal increase seems possible with higher bias voltages. 60% charge collection efficiency was achieved at* 1000 *V. b) Signal to noise ratio. An excellent value of around 20 was seen at* 1000 *V.*

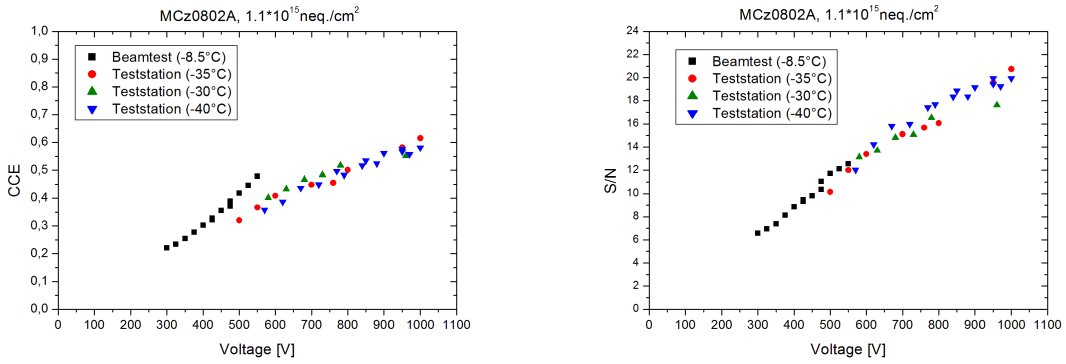

(a) (b)

Figure 10.8: ***Comparison of the beamtest results with the measurements of the teststation.*** *a) Charge collection efficiency. The outcome reveals a discrepancy between the CCE results of the two experiments at the highest beamtest voltages. If one follows the slope of the teststation curves, an agreement between the two data sets can be assumed at voltages lower than* 450 *V. Exactly the runs with voltages higher than this value were affected mostly by thermal runaways in the beamtest, so that one might speculate about an influence here. b) Signal to noise ratio. Due to the higher noise resulting from the higher leakage currents, the difference in the charge does not lead to a higher signal to noise at the testbeam, so that the curves match.*

sets can be assumed at voltages lower than 450 V. Exactly the runs with voltages higher than this value were affected mostly by thermal runaways in the beamtest, so that one might speculate about an influence here. This guess gets encouraged additionally as simulations, which will be presented in chapter 11, show an agreement of the teststation data and the lower voltage data of the beamtest with the theoretical curve. A possible mechanism might be, that charges of the high leakage currents fill some of the traps, so that less unoccupied trapping centers exist for the trapping of charge carriers generated by traversing particles. The current could also beneficially influence the electrical field distribution. Such a model is the basis for the explanation of the functionality of current injected detectors [ea07], which get powered in forward direction at low temperatures exactly for that purpose. Nevertheless, the higher currents also lead to higher noise, so that only a minor difference can be seen in figure 10.8(b) at the comparison of the signal to noise evolution in the two setups.

10.3.3 Results of the MCz Module, irradiated with $1.6 \cdot 10^{15}\ neq./cm^2$

The sensor MCz0804B was irradiated with a fluence of $1.6 \cdot 10^{15}\ neq./cm^2$. This is already in the range of what has to be expected for the outer pixel layers at a radius of around 15 cm. The study of this sensor failed in the beamtest at voltages higher than 375 V, because of thermal runaways, and the lower voltages revealed no useful data, as the detector was by far not depleted. Therefore the tests in the teststation at lower temperatures and with higher voltages were of great importance. Data were taken between -30°C and -40°C with voltages between 500 V and 1000 V in the same way like with the sensor described above. Again the setup provided a good survey of the temperatures. The exponential temperature dependence of the leakage current lead to a significant current reduction at lower temperatures, so that no thermal runaways occurred. The currents at 900 V lay in the range of 250 μA at -30°C and 75 μA at -40°C .
This highly irradiated module still collects nearly 50 % of the charge generated by a MIP at a voltage of 1000 V and a temperature of -40°C , as figure 10.9(a) presents. No saturation is visible and even at the highest test temperature the slope of the curve does not change, so that also here higher signals should be possible at voltages higher than the applied 900 V where a charge collection efficiency of roughly 45 % is seen. The noise at higher temperatures is higher due to the increased leakage currents, so that the highest signal to noise ratio of about 16 is achieved at the lowest temperature of -40°C at a voltage of 1000 V (see figure 10.9(b)). This is a good result, because the value is far above the one still acceptable for many authors, which is about 10 [Mol06].

Conclusion

The measurements of the highest irradiated sensors in the Karlsruhe Diagnostic Teststation in the low temperature range between -30°C and -40°C confirm the good results of the testbeam. They further provide the important information about the sensor behavior at the deep temperatures, which are most probably relevant for a SLHC CMS tracker and about the properties of a sensor irradiated with fluences expected in the pixel region.
A comparison of the results with a simulation will be presented in chapter 11, followed by a discussion and a review of the data in chapter 13.

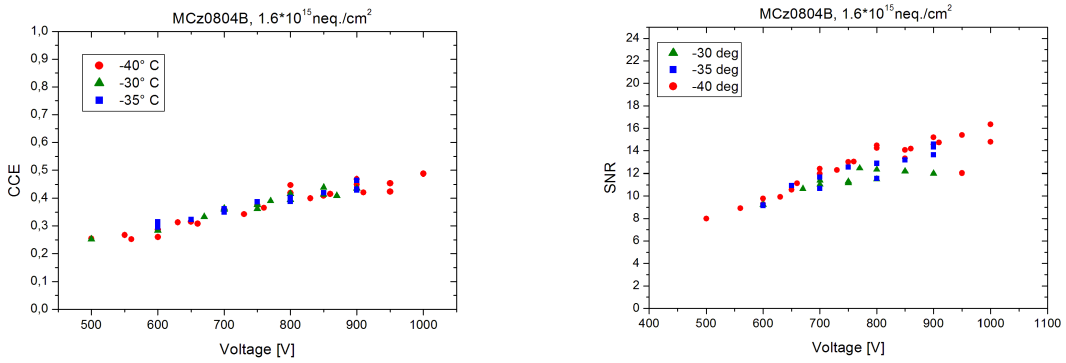

(a) (b)

Figure 10.9: ***Results of the module MCz0804B, irradiated with*** $1.6 \cdot 10^{15}$ *neq./cm*^{2}**.** *a) Charge collection efficiency. Also here higher signals should be possible at voltages higher than the applied* 900 *V where a charge collection efficiency of roughly* 45 *% was seen. b) Signal to noise ratio. A SNR of about 16 was achieved at the temperature of -40 °C and a voltage of* 1000 *V.*

Chapter 11

Simulations of Charge Collection Efficiencies

The charge collection efficiency results obtained in the beamtest and in the teststation, presented in chapter 9 and 10, were compared with an established model for the charge transport and the trapping in silicon sensors, like the one to be found in chapter 4. For this purpose a simulation of the charge collection process in irradiated segmented silicon sensors was done, based on established physical models.

11.1 Properties of the Simulation Script

For the simulation of the charge collection efficiency, a program written by Vladimir Eremin was used, which simulates the behavior of the charge generated by a MIP in an irradiated sensor. After an adaptation of the software, also not fully depleted sensors could be simulated.
In user defined finite elements, the program calculates the generated charge and its transport in the electrical field under the influence of trapping, considered by effective trapping time constants for electrons and holes. It sums up the collected charge of all elements and compares it with the totally generated one to get the charge collection efficiency. The square root of the ratio of the applied voltage to the full depletion voltage defines the ratio of the active to the non-active volume, according to formula 3.48. The program also considers the influence of the temperature on the charge collection, as well as the consequences of the pitch of segmented devices on the electrical field. Further input parameters are the bulk thickness, the material type (p-in-n, n-in-p), the effective doping concentration, the weighting of the electrical field to account for the influence of strip and pitch structures, the choice of a possible presence of type inversion and the irradiation fluence. The most important parameter for the trapping calculation is the β in formula 4.26, which describes the evolution of the inverse trapping time with the fluence.
The measured full depletion voltages of the test sensors were used for the simulation. As for the higher irradiated sensors, in none of the tests a determination of the full depletion voltages was possible, estimated values were applied, based on the so far known results, sensor behaviors and the comparison of the differences in measured full depletion voltages with the differences in the corresponding irradiation fluences.

	β_e (10^{-7} cm^2/s)	β_h (10^{-7} cm^2/s)
FZ	5.59 ± 0.29	7.16 ± 0.32
DOFZ	5.73 ± 0.29	6.88 ± 0.34
MCz	5.81 ± 0.32	7.78 ± 0.39
DOFZ	5.48 ± 0.22	6.02 ± 0.29
Dortmund DOFZ	5.08 ± 0.16	4.90 ± 0.16
Ljubljana DOFZ and FZ	5.34 ± 0.19	7.08 ± 0.18
Lancaster / Hamburg FZ	5.32 ± 0.30	6.81 ± 0.29
Hamburg FZ, DOFZ and MCz	5.07 ± 0.16	6.20 ± 0.54

Table 11.1: ***Measured trapping parameters for electrons*** β_e ***and holes*** β_h ***[BM05].*** *The trapping parameters were measured by several groups for MCz, FZ, and DOFZ silicon, irradiated with* 24 *GeV protons.*

11.2 Simulations with established and adjusted Trapping Time Parameters

11.2.1 Chosen Trapping Time Parameters

The trapping parameter β has been measured by several groups like [K$^+$02] or [BM05] for different material types with p-in-n MCz among them. A summary and mean values of many measurements and groups have been published in [RD507]. Due to these results (table 11.1), a value of $5 \cdot 10^{-7}$ cm^2/s for β_e and a value of $6 \cdot 10^{-7}$ cm^2/s for β_h were chosen for the simulation, also considering that the the tested sensors were irradiated with minor fractions of neutrons.

Surprisingly the simulation underestimated the charge collection efficiency, regardless of what had been chosen for the electrical field distribution concerning the existence of type inversion. As another group reports an anomalously high charge collection efficiency in p-type MCz silicon detectors [M$^+$09], the value of β_e and β_h were changed to achieve agreement between the simulations and the measurements. This was possible with the choice $\beta_e = 2 \cdot 10^{-7}$ cm^2/s and $\beta_h = 2.4 \cdot 10^{-7}$ cm^2/s. The same value for β_e was experimentally found by [B$^+$07] after also having measured a higher CCE than expected for p-type material. As no difference between n-type and p-type MCz silicon has been observed for the trapping time constants according to [RD507], the two results are in agreement. A result for β_h has not been presented in this article and it has to be stressed, that the value for β_h is the more important one for a readout at p-type strips like here. Anyway the reported β_e and the known ratio between β_e and β_h of the old values show that the choice for β_h is reasonable.

11.2.2 Comparison between Beamtest Results and Simulation Results

For the sensor n017A, irradiated with the lowest fluence of $1 \cdot 10^{14}$ $neq./cm^2$, a comparison between the measured charge collection efficiencies and the simulated ones of the different beta values described above, can be found in figure 11.1. It is apparent, that a very good agreement with the measurement can be obtained by these lower beta values, while the reported ones lead to a much too low charge collection efficiency.

After this success, simulations with the new found parameter values were done also for the other explored sensors and the important outcome is, that for all of them manifest conformance with the measurements is seen. The corresponding plots for the sensors irradiated with $5 \cdot 10^{14}$ $neq./cm^2$ and $5.8 \cdot 10^{14}$ $neq./cm^2$ are presented in the figures 11.2 and 11.3. The measured full depletion voltages

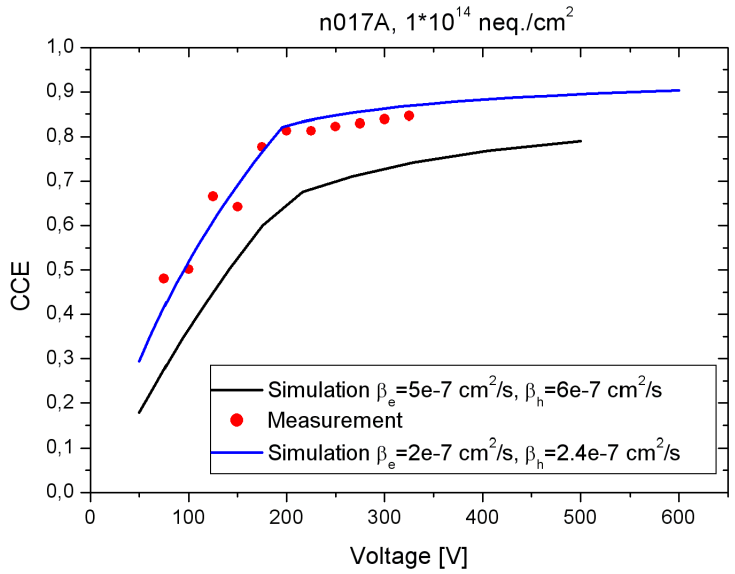

Figure 11.1: ***Module irradiated with*** $1 \cdot 10^{14}$ *neq./cm*^{2}***. Comparison of the measured CCEs and the simulated CCEs for two different*** β***-values.*** *With the so far known* β*-values no agreement with the measurement exists, while with the adjusted ones the simulation fits the measurement curve. The once adjusted values were used in all simulations for all fluences.*

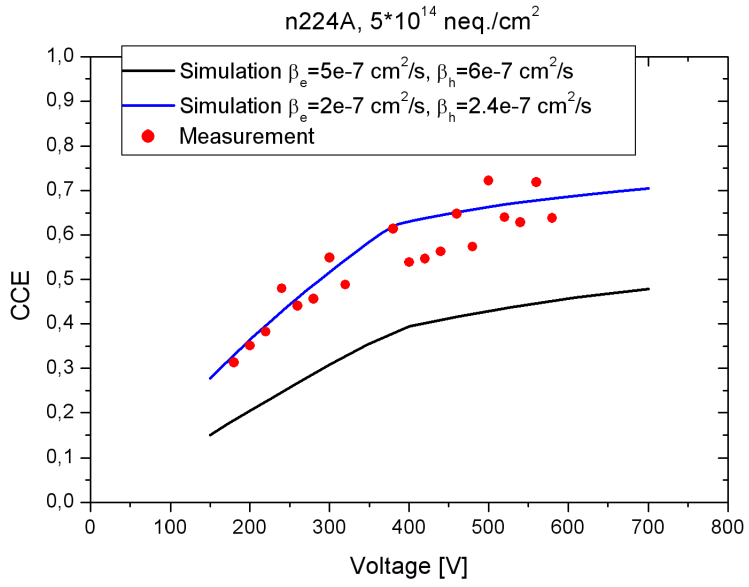

Figure 11.2: ***Module irradiated with*** $5 \cdot 10^{14}$ *neq./cm*^{2}***. Comparison of the measured CCEs and the simulated CCEs for two different*** β***-values.*** *With the so far known* β*-values no agreement with the measurement exists, while with the adjusted ones the simulation fits the measurement curve. The once adjusted values were used in all simulations for all fluences.*

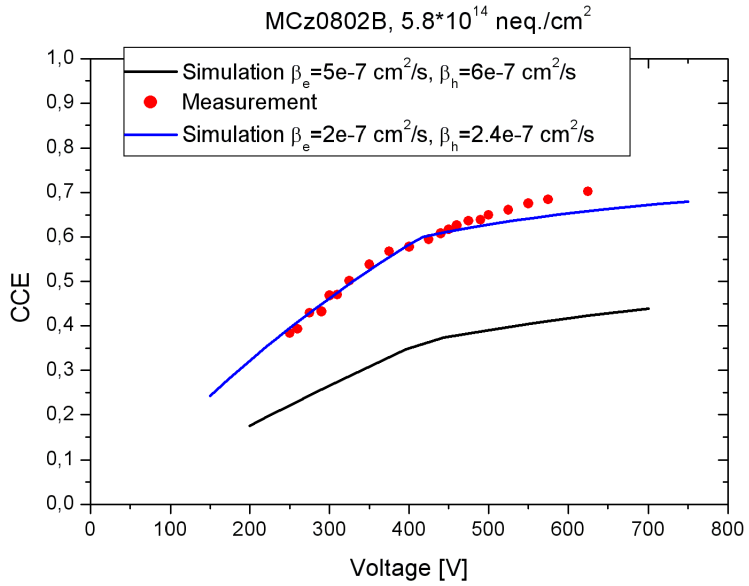

Figure 11.3: ***Module irradiated with*** $5.8 \cdot 10^{14}$ *neq./cm*^{2}***. Comparison of the measured CCEs and the simulated CCEs for two different*** β***-values.*** *With the so far known* β*-values no agreement with the measurement exists, while with the adjusted ones the simulation fits better the measurement curve. Only some measurement points do not lie on the curve, but they nevertheless agree better with the simulation of the adjusted parameters. The once adjusted values were used in all simulations for all fluences.*

were used in both cases. Figure 11.4(a) shows the comparison of the simulations with the beamtest data of the sensor irradiated with a fluence of $1.1 \cdot 10^{15}$ *neq./cm*^{2}. While also here the calculated values of the higher betas do not fit at all to the measured curve, the ones of the adjusted and lower betas do much better, even though for the highest bias voltages not as well as seen before. This is hardly surprising, as it were exactly theses points, that did not fit well to the rest of the values in the figure 10.8(a) and that lead to a slope different to the ones observed for the other fluences. A possible explanation was given in the same chapter by the high leakage currents resulting from thermal runaways.

11.2.3 Comparison between Teststation Results and Simulation Results

In contrast to the minor mismatch for the module with a fluence of $1.1 \cdot 10^{15}$ *neq./cm*^{2} at the voltages that lead to thermal runaways in the beamtest, the simulated charge collection efficiencies at higher voltages and at a temperature of -40 °C matched very well the corresponding curve observed in the teststation (see figure 11.4(b)). As the measured signal to noise graph shows no saturation in figure 10.7(b), one has to calculate with a higher full depletion voltage, having changed due to a reverse annealing during the time between the beamtest and the teststation experiment, when an appropriate cooling could not always be ensured. Therefore a voltage of 950 *V* was assumed. The same circumstances demand a revision of the full depletion voltage of the highest irradiated sensor with a fluence of $1.6 \cdot 10^{15}$ *neq./cm*^{2}. Also for that highly irradiated sensor a very good agreement of the measured values with the simulation based on the changed trapping parameter is existent, like it can be seen in

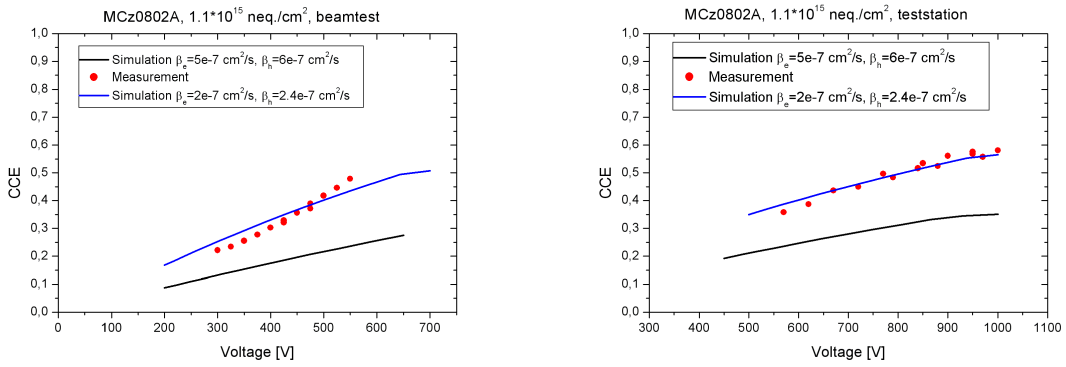

(a) (b)

Figure 11.4: ***Module irradiated with*** $1.1 \cdot 10^{15}$ *neq./cm*^{2}***. Comparison of the measured CCEs and the simulated CCEs for two different*** β***-values.*** *With the so far known* β*-values no agreement with the measurement exists, while with the adjusted ones the simulation fits the measurement curve. a) Comparison with the beamtest results. b) Comparison with the teststation results.*

figure 11.5. An estimated full depletion value of 1300 V was used for the calculation.

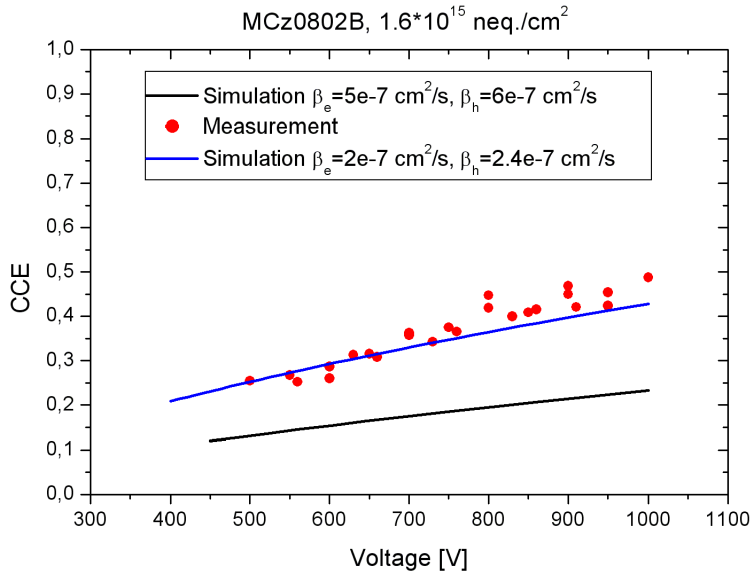

Figure 11.5: ***Module irradiated with*** $1.6 \cdot 10^{15}$ *neq./cm*^{2}***. Comparison of the measured CCEs and the simulated CCEs for two different*** β***-values.*** *With the so far known* β*-values no agreement with the measurement exists, while with the adjusted ones the simulation fits the measurement curve. The once adjusted values were used in all simulations for all fluences.*

Although the step of estimating the full depletion voltage is unpleasant, the actual consequences of this imprecision are marginal for very highly irradiated sensors. The reason is, that the limiting factor on the charge collection efficiency at higher fluences is the trapping and not the presence of non-depleted sensor volumes. Figure 11.6 confirms this by a comparison of simulation outputs with different full depletion voltages of the highly irradiated sensor. Further the figure expresses again that the old beta values do not deliver results that fit to the measurements at any of the assumed full depletion voltages.

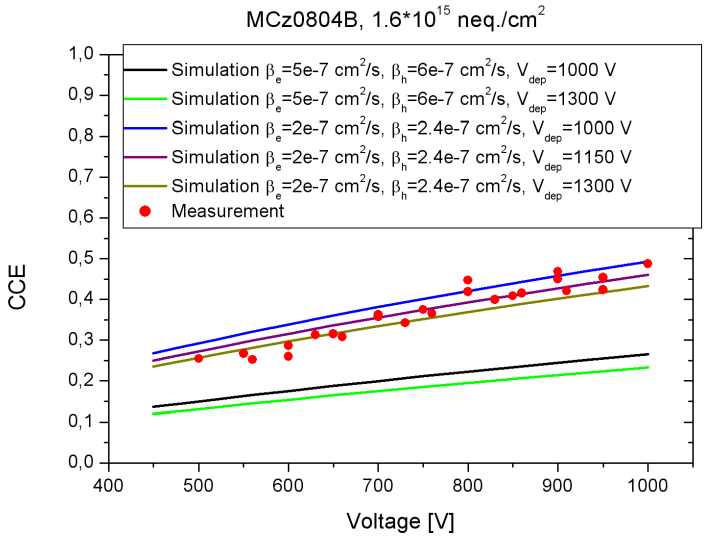

Figure 11.6: ***Module irradiated with*** $1.6 \cdot 10^{15}$ $neq./cm^2$***. Comparison of the measured CCEs and the simulated CCEs of different assumptions for the full depletion voltage.*** *The full depletion voltage of the highly irradiated module could not be measured, so that an estimation was necessary. The result shows that the uncertainty is unimportant as the limiting factor on the CCE at higher fluences is the trapping and not the presence of non-depleted sensor volumes*

11.2.4 Conclusion

The simulated charge collection efficiencies were compared with the measurement results of the two beamtests and the teststation. For the appraisal of the results it has to be mentioned that the NIEL concept is limited for the trapping effect. Equal neutron equivalent fluences of different particle energies and particle types might lead to noticeably differences in the trapping behaviors. The irradiations of the sensors with fluences between $1 \cdot 10^{14}$ $neq./cm^2$ and $1.6 \cdot 10^{15}$ $neq./cm^2$ were done with 25 MeV protons and partly neutrons of an average energy of 20.4 MeV according to the ratios in table 9.2. A controlled standard annealing was not accomplished, but an annealing at room temperature for around two weeks took place during transport, testing and installation. These circumstances have to be considered.

The important fact for the presented results is, that the beta factors were adjusted only once and not for each data set individually, which means that the values $\beta_e = 2 \cdot 10^{-7}$ and $\beta_h = 2.4 \cdot 10^{-7}$ cm^2/s lead to agreements between the simulations and the measurements in the fluence range between $1 \cdot 10^{14}$ $neq./cm^2$ and $1.6 \cdot 10^{15}$ $neq./cm^2$ and not only for one measurement.

In all simulated cases, a space charge sign inversion has been assumed in agreement with observations

of other groups (see e.g. [Här04]). Nevertheless this topic is still controversial, as also contradicting measurements exist [S$^+$07]. Others observe that the appearance of the effect is dependent on the particle type and energy [M$^+$07], which might explain the dispute. With the choice of an absence of type inversion it was actually possible to obtain agreement with the one measurement data set at the lowest fluence of $1 \cdot 10^{14}$ $neq./cm^2$ by using the old betas, but then there was no agreement with the observations for all higher fluences. Figure 11.7 shows an example of this disagreement with the measurements of the sensor MCz0802A. This contradiction and the good results with the postulation of type inversion are regarded as a considerable indication of the correctness of the simulation approach to calculate with the junction being dominant at the n^+-backplane.

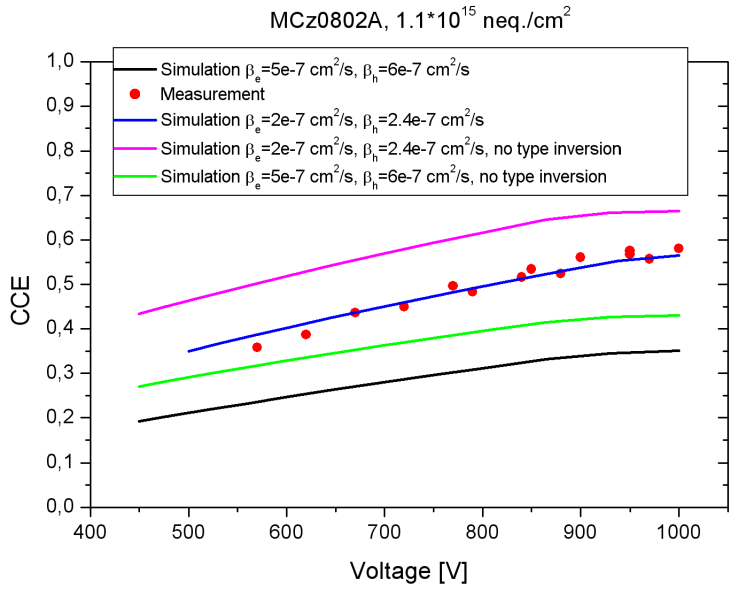

Figure 11.7: ***Module irradiated with*** $1.6 \cdot 10^{15}$ $neq./cm^2$***. Influence of the assumption for type inversion on the simulation results and the fit to the measurement data.*** *For any of the* β*-values an agreement with the measurement could be achieved, if the absence of type inversion was assumed.*

The overall outcome of the simulations is, that for the tested sensors the charge loss by trapping is less significant than predicted by a common model. The hitherto existing parameter values for the description of the trapping effect evidently overestimate the damaging impact of radiation on the charge collection efficiency. Results of other experiments, that show a comparable tendency, can be found in [M$^+$09].
The measurements of this work were not designated to detect reasons for this beneficial tendency of higher charge collection efficiencies. Based on the results it can only be speculated about it. Further investigations on the mechanisms of trapping should be fulfilled to give an answer.

Chapter 12

Testing for Double Junctions in irradiated n-Type MCz Diodes

In chapter 4 it has been shown, that the double junction effect can improve the performance of irradiated sensors. Therefore experiments have been done in this work to look for the existence of the two junctions near both sensor ends. They were related to the ones presented in [Pit92] or [KL93].

12.1 Setup of the Test

The basic principle of the measurements is to generate electron-hole pairs in the silicon in narrow volumes at the front and the backside of the sensor and to measure the signal response in dependance of the bias voltage. If the active depleted volume grows from the opposite side from where the electron-hole pairs are generated, no signal will be detected, whereas a signal appears if the generation takes place in a depleted volume. Therefore one needs light or particles which have a short penetration depth in silicon.
The alpha particles of an ^{241}Am source were chosen for the tests. The particle spectrum has high energetic peaks at energies of around 5.5 MeV [NDD], so that enough charge is generated whereas the exact magnitude is unimportant for the intention of this exploration. By using the SRIM-software [Zie04], the maximal penetration depth of the alphas was calculated to be around 28 μm, so that the particles fulfill the requirements not to penetrate too deep into the bulk.
For the measurements the transient current technique setup in Karlsruhe [Die03] has been used. The hole current signals are coupled out capacitively, get amplified and are displayed and saved on a PC with the help of a LeCroy LC684DXL oscilloscope. The self-trigger option of this device was used, which is possible, as the signal height of the alphas and the trigger level were significantly above the noise level. Therefore noise triggers were almost excluded, especially as every measurement point represents a mean value of 1000 triggers taken during a period of 60 seconds. Hence every data point in the following plots reflects real particle signals.
The measured values are given in arbitrary units, as the actual physical values were not of interest as only the appearance of a signal was important in this experiment. Comparisons of the relative signal height in the plots are nevertheless possible. The integrated signal is a measure for the collected charge, so that with an appropriate calibration even the actual value in Coulomb could be determined, if necessary.

12.2 Results of the Tests for Double Junctions

Planar p-in-n MCz diode structures, which had been produced on the same wafer like the sensors presented and explored in this work (for the wafer design see picture 7.1), were used for the tests, so that no difference to the actual sensors existed concerning the thickness, the resistivity and the doping profile. A comparative study was done with similar p-in-n FZ diodes of the CMS sensor production. In each case one diode was irradiated with neutrons of a fluence of $3.8 \cdot 10^{14}$ $neq./cm^2$ and one served as a non-irradiated reference respectively. The fluence was above the necessary one for type inversion of that FZ material [Ble07]. The appearance of a type inversion in MCz silicon is still controversial [Här04], [S$^+$07].

12.2.1 Results of the FZ comparative Study

The full depletion voltage of the non-irradiated CMS FZ diode was around 175 V. Before irradiation, the alpha particles that penetrated in the front side material, where the p-implant can be found, generated electron-hole pairs which could be detected even at voltages far below the full depletion voltage. This happened because the depletion zone started growing from there so that a pn-junction existed. Figure 12.1 shows that the signal appeared already at low voltages and nearly stayed constant without any increase even after the full depletion voltage.
The opposed behavior existed for a charge generation at the backside of this non-irradiated sensor, like it can be seen in figure 12.2. No signal could be detected unless the full depletion voltage was reached, which proved that no junction existed at the backplane before irradiation.
The picture changed drastically after irradiation. Like expected, the irradiated FZ silicon showed the attributes of a sensor with junctions at both sides. The full depletion voltage of the irradiated FZ diode can be read out of the $1/C^2$ against voltage plot in figure 12.3 to be roughly 450 V. In the result for the irradiated FZ diode and a particle intrusion at the front side, presented in figure 12.4, one can see that signals were generated already at low voltages and that the signal height increased until the full depletion voltage was applied. Further, a second junction existed at the backside, as with an alpha irradiation at the backplane signals could be created at voltages significantly below the full depletion voltage (figure 12.5).

12.2.2 Results of the Tests with MCz Diodes

Like it has been shown in chapter 8, the full depletion voltages of the non-irradiated MCz sensors were around 350 V, so that the same holds for the diodes. The non-irradiated MCz diode behaves just as the FZ diode, which means that penetrating alpha particles generate a signal at any voltage when it takes place at the front side of the implants, while at the backside no signal can be seen until the sensor is fully depleted. Figure 12.6 illustrates the first case, while figure 12.7 presents the latter.

After the irradiation with a neutron fluence of $3.8 \cdot 10^{14}$ $neq./cm^2$, the full depletion voltage of the sensor lay around 400 V like the $1/C^2$ over voltage plot (figure 12.8) shows. Electron hole pairs created at the front side of the p-implant could be measured even at voltages far below these 400 V, so that just as before irradiation, an active junction existed around the implants. Figure 12.9 illustrates this. It is also visible, that the signal height increases until the full depletion voltage is applied and a saturation appears. When an alpha irradiation happens at the backside of the detector, a comparable behavior can be seen, clearly indicating the existence of a second junction at the backplane. Accord-

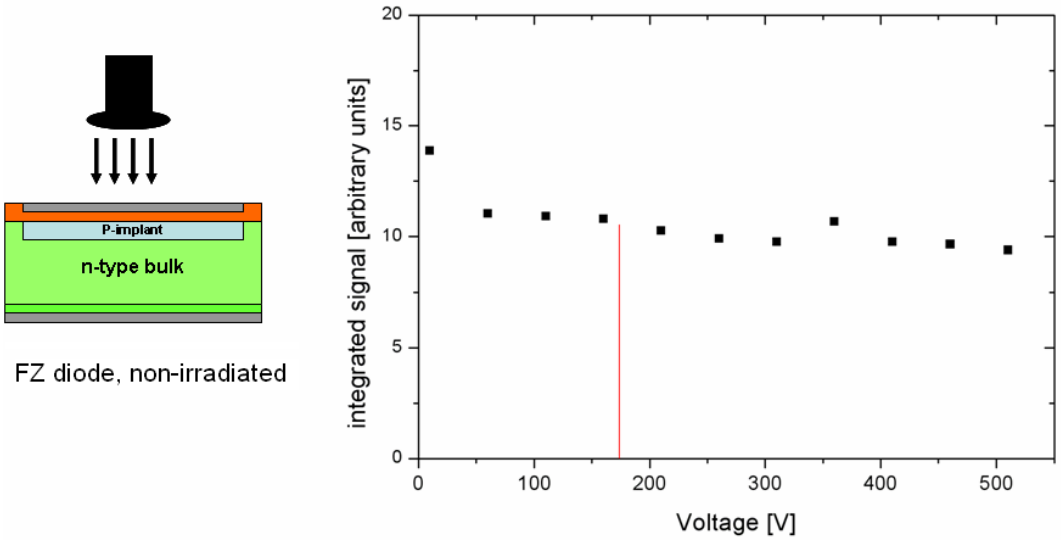

Figure 12.1: ***Electron hole pair generation at the front side of a non-irradiated FZ diode.*** *The charge generated by alpha-particles in a thin layer at the front side of the p-implants can be detected even with bias voltages significantly lower than the full depletion voltage (red vertical line), so that a depleted zone must exist there.*

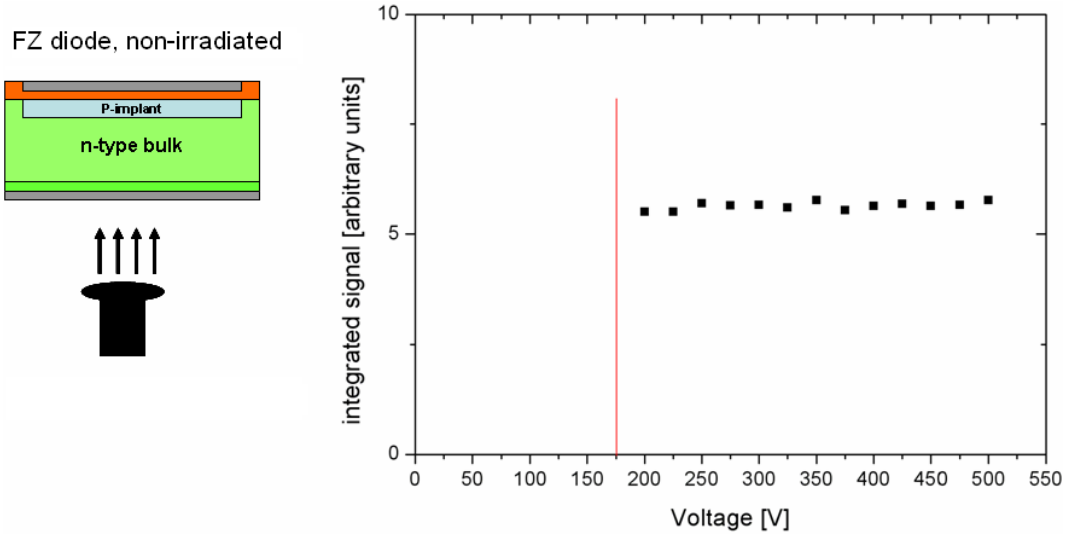

Figure 12.2: ***Electron hole pair generation at the backside of a non-irradiated FZ diode.*** *The charge generated by alpha-particles in a thin layer at the backside of the sensor cannot be detected with bias voltages lower than the full depletion voltage (red vertical line), so that no depleted zone exist there before. As soon as the bias-voltage is reached or higher voltages are applied, the signal gets detected.*

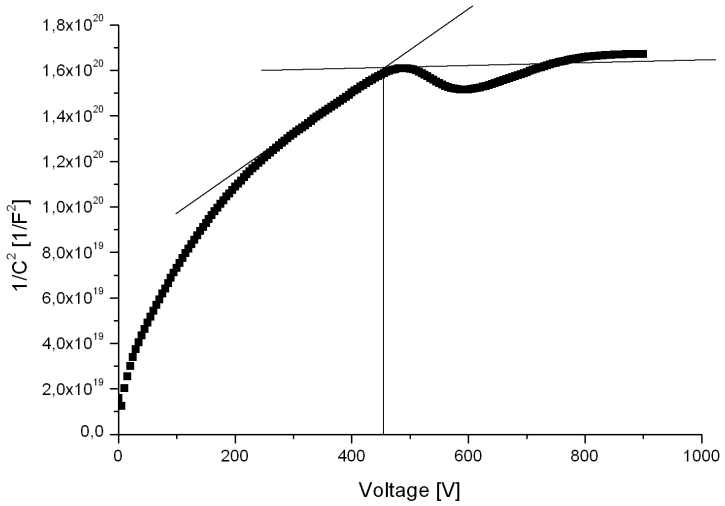

Figure 12.3: $1/C^2$ ***over voltage plot of the tested FZ diode irradiated with*** $3.8 \cdot 10^{14}$ $neq./cm^2$**.** *The plot allows to determine the full depletion voltage. It lay around* 450 V *(vertical line).*

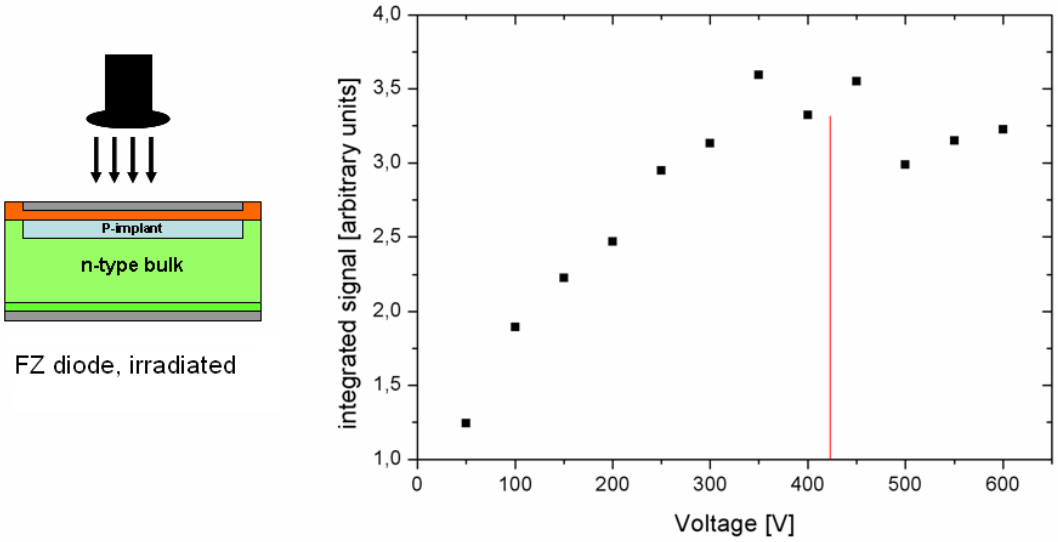

Figure 12.4: ***Electron hole pair generation at the front side of an irradiated FZ diode.*** *The charge generated by alpha-particles in a thin layer at the front side of the p-implants can be detected even with bias voltages lower than the full depletion voltage (red line), so that a depleted zone must exist there.*

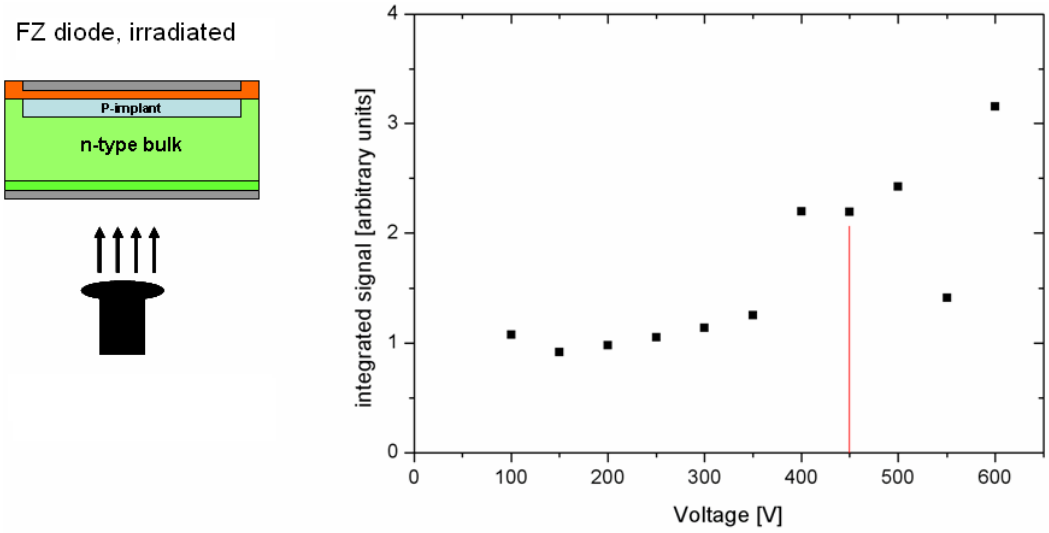

Figure 12.5: ***Electron hole pair generation at the backside of an irradiated FZ diode.*** *The charge generated by alpha-particles in a thin layer at the backside of the sensor can be detected even with bias voltages lower than the full depletion voltage (red line), so that a depleted zone must exist there.*

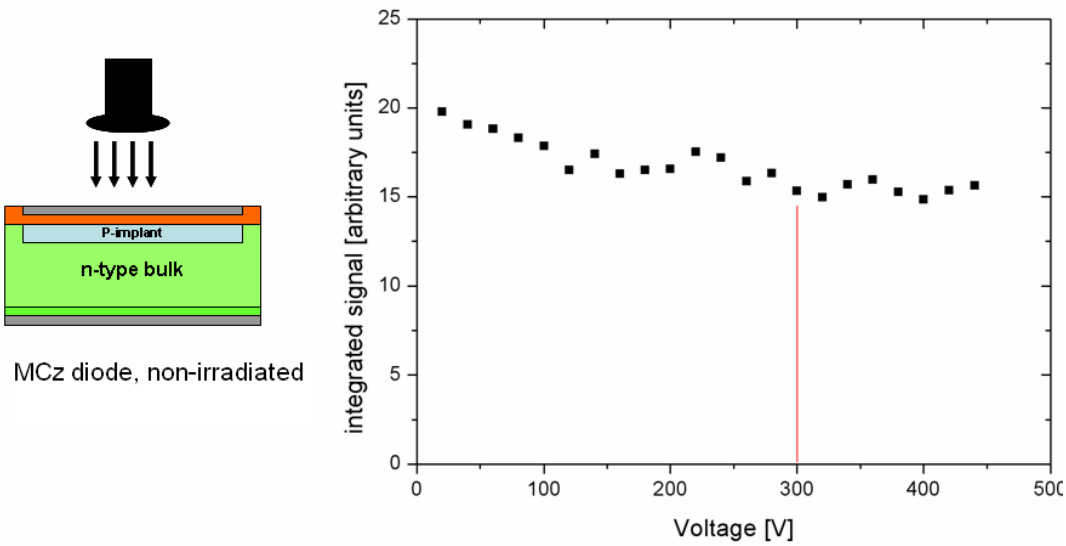

Figure 12.6: ***Electron hole pair generation at the front side of a non-irradiated MCz diode.*** *The charge generated by alpha-particles in a thin layer at the front side of the p-implants can be detected even with bias voltages significantly lower than the full depletion voltage (red vertical line), so that a depleted zone must exist there.*

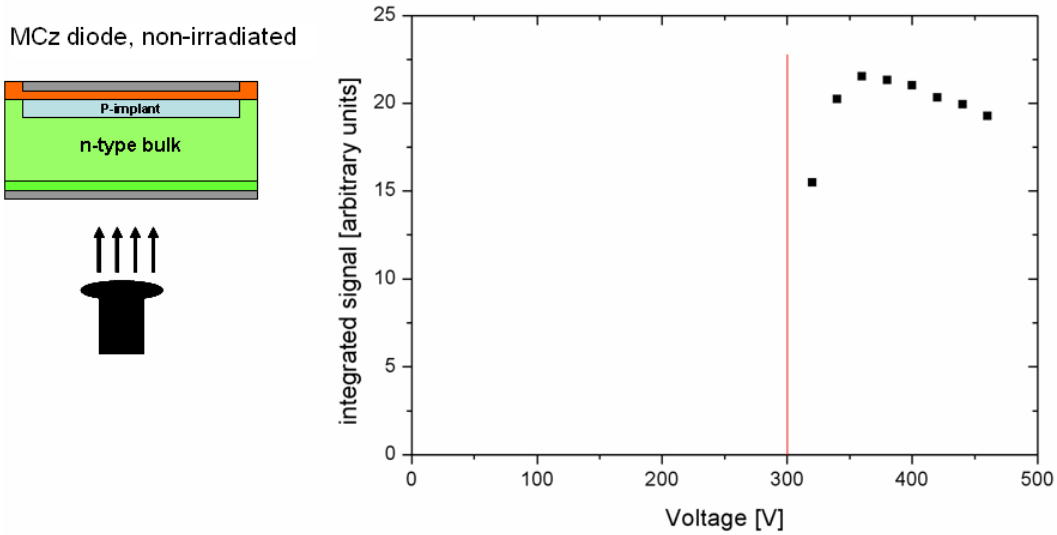

Figure 12.7: ***Electron hole pair generation at the backside of a non-irradiated MCz diode.*** *The charge generated by alpha-particles in a thin layer at the backside of the sensor cannot be detected with bias voltages lower than the full depletion voltage (red vertical line), so that no depleted zone exist there before. As soon as the bias-voltage is reached or higher voltages are applied, the signal gets detected.*

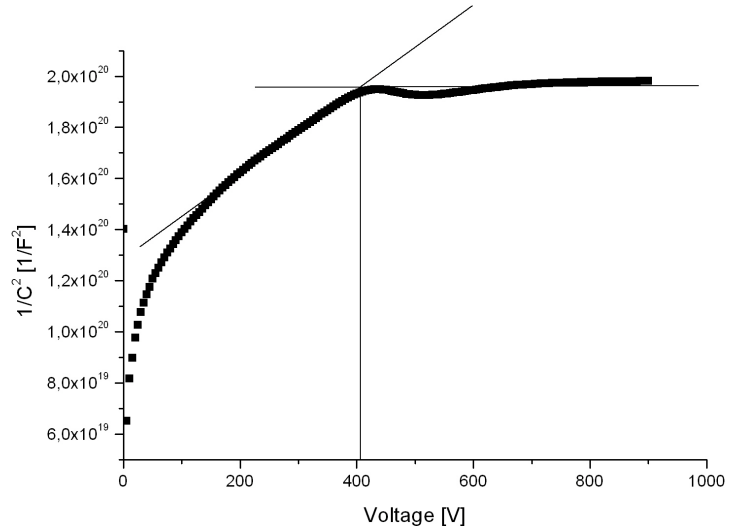

Figure 12.8: $1/C^2$ ***over voltage plot of the tested MCz diode irradiated with*** $3.8 \cdot 10^{14}$ $neq./cm^2$**.** *The plot allows to determine the full depletion voltage, which lay around* 400 V *(vertical line).*

ing to figure 12.10, here again alphas can be detected at voltages lower than the full depletion voltage and the signal height increases up to the saturation value, which is reached at full depletion.
These measurements unambiguously show that also for sensors based on MCz silicon two sensitive zones exist at the front and the backside, after higher fluences of radiation. In comparison to a complete movement of the dominant junction to the backplane after high irradiation fluences, this should have beneficial implications for applications in which the sensors can not be fully depleted anymore, as active zones at the position sensitive segmentations still exist.

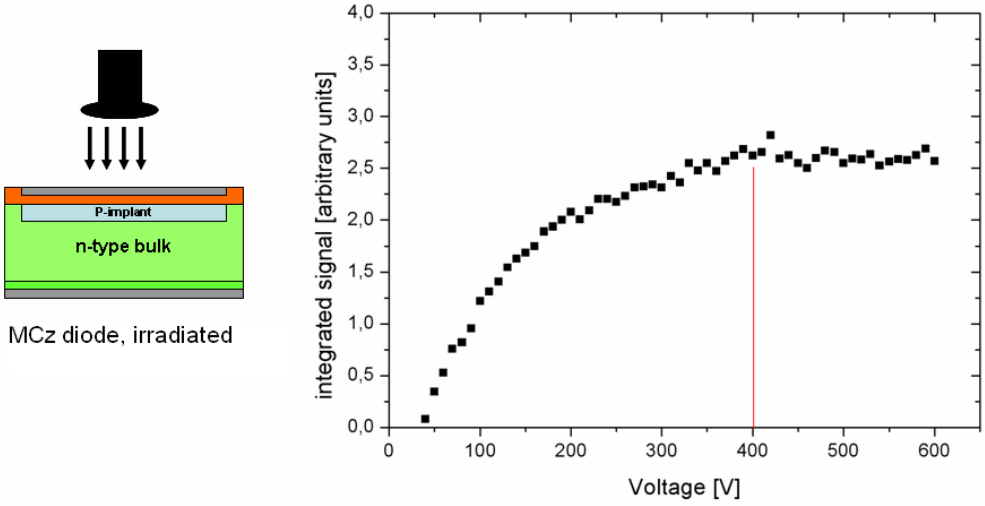

Figure 12.9: ***Electron hole pair generation at the front side of an irradiated MCz diode.*** *The charge generated by alpha-particles in a thin layer at the front side of the p-implants can be detected even with bias voltages lower than the full depletion voltage (red line), so that a depleted zone must exist there.*

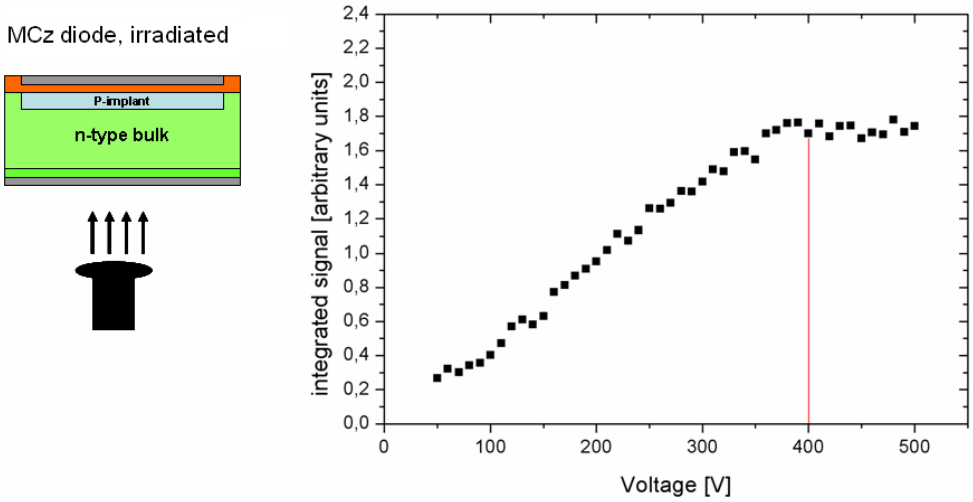

Figure 12.10: ***Electron hole pair generation at the backside of an irradiated MCz diode.*** *The charge generated by alpha-particles in a thin layer at the backside of the sensor can be detected even with bias voltages lower than the full depletion voltage (red line), so that a depleted zone must exist there.*

Chapter 13

Review and Appraisal of the Results

The plans for the SLHC envisage a luminosity increase by a factor of ten, up to a peak luminosity of $10^{35}\ cm^{-2}s^{-1}$. As a consequence the radiation stress for the detectors rises. Inner sub-detectors are much more affected than the outer ones. For a CMS tracker at the SLHC with a comparable design like the current one, the expected total fluences have been presented in figure 2.6, for an integrated luminosity of 2500 fb^{-1}. Different particle types with different energies sum up to these total fluences. The influence of the radiation type and the particle energy on the macroscopic degradation of the silicon sensor properties is considered in the hardness factor. It reflects a comparison with neutrons of an energy of 1 MeV. Like presented in chapter 4, the 1 MeV neutron equivalent quantity corresponds to a non-ionizing energy loss (NIEL) of 95 $MeV \cdot mb$. As it is not possible in any irradiation test program to irradiate the test sensors or devices realistically according to the actual radiation composition, one has to work with the hardness factor concept to achieve comparable damage scenarios. The calculations for CMS show, that for different tracker regions the damage functions of the LHC spectrum can be averaged in different NIEL damage constants [CMSb]. The results in table 13.1 demonstrate, that the NIEL decreases in the inner part of the detector, due to the higher particle energies. This is also valid for the SLHC, as no energy change is planned. As so far only the total fluences have been calculated, the neutron equivalent fluences have been evaluated by multiplying the total fluences with the ratio between the value in table 13.1 and 95 $MeV \cdot mb$. This leads to the plot in figure 13.1. It shows the expected neutron equivalence fluences in a CMS tracker at the SLHC. Results which rely on neutron equivalent fluences, in particular the ones presented in this thesis, can then be directly compared with this calculated scenario.

One aim of the research work presented in this thesis was, to test whether sensors based on n-type MCz silicon offer the essential radiation hardness for an application in the strip or short-strip ("strixel") region of a future CMS tracker at the SLHC. Sufficiently high charge collection efficien-

	$\|\eta\| = 0-0.9$	$\|\eta\| = 0.9-1.8$	$\|\eta\| = 1.8-2.7$
$r = 0-20\ cm$	75 $MeV \cdot mb$	69 $MeV \cdot mb$	62 $MeV \cdot mb$
$r = 20-40\ cm$	88 $MeV \cdot mb$	85 $MeV \cdot mb$	82 $MeV \cdot mb$
$r = 40-65\ cm$	100 $MeV \cdot mb$	95 $MeV \cdot mb$	92 $MeV \cdot mb$
$r = 65-120\ cm$	109 $MeV \cdot mb$	106 $MeV \cdot mb$	104 $MeV \cdot mb$

Table 13.1: ***Average non-ionizing energy loss at different parts of the CMS tracker. [CMSb]*** *The reference NIEL for* 1 MeV *neutrons is* 95 $MeV \cdot mb$. *The damaging effects are smaller in the inner parts of the detector.*

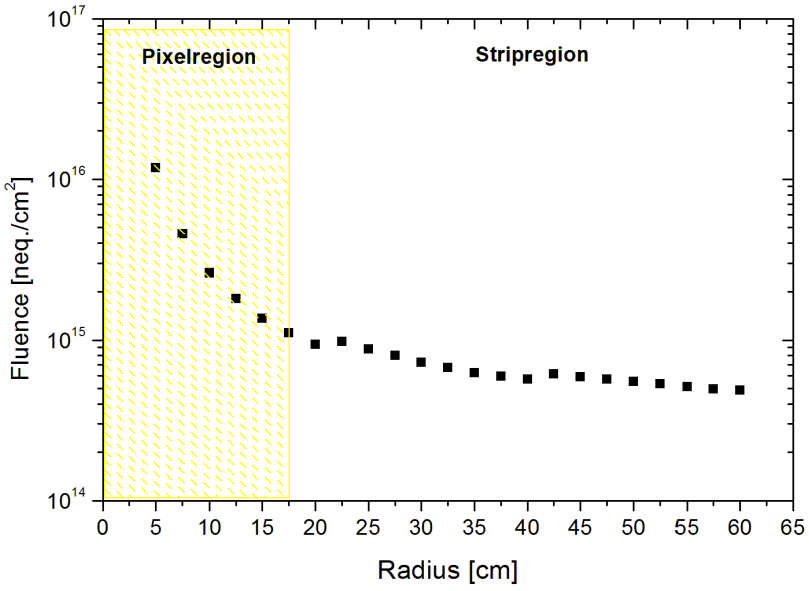

Figure 13.1: ***Expected total neutron equivalent fluences for a SLHC CMS tracker.*** *The damage constants differ at different radii. In the inner parts the damage effects for a given fluence are smaller. The adjusted plot with the neutron equivalent fluence allows direct comparisons and appraisals of the results generally based on neutron equivalent fluences.*

cies and low noise levels of the tracking sensors even after irradiations are needed to ensure good signal to noise ratios. Many authors state that for a reliable detection of a minimum ionizing particle and a suppression of fake events triggered by noise, the signal to noise ratio should not drop below around 10 [Mol06]. The charge of at least around 7000 electron-hole pairs is needed for this with the currently available readout electronics [H^+09a]. The resolution of the sensors should also not worsen significantly. For testing how these important sensor parameters get affected by radiations of SLHC fluences, testsensors were irradiated with neutron equivalent fluences between $1 \cdot 10^{14}/cm^2$ and $1.6 \cdot 10^{15}/cm^2$. It can be seen in figure 13.1, that the whole fluence range of the strip regions was considered thereby, covering even the outer pixel layers. The irradiations were done with 25 MeV protons and partly neutrons of an average energy of 20.4 MeV. Annealing programs after the irradiations were not foreseen, but an annealing at room temperature for about two weeks has to be considered.
The irradiated sensors have been tested in two beamtests and at a modules teststation. The special setup of the station allowed to apply higher bias voltages and to test at lower temperatures than during the beamtest. The higher bias voltages provided larger depleted volumes, while the lower temperatures lead to reductions of the noise generating leakage currents and a reduction of the trapping effect. Consequently higher charge collection efficiencies and higher signal to noise ratios were measured. In the following comparison of the results, only the highest measured values are presented. The measured charge collection efficiencies of the explored sensors are presented in figure 13.2, plotted against the radius that corresponds to the irradiation fluence of the tested sensor. The value that corresponds to a radius of 60 cm was obtained with a fully depleted sensor at 500 V and a temperature of around -10°C . For the result plotted at a radius of 40 cm, a bias voltage of 625 V ensured a full depletion

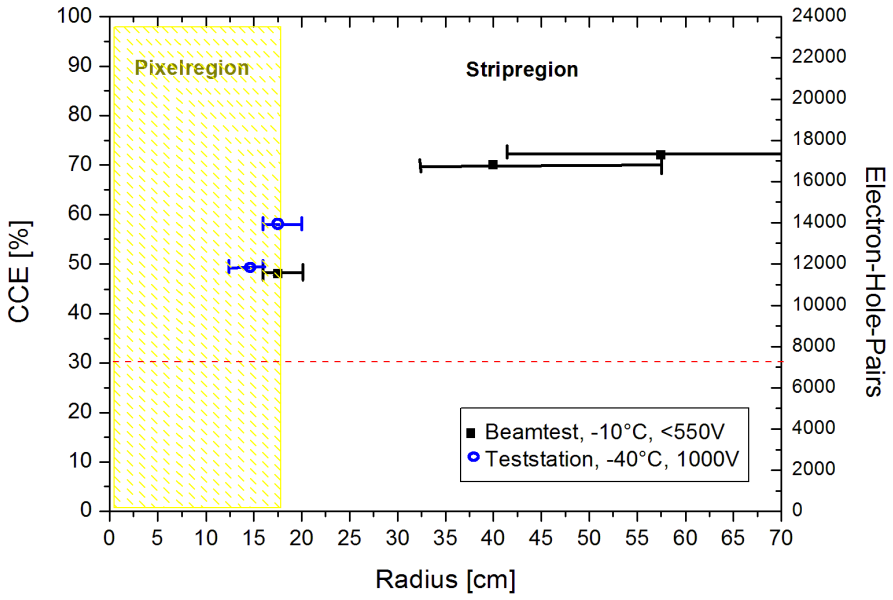

Figure 13.2: ***Measured charge collection efficiencies versus the tracker radii that correspond to the irradiation fluences.*** *Black quadratic dots correspond to measurements at the beamtest setup and blue circular ones to results of the teststation measurements. The error bars in x-direction are a consequence of the uncertainties in the determination of the irradiation fluences, while the statistical errors on the y-values are that small that they lie within the symbols. Measurements in the whole fluence range of the strip regions were done, also with fluences of the outer pixel layers. Even there a charge collection efficiency of still* $\sim 50\%$ *is possible. This corresponds to about 12000 electron hole pairs, being significantly more than the necessary limit of 7000 electron hole pairs that are represented by the dashed red line. A sufficient amount of charge can be collected with n-type MCz silicon sensors.*

during the test at a temperature of around -8°C . The two results at a radius of 17.5 *cm* already correspond to the first pixel layer. One was measured at the beamtest with the sensor being not fully depleted (550 *V*, -8°C) and one with the sensor fully depleted at the teststation (1000 *V*, -40°C). Even a sensor with a fluence of a position completely inside the pixel region was tested. At the teststation its charge collection efficiency was measured in a nearly completely depleted mode at 1000 *V* bias voltage and a temperature of -40°C . It can be seen that under these circumstances even in the pixel region a charge collection efficiency of still $\sim 50\%$ is possible. This corresponds to about 12000 electron hole pairs, being significantly more than the necessary limit of 7000 electron hole pairs that are represented by the dashed red line. It also illustrates that the collected charge of any of the tested sensors exceeded this limit, meaning that over the whole fluence range of the strip/strixel tracker the trapping is low enough so that a sufficient amount of charge can be collected with n-type MCz silicon sensors and reliable signals are generated.

The measured maximal signal to noise ratios were all higher than the demanded value of 10, due to the good CCE and as the noise increase could be suppressed by a reduction of the leakage currents by cooling. This can be seen in figure 13.3. The reference value of the non-irradiated module was

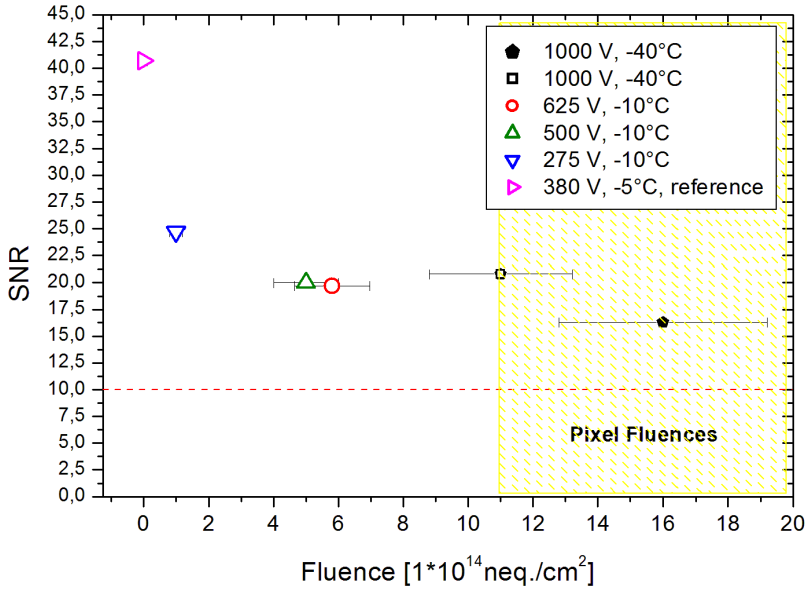

Figure 13.3: ***Measured signal to noise ratios against the fluence.*** *Even the sensors irradiated with pixel fluences show a considerably higher SNR than the desired 10 (illustrated by the red dashed line). A very good value of around 16 was measured for the sensor irradiated with a fluence of* $1.6 \cdot 10^{15}$ *neq./cm*^{2}*. An uncertainty in the measurement of the irradiation fluence leads to the error bars in x-direction, while the statistical error bars for the determination of the signal to noise ratios vanish in the symbol sizes.*

measured at -5°C with a bias voltage of 380 V, completely depleting the sensor. The sensor with a fluence of $1 \cdot 10^{14}$ *neq./cm*^{2}, tested at -10°C was also fully depleted with an applied voltage of 275 V. For the other results, the conditions were the same as the ones described above for the CCE measurements. Even the sensors irradiated with pixel fluences show a considerably higher SNR than the desired 10 (illustrated by the red dashed line). A very good value of around 16 was measured for the sensor irradiated with a fluence of $1.6 \cdot 10^{15}$ *neq./cm*^{2}. The results of the tests are summarized in table 13.2.

The significance of signal to noise results for a prediction of the performance that has to be expected for future sensor modules, is normally limited in the way that the value is not only affected by the used readout electronics, but also as it is dependent on the sensor design. In the present case, the SNR results are much more important. As it has been explained in chapter 2.2.2, the particle density at the SLHC will be much higher than at the LHC. To keep the occupancy of the sensors low, the strip length must definitely be reduced compared to the ones in use at CMS. Current plans for short strip sensors calculate with lengthes in the size of the 4 *cm* of the explored testsensors or even with smaller ones. Therefore the SNR results presented in this thesis serve as quite good lower limits of what is obtainable with strixel sensors where in the case of shorter strips the strip capacitances and the strip leakage currents are lower and higher signal to noise ratios have to be expected.

The positive outcome of the experiments get supported by the simulation results presented in chapter 11. They show, that the CCE of highly irradiated sensors is higher than a common charge collection

Name Fluence in $neq./cm^2$	n224B 0, reference	n017A $1 \cdot 10^{14}$	n224A $5 \cdot 10^{14}$	MCz0802B $5.8 \cdot 10^{14}$	MCz0802A $1.1 \cdot 10^{15}$	MCz0804B $1.6 \cdot 10^{15}$
prot.[%]/neutr.[%]	-	100 / 0	100 / 0	84 / 16	91 / 9	94 /6
Radius	-	$> 60\ cm$	$\approx 55\ cm$	$\approx 45\ cm$	$\approx 17.5\ cm$	$\approx 15\ cm$
Full depl. volt. in V	350	200	380	420	870 (e)	1300 (e)
Bias voltage in V	380	275	500	625	1000	1000
Temperature	-5°C	-10°C	-10°C	-10°C	-40°C	-40°C
Resolution in μm	12.8	13.8	16.1	11.4	12.8	-
CCE in %	100	83	72	70	58	49
SNR	40.9	24.8	20	19.4	20.8	16.3

Table 13.2: ***Summary of the results.*** *The table shows the name of the sensor, its fluence, the fraction of neutrons and protons of the irradiation, the corresponding radius at an SLHC CMS tracker, the measured or estimated (e) full depletion voltages, the bias voltage at which the following values were measured, the test temperature, the resolution, the charge collection efficiencies (CCE) and the signal to noise ratios (SNR).*

model predicts with the so far known parameter values. The influence of trapping on the signal seems to be less strong than supposed, as an adjustment of the concerned trapping parameters towards lower values ($\beta_e = 2 \cdot 10^{-7}\ cm^2/s$ and $\beta_h = 2.4 \cdot 10^{-7}\ cm^2/s$), reflecting higher trapping time constants, lead to an agreement of the measurements with the simulations. One group [B^+07] has measured values comparable with the one found in the simulation, even though for p-type MCz. In the model, the trapping does not depend on the bulk material type, so that also the anomalously high charge collection efficiencies for p-type MCz reported by [M^+09] seem to support the results presented before. In addition to these positive attributes, experiments presented in chapter 12 have proved that highly irradiated n-type MCz silicon sensors offer the feature of a double junction. This effect has the beneficial consequence that depleted zones around the position sensitive strip segments exist even before full depletion of a type inverted sensor.
It has been shown that the reduction of the charge collection efficiencies by the trapping effect of radiation damages is evidently less severe than expected by existing parameterizations of theoretical models. Tests to clarify whether this is a special MCz feature or whether this is also valid for standard FZ, as an adjustment of the model parameters is necessary in general, should be accomplished. The parameters might be dependent of the particle type and particle energy. Compared to highly irradiated standard FZ silicon sensors, highly irradiated MCz silicon sensors can get depleted at lower voltages, respectively a given bias voltage can generate a larger sensitive volume. This is an advantage of MCz silicon. The sufficiently high charge collection efficiencies and signal to noise ratios allow an operation of n-type MCz sensors at all radii of the strip tracker. An application even at the outer pixel layers seems possible, when applying higher voltages at lower temperatures than inside the current tracker. The question whether the material can also be used at the inner pixel radii has to be answered by tests with accordingly higher irradiated pixel testsensors. Nevertheless alternative sensor technologies and other materials are explored, possibly offering different options for the inner pixel layers. A positive aspect is, that for profiting of the beneficial material features of MCz silicon, the sensor design can be based on well established and well understood functional elements. Therefore no special or new sensor technologies are required for the inner strip regions of a future SLHC CMS tracker.

Chapter 14

Summary

The future Super Large Hadron Collider will be designed for a peak luminosity of $10^{35}\ cm^{-2}s^{-1}$, ten times higher than the one of the LHC. The higher particle densities result in higher radiation stresses for the detectors, in particular exceeding the radiation hardness limits of the current CMS tracker technology. One task is to find appropriate materials with beneficial features for the development of radiation hard sensors.
Magnetic Czochralski silicon has been identified as a promising candidate to serve as a basic material for semiconductor particle sensors. The concept of the research work presented in this thesis was, to investigate general properties of highly irradiated n-type MCz silicon sensors in view of testing their overall radiation hardness for a possible application in the strip and short-strip region of a future SLHC CMS tracker. Its positive feature considering the radiation hardness is, that the intrinsically higher oxygen content suppresses the formation of special radiation induced acceptor-like lattice damages and conglomerates that are responsible for changes of the effective doping concentration. Consequently the full depletion voltage increases less with higher radiation fluences compared with standard float zone silicon sensors.
A usage of sensors for the detection of ionizing particles is only possible together with an appropriate readout electronics. Normally they are both assembled on a carrier structure as a sensor module. Speaking of radiation hardness, one is mainly interested in a sufficiently high signal to noise ratio for the detection of minimum ionizing particles even after the damaging influence of radiation. The resolution, which has an upper limit by the design of the strip pitch, should also not degrade significantly. The signal is based on the amplified collected charge of electron-hole pairs, generated in the sensor bulk by the ionizing particle to be detected. The ratio between the collected charge and the totally generated one defines the charge collection efficiency. For a high signal to noise ratio, a high charge collection efficiency and a low noise level are of interest. Both parameters are negatively influenced by radiation damages. The noise normally rises with the leakage currents and the charge collection is reduced by the effect of trapping, when charge carriers are temporarily trapped at defects being lost for the signal thereby.
The main test programs presented in this thesis were planed for the determination of the so far unknown charge collection efficiences, the signal to noise ratios and the resolutions of p-in-n MCz strip sensors irradiated with SLHC fluences. In the first step of the program, the quality of dedicated 300 μm thick and $4x4\ cm^2$ large testsensors were checked. The importance of intensive sensor quality test programs in the preparation of the actual experiments became apparent before the beamtest in 2007, when problematic sensor parameters were found. The reason and a problem solving process could be identified. This finally ensured a good sensor quality and lead to consequences in the production of the

sensors for the beamtest in 2008. After the irradiations with protons and partly also neutrons with fluences between $1 \cdot 10^{14}$ $neq./cm^2$ and $1.6 \cdot 10^{15} neq./cm^2$, the sensors were tested again to receive the information of macroscopic effects of radiation damages on important sensor parameters, useful for the final analysis of the experimental data. The complete fluence range of the inner strip tracker was considered by the irradiations. In two beamtests with minimum ionizing 225 GeV muons of the CERN SPS, the actual measurements of mainly the charge collection efficiencies, the signal to noise ratios and the resolutions of the sensors were accomplished with the help of a new beamtelescope (SiBT) that delivered the essential information of the particle tracks.
After an adjustment of an analysis software, written at the IEKP, the data were analyzed. The results of irradiated sensors could be compared with the ones of tests with a non-irradiated MCz reference sensor and with a non-irradiated FZ reference sensor. They further provided the information of the maximally collectable charge for the determinations of the charge collection efficiencies. In a temperature range between 0°C and -10°C , sensors with fluences of up to $1.1 \cdot 10^{15}$ $neq./cm^2$, roughly expected at the edge between the strip part and the pixel part of the tracker, were tested in the beamtests. The highest irradiated sensor could not be fully depleted, so that the results for the charge collection efficiency and the signal to noise ratio must be regarded as lower limits, while the resolution result serves as an upper limit. This sensor nevertheless already showed a very good charge collection efficiency of 48 %, corresponding to about 11500 electron hole pairs. The signal to noise ratio of 12.3 was higher than the desired value of 10. A resolution of 12.8 μm was measured, which is better than the binary resolution of 14.4 μm for a 50 μm pitch device.
One MCz sensor was irradiated with a fluence of even $1.6 \cdot 10^{15}$ $neq./cm^2$ corresponding to a radius of about 15 cm in the pixel region of a SLHC CMS tracker. The module was tested in the Karlsruhe Diagnostic Teststation together with the highest irradiated sensor of the beamtest. To suppress the high leakage currents, the measurements were fulfilled at temperatures in the range between -30°Cand -40°C, which allowed to apply voltages of up to 1000 V without thermal runaways. The tests provided for the first time the essential information of the properties of such highly irradiated segmented MCz sensors at these low temperatures and high bias voltages. For the sensor with a fluence of $1.1 \cdot 10^{15}$ $neq./cm^2$, the charge collection efficiency was 58 %, higher than in the beamtest due to the different voltages and temperatures. The signal to noise ratio was 20.8. The charge collection efficiency of 49 % of the highest irradiated sensor ($1.6 \cdot 10^{15}$ $neq./cm^2$) and its low noise level lead to a signal to noise ratio of 16.3, which is excellent for a sensor that was more than eight times higher irradiated than the current CMS sensors will be. The very good signal to noise results of the used testsensors with a strip length of 4 cm can be regarded as lower limits of what is obtainable with short strip "strixel" sensors.
Simulations of the charge collection processes in highly irradiated sensors have been carried out. They further underline the very good results. In the process to achieve an agreement between the measurements and the simulations, values for the parameters β_e and β_h have been found to be $2 \cdot 10^{-7}$ cm^2/s, respectively $\beta_h = 2.4 \cdot 10^{-7}$ cm^2/s, differing from the so far known ones. The parameters describe in an established model the change of the inverse trapping time constants with the fluence. Evidently the currently known values overestimate the influence of trapping on the charge collection efficiency of the explored highly irradiated MCz sensors.
With a transient current technique setup further qualities of the MCz material have been studied. Measurements have been done, which prove that also for irradiated n-type MCz sensors, the double junction effect appears. The effect has the consequence that even for irradiated but not fully depleted sensors, active volumes around the position sensitive strip segments exist. This beneficial property adds to the sum of good attributes found in the other experiments.
Beside the idea to study principle features of n-type MCz silicon, the goal of the research work pre-

sented in this thesis was, to test the applicability of sensors based on this material for the regions in a future SLHC CMS tracker where an equipment with strip or short-strip sensors is foreseen. This task has been successfully fulfilled.
Summarizing the promising results, it can finally be concluded that n-type MCz silicon offers more than sufficient qualities and properties to serve as a basic material for tracking sensors that can withstand the harsh conditions in the strip and short strip regions of a CMS tracking detector at the Super Large Hadron Collider.

Appendix A

Expected Fluences at a CMS tracker at the SLHC

R	charged hadrons / cm^{-2}	neutrons / cm^{-2}	total / cm^{-2}	ratio p/n	
5	1.39E+016	9.96E+014	1.49E+016	13.9	pixel
7.5	5.13E+015	6.31E+014	5.76E+015	8.1	pixel
10	2.74E+015	5.52E+014	3.30E+015	5.0	pixel
12.5	1.78E+015	5.17E+014	2.30E+015	3.5	pixel
15	1.25E+015	4.85E+014	1.74E+015	2.6	pixel
17.5	9.40E+014	4.61E+014	1.40E+015	2.0	pixel
20	7.41E+014	4.47E+014	1.19E+015	1.7	inner tracker
22.5	6.05E+014	4.41E+014	1.05E+015	1.4	inner tracker
25	5.12E+014	4.31E+014	9.42E+014	1.2	inner tracker
27.5	4.39E+014	4.23E+014	8.62E+014	1.0	inner tracker
30	3.72E+014	4.10E+014	7.83E+014	0.9	inner tracker
32.5	3.19E+014	4.09E+014	7.27E+014	0.8	inner tracker
35	2.79E+014	3.96E+014	6.75E+014	0.7	inner tracker
37.5	2.47E+014	3.94E+014	6.40E+014	0.6	inner tracker
40	2.17E+014	3.99E+014	6.15E+014	0.5	inner tracker
42.5	1.91E+014	3.96E+014	5.87E+014	0.5	inner tracker
45	1.75E+014	3.87E+014	5.62E+014	0.5	inner tracker
47.5	1.54E+014	3.91E+014	5.46E+014	0.4	inner tracker
50	1.38E+014	3.87E+014	5.25E+014	0.4	inner tracker
52.5	1.20E+014	3.89E+014	5.09E+014	0.3	inner tracker
55	1.07E+014	3.80E+014	4.87E+014	0.3	inner tracker
57.5	9.62E+013	3.76E+014	4.72E+014	0.3	inner tracker
60	8.70E+013	3.76E+014	4.63E+014	0.2	outer tracker

Table A.1: ***Fluences of charged hadrons, neutrons and the total fluences expected at different radii of a CMS tracker at the SLHC [Huh04].***

List of Figures

List of Tables

Bibliography

[A+99] L. Andricek et al. Radiation hard strip detectors for large-scale silicon trackers. *Nuclear Instruments and Methods in Physics Research A*, 436, 1999.

[B+04] Hans Bichsel et al. Passage of Particles through Matter. *Physics Letters*, B592, 2004.

[B+07] Mara Bruzzi et al. Comparing radiation tolerant materials and devices for ultra rad-hard tracking detectors. *Nuclear Instruments and Methods in Physics Research A*, 579, 2007.

[Bic88] Hans Bichsel. Straggling in thin silicon detectors. *Reviews of Modern Physics*, 60, 1988.

[Bic92] Hans Bichsel. Stopping power and ranges of fast ions in heavy elements. *Physical Review A*, 46, 1992.

[Ble07] M. Bleyl. Signal-to-noise measurements on irradiated CMS tracker detector modules in an electron testbeam. *Nuclear Instruments and Methods in Physics Research A*, 583, 2007.

[BM05] Alison G. Bates and Michael Moll. A comparison between irradiated magnetic Czochralski and float zone silicon detectors using the transient current technique. *Nuclear Instruments and Methods in Physics Research A*, 555, 2005.

[C+75] C. Canali et al. Electron drift velocity in silicon. *Physical Review B*, 12, 1975.

[C+05] M. Casati et al. Characterization of standard and oxygenated float zone Si diodes under radiotherapy beams. *Nuclear Instruments and Methods in Physics Research A*, 552, 2005.

[CC2] http://cerncourier.com/cws/article/cern/35872/2/CCcol3_10_08.

[CMSa] Supply of Silicon Micro-Strip Sensors for The CMS Silicon Strip Tracker (SST), Technical Specification.

[CMSb] The Tracker Project, Technical Design Report, CMS Tracker TDR 5, CERN/LHCC 98-6. http://cmsdoc.cern.ch/ftp/TDR/TRACKER/final/chapters/tdrapp.pdf.

[CMSc] CMS. http://cms.web.cern.ch/cms/Resources/Website/Media/Images/Detector/ Detector-Drawings/fromGEANT/cms_complete_labelled.pdf.

[CMS00] CMS TDR 5 Addendum 1, CERN/LHCC 2000-016, February 2000.

[dBE08] Wim de Boer and Jochen Ebert. Powering via Cooling Pipes: An Optimized Design for an SLHC Silicon Tracker. *arXiv:0811.2886v1 [physics.ins-det] 18 Nov 2008*, 2008.

[Die03] A. Dierlamm. *Untersuchungen zur Strahlenhärte von Siliziumsensoren*. PhD thesis, Universität Karlsruhe, 2003.

[Die09] A. Dierlamm. CMS Tracker upgrade issues and plans. *Nuclear Instruments and Methods in Physics Research A*, Article in press, 2009.

[Dir03] Guido Dirkes. *Development and Implementation of Quality Control Strategies for CMS Silicon Strip Tracker Modules*. PhD thesis, Universität Karlsruhe, 2003.

[ea07] Z. Li et al. Cryogenic Si detectors for ultra radiation hardness in SLHC environment. *Nuclear Instruments and Methods in Physics Research A*, 579, 2007.

[edm] Documents 314986/1, 314987/1, 314983/1, 318639/5, 318642/5 and 318641/5, CERN engineering data management service.

[EL08] Lyn Evans and Lucie Linssen. The Super-LHC is on the starting blocks. *CERN Courier, July / August*, 2008.

[Fah06] Manuel Fahrer. *Beam Loss Studies on Silicon Strip Detector Modules for the CMS Experiment*. PhD thesis, Universität Karlsruhe, 2006.

[Fre04] M. Frey. Studien zur Langzeitstabilität und Qualität von Siliziumstreifensensoren für das CMS-Experiment, Diplomarbeit, Universität Karlsruhe, 2004.

[Fur06] A. Furgeri. *Qualitätskontrolle und Bestrahlungsstudien an CMS Siliziumstreifensensoren*. PhD thesis, Universität Karlsruhe, 2006.

[H+96] G. Hall et al. Defect evolution in irradiated silicon detector material. *Nuclear Instruments and Methods in Physics Research A*, 374, 1996.

[H+00] F. Hügging et al. Design and test of pixel sensors for operation in severe radiation environments. *Nuclear Instruments and Methods in Physics Research A*, 439, 2000.

[H+02] K. Hagiwara et al. Review of Particle Physics. *Phys. Rev. D66:010001+*, 2002.

[H+07] J. Härkönen et al. Magnetic Czochralski silicon as detector material. *Nuclear Instruments and Methods in Physics Research A 579*, 2007.

[H+09a] J. Härkönen et al. Development of cryogenic tracking detectors for very high luminosity experiments. *Nuclear Instruments and Methods in Physics Research A*, Article in Press, 2009.

[H+09b] J. Härkönen et al. Test beam results of a heavily irradiated Current Injected Detector (CID). *in preparation*, 2009.

[Hae] Private communication.

[Har02a] Frank Hartmann. http://cms.web.cern.ch/cms/Resources/Website/Media/ Publications/Posters/DetectorPosters/files/Trackers.pdf, 2002.

[Har02b] Frank Hartmann. The CMS All-Silicon Tracker - Strategies to ensure a high quality and radiation hard Silicon Detector. *Nuclear Instruments and Methods in Physics Research A*, 478, 2002.

[Har08] Frank Hartmann. *Evolution of Silicon Sensor Technology in Particle Physics*. Springer, 2008.

[Hei] http://www.kip.uni-heidelberg.de/ti/TRD/images/over_lhctunnel.jpg.

[Hön07] Frank Hönniger. *Radiation Damage in Silicon - Defect Analysis and Detector Properties*. PhD thesis, Universität Hamburg, 2007.

[Hof08] Karl-Heinz Hoffmann. Vorbereitende Arbeiten zur Qualitätskontrolle zukünftiger Halbleiterdetektoren in Hochenergieexperimenten, Diplomarbeit, Universität Karlsruhe, 2008.

[Hon] Alan Honma, private communication.

[Här04] J. Härkönen. Radiation hardness of Czochralski silicon, Float Zone silicon and oxygenated Float Zone silicon studied by low energy protons. *Nuclear Instruments and Methods in Physics Research A*, 518, 2004.

[Huh02] M. Huhtinen. Simulation of non-ionising energy loss and defect formation in silicon. *Nuclear Instruments and Methods in Physics Research A*, 491, 2002.

[Huh04] M. Huhtinen. Radiation issues for SLHC, SLHC Electronics workshop, 2004.

[IPN] *CMS, Trigger Sequencer Card, User Manual, Version 2.0, Institut de Physique Nucleaire de Lyon, 2002 ftp://lyoftp.in2p3.fr/cms/Tsc/tsc02.pdf*.

[K$^+$02] G. Kramberger et al. Effective trapping time of electrons and holes in different silicon materials irradiated with neutrons, protons and pions. *Nuclear Instruments and Methods in Physics Research A*, 481, 2002.

[KL93] H.W. Kraner and Z. Li. The use of the signal current pulse shape to study the internal electric field profile and trapping effects in neutron damaged silicon detectors. *Nuclear Instruments and Methods in Physics Research A*, 326, 1993.

[Kop93] K. Kopitzki. *Einführung in die Festkörperphysik*. Teubner, 1993.

[L$^+$96] Z. Li et al. Development of transient current and charge techniques for the measurement of effective net concentration of ionized charges (Neff) in the space charge region of p-n junction detectors. *Nuclear Instruments and Methods in Physics Research A*, 372, 1996.

[L$^+$01a] G. Lindström et al. Developments for radiation hard silicon detectors by defect engineering - results by the CERN RD48 (ROSE) Collaboration. *Nuclear Instruments and Methods in Physics Research A 465*, 2001.

[L$^+$01b] G. Lindström et al. Radiation hard silicon detectors - developments by the RD48 (ROSE) collaboration. *Nuclear Instruments and Methods in Physics Research A*, 466, 2001.

[L$^+$09] P. Luukka et al. TCT and testbeam results of irradiated magnetic Czochralski silicon (MCz-Si) detectors. *Nuclear Instruments and Methods in Physics Research A*, Article in press, 2009.

[Led06] B. Ledermann. *Entwicklungsstudien für den ILC : Messungen und Simulationen für eine Zeit-Projektionskammer mit GEM-Technologie*. PhD thesis, Universität Karlsruhe, 2006.

[LHC] The LHC Design Report, http://doc.cern.ch/cernrep/2004/2004-003-v1/2004-003-v1.html.

[Lia07] Thiansin Liamsuwan. Untersuchung zur Strahlenhärte von Magnetic Czochralski-Siliziumstreifensensoren, Diplomarbeit, Universität Karlsruhe, 2007.

[Lin87] Victor A.J. Van Lint. The Physics of Radiation Damage in Particle Detectors. *Nuclear Instruments and Methods in Physics Research A 253*, 1987.

[Lin03] Gunnar Lindström. Radiation damage in silicon detectors. *Nuclear Instruments and Methods in Physics Research A*, 512, 2003.

[LN62] J. Lindhard and V. Nielsen. Nuclear Collisions and Ionisation Fluctuations in Chaged Particle Detectors. *Physics Letters*, 2, 1962.

[Lut99] G. Lutz. *Semiconductor Radiation Detectors*. Springer, 1999.

[M+96] J. Matheson et al. A microscopic explanation for type inversion and the annealing behaviour of radiation damaged silicon detectors. *Nuclear Instruments and Methods in Physics Research A*, 371, 1996.

[M+03] G. Magazzu et al. *DCUF User Guide http://cmstrackercontrol.web.cern.ch/cmstrackercontrol/documents/Magazzu/DCUF_User_Manual_v3.0.pdf*, 2003.

[M+07] N. Manna et al. Space charge sign inversion investigation in n-type MCz silicon diodes irradiated by 24 GeV/c and 26MeV protons and reactor neutrons. *Nuclear Instruments and Methods in Physics Research A*, 583, 2007.

[M+08] T. Mäenpää et al. Silicon beam telescope for LHC upgrade tests. *Nuclear Instruments and Methods in Physics Research A*, 593, 2008.

[M+09] Igor Mandic et al. Measurement of anomalously high charge collection efficiency in n^+p strip detectors irradiated by up to 10^16 neq/cm^2. *Nuclear Instruments and Methods in Physics Research A*, 2009.

[Men99] D. Menichelli. Modelling of observed double-junction effect. *Nuclear Instruments and Methods in Physics Research A*, 426, 1999.

[Mes07] Alberto Messineo. Czochralski silicon sensors: Status of development. *Nuclear Instruments and Methods in Physics Research A 582*, 2007.

[Mol99] M. Moll. *Radiation Damage in Silicon Particle Detectors*. PhD thesis, Universität Hamburg, 1999.

[Mol06] M. Moll. Radiation Tolerant Silicon Detectors. Scientific Meeting, CERN, ph-dt2.web.cern.ch/PH-DT2/Documents/061013-DT2-Tea-RD50-silicon.ppt, Oktober 2006.

[Mos09] Hans-Günther Moser. Silicon detector systems in high energy physics. *Progress in Particle and Nuclear Physics*, Article in Press, 2009.

[Nas07] J. Nash. CMS Expression of Interest in the SLHC. *CERN/LHCC 2007-014 LHCC-G-131*, 2007.

[NDD] http://www.nndc.bnl.gov/.

[Neu09] Maike Neuland. Untersuchungen der Kenngrößen von hochbestrahlten Magnetic-Czochralski-Siliziumstreifensensoren im Rahmen des SLHC-Projekts, Diplomarbeit, Universität Karlsruhe, 2009.

[P+02] C. Paillard et al. The CCU25: A network oriented Communication and Control Unit integrated circuit in a 0.25 micrometer CMOS technology http://lhc-electronics-workshop.web.cern.ch/LHC-electronics-workshop/2002/Tracker/A48.pdf, 2002.

[P+05] G. Pellegrini et al. Characterization of magnetic Czochralski silicon radiation detectors. *Nuclear Instruments and Methods in Physics Research A 548*, 2005.

[P+06] I. Pintilie et al. Stable radiation-induced donor generation and its influence on the radiation tolerance of silicon diodes. *Nuclear Instruments and Methods in Physics Research A*, 556, 2006.

[Pit92] D. Pitzl. Type Inversion in Silicon Detectors. *Nuclear Instruments and Methods in Physics Research A*, 311, 1992.

[Pri02] M.J. Price. The LHC project. *Nuclear Instruments and Methods in Physics Research A*, 478, 2002.

[RD5] http://rd50.web.cern.ch/rd50/doc/Internal/rd50_2003_003_version_15-10-2004.doc.

[RD507] Rd50 status report 2007. *CERN-LHCC-2008-001 and LHCC-RD-015*, 2007.

[Ruz00] A. Ruzin. Recent results from the RD-48 (ROSE) Collaboration. *Nuclear Instruments and Methods in Physics Research A 447 (2000) 116-125*, 2000.

[S+02] V. Savolainen et al. Simulation of large-scale silicon melt flow in magnetic Czochralski growth. *Journal of Crystal Growth*, 243, 2002.

[S+07] M. Scaringella et al. Localized energy levels generated in Magnetic Czochralski silicon by proton irradiation and their influence on the sign of space charge density. *Nuclear Instruments and Methods in Physics Research A*, 570, 2007.

[Sze81] S.M. Sze. *Physics of Semiconductor Devices*. John Wiley & Sons, 1981.

[T+01] R. Turchetta et al. Design and results from the APV25, a Deep Submicron CMOS Front-End Chip for the CMS Tracker. *Nuclear Instruments and Methods in Physics Research A*, 466, 2001.

[Tri08] Alesio Tricomi. SLHC: The LHC luminosity upgrade. *Nuclear Instruments and Methods in Physics Research A*, 596, 2008.

[V+02] E. Verbitskaya et al. The origin of double peak electric field distribution in heavily irradiated silicon detectors. *Nuclear Instruments and Methods in Physics Research A*, 476, 2002.

[Vir04] Tejinder S. Virdee. Detectors at LHC. *Physics Reports*, 403-404, 2004.

[vL+80] V.A.J. van Lint et al. *Mechanisms of radiation effects in electronic materials*. Wiley, 1980.

[Zie04] James F. Ziegler. SRIM-2003. *Nuclear Instruments and Methods in Physics Research B*, 219-220, 2004.

[Zim07] F. Zimmermann. LHC Upgrade Scenarios. In *Contribution to the 22nd Particle Accelerator Conference PAC07, Albuquerque (USA), CARE-Conf-07-019-HHH*, 2007.

Acknowledgement

First of all I want to thank Prof. Dr. Thomas Müller for giving me the possibility to accomplish this thesis in the exciting research field of silicon sensors and detector technology. His support allowed for the great and precious experience I got during my stay at CERN and during the research work in international collaborations.
Prof. Dr. Wim de Boer I want to thank for taking the co-reference and for encouraging me to proceed with measurements at the TCT.
I thank Dr. Frank Hartmann for his support in so many fields and his help and the fruitful discussions on topics of semiconductor sensors and detector control systems. Thanks a lot for the useful contributions to my script.
Dr. Alexander Dierlamm I thank for being an all-round contact person with numerous important tips on topics like Linux, Root, TCT, analysis etc. Also I want to thank him for the irradiations and the corrections to my script.
Dr. Hans-Jürgen Simonis I want to thank for his help with computer and network problems and the gluing of the modules.
I want to thank Dr. Peter Blüm for his useful advices, his experience and the organization of the great hiking tours.
Many thanks to Dr. Bernhard Ledermann for his SiBTStar analysis script.
Dr. Manuel Fahrer I thank for his changes in his teststation software.
I thank Dr. Alexander Furgeri for the irradiations.
Our technicians Pia Steck and Tobias Barvich, I want to thank for their work in the module productions and in the modifications of the teststations. They always found quickly solutions for numerous suddenly arising technical problems, which was essential to keep projects in time.
The former diploma students Dipl.-Phys. Thiansin Liamsuwan, Dipl.-Phys. Maike Neuland and Dipl.-Phys. Karl-Heinz Hoffmann, I thank for their good work. I had a great time with you all.
My colleagues Dr. Andreas Sabellek, Dr. Mike Schmanau and Dr. Thomas Weiler I thank for useful hints in the preparation for the examination.
For helping through administrative problems I thank Diana Fellner and Brigitte Schulz.
All my colleagues of the DCS project I thank a lot for the teamwork and the nice time at CERN. Special thanks to Dr. Guido Dirkes for his help on power supplies and to Lorenzo Masetti for the time working together on the DCS.
Thanks a lot to all the members of the SiBT-collaboration for their different contributions to the successful beamtests.
Zum Schluss möchte ich ganz herzlich meiner Familie danken für den Rückhalt den sie mir gab. Meiner Cousine Christina Dahl danke ich für die vielen und langen, oft philosophischen Gespräche, die eine Abwechslung in der Zeit des Schreibens waren. Ganz besonders bedanke ich mich bei meinen Eltern Ilse Frey und Gerhard Frey für ihre Unterstützung über diese lange Zeit. Danke dass ihr mir das Studium ermöglicht habt!